UNIVERSIDAD COMPLUTENSE DE MADRID

FACULTAD DE CIENCIAS QUÍMICAS

Departamento de Química Inorgánica I

TESIS DOCTORAL

Influencia de la variación de la composición en la microestructura de óxidos luminiscentes

MEMORIA PARA OPTAR AL GRADO DE DOCTOR

PRESENTADA POR

Margarita Andrea Peche-Herrero

Directores

José Mª González-Calbet
Julio Ramírez-Castellanos

Madrid, 2017

UNIVERSIDAD COMPLUTENSE DE MADRID

FACULTAD DE CIENCIAS QUÍMICAS

Departamento de Química Inorgánica I

Influencia de la variación de la composición en la microestructura de óxidos luminiscentes

MEMORIA PARA OPTAR AL GRADO DE DOCTOR EN CIENCIAS QUÍMICAS

PRESENTADA POR

MARGARITA ANDREA PECHE-HERRERO

DIRECTORES:

Prof. José Mª González-Calbet

Dr. Julio Ramírez-Castellanos

MADRID 2015

A mi madre.

“Caí herido,

descansaré sobre mi joven sangre,

y continuaré el camino.”

AGRADECIMIENTOS

Esta tesis ha sido realizada en el Departamento de Química Inorgánica de la Facultad de Ciencias Químicas de la Universidad Complutense de Madrid, a cuyos directores, Emilio Morán y José Antonio Campo quiero manifestar mi agradecimiento.

Quiero agradecer a mis directores, Dr. Julio Ramírez-Castellanos y Dr. José-Mª González-Calbet, el haberme dado la oportunidad de realizar esta tesis.

Al Ministerio de Innovación y Ciencia y al Ministerio de Economía) por concederme la beca-contrato FPI y las estancias breves asociadas de las que he podido disfrutar.

Al Centro Nacional de Microscopía Electrónica de la Universidad Complutense, por las facilidades prestadas, a su director científico Dr. Javier García, y a los técnicos por su ayuda desinteresada y el tiempo dedicado, en especial a Juan Luis Baldonedo.

Así mismo, quisiera agradecer a los miembros del CAI de Difracción de Rayos X, Dr. Emilio Matesanz y Dr. Julián Vázquez su paciencia y ayuda.

A mis compañeros de doctorado: Irma, Achraf, Daniel, Ángel, Isa, Lau, y Alberto; A los proyectandos: Víctor, Bea y Jaime. Muchas gracias por todos los buenos momentos que hemos pasado.

Al grupo de investigación de Materiales Inorgánicos No Moleculares, por el apoyo recibido. Y al resto de compañeros del Departamento de Química Inorgánica.

A los miembros del grupo del Prof. Javier Piqueras: Dra. Ana Cremades, Dra. Bianchi Méndez, Dr. David Maestre, Dr. Emilio Nogales, Cristian Vasquez, Iñaki López y Javier Bartolomé, por su imprescindible colaboración, ayuda y conocimientos proporcionados.

Al Prof. Yoshio Matsui por recibirme tan amablemente en el NIMS. Al Prof. Koji Kimoto y al Dr. Toru Hara, por permitirme aprender con sus equipos y proporcionarme toda la ayuda necesaria.

Al Dr. Duncan Alexandre, Dra. Cecile Hebert y Prof. Pierre Stadelmann, que tan bien me acogieron en el CIME (EPFL). Un agradecimiento en particular al Dr. Alexandre por su dedicación y sus enseñanzas. A mis compañeros del EPFL, que se convirtieron en amigos.

Por último y no por ello menos importante, agradecer a mi familia y amigos por su paciencia conmigo, sin su apoyo nada hubiera sido posible.

INDICE

CAPITULO IV. NANOMATERIALES BASADOS EN β-Ga_2O_3.

1. In-DOPED GALLIUM OXIDE MICRO-AND NANOSTRUCTURES: MORPHOLOGY, STRUCTURE, AND LUMINESCENCE PROPERTIES
2. INFLUENCE OF Sn AND Cr DOPING ON MORPHOLOGY AND LUMINESCENCE OF THERMALLY GROWN Ga_2O_3 NANOWIRES

CAPITULO V. ÓXIDOS DE LA SERIE HOMOLOGA $In_2Zn_kO_{3+k}$.

1. INTRODUCCION
2. PREPARACIÓN DE LOS MATERIALES
3. CARACTERIZACIÓN ESTRUCTURAL Y MICROESTRUCTURAL.
    3.1. DIFRACCIÓN DE RAYOS X
    3.2. ESPECTROSCOPIA POR DISPERSIÓN DE ENERGÍAS (EDS)
    3.3. DIFRACCIÓN DE ELECRONES DE AREA SELECCIONADA (SAED) Y MICROSCOPÍA ELECTRÓNICA DE ALTA RESOLUCIÓN (HRTEM)
4. PROPIEDADES CATODOLUMINISCENTES
5. CONCLUSIONES

CONCLUSIONES

ANEXO I TÉCNICAS DE CARACTERIZACIÓN DE PROPIEDADES FÍSICAS

1. CATODOLUMINESCENCIA
2. ESPECTROSCOPIA RAMAN
3. ESPECTROSCOPIA DE FOTOEMISION DE RAYOS X

RESUMEN

El objetivo de este trabajo es un estudio detallado de la síntesis, caracterización estructural y microestructural de los sistemas $M_{1-x}M'_xO_2$ (M= Ti, Sn; M'= Al, V, Cr, Mn, Fe; 0≤x≤0.3), β-$Ga_{2-x}M_xO_3$ (M=In, Sn y Cr) y la serie homóloga $Zn_kIn_2O_{3+k}$ (3≤k≤13).

Todos ellos son materiales semiconductores cuya composición y morfología son clave para sus aplicaciones tecnológicas. En este sentido, es necesario utilizar métodos de síntesis que aseguren la homogeneidad composicional y morfológica de los materiales obtenidos. El estudio estructural de los materiales se ha realizado mediante técnicas de difracción de rayos X y microscopía electrónica. La caracterización de las propiedades físicas se ha llevado a cabo mediante técnicas de catodoluminiscencia, espectroscopía Raman y espectroscopía de fotoemisión de rayos X. Estas técnicas proporcionan información de la estructura de bandas de los materiales, responsable de sus propiedades optoelectrónicas.

El *Capítulo I* revisa brevemente la situación actual de los materiales semiconductores con aplicaciones optoelectrónicas, haciendo especial hincapié en los denominados óxidos conductores transparentes (*transparent conducting oxides*, TCO), ya que los materiales estudiados son excelentes candidatos en aplicaciones tecnológicas.

El *Capítulo II* se ha dividido en dos partes. En la primera de ellas, se describen los aspectos básicos de los métodos de síntesis empleados en la obtención de los materiales estudiados. En la segunda parte, se expone una breve descripción de los equipos de caracterización estructural y composicional empleados, como la *difracción de rayos X* y la *microscopia electrónica de transmisión*. Por último, se describen las técnicas utilizadas en el estudio de las propiedades de los materiales, como la *espectroscopia de fotoemisión de rayos X*, la *espectroscopía Raman* y la *cátodoluminiscencia*.

El *Capítulo III* recoge los resultados obtenidos en el estudio de los óxidos binarios dopados con metales de transición, de fórmula general $M_{1-x}M'_xO_2$ (M= Ti, Sn; M'= V, Cr, Mn, Fe, Al; 0≤x≤0.3), así como la obtención y caracterización de microtubos de TiO_2 dopado con Cr. Se discute la influencia del dopado en la morfología, la estabilización de las distintas fases y la variación de las propiedades cátodoluminiscentes de estos materiales.

En el *Capítulo IV* se presentan los resultados del estudio de nanoestructuras alargadas de β-Ga_2O_3, dopadas con distintos metales. Se discute la influencia del dopante en los mecanismos de crecimiento, la presencia de defectos estructurales y la morfología de las nanoestructuras, así como el control de la respuesta luminiscente, ampliando su versatilidad como materiales potencialmente útiles.

Por último, en el *Capítulo V*, se presenta y discute la obtención de diferentes términos ordenados de la serie homóloga del sistema In-Zn-O, de fórmula general $Zn_kIn_2O_{k+3}$ con $3 \leq k \leq 13$. Se han obtenido mediante reacción en estado sólido, con un control riguroso de la temperatura y el tiempo. Se caracteriza la estructura que presentan, así como la variación de las propiedades luminiscentes de los distintos términos. Se ha prestado especial atención a la distribución de los átomos de In, presentando una revisión de los distintos modelos estructurales propuestos. La microscopía electrónica con aberración corregida ha permitido estudiar la modulación en la estructura que presentan estos materiales.

Los resultados se resumen en las publicaciones científicas presentadas en cada capítulo. Finalmente, se recogen las principales conclusiones de este trabajo.

CAPITULO I. INTRODUCCIÓN

Los materiales luminiscentes eficientes se emplean en una amplia gama de dispositivos, entre los que pueden citarse los láseres, las lámparas fluorescentes, las pantallas planas electro-luminiscentes, las pantallas de plasma, los tubos de rayos catódicos, los dispositivos de centelleo, etc. Este comportamiento se consigue cuando se obtienen materiales que presentan una señal de catodoluminiscencia con alta eficiencia de emisión en las tres bandas de emisión principales, denominadas banda naranja, asociada a la presencia de vacantes de oxígeno, banda verde y banda azul (2.58 eV). Y aún mejor, los materiales con emisión blanca por combinación de las anteriores. Los óxidos luminiscentes basados en semiconductores y aislantes son muy prometedores para estas aplicaciones debido a los valores amplios de sus gaps de energía (E_g) y a los valores bajos de absorbancia en la región visible del espectro. Presentan, además, las ventajas propias de los óxidos, estabilidad química y térmica, respecto de otros compuestos como los sulfuros y oxisulfuros. Actualmente, son muchos los materiales que son excitados ópticamente con un haz de electrones, entre los que cabe destacar las pantallas de los microscopios electrónicos de transmisión, los monitores de los osciloscopios, los detectores de rayos beta y las pantallas de alta resolución o dispositivos que hacen uso de los tubos de rayos catódicos. Esta profusión de dispositivos justifica el enorme número de investigaciones que se dirigen al estudio de materiales cátodoluminiscentes.

Sin embargo, los materiales que existen en el mercado admiten todavía un margen de mejora. Desventajas tales como el deterioro del brillo con el tiempo, el relativamente alto coste de producción, la contaminación ambiental… son aspectos a superar. Incluso, la posibilidad de generar la banda azul de manera más eficiente, todavía es un reto a conseguir, dado que este color es el más energético. Todo esto hace que la investigación en torno a estos materiales sea muy activa, de forma que los trabajos de numerosos grupos se dirigen al desarrollo de diversos métodos de síntesis que permitan explorar diferentes estructuras cristalinas con variedad de tamaño y morfología, habiéndose incrementado enormemente en los últimos años el interés por los óxidos nanocristalinos.

Efectivamente, las propiedades ópticas de un material están directamente relacionadas con

la interacción entre la materia y las ondas electromagnéticas y su comportamiento puede ser modelado con las ecuaciones de Maxwell. Sin embargo, en un sistema nanométrico las partículas están confinadas en regiones de dimensiones comparables a la longitud de onda por lo que la física de estos sistemas no puede ser explicada con conceptos clásicos pero sí con los de la mecánica cuántica. Actualmente, existe toda una gama de materiales nanoestructurados tales como nanopartículas, nanotubos, nanoláminas, puntos cuánticos, nanofibras, nanobarras, cuyo uso se ha extendido a diversas áreas como la electrónica, la aeronáutica, la comunicación, los dispositivos ópticos, los sensores... [1, 2].

En la intensa búsqueda de nuevos materiales, en los últimos años se ha incrementado el interés por los óxidos nanocristalinos cátodoluminiscentes. El estudio de la generación de colores primarios en materiales nanoestructurados ha sido muy amplio y se ha utilizado una gran variedad de materiales para la generación de alguno de los colores individualmente o la combinación de ellos para la generación del color blanco. Actualmente, la búsqueda de nuevos materiales de mayor eficiencia continúa, sin que se conozca con precisión la relación entre la morfología, tamaño de partícula y propiedades ópticas. El reto actual es complementar esta información para lograr la optimización que permita el desarrollo de dispositivos tecnológicos más avanzados.

Óxidos semiconductores

Al reducir las dimensiones de los óxidos hasta alcanzar tamaños nanométricos, disminuye la escala de los fenómenos analizados por lo que, como se ha mencionado, deberán incluirse en ocasiones fenómenos cuánticos en su estudio. No solo las propiedades físicas sino también las químicas varían considerablemente en función de las dimensiones del material. Así, en el caso de los óxidos semiconductores se ha comprobado experimentalmente que al disminuir su tamaño mejoran sus propiedades mecánicas, aumentando su flexibilidad y extensibilidad plástica. Del mismo modo, en el caso de los sensores de gases, la elevada relación superficie/volumen que presentan los sistemas nanoestructurados, incrementa significativamente su eficiencia y sensibilidad a la interacción con gases. Los fenómenos cuánticos amplían las posibilidades de aplicación de estos materiales en dispositivos SET (*Single Electron Transistor*), cristales fotónicos o microláseres. En general, la síntesis controlada de materiales nanoestructurados funcionales con dimensiones y morfología

controladas, posibilita su aplicación en múltiples dispositivos de elevado interés tecnológico tales como fotodetectores, diodos emisores de luz (LED), nanotransistores, dispositivos de lógica óptica o electrónica molecular, entre otros muchos [3-6]. Por lo tanto, el estudio de los procesos de crecimiento y caracterización de nanoestructuras representa un impulso básico en el desarrollo de la nanociencia y tecnología, recibiendo especial atención la obtención de materiales con dimensionalidad reducida como nanopartículas, nanohilos y cintas.

El tamaño de partícula afecta a las distintas propiedades del material. El primer grupo de propiedades que se ven afectadas, se refiere a las características estructurales como parámetros de red y simetría del cristal. Los materiales masivos son, generalmente, sistemas estables con estructuras cristalográficas bien definidas. Sin embargo, al reducir el tamaño de partícula, se modifican las tensiones de red y la energía superficial, produciendo cambios en la estabilidad termodinámica del material, que pueden inducir cambios en los parámetros de red y/o generar transformaciones estructurales. Para estabilizar una nanopartícula es necesario que se minimice su energía superficial; como consecuencia, fases que en el material masivo pueden ser inestables, se pueden estabilizar con la reducción del tamaño ya que aumenta el número de átomos localizados en la superficie, generando tensiones de red que pueden alterar la estructura del material. Más allá de la tensión "intrínseca" generada por la disminución del tamaño de partícula, se puede introducir una tensión "extrínseca" asociada con el método de síntesis empleado y/o tratamientos térmicos posteriores [7].

El segundo efecto significativo que origina la reducción del tamaño de partícula tiene relación con las propiedades electrónicas del óxido. La respuesta óptica y electrónica de un semiconductor está controlada por su estructura de bandas y la energía de su intervalo de energías prohibidas, *band-gap* (E_g), que proporciona el margen de energía para una transición entre la banda de valencia (BV) a la banda de conducción (BC) del material. Al reducir las dimensiones de los materiales, disminuye la escala de los fenómenos que tienen lugar en la estructura de bandas del material, llegando a producirse fenómenos de confinamiento cuántico de los portadores de carga (*figura 1*). Cuando el radio de una nanopartícula de un óxido semiconductor es igual o menor al radio de Bohr de un excitón (cuasipartícula formada por la interacción coulombiana de un electrón y un hueco), los portadores de carga, electrones (e^-) y huecos (h^+), se encuentran confinados

tridimensionalmente de modo que sus energías se cuantizan en niveles discretos de energía, en los denominados “puntos cuánticos”. Estos puntos cuánticos representan una situación intermedia entre el material masivo y las moléculas, donde el intervalo de energías prohibidas aumenta, produciendo un desplazamiento de la emisión intrínseca a mayores energías (desplazamiento al azul) [8-11].

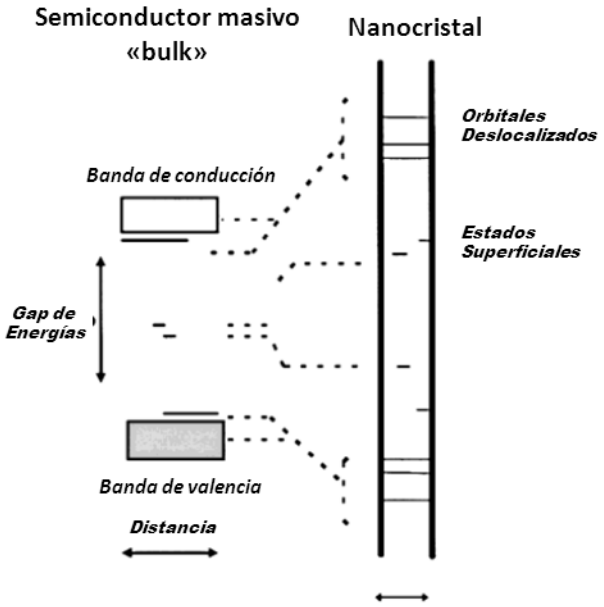

Figura 1. Evolución de la estructura de bandas de un material masivo “bulk” a un nanocristal.

La estructura y las propiedades electrónicas del material condicionan las propiedades físicas y químicas del sólido, y constituyen el tercer grupo de propiedades que se ven afectadas por la reducción de tamaño. En su forma de material masivo, muchos óxidos presentan un amplio intervalo de energías prohibidas y una baja reactividad. Al disminuir el tamaño de partícula se produce un cambio en el intervalo de energías prohibidas que provoca un cambio en la conductividad y reactividad del óxido. Las propiedades superficiales derivadas de estos cambios tienen una importancia especial en la aplicación tecnológica de los materiales. La naturaleza bidimensional de las superficies provoca consecuencias estructurales, como el reordenamiento atómico de los átomos en la superficie, alterando la estructura con respecto al material masivo; del mismo modo, tiene consecuencias en la estructura de bandas al introducir niveles energéticos intermedios en el intervalo de energías prohibidas. La presencia en la superficie de átomos con menor coordinación y/o vacantes oxígeno en una nanopartícula de un óxido producirá reordenamientos estructurales, así como niveles electrónicos ocupados por debajo de la banda de valencia respecto del material masivo, lo que aumenta notablemente la actividad química del óxido [12].

Propiedades luminiscentes

Al incidir una radiación de suficiente energía sobre un material semiconductor, se excitan múltiples señales con las que poder caracterizar sus propiedades químicas, electrónicas y estructurales. Uno de los procesos excitados durante la interacción electrón-muestra, es la generación de pares electrón-hueco. Cada electrón incidente puede generar miles de estos pares electrón-hueco, una parte de los cuales se recombinan mediante mecanismos radiativos, dando lugar a la emisión de fotones en el rango espectral ultravioleta, visible o infrarrojo. Los mecanismos radiativos implicados pueden ser *intrínsecos*, mediante transiciones banda-banda, o *extrínsecos* a través de niveles energéticos asociados a defectos, impurezas o una combinación de ambos. Los procesos de desactivación radiativa, que resultan de la recombinación de los excitones (pares electrón-hueco, e^--h^+), producen la emisión de luz o **luminiscencia**.

Por ello, la disminución del tamaño de partícula permite variar la respuesta luminiscente de los materiales, ya que estos portadores de carga se encuentran más próximos y poseen mayor energía. Esto afecta a sus propiedades optoelectrónicas y redox y, por tanto, amplían sus posibles campos de aplicación [13].

Para poder caracterizar y estudiar las propiedades que presentan estos materiales se recurre a técnicas que proporcionen información sobre su estructura de bandas y las posibles transiciones que pueden ocurrir. En este trabajo, se ha empleado principalmente la catodoluminiscencia (CL) como herramienta de caracterización de las propiedades luminiscentes de los materiales, ya que es idónea para estudiar materiales con un amplio intervalo de energías prohibidas y nanoestructuras, puesto que requieren una fuente de excitación que aporte fotones de alta energía. En la catodoluminiscencia se emplea un haz de electrones de alta energía, lo que hace que se produzca emisión mediante todos los mecanismos presentes en el semiconductor, de modo que proporciona una información completa de las transiciones y, por tanto, de la estructura de bandas del material semiconductor. Además, esta técnica permite focalizar el haz electrónico sobre pequeñas áreas del material, pudiéndose obtener información muy localizada variando la energía del haz de electrones [14].

Óxidos transparentes conductores

Los óxidos semiconductores transparentes (*transparent conducting oxides*, TCO), constituyen una clase única de materiales al combinar dos propiedades físicas: la elevada transparencia que presentan en el visible, junto con una elevada conductividad eléctrica [15], generalmente consideradas como mutuamente excluyentes, pero que se consiguen al generar electrones libres o huecos móviles en un semiconductor con un intervalo de energías suficientemente amplio (> 3.1 eV), de modo que no se produzca absorción en el visible. Los portadores de carga adicionales se generan normalmente mediante el dopado o la presencia de defectos intrínsecos, aumentando la población de electrones en el material [16, 17]. Los tipos de dopado o defectos que favorecen la obtención de un TCO dependen del óxido específico que se estudie así como de su síntesis, por lo que existe gran variedad de candidatos a TCO y diversos métodos para su obtención. El defecto intrínseco predominante en la mayoría de materiales es la presencia de vacantes oxígeno, dado que su energía de formación es menor respecto a otros tipos de defectos, lo que favorece su elevada concentración quees responsable desu comportamiento como semiconductor tipo *n*.

En concreto, las principales aplicaciones de estos materiales se encuentran en el campo de la optoelectrónica, entre las que cabe destacar:

- *Células solares:* Actúan como colectores de los portadores de carga foto-generados, a la vez que permiten el paso de la radiación solar hasta el material que absorbe dicha radiación.
- *Pantallas planas y pantallas táctiles:* Se emplean materiales TCO en los distintos estilos de dispositivos como electrodo frontal. El papel de los TCO en estos materiales es transferir las señales eléctricas a los pixeles que conforman la pantalla y, simultáneamente, permitir el paso de la luz generada hacia el observador.
- *Ventanas inteligentes:* Se emplean TCO como recubrimientos para el cristal. La función de una ventana inteligente consiste básicamente en bloquear parte o la totalidad de la radiación incidente en la ventana. Gracias al diseño de materiales, se pueden hacer recubrimientos que absorban la radiación infrarroja o ultravioleta, a la vez que permiten el paso de la visible, pudiendo, por ejemplo, controlar la temperatura interior o proteger de la radiación UV los objetos [18].

- *Electrónica transparente:* Dado que la mayoría de materiales TCO son conductores tipo *n*, si se consiguen a su vez TCO con semiconductividad tipo p, se podrían crear uniones p-n transparentes, lo que abriría un nuevo campo de circuitos electrónicos transparentes, que permiten desarrollar dispositivos como periódicos electrónicos o materiales textiles transparentes. [19]

Los materiales TCO más comunes en la actualidad son los óxidos de indio dopado con estaño (ITO, *indium tin doped oxide*), óxido de estaño dopado con flúor y óxido de zinc dopado con aluminio [20, 21]. Sin embargo, su conductividad eléctrica sigue siendo inferior a las deseadas en un TCO, lo que tiene consecuencias negativas en su aplicación tecnológica. Por esta razón, resulta necesario investigar nuevos materiales que puedan reunir estas propiedades, recibiendo especial atención como matrices para TCO óxidos como ZnO, In_2O_3, SnO_2, e incluso TiO_2 por su elevada versatilidad como material funcional [22-26].

Oxido de titanio, TiO_2

Las propiedades y aplicaciones más relevantes del óxido de titanio están relacionadas habitualmente con procesos asociados a su superficie. Desde el punto de vista tecnológico, una de las propiedades más atractivas del TiO_2 consiste en su actividad fotocatalítica. Los pares electrón-hueco generados mediante irradiación solar pueden separarse, de modo que los portadores de carga resultantes logren migrar a la superficie y reaccionar con las moléculas adsorbidas. Los estados superficiales del TiO_2 desarrollan un papel primordial en el proceso de descomposición de agua en H_2 y O_2. La base de estos dispositivos fotocatalíticos reside en las reacciones químicas o de transferencia de carga entre la superficie y las moléculas adsorbidas. El elevado índice de refracción del óxido de titanio, así como su elevada transmitancia en el visible y el infrarrojo cercano, posibilitan su uso en la fabricación de guías de onda y recubrimientos antirreflectantes. Igualmente se ha empleado en múltiples dispositivos ópticos como filtros o espejos dieléctricos para láseres. Además de un elevado índice de refracción, el TiO_2 presenta muy reducidos índices de toxicidad por lo que ha sido ampliamente utilizado como pigmento. El TiO_2 se emplea en células fotovoltaicas para la conversión de luz solar en energía eléctrica, así como en sensores de gases.

El TiO_2 puede cristalizar en tres estructuras diferentes: Anatasa (tetragonal), Rutilo (tetragonal) y Brookita (ortorrómbico). Los dos tipos estructurales más ampliamente estudiados, **anatasa** y **rutilo**, presentan diferentes propiedades físicas que juegan un papel primordial en los dispositivos que generan. La fase metaestable **anatasa** sufre una transformación de primer orden a **rutilo**, que es estable a elevada temperatura. Esta transformación de fase no presenta una única temperatura, ya que los procesos que están involucrados son de distinta naturaleza.

El óxido de titanio con estructura **anatasa** (*figura 2a*), se comporta como un semiconductor tipo *n*, con un intervalo de energías prohibidas (indirecto) de 3.2 eV, por lo que se considera la fase más activa fotocatalíticamente.

El óxido de titanio tipo **rutilo** (*figura 2b*) se comporta, generalmente, como un semiconductor tipo *n*, presentando un intervalo de energías prohibidas (indirecto) a 300 K de 3.05 eV. Los defectos que aparecen con mayor frecuencia en este óxido semiconductor corresponden a vacantes de oxígeno y, fundamentalmente, intersticiales de titanio (Ti^{3+}, Ti_{4+}), además de defectos extensos.

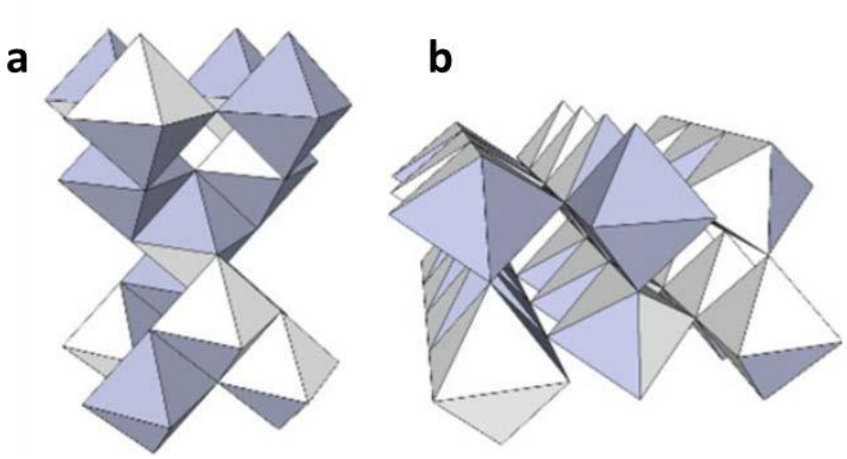

Figura 2. Representación tridimensional de las estructuras anatasa(a) y rutilo (b).

La presencia en el material de una o ambas fases determina su comportamiento optoelectrónico y fotocatalítico. Por ello, se han realizado muchos estudios sobre la estabilización de las fases anatasa y rutilo del TiO_2 y, especialmente, de la transición de fase. Además, estas fases pueden prepararse con diferentes morfologías y tamaños de partícula, modificando las estrategias de síntesis. La transición de fase es un proceso no reversible

debido a la estabilidad termodinámica del rutilo, donde la cinética de la transformación viene determinada por el tamaño y morfología de las partículas, su composición y las condiciones de la síntesis. Parece claro que el mecanismo de la transición de fase está dominado por efectos de nucleación y crecimiento de grano, lo que podría ser debido a la presencia de concentración de defectos, fronteras de grano, y faltas de apilamiento.

El rutilo puede presentar deficiencia de oxígeno que, para determinadas concentraciones, se acomoda por la formación de planos CS (*crystallographic shear planes*) [27]. La disminución del contenido en oxígeno requiere, en principio, de la presencia de Ti^{3+} intersticial o, en ocasiones, otros dopantes trivalentes, para mantener el balance de cargas. En el caso de la anatasa no se produce este tipo de acomodación de la deficiencia aniónica ya que, en este caso, las vacantes oxígeno promueven la transición a rutilo al facilitar el reordenamiento atómico.

El rutilo en su forma de material masivo es termodinámicamente más estable que la anatasa a cualquier temperatura debido a su menor energía libre. Pero la menor energía superficial de los planos de la anatasa, respecto a los del rutilo, hacen que para tamaños de cristal muy pequeños y, por tanto, elevada área superficial, la anatasa sea más estable. En estos casos, hay que considerar la energía superficial de las nanopartículas antes que la termodinámica del material masivo. En su tamaño nanométrico la anatasa posee una menor energía libre total (de la superficie y el interior). También se ha observado que cuanto mayor es el tamaño de partícula de la anatasa, la transformación a rutilo es más lenta que a tamaños menores. Esto parece ser debido a la menor energía superficial y a la existencia de pocas intercaras de partículas grandes de anatasa en las que pueda nuclear el rutilo. Por ello, se puede considerar que la transición a rutilo y el crecimiento de grano de la anatasa, son procesos competitivos. Hay un aumento de tamaño considerable del rutilo cuando se produce la transición de fase, lo que es debido a que las partículas de rutilo crecen a expensas de las partículas de anatasa vecinas durante la coalescencia, hasta que las partículas grandes de rutilo impiden el crecimiento. Este aumento de tamaño provoca una disminución en el área superficial y, por tanto, una disminución en la actividad fotocatalítica del material.

Las transiciones de fase suelen implicar cambios en las propiedades de los materiales por lo que es de esperar una variación de la respuesta luminiscente del TiO_2 en las fases anatasa y rutilo. La trasformación puede modificarse mediante el dopado con diferentes elementos, debido a que los dopantes pueden: (i) reducir el intervalo de energías prohibidas del TiO_2, (ii) introducir estados energéticos intermedios, (iii) producir mejoras en la separación de portadores de carga y (iv) provocar un aumento del nivel de especies adsorbidas en la superficie.

La presencia de un dopante en el óxido de titanio juega un papel en la transición de fase que ha sido ampliamente debatido en la bibliografía. Efectivamente, se han descrito diversos resultados sobre el efecto que producen los dopantes en el TiO_2 a la hora de inhibir o promover la transformación de anatasa a rutilo. En la formación de soluciones sólidas *sustitucionales*, los dopantes pueden introducirse en la red de la anatasa modificando los niveles de las vacantes oxígeno, promoviendo o inhibiendo la transformación a rutilo. En el caso de soluciones sólidas *intersticiales*, la alteración de la red puede dar lugar a la estabilización o desestabilización de la fase, dependiendo del tamaño de partícula y la valencia del dopante, de nuevo promoviendo o inhibiendo la transformación de fase. Si se sobrepasa el límite de solubilidad de los dopantes, su precipitación también puede facilitar la transformación de fase vía nucleación heterogénea [28].

En el presente trabajo se ha estudiado la influencia de distintos dopantes en la estabilización de rutilo y/o anatasa de tamaño nanométrico, así como la variación de sus propiedades con la composición. Así mismo, se ha estudiado el uso de nanopartículas de rutilo dopadas con cromo como precursores para la obtención de nanoestructuras alargadas mediante el método de vapor-sólido (VS).

Oxido de estaño, SnO_2

El óxido de estaño, SnO_2, presenta una única fase estable comúnmente denominada *casiterita* (forma mineral). Este óxido semiconductor cristaliza en la estructura tetragonal del *rutilo*. El SnO_2 es un semiconductor tipo *n* con un intervalo de energías prohibido (directo) de 3.6 eV a 300 K. Presenta elevada transparencia en el rango visible del espectro electromagnético, además de buena estabilidad química y mecánica. Las vacantes de oxígeno son los defectos intrínsecos que aparecen con mayor frecuencia en su estructura.

El elevado intervalo de energías prohibidas del SnO_2 dificulta las transiciones interbanda en el rango visible. Sin embargo, el SnO_2 se comporta como un buen conductor degenerado por la presencia de vacantes oxígeno. La energía de formación de estos defectos intrínsecos es muy reducida [29], de modo que estas vacantes termodinámicas generalmente aparecen en una concentración relativamente alta en la estructura del SnO_2. Estos defectos generan niveles donadores poco profundos bajo la banda de conducción del SnO_2 responsables de su conductividad tipo *n*. Además, la concentración de portadores de carga y, por tanto, la conductividad pueden incrementarse mediante la adición de dopantes. Debido a estas propiedades, el SnO_2 se ha empleado en la fabricación de células solares. Generalmente, los frontales de estos dispositivos están recubiertos de electrodos transparentes a la luz solar, consiguiendo así aumentar su área efectiva. Las aplicaciones en dispositivos optoelectrónicos suelen requerir que se maximice la transparencia óptica en el visible, a la vez que se mantiene una mínima resistencia eléctrica. El SnO_2 es uno de los materiales más extensamente utilizados en la fabricación de estos dispositivos, debido además a su buena estabilidad térmica y a su bajo coste.

Otra importante propiedad del SnO_2 es su elevada reflectividad a la luz infrarroja, manteniendo a la vez su transparencia en el visible. Por lo general, el borde de la banda de absorción de este material se encuentra en la región del infrarrojo, por lo que las radiaciones con longitudes de onda superiores serán reflejadas. El SnO_2 se emplea por tanto en filtros de infrarrojo, transparentes a la luz visible. Esta banda de absorción puede modificarse en función de los elementos con los que se dope el material, de modo que se transmita un mayor o menor intervalo energético del espectro solar, ampliando en consecuencia las aplicaciones del SnO_2.

Algunos de los dispositivos donde se emplea el SnO_2, así como otras nuevas aplicaciones, requieren el uso de materiales con dimensiones micro- y nanométricas. Por ejemplo, en el caso de los sensores de gases, las nanoestructuras aumentan la relación superficie-volumen y, por tanto, la eficiencia de respuesta ante distintas atmósferas.

En este trabajo se investiga la influencia del dopado de nanopartículas de SnO_2 con metales de transición (V, Cr, Mn) en sus propiedades luminiscentes.

Oxido de galio β-Ga_2O_3

De los materiales TCO, el β-Ga_2O_3 es uno de los semiconductores con un intervalo de energías prohibidas más amplio (4.9 eV), con conductividad tipo *n*, relacionada con la presencia de vacantes oxígeno y/o dopantes y una transparencia en el rango azul-UV.

En la *figura 3* se muestra una representación tridimensional de su estructura, monoclínica, con los átomos de Ga en posiciones tetraédricas (naranja) y octaédricas (verde).

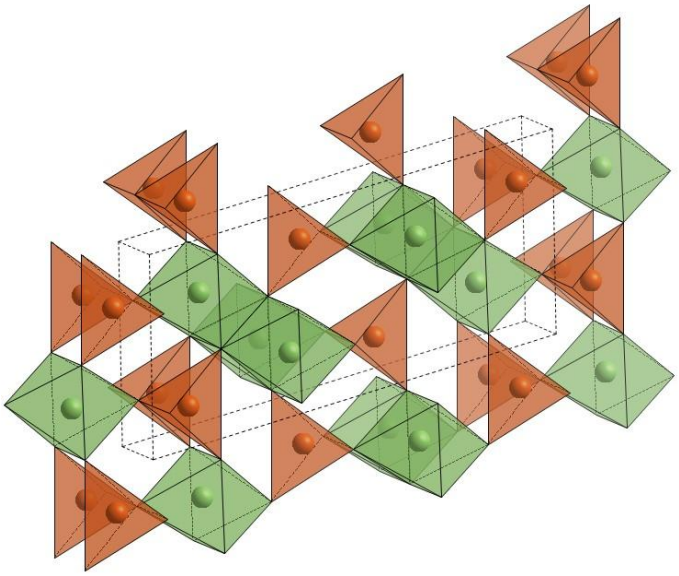

Figura 3. Representación tridimensional de la estructura de la β-Ga_2O_3.

Su elevada estabilidad química a la vez que una elevada conductividad térmica le convierte en unos de los materiales funcionales más prometedores como sensor de gases a alta temperatura. Este óxido está considerado como uno de los materiales con mayor potencial tecnológico en aplicaciones de optoelectrónica, como pantallas planas, emisores ópticos y células de energía solar, debido a sus propiedades conductoras y luminiscentes. El factor clave para su aplicación en optoelectrónica reside en la presencia de vacantes oxígeno y en su interacción con los dopantes que se introducen en la estructura.

Los dopantes son determinantes para mejorar propiedades como la conductividad eléctrica, al proporcionar portadores de carga como electrones o huecos, responsable de la respuesta optoelectrónica del material. Las condiciones de síntesis también influyen enormemente en la funcionalidad de las nanoestructuras obtenidas, ya que determinan la distribución de dopantes y defectos, así como la morfología que presenten. Actualmente, el control de las

propiedades optoelectrónicas mediante el dopado de nanohilos de β-Ga_2O_3 continúa representando un reto, debido a los procesos de difusión que provocan la segregación del dopante y la baja difusividad de los mismos en nanoestructuras.

En este sentido, en el presente trabajo se estudia la influencia de la presencia de dopantes en el crecimiento de nanoestructuras alargadas de β-Ga_2O_3 y su influencia en la morfología, así como en sus propiedades luminiscentes. Se estudia la incorporación directa de los dopantes al incluirse como precursores de la síntesis y la incorporación indirecta mediante tratamiento posterior de las nanoestructuras.

Óxidos de indio-zinc $In_kZn_2O_{3+k}$

Los óxidos de estaño e indio (conocidos como *indium tin oxides, ITO*) son los materiales TCO que mejores propiedades presentan hasta la actualidad, pero la escasez de Indio y, por tanto, su elevado coste hacen necesaria la búsqueda de nuevos materiales TCO, que se consoliden como alternativas más económicas. Entre ellas, cabe resaltar el estudio de óxidos de indio-zinc de la serie homóloga $In_kZn_2O_{3+k}$, que mejoren las propiedades con respecto a los ITO. Los materiales de esta serie homóloga presentan tres ventajas: (1) poseen una excelente estabilidad estructural y química incluso a elevada temperatura; (2) su elevado intervalo de energías prohibidas evita la excitación térmica de los portadores de carga, pudiendo emplearse como material termoeléctrico; (3) por su estructura en capas posee baja conductividad térmica, ampliando su aplicación bajo condiciones a alta temperatura.

La generación de portadores de carga es de especial importancia, ya que, como los óxidos de partida, estos materiales presentan una semiconductividad tipo *n*. De modo general, se asocian las vacantes oxígeno y la presencia de cationes intersticiales como las principales fuentes de portadores de carga. Para poder comprender y controlar las propiedades de los materiales de esta serie homóloga, es necesario realizar una adecuada caracterización estructural que permita comprender los caminos de conducción y, por tanto, la variación de las propiedades en función de *k*, es decir, el término de la serie.

En este trabajo se presenta una revisión de los modelos estructurales propuestos para estos óxidos, junto con el estudio de la modulación estructural para los términos con $k>7$. Así mismo, se estudian las propiedades catodoluminiscentes, para cada uno de los términos preparados.

BIBLIOGRAFÍA

[1] Matt Law. et al. *Nature Materials,* 4 **(2005)** 445-459.

[2] David Sikharulidze. *Appl. Phys. Lett*. 86 **(2005)** 033507.

[3] J. F. Wang, M. S. Gudiksen, X. F. Duan, Y. Cui, C. M. Lieber, *Science*, 293, **(2001)** 1455.

[4] M. S. Gudiksen, L. J. Lauhon, J. Wang, D. C. Smith, C. M. Lieber, *Nature* 415 **(2002)** 617.

[5] Y. Huang, X. F. Duan, Y. Cui, L. J. Lauhon, K. H. Kim, C. M. Lieber. *Science,* 294 **(2001)** 1313.

[6] F. Quian, Y. Li, S. Gradccak, D. Wang, C. J. Barrelet, C. M. Lieber. *Nano Lett.* 4 **(2004)** 1975.

[7] M. Fernández-García, X. Wang, C. Belver, A. Hanson, J. C. Iglesias-Juez, J. A. Rodriguez, *Chem. Mater.* 17 **(2005)** 4181.

[8] D. Koziej, A. Lauria, M. Niederberger, *Adv. Mater.* 26 **(2014)** 235-257.

[9] D. Maestre, *"Crecimiento y caracterización mediante técnicas de microscopía de nano- y microestructuras de SnO2 y TiO2"*, Tesis de Doctorado **(2007)**.

[10] T. Trindade, P. O'Brien, N. L. Pickett, Chem. Mater. 13 **(2001)** 3843-3858.

[11] K. Rajeshwar, N. R. de Tacconi, C. R. Chenthamarakshan, *Chem Mater.* 13 **(2001)** 2765-2782.

[12] J. A. Rodríguez, M. Fernández-García, *Synthesis, Properties, and Applications of Oxide Nanomaterials*, Ed. Wiley **(2007)**.

[13] G. R. Patzke, Y. Zhou, R. Kontic, F. Conrad, *Angew. Chem. Int. Ed.* 50 **(2011)** 826-859.

[14] M. Fox, *"Optical Properties of Solids"*, 2nd Ed. Oxford University Press **(2010)**.

[15] A. Stadler, *Materials,* 5 **(2012)** 661-683.

[16] P. D. C. King, T. D. Veal, *J. Phys.: Condens. Matter.* 23 **(2011)** 334214.

[17] G. B. González, *Materials*, 5 **(2012)** 818-850.

[18] B. A. Korgel, *Nature,* 500 **(2013)** 278.

[19] J. F. Wager*, Science,* 300 **(2003)** 1245.

[20] T. Minami, *Semicond. Sci. Technol.* 20 **(2005)** S35-S44

[21] A. Walsh, J. L. F. Da Silva, S.-H. Wei, *J. Phys.: Condens. Mater.* 23 **(2011)** 334210

[22] C. A. Hoel, T. O. Manson, J. F. Gaillard, K. R. Poeppelmeier, *Chem. Mater.* 22 **(2010)** 3569-3579.

[23] A. Kumar, C. Zhou, *AcsNano,* 4 **(2010)** *1,* 11-14.

[24] J. E. Medvedeva, C. L. Hettiarachchi, *Phys. Rev. B,* 81 **(2010)** 125116.

[25] Y. Furubayashi, T. Hitosugi, Y. Yamamoto, K. Inaba, G. Kinoda, Y. Hirose, T. Shimada T. Hasegawa*, Appl. Phys. Lett.* 86 **(2005)** 252101.

[26] A. Klein, *J. Am. Ceram. Soc.* 96 **(2013)** 331-345.

[27] S. Andersson and L. Jahnberg, Ark. Kemi 21 **(1963)** 413.

[28] D. A. H. Hanaor, C. C. Sorrell, *J. Mater. Sci.* 46 **(2011)** 855-874.

[29] C.Kiliç y A.Zunger. *Phys. Rev. Lett.* 88 **(2002)** 095501.

OBJETIVOS

El objetivo de la presente tesis doctoral se dirige a la síntesis de óxidos semiconductores funcionales para establecer la relación entre composición química, estructura, tamaño de partícula y morfología con las propiedades luminiscentes que presentan. Los sistemas objeto de estudio son:

1. Obtención de nanoóxidos de TiO_2 dopados con metales de transición, de fórmula general $Ti_{1-x}M_xO_2$ (M=Al, V, Cr, Mn, Fe; $0 \leq x \leq 0.3$), controlando la estructura cristalina mediante las condiciones de síntesis y el empleo de distintos dopantes para estudiar su influencia en las propiedades luminiscentes.

Así mismo, se estudiará la obtención de nanopartículas de SnO_2 dopadas con metales de transición (V, Cr, Mn) mediante distintas rutas sintéticas, estudiando la influencia del dopante en la morfología y en sus propiedades luminiscentes.

2. Obtención de nanoestructuras basadas en la β-Ga_2O_3, estudiando el control de la luminiscencia de los materiales en función de su morfología y la presencia controlada de impurezas. Se estudiará la influencia del dopado de estos materiales en su morfología, composición y respuesta luminiscente. La microscopía electrónica de transmisión de alta resolución permitirá establecer el mecanismo de crecimiento de las nanoestructuras, así como la presencia de defectos estructurales.

3. Estabilización de diferentes términos de la serie homóloga $Zn_kIn_2O_{3+k}$ ($3 \leq k \leq 13$), y estudio de la relación composición-estructura-propiedades físicas. Se llevará a cabo una rigurosa caracterización estructural de los materiales, estudiando por microscopia electrónica los modos de acomodación de las variaciones de composición catiónica con objeto de establecer si se producen fenómenos de orden a larga o corta distancia. El estudio de la cátodoluminiscencia de los términos profundiza en la comprensión de los fenómenos responsables de su respuesta luminiscente y, por tanto, de sus propiedades como TCO.

CAPITULO II. ASPECTOS GENERALES DE LA PREPARACIÓN Y CARACTERIZACIÓN DE MATERIALES

1. SINTESIS DE LOS MATERIALES

1.1. NANOMATERIALES BASADOS EN TiO_2 y SnO_2

1.2. MATERIALES NANOESTRUCTURADOS BASADOS EN β-Ga_2O_3

1.3. ÓXIDOS DE LA SERIE HOMOLOGA $In_2Zn_kO_{3+k}$

2. ANÁLISIS Y CARACTERIZACIÓN DE MATERIALES

2.1. ANALISIS COMPOSICIONAL

- ANALISIS ELEMENTAL: C, N, H
- ESPECTROSCOPIA POR DISPERSIÓN DE ENERGÍAS DE RAYOS X

2.2. CARACTERIZAQCIÓN ESTRUCTURAL Y MICROESTRUCTURAL

- DIFRACCION DE RAYOS X
- DIFRACCION DE ELECTRONES (SAED) Y MICROSCOPIA ELECTRONICA DE ALTA RESOLUCIÓN (HRTEM)
- MICROSCOPIA ELECTRÓNICA DE BARRIDO
- MODELIZACION Y SIMULACION DE ESTRUCTURAS

3. PROPIEDADES FÍSICAS DE LOS MATERIALES

3.1. CATODOLUMINESCENCIA

3.2. ESPECTROSCOPIA RAMAN

3.3. ESPECTROSCOPIA DE FOTOEMISION DE RAYOS X

1. SÍNTESIS DE MATERIALES

1.1. NANOMATERIALES BASADOS EN TiO_2 y SnO_2

Las rutas de síntesis por **vía húmeda** permiten obtener precursores de composición homogénea a nivel atómico y reducen sustancialmente los caminos de difusión, lo que permite trabajar a temperaturas más bajas y obtener tamaños de partícula menores y más homogéneos [1-4].

Los reactivos para la síntesis sol-gel suelen ser cloruros o compuestos metalorgánicos, especialmente alcóxidos, de los cationes de interés que se mezclan en las proporciones adecuadas frecuentemente con su correspondiente alcohol y agua. Entre las diferentes opciones que plantea el método sol-gel, para la obtención de nanoóxidos binarios dopados con metales de transición se ha empleado en este trabajo el denominado método "de precursores poliméricos" [5], representado esquemáticamente en la *figura 1*. Este procedimiento es particularmente sencillo y solo requiere el control de unos pocos parámetros que afectan a la síntesis. En la obtención de nanoóxidos de titanio, el control de las relación disolvente/precursores, el pH, la presencia de ácidos con función catalítica y los dopantes empleados, permiten la síntesis del dióxido de titanio en fase anatasa o rutilo.

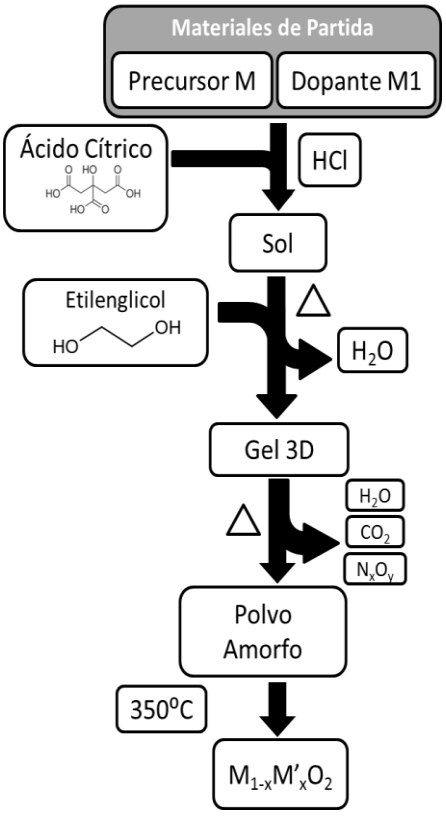

Figura 1. Esquema del método de los precursores poliméricos

Síntesis hidrotermal

Se ha utilizado la síntesis hidrotermal para la obtención de nanopartículas de SnO_2 y se han comparado los resultados con los obtenidos mediante el método de precursores poliméricos.

En un recipiente cerrado, como el autoclave mostrado en la *figura 2,* los disolventes pueden alcanzar la ebullición a temperaturas por debajo de su punto de ebullición, debido a las presiones autógenas que se generan al calentar el recipiente. En el caso del agua, su punto crítico se encuentra a 374 °C a 218 atm; por encima de estas condiciones, el agua se encuentra en su estado supercrítico y presenta características de líquido y gas simultáneamente. Las interfases entre sólidos y fluidos supercríticos carecen de tensión superficial ya que los fluidos supercríticos presentan elevada viscosidad y, por ello, son capaces de disolver compuestos químicos que serían insolubles en condiciones atmosféricas. Generalmente, en los métodos hidrotermales se aprovecha, simplemente, el aumento de la solubilidad y de la reactividad de los precursores metálicos a temperaturas y presiones por debajo del punto crítico. Por ello, estos métodos permiten obtener materiales a temperaturas inferiores que las requeridas por reacciones en estado sólido. Al contrario que en los métodos de coprecipitación y sol-gel, los productos obtenidos en condiciones hidrotermales son normalmente cristalinos y no necesitan tratamientos térmicos posteriores [6].

Figura 2. Reactor típico para la síntesis hidrotermal.

Finalmente, la simpleza del proceso junto con la baja temperatura de trabajo hace de estos procesos un medio recurrente para la obtención de diversos tipos de nanomateriales. Cabe resaltar que lo que en principio es una gran ventaja, variación de la morfología y composición en función de las condiciones hidrotermales, conlleva la necesidad de

establecer con precisión dichas condiciones. La búsqueda de estas condiciones para la optimización de la ruta hidrotermal adecuada constituye la parte más extensa y laboriosa de este proceso.

1.2 MATERIALES NANOESTRUCTURADOS BASADOS EN β-Ga_2O_3

Depósito en fase vapor

Ante la creciente demanda de dispositivos de interés tecnológico basados en semiconductores de dimensionalidad reducida y la necesidad de comprender los fenómenos cuánticos que controlan su comportamiento resulta necesario desarrollar nuevos procesos de síntesis que permitan controlar micro- y nanoestructuras de óxidos semiconductores con morfologías alargadas. El denominado método VLS (*Vapor-Liquid-Solid*) permite el crecimiento unidimensional. Este método se caracteriza por la presencia del metal catalizador en el extremo final de las estructuras resultantes [7]. Sin embargo, se pueden emplear métodos que tan sólo involucren mecanismos de evaporación-solidificación (método *VS o de evaporación solidificación*), sin incluir ningún catalizador ni sustrato externo. A diferencia de otros métodos, en este caso el crecimiento de micro- y nanoestructuras alargadas se desarrolla sobre la propia superficie de la muestra evitándose la presencia de catalizador en el extremo de las estructuras. Esta situación permite un mejor control de la morfología de las nanoestructuras en función de los parámetros que definen el tratamiento térmico (temperatura, tiempo, caudal de gas…).

Para la obtención de nanoestructuras dopadas se han descrito distintos métodos: dopado *in-situ* durante el crecimiento (donde el precursor ya se encuentra dopado) [8], difusión térmica [9], o implantación de iones [10]. Estos dos últimos se producen tras el tratamiento térmico sobre las nanoestructuras obtenidas sin dopar. Es necesario que el óxido sin dopar presente una estructura cristalina estable para que estos métodos de dopado no modifiquen la morfología de las estructuras. Cuando se realiza el crecimiento con la presencia *in situ* del dopante, estos pueden modificar tanto la estructura como la morfología de las estructuras obtenidas.

Por medio de un procedimiento rutinario de síntesis se preparan pastillas por compactación de los sólidos precursores de 7 mm de diámetro y 1-2 mm de grosor, bajo una carga

compresiva de 1-2 toneladas. Estas pastillas se colocan sobre un crisol de alúmina y se someten a un tratamiento térmico de recocido a alta temperatura en un horno Carbolite RF 15/3 (esquema en la *figura 3*). Ambos hornos disponen de una entrada externa de gases, lo que permite realizar los tratamientos en presencia de una atmósfera gaseosa controlada (atmósfera dinámica) [11].

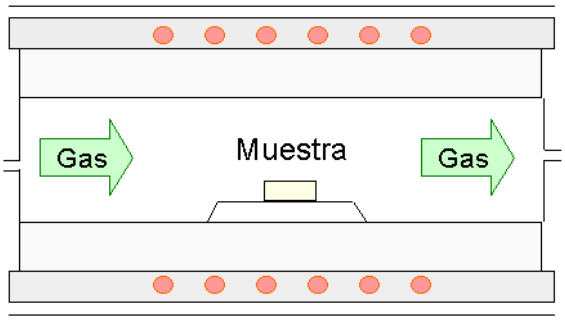

Figura 3. Esquema de un horno para la obtención de materiales mediante el método vapor-sólido

Mediante esta técnica se han obtenido nanoestructuras de óxidos de Ga_2O_3 [12-15] dopadas con Er [13, 15], Eu [14, 15, 16], Cr [18], In y Al [17].

1.3 ÓXIDOS DE LA SERIE HOMÓLOGA $In_2Zn_kO_{3+k}$

La síntesis de los materiales de esta serie homóloga de óxidos semiconductores se ha llevado a cabo mediante reacción en estado sólido a partir de los correspondientes óxidos y/o carbonatos de los precursores metálicos. En este caso, la estrategia de síntesis ha sido distinta puesto que se ha dirigido a la búsqueda de materiales con elevada cristalinidad. Efectivamente, una serie de procesos sistemáticos de molienda y compactación (formación de pastillas) intermedios favorecen el contacto superficial y la difusión de los reactivos, dando lugar a un óxido mixto final de elevada cristalinidad. Pese a la aparente simplicidad del método, es necesario un control exhaustivo de las variables que afectan a los tratamientos térmicos, temperaturas y tiempos de reacción, con objeto de obtener materiales monofásicos de composición controlada y elevado grado de cristalinidad.

2. ANÁLISIS Y CARACTERIZACIÓN DE MATERIALES

2.1 ANALISIS COMPOSICIONAL

2.1.1 ANALISIS ELEMENTAL: C, N, H

El empleo de precursores metalorgánicos puede ocasionar la presencia de impurezas residuales de carbono, nitrógeno o hidrógeno, que puedan quedar incorporadas en las partículas del material [19], pudiendo interferir en las propiedades. Por esta razón, se ha llevado a cabo el análisis elemental de las mismas en el Centro de Ayuda a la Investigación (CAI) de Microanálisis Elemental de la Universidad Complutense de Madrid (https://www.ucm.es/microanalisis), empleando un microanalizador elemental LECO CHNS-932, siguiendo un procedimiento normalizado de trabajo. Es una técnica de microanálisis elemental por combustión por la que se determina el contenido en peso de carbono, hidrógeno, nitrógeno y azufre. El procedimiento es aplicable a muestras homogéneas, sólidas, líquidas y viscosas que experimenten combustión a T≤990 °C. El alcance validado de este análisis posee unos límites de determinación de C, H y N, recogidos en la *tabla I*.

Tabla I. Alcance validado del microanálisis elemental

	%C	%H	%N
Alcance Validado	0.5 - 94.7	0.5 - 7.6	0.5 - 23.0

Todos los materiales sintetizados y analizados por este método en la presente tesis muestran valores inferiores al límite de detección, por lo que se puede descartar la presencia de estos elementos en las muestras obtenidas.

2.1.2 ESPECTROSCOPIA POR DISPERSIÓN DE ENERGÍAS DE RAYOS X (EDS)

El contenido catiónico medio de cada muestra se ha determinado mediante espectroscopía de rayos X por dispersión de energías (EDS). Para ello, se ha empleado un detector Oxford INCA, acoplado a un microscopio electrónico de transmisión JEOL 3000 FEG (*figura 4*).

Figura 4. Detector EDS Oxford INCA acoplado a un microscopio electrónico Jeol 3000FEG del Centro Nacional de Microscopia Electrónica en la UCM

La posición de los máximos de emisión de los distintos elementos se encuentra tabulada y almacenada en la base de datos del programa de análisis empleado, en este caso INCA de Oxford Instruments. La sensibilidad de esta técnica para cuantificar alcanza las 100 ppm.

El detector empleado posee una ventana de Be para evitar una posible contaminación de la cámara del microscopio. Su principal limitación es que no permite cuantificar con precisión elementos con Z≤11 (Na). Esto se debe a que la ventana de Be absorbe la radiación proveniente de dichos elementos, mientras que es transparente para elementos de mayor número atómico. Por tanto, en el caso de óxidos se utiliza la técnica para determinar la relación catiónica. El límite de detección de este detector para elementos con Z≥11 es de un mínimo del 0.1% en peso del elemento a analizar.

2.2 CARACTERIZACIÓN ESTRUCTURAL Y MORFOLÓGICA

2.2.1 DIFRACCIÓN DE RAYOS X

En todos los casos se ha utilizado la caracterización por difracción de rayos X para la identificación primaria de las fases cristalinas presentes en las diferentes muestras estudiadas, así como la fracción en la que se encuentran presentes mediante un análisis cuantitativo. Para ello, se han empleado los difractómetros del CAI de Difracción de Rayos X de la UCM (http://www.ucm.es/centros/webs/cai5084).

Se ha utilizado un difractómetro automático de polvo Siemens D-5000 (*figura 5*) equipado con una fuente de Cu ($K\alpha_1$ = 1.54056 Å y $K\alpha_2$ = 1.54439 Å).

Figura 5.- Difractómetro Siemens D5000.

Las condiciones estándar de trabajo han sido 40 kV y 30 mA, en intervalos de barrido de 2θ entre 10 y 70°, con un tamaño de paso de 0.04° y un tiempo de recogida de datos de 1 segundo por paso.

Para un análisis más preciso de la evolución del parámetro de celda en función de la cantidad de dopante se han recogido datos a temperatura ambiente en un difractómetro automático de polvo Panalytical X´PERT PRO *Alpha1* (*figura 6)* equipado con un monocromador primario de germanio (111), una fuente de radiación de Cu ($K\alpha_1$=1.54056 Å) y un detector rápido X'Celerator.

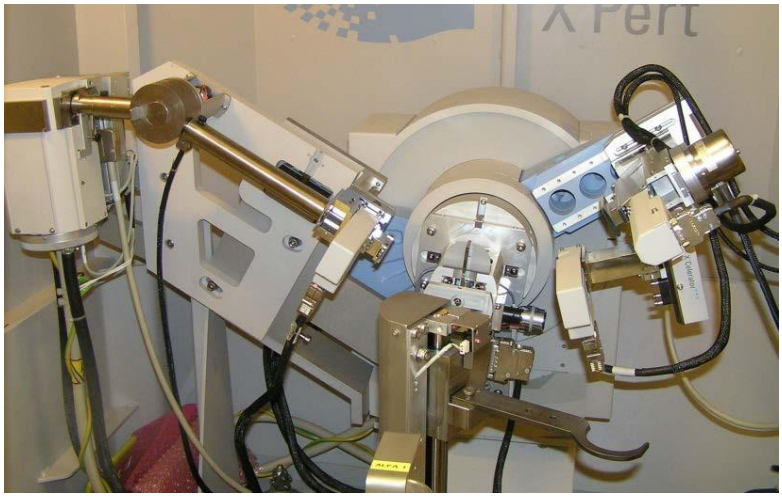

Figura 6. Difractómetro X'Pert Alpha1 Panalytical

Las condiciones de trabajo estándar del difractómetro fueron 45 kV y 40 mA. Los datos se recogieron en un intervalo de barrido entre 10° y 110°, con un tamaño de paso de 0.0167° o 0.033° dependiendo del ancho a media altura (FWHM) de la reflexión principal de la fase y 4 segundos por paso.

Para los estudios de termodifracción se ha empleado un difractómetro automático Panalytical *X'Pert MPD* (*figura 7*). Equipado con una cámara de alta temperatura *Anton Paar HTK2000*, que permite el análisis y caracterización de fases desde temperatura ambiente hasta 2300 °C. Dispone de un detector rápido X'Celerator.

Figura 7. Termodifractómetro X'Pert MPD Panalytical

2.2.2 DIFRACCIÓN DE ELECTRONES (SAED) Y MICROSCOPIA ELECTRÓNICA DE ALTA RESOLUCIÓN (HRTEM)

El estudio por difracción de electrones y microscopia electrónica de transmisión se ha realizado en el Centro Nacional de Microscopia Electrónica (CNME, www.cnme.es) en la UCM. La difracción de electrones de área seleccionada (SAED, *Selected Area Electron Diffraction*) y el estudio por microscopía electrónica de transmisión de alta resolución (HRTEM, *High Resolution Transmission Electron Microscopy*) se han llevado a cabo en un microscopio electrónico con filamento de emisión de campo (FEG, *Field Emission Gun*) JEOL-3000F, (*figura 8*) con un voltaje de aceleración de 300 keV, una resolución entre puntos de 0.17 nm y una aberración esférica C_s = 0.6 mm, empleando un goniómetro de doble inclinación (±25 °).

Figura 8.- Microscopio electrónico de transmisión JEOL 300 FEG

Las imágenes de campo oscuro anular de alto ángulo (HAADF, High Angle Annular Dark Field) adquiridas en modo (S)TEM, se han obtenido en un microscopio JEOL JEM ARM200cF con aberración corregida en la lente condensadora (*figura 9*) operando a 200 kV con resolución de 0.078 nm en modo STEM, con una densidad de corriente de emisión de ~1.4×10^{-9}A, equipado con un espectrómetro para espectroscopia EELS GIF- QuantumERTM y un detector EDS Oxford INCA-350.

Figura 9.- Microscopio de emisión de campo JEOL JEM ARM200cF

El procesado digital de las imágenes recogidas se ha realizado con el software *Digital Micrograph*, diseñado por Gatan Inc. Este programa permite el procesado mediante el empleo de las transformadas de Fourier (FFT: *Fast Fourier Transform*) [20] de las imágenes experimentales, así como el filtrado y eliminación de ruido de las mismas mediante la selección de los máximos de difracción de la FFT empleando máscaras, y la realización posterior de la inversa de la transformada de Fourier (IFFT). En la *figura 10* se muestra un ejemplo del proceso.

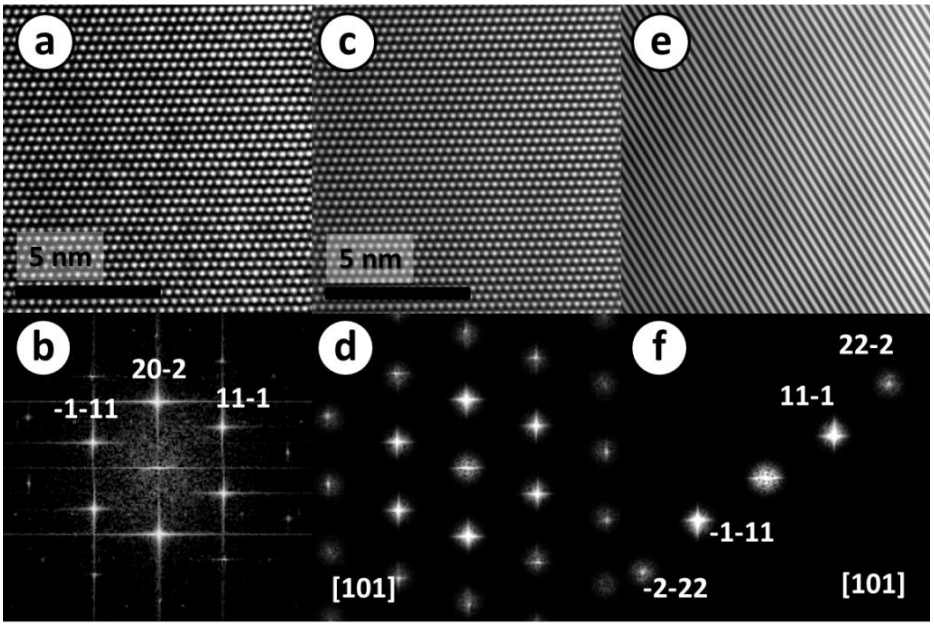

Figura 10.-a) Imagen HRTEM del plano [101] de la β-Ga_2O_3; b) FFT de la anterior; c) imagen I-FFT en la que se ha filtrado el ruido; d) máximos de difracción seleccionados para el filtrado de la imagen anterior; e) imagen filtrada donde se ha seleccionado una familia de planos específica (11-1), f) FFT con los máximos correspondientes a la familia de planos seleccionada.

El empleo de filtros disminuye el efecto del ruido electrónico en las imágenes obtenidas. Este proceso puede verse, a modo de ejemplo, al comparar las imágenes de las *figuras 10a* y *10c*, donde se observa una imagen de mayor nitidez al haberse eliminado el ruido electrónico. En la imagen de la *figura 10e* se observa el efecto que produce en la imagen la aplicación de una máscara para una sola familia de planos, dando como resultado una imagen que no corresponde con la que debe extraerse del diagrama de difracción de electrones correspondiente.

2.2.3 MICROSCOPIA ELECTRÓNICA DE BARRIDO

La morfología de los materiales obtenidos se ha estudiado mediante microscopia electrónica de barrido (SEM, *Scanning Electron Microscopy*). Se ha empleado un microscopio SEM de emisión de campo JEOL JSM 6335F, (*figura 11*), del CNME.

Figura 11- Microscopio SEM de emisión de campo JEOLJSM 6335F

En un microscopio electrónico de barrido los electrones son acelerados entre 1 y 40 keV. Este haz se focaliza hasta un diámetro de entre 2 y 10 nm, y se barre sobre la superficie de la muestra.

2.2.4 MODELIZACION Y SIMULACION DE ESTRUCTURAS

Todos los modelos tridimensionales de las estructuras representadas en el presente trabajo se han realizado utilizando el programa *Crystal Maker®* [21] a partir de datos cristalográficos obtenidos tras refinamiento a partir de los existentes en las bases de datos cristalográficas ICDD (*International Centre for Diffraction Data*) [22].

Para calcular las imágenes generadas en un microscopio electrónico de transmisión se emplea el método de "multicapa" o *multislice* (*figura 12*). Fue descrito por Cowley y Moodie [23] y, posteriormente, ampliado por Goodman y Moodie [24]. El empleo de la *Fast Fourier Transform* fue un aporte de Ishzuka y Uyeda [25] y Bursil y Wilson [26], lo que redujo considerablemente el procesado de datos en el método. La aproximación de este método divide la muestra en varias capas delgadas, de modo que cada una de ellas es suficientemente fina para causar un cambio de fase simple en la onda del electrón que se propaga entre capas como una onda en el vacío. De tal modo, el método reduce las sucesiones consecutivas de operaciones matemáticas de transmisión y propagación de las ondas, empleando la FFT [27].

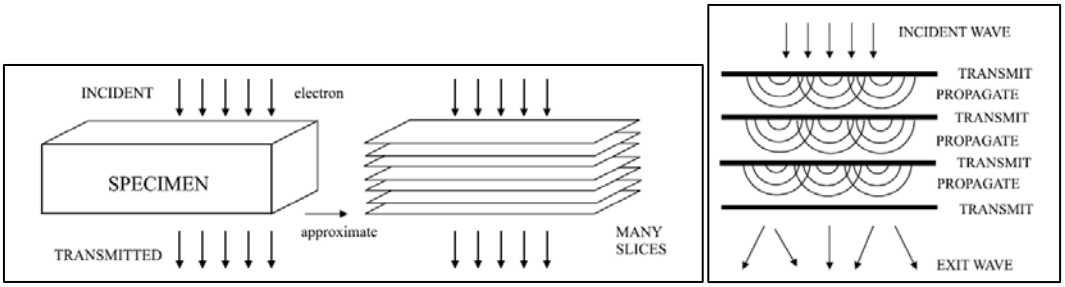

Figura 12. Ilustración esquemática del método multicapa.

En este trabajo se ha utilizado el programa Mac Tempas (*Mac TEM processing and simulation*) que ha sido desarrollado sobre la base de la versión original del SHRLI por R. Kilaas [28].

3. PROPIEDADES FÍSICAS DE LOS MATERIALES

3.1. CATODOLUMINESCENCIA

Las medidas de catodoluminescencia (CL) se han realizado en un microscopio electrónico de barrido (SEM) Hitachi S2500, que posee un sistema de control de temperatura compuesto por una termo-resistencia, un termopar y un sistema de enfriamiento mediante N_2 líquido que permite trabajar en un margen de temperaturas de 77 a 300 K y emplea un haz de 18 keV. Para el análisis de la señal CL se ha empleado un fotomultiplicador Hamamatsu R928, de respuesta rápida y sensible a la radiación de longitud de onda comprendida entre 300 y 900 nm (4.13 – 1.38 eV) y una cámara CCD (*charged couple-device camera*) Hamamatsu PMA-11 con un espectrógrafo incorporado. Para la obtención de imágenes monocromáticas se introduce un monocromador Oriel 78215 en la ventana del microscopio que permite seleccionar una longitud de onda determinada y analizar la distribución espacial de los centros radiativos responsables de la emisión. Estos equipos están instalados en el laboratorio del grupo de investigación de "*Física de Nanomateriales Electrónicos*" de la Facultad de Ciencias Físicas de la UCM, dirigido por el Prof. J. Piqueras.

3.2. ESPECTROSCOPIA RAMAN

Para medir los espectros Raman se ha empleado un láser He-Cd con una longitud de onda de 325 nm, en un microscopio confocal *CLSM3 Horiba Jobin Yvon LabRAM HR 800* (*figura 13*), con una cámara CCD con red de 600 líneas/mm para visible y 2400 para Raman, que permite estudiar secciones de la muestra con una profundidad de campo de aproximadamente 10 nm y adquirir espectros puntuales sobre el material.

Figura 13. Microscopio confocal *CLSM3 Horiba Jobin Yvon LabRAM HR 800*

3.3. ESPECTROSCOPIA DE FOTOEMISION DE RAYOS X

La caracterización de materiales mediante espectroscopia de fotoemisión de rayos X (*X-ray photoemission spectroscopy, XPS*) se realizó en la línea *ESCA-Microscopy* de la instalación de sincrotrón *Elettra*, en Trieste, Italia (*figura 14*). Los espectros de fotoemisión se midieron con una energía de fotón de 640 eV, y con una resolución energética de 0.2 eV.

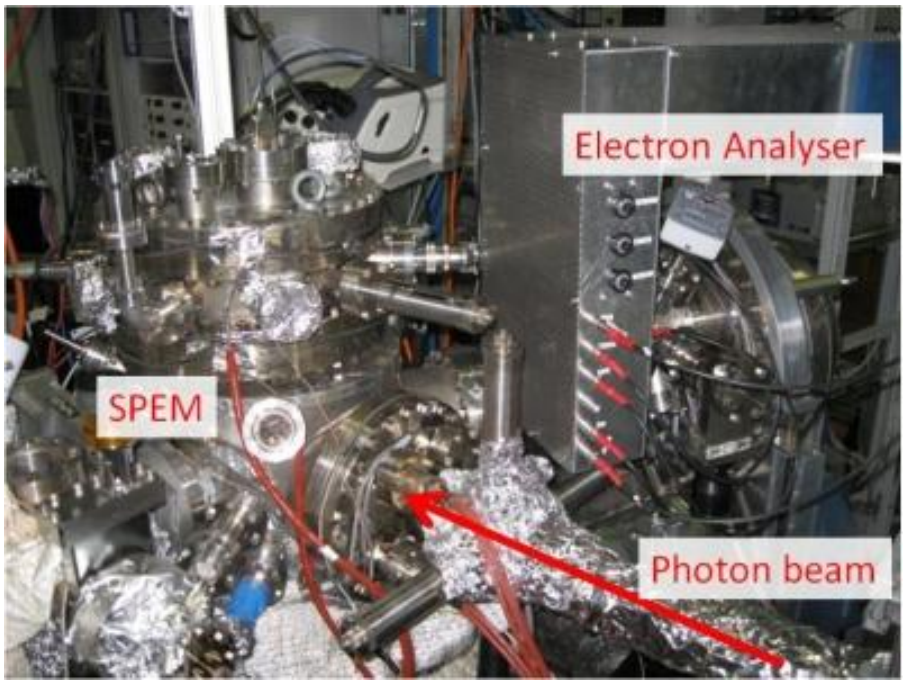

Figura 14. Espectrómetro de fotoemisión de rayos X, línea ESCA del sincrotrón *Elettra* (Trieste, Italia)

BIBLIOGRAFIA

[1] P. Hagenmuller, *C. R. Acad. Sci. Paris,* t.2, série IIc **(1999)** 537-545.

[2] M. G. Kanatzidis, K. R. Poeppelmeier, *Prog. Solid State Chem.* 36 **(2007)** 1-133.

[3] C. N. R. Rao, *"New directions in solid state chemistry",*2nd. Ed. **(1997)** Cambridge Univ. Press.

[4] A. R. West, *"Basic Solid State Chemistry",* 2nd. Ed. (2010) J. Wiley & Sons.

[5] T. Graham, *J Chem Soc. 17* **(1864)** 318.

[6] R. Roy, *J Am Ceram Soc.* 39 **(1956)** 145.

[7] M. P. Pechini, *Patent C. A.* 759514 **(1967)**.

[8] A. Querejeta, A. Varela, M. Parras, F. del Monte, M. García-Hernandez, J. M. González-Calbert, *Chem. Mater.* 21 **(2009)** 1898-1905.

[9] H. Lee, M. Hong, S. Bae, H. Lee, E. Park, K. Kim, *J. Mater. Chem.* 13 **(2003)** 2626-2632.

[10] B. L. Cushing, V. L. Kolesnichenko, C. J. O'Connor, *Chem. Rev.* 104 **(2004)** 3893-3946.

[11] R. S. Wagner, W. C. Ellis, *Appl. Phys. Lett.* 4 **(1964)** *5,* 89-90.

[12] K. W. Kolasonski, *Curr. Opin. Solid St. M.* 10 **(2006)** 182-191.

[13] E. Nogales, B. Méndez, J. Piqueras, *Nanotechnology*, 19 **(2008)** 035713.

[14] E. Nogales, B. Méndez, J. Piqueras, J. A. García, *Nanotechnology,* 20 **(2009)** 115201.

[15] E. Nogales, J. A. García, B. Méndez, J. Piqueras, K. Lorenz, E. Alves, *J. Phys. D: Appl. Phys.* 41 **(2008)** 065406

[16] D. Maestre, *Tesis Doctoral,* Dept. Física de Materiales, UCM **(2007)**.

[17] X. C. Wu, W. H. Song, W. D. Huang, M. H. Pu, B. Zhao, Y. P. Sun, J. J. Du, *Chem. Phys. Lett.* 328 **(2000)** 5-9.

[18] E. Nogales, J. A. García, B. Méndez, J. Piqueras, *J. Appl. Phys.* 101 **(2007)** 033517.

[19] M. Vallet-Regí, J. Ramírez, C. V. Ragel, J. M. González-Calbet, *Physica C,* 230 **(1994)** 407-411.

[20] E. J. Kirkland, *"Advanced Computing in Electron Microscopy"* **(2010)** Springer.

[21] http://www.crystalmaker.com

[22] http://www.icdd.com

[23] J. M. Cowley, A. F. Moodie, *Acta Cryst.* 10 **(1957)** 609-619

[24] P. Goodman, A. F. Moodie, *Acta Cryst. A,* 30 **(1974)** 280-290

[25] K. Ishizuka, N. Uyeda, *Acta Cryst. A,* 33 **(1977)** 740-749

[26] L. A. Bursill, A. R. Wilson, *Acta Cryst. A,* 33 **(1977)** 672-676

[27] M. A. O'Keefe, P. R. Buseck, *Trans. American Crystallography Assoc.* 15 **(1979)** 27-46.

[28] R. Kilaas, **(2006)**, www.totalresolution.com.

CAPITULO III. NANOMATERIALES BASADOS EN TiO_2 Y SnO_2

1. INFLUENCE OF Fe AND Al DOPING IN THE STABILIZATION OF ANATASE TiO_2 NANOPARTICLES
2. EFFECTS OF TRANSITION METAL DOPING ON THE GROWTH AND PROPERTIES OF RUTILE TiO_2 NANOPARTICLES
3. Cr DOPED TITANIA MICROTUBES AND MICRORODS SYNTHESIZED BY A VAPOR-SOLID METHOD
4. CONTROLLED TRANSITION-METAL DOPING OF SnO_2 NANOPARTICLES WITH TUNABLE LUMINESCENCE

1. INFLUENCIA DEL DOPADO CON Fe Y Al EN LA ESTABILIZACIÓN DE ANATASA EN NANOPARTÍCULAS DE TiO_2

Como es bien conocido, el óxido de titanio con estructura tipo anatasa transita a la fase estructural tipo rutilo a temperaturas que, en función de las condiciones de síntesis, superan los 700 ˚C. Esta situación varía al dopar los materiales con distintos cationes metálicos. Con objeto de realizar este estudio se han sintetizado nanopartículas de TiO_2 en su fase anatasa, dopadas con Al o Fe, empleándose una modificación del método *Pechini* para la síntesis, que permite controlar el tamaño y la composición de las nanopartículas. El análisis microestructural de los materiales obtenidos confirma que las nanopartículas dopadas de anatasa presentan un tamaño medio de 5 nm. Asimismo, se ha establecido que, mediante este método, las nanopartículas aceptan un contenido catiónico de hasta un 30%. La transición anatasa-rutilo (*anatase to rutile transition*, ART) que se da en los óxidos de titanio se puede controlar térmicamente en función del dopante. Se establece la cantidad y tipo de dopante introducido en la estructura y su influencia en la estabilización de la fase anatasa. Estos resultados se analizan mediante termodifracción que indica que la transición de fase se puede favorecer o inhibir en función del dopante (Fe o Al, respectivamente). Se discute, por último, según las medidas de espectroscopia *Raman*, fotoluminiscencia y espectroscopia fotoelectrónica de rayos X, prestando especial atención al papel que juega la presencia de Ti^{3+} en la superficie. Se concluye que el dopado adecuado del óxido de titanio con Al estabiliza la fase anatasa hasta temperaturas del orden de 900 °C.

Journal of Materials Chemistry C

PAPER

Influence of Fe and Al doping on the stabilization of the anatase phase in TiO_2 nanoparticles

G. Cristian Vásquez,[a] M. Andrea Peche-Herrero,[b] David Maestre,*[a] Belén Alemán,[c] Julio Ramírez-Castellanos,[b] Ana Cremades,[a] José M. González-Calbet[b] and Javier Piqueras[a]

Cite this: *J. Mater. Chem. C*, 2014, **2**, 10377

Received 18th September 2014
Accepted 7th October 2014

DOI: 10.1039/c4tc02099e

www.rsc.org/MaterialsC

Anatase TiO_2 nanoparticles doped with Al or Fe have been synthesized *via* a modified Pechini method which allows us to reach high control in size and composition. Microstructural analysis confirms the good crystallinity of the doped anatase nanoparticles with average sizes around 5 nm and dopant cationic concentrations up to 30%. The anatase to rutile transition (ART) has been thermally driven and analyzed as a function of the doping. Thermo-diffraction measurements indicate that the phase transition can be either promoted or inhibited by Fe or Al doping, respectively. The influence of Al and Fe doping on the phase transition has been discussed by means of Raman spectroscopy, photoluminescence and X-ray photoelectron spectroscopy, with special attention paid to the role played by Ti^{3+} at the surface. The anatase phase has been stabilized up to temperatures above 900 °C by appropriate Al doping.

Introduction

Titanium oxide (TiO_2) is one of the most investigated semiconducting oxides due to its versatility and widespread applications in catalysis, gas sensing, photovoltaics, the chemical industry, energy storage, or medicine.[1–4] In particular the use of TiO_2 (titania) stands out mainly in the field of photocatalysis, in which this material is widely exploited. As most of these applications are highly dependent on the dimensions and the presence of dopants, during the last few years increasing research has been focused on the synthesis and study of TiO_2 nanostructures doped with different elements, such as transition metals or rare earths,[5,6] in order to optimize the response of TiO_2. In addition, the crystallographic phase of TiO_2 should also be considered in the improvement of its applicability, as titania is a polymorphic material which can crystallize as rutile, anatase or brookite. Anatase and rutile phases, both of them with a tetragonal crystalline structure, have been widely used and deeply investigated so far as they exhibit different properties, which make them suitable to be used in different applications. As an example, rutile is widely employed in semiconductor electronics and optoelectronics,[7] while anatase is more appropriate in photovoltaics,[7] antibacterial performance and as electrodes for Li-ion batteries.[8] Moreover, it has been recently demonstrated that a mixed anatase/rutile phase enhances the photocatalytic performance of TiO_2.[9,10] Most applications based on titania have been focused on the more typical phase of TiO_2, rutile, yet the anatase phase, which has greater photocatalytic activity, has remained largely unexplored. The main reason is that the anatase phase is metastable, which hinders its use in devices which operate at high temperature. Actually the anatase phase transforms into rutile by means of a non-reversible process, due to the higher thermodynamic stability of rutile, at temperatures around 700 °C, or even lower for low dimensional TiO_2. Therefore, apart from monitoring the dimensions and doping of low dimensional TiO_2, control of its crystallographic phase is crucial to the ensuing performance of this material, which motivates this study. Stabilization of anatase at high temperatures, by avoiding the ART process, is considered a key challenge in the fields of smart coating technology, photocatalyst ceramics, or gas sensors. As some of these applications operate at high temperatures, the transition to rutile can occur and therefore the performance of the anatase-based device would be altered, which should be necessarily avoided. Therefore great efforts are recently focused on the control of the ART and the stabilization of the anatase phase at high temperatures ($T > 800$ °C) which can broaden the use of anatase in processes and applications requiring high temperature. Different approaches have been followed so far in order to modify the ART. The use of different cationic dopants, such as Ce, Cu, V, Al, rare earths or sulfate ions among others, has been found to retard the kinetics of the phase transformation.[3] However, in that case a major drawback is the possible formation of dopant-based secondary phases, which usually decreases the performance of titania, or the precipitation of the excess of dopants which can facilitate the phase transition.[11] Some other

[a]*Departamento de Física de Materiales, Facultad de CC. Físicas, Universidad Complutense de Madrid, 28040, Madrid, Spain. E-mail: davidmaestre@fis.ucm.es*
[b]*Departamento de Química Inorgánica I, Facultad de CC. Químicas, Universidad Complutense de Madrid, 28040, Madrid, Spain*
[c]*Sincrotrone Trieste, Area Science Park, 34012 Basovizza-Trieste, Italy*

ideas are considered in order to reach this aim, most of them involving surface modification, however, the physical and chemical processes involved in the ART, as well as the mechanisms to promote or inhibit it, have not been totally understood so far. Hence, further research is required to be developed in this field.

This work reports on the synthesis, and the study of the microstructural, chemical and luminescence properties of $Ti_{1-x}M_xO_2$ (M = Fe, Al, and $0 \leq x \leq 0.3$) anatase nanoparticles prepared by a Pechini[12] modified method. Among the most extended methods used to fabricate nanoparticles, such as evaporation, sputtering, or CVD, the one employed in this investigation, based on the use of polymeric precursors, not only facilitates precise control of the cationic concentration but also the diffusion process is enormously favored by means of the liquid solution. In addition to the study of the influence of Al and Fe doping on the optical and structural properties of anatase TiO_2 nanoparticles, in this work special attention has been focused on the effect of doping on the promotion or inhibition of the ART.

The structural, compositional and optical characterization have been carried out by X-ray diffraction (XRD), scanning electron microscopy (SEM), conventional and high resolution transmission electron microscopy (TEM, HRTEM), selected area electron diffraction (SAED), X-ray energy dispersive spectroscopy (EDS), photoluminescence (PL), Raman spectroscopy, and X-ray photoelectron spectroscopy (XPS).

Materials and methods

A "liquid-mix method" using polymeric precursors has been used for the synthesis of $Ti_{1-x}M_xO_2$ ($0 \leq x \leq 0.3$; M = Al, Fe) nanopowders.[13] $Ti(OBu)_4$ (Aldrich 97%), $Al(NO_3)_3 \cdot 9H_2O$ (Aldrich 99%), $Fe(NO_3)_3 \cdot 9H_2O$ (Aldrich 99%), citric acid, and ethylene glycol (Aldrich 99.99%) were used for the material synthesis. First of all, a 0.65 M solution of citric acid was prepared with deionized water. Secondly, stoichiometric amounts of $Ti(OBu)_4$ and the selected dopant precursor were added to the aqueous solution while continuously stirring it. Afterward, 5% (v/v) of ethylene glycol was added to start the gelation, and as the water evaporates, resin was formed containing all the cations in the desired stoichiometric amounts. Finally, the resin was calcined and a fine powder consisting of doped titanium oxide nanoparticles was obtained for each dopant. The powders were treated at 350 °C for 30 hours in order to completely remove organic residues. In order to obtain a well crystallized anatase single phase, the Fe-doped samples were treated at 450 °C for 15 hours, while Al-doped samples were treated at 550 °C for 15 hours. A carbon-content analysis was performed on a Perkin Elmer 2400 CHN analyser, with ±0.01% error. This elemental carbon analysis shows a carbon content lower than the quantification limit of the equipment, so carbon impurities can be neglected.

The synthesized nanopowders were studied by X-ray diffraction (XRD) using a Siemens D5000 diffractometer, with $Cu(K_\alpha)$ (λ = 1.5418 Å) as the working radiation. Data were collected at 2θ between 10° and 80°, with a step size of 0.04° and a collection time of 1 s per step. In order to obtain the cell parameters and Rietveld refinement analysis, XRD patterns were recorded by using a Panalytical X'Pert Pro Alpha1 instrument equipped with a primary fast X'Celerator detector operating at 45 kV and 40 mA, and fitted with a primary curved Ge 111 monochromator in order to obtain Cu $K_{\alpha 1}$ radiation. Thermo-diffraction measurements were performed by acquiring XRD patterns with a step size of 0.033° at increasing temperatures from 25 to 1000 °C at a rate of 6 °C min^{-1}. Conventional and High Resolution Transmission Electron Microscopy (TEM, HRTEM) as well as Selected Area Electron Diffraction (SAED) were performed using a Jeol 3000 FEG electron microscope, fitted with a double tilting goniometer stage (±22°, ±22°). For the analysis of the local composition, Energy-Dispersive X-ray Spectroscopy (EDS) was performed with an Oxford INCA analyser system attached to the afore-mentioned microscope. Further HRTEM characterization was carried out with Digital Micrograph 3.9.3 software (Gatan Inc.) by using Fast Fourier Transform (FFT) and Inverse Fast Fourier Transform (I-FFT) calculations. A MacTempas 2.3.24 program (Total Resolution Inc.) was used for the image simulation. A Horiba Jobin-Yvon LabRam Hr800 confocal microscope equipped with a 325 nm He–Cd laser was used to perform the micro-Raman and micro-PL studies reported in this work. Prior to their study the nanopowders were pressed into pellets in order to achieve higher compaction and lesser roughness at the surface. Raman spectra were recorded at room temperature and the scattered light was collected by a charge coupled device. The excitation light can be attenuated by using neutral density filters which allow us to reduce the total laser intensity of about 20 mW (I_0) by a factor of 0.5, 0.25 and 0.1, thus involving variable laser power densities. According to previous work[14] a laser power density around 8×10^4 W cm^{-2} can be achieved if neutral filters are not used. Photoluminescence (PL) spectra have been acquired at room temperature with a 325 nm He–Cd laser using the lowest laser intensity (0.1 I_0) in order to avoid the anatase to rutile phase transformation during the PL acquisition. For TEM characterization the as-grown nanopowders were previously dispersed in isopropanol and deposited in TEM grids. Spatially resolved X-ray photoemission spectroscopy measurements were carried out at the ESCA microscopy beamline of the Elettra-Synchrotron facility in Trieste. Photoemission spectra were acquired with a 640 eV photon energy and a 0.2 eV energy resolution.

Results and discussion

Powder XRD characterization confirms that all the analyzed samples can be indexed on the basis of the TiO_2 anatase structure (sp. gr. $I4_1/amd$, $z = 2$ with lattice parameters $a = b =$ 3.77 Å, c = 9.44 Å). In Fig. 1a, the XRD pattern corresponding to undoped anatase TiO_2 nanoparticles is shown. Size effects result in a broadening of the XRD peaks corresponding to nanoparticles, as compared with bulk TiO_2 anatase. The range of stability of the $Ti_{1-x}M_xO_2$ solid solutions synthesized in this work depends on the amount of cationic dopant. Al-doped anatase samples were obtained up to a doping level of 30%

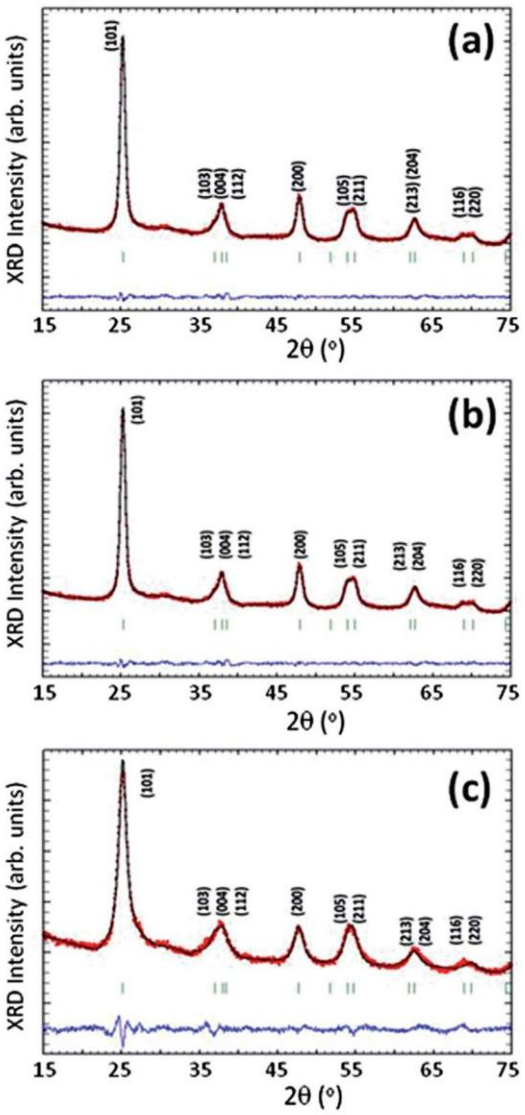

Fig. 1 XRD patterns from anatase (a) undoped TiO_2, (b) $Ti_{0.7}Al_{0.3}O_2$ and (c) $Ti_{0.8}Fe_{0.2}O_2$.

cationic fraction, due to the high solubility of Al in the anatase phase (see the corresponding XRD pattern in Fig. 1b). Fe-doped samples show an anatase structure only up to 20%, as shown in the XRD pattern of Fig. 1c, whereas for higher Fe concentrations small amounts of brookite, also a metastable phase, and a ternary Fe-based compound (Fe_2TiO_5) were occasionally observed. Therefore in this work cationic concentrations of 10, 20 and 30% have been studied in the case of Al doped TiO_2, while for Fe doped TiO_2 only 10 and 20% cationic concentrations were investigated. The incorporation of the dopants in the TiO_2 lattice and their compositional homogeneity have been confirmed by means of EDS in a TEM.

As an example, EDS atomic concentration values corresponding to the nanoparticles with the upper limit of dopant solubility ($Ti_{0.7}Al_{0.3}O_2$ and $Ti_{0.8}Fe_{0.2}O_2$) are shown in Table 1.

Table 1 Atomic concentrations of Ti, M (Al, Fe) and O estimated from EDS measurements performed on $Ti_{0.7}Al_{0.3}O_2$ and $Ti_{0.8}Fe_{0.2}O_2$

	Ti (at.%)	M (at.%)	O (at.%)
Al-30%	23.64 ± 0.38	11.63 ± 0.32	64.73 ± 0.06
Fe-20%	26.39 ± 0.12	6.76 ± 0.18	66.85 ± 0.06

The at.% values are in agreement with the theoretical ones expected for all the analyzed samples. The unintentional presence of the rutile phase formed during the synthesis of anatase TiO_2 by means of different techniques is commonly reported. However, the liquid-mix method employed in this work for the synthesis of the nanoparticles allows us to grow monophasic anatase samples with precise control of the cationic concentration, which can reach high values as the diffusion process is enormously favored by means of the liquid solution, in comparison to other synthesis methods. Once the Rietveld analysis of the monochromatic X-ray data was performed, the average grain sizes of the prepared undoped and doped TiO_2 nanoparticles were calculated using the Scherrer formula:

$$D = \frac{K\lambda}{B\cos\theta},$$

where θ is the peak position, λ is the X-ray wavelength and B is the Full Width at Half Maximum (FWHM) of the diffraction maxima.

Table 2 shows the average cell parameters and dimensions of the undoped TiO_2 nanoparticles, as well as the Al and Fe doped ones with the corresponding higher amount of dopant. Wellness factors of the corresponding Rietveld analysis are also indicated. An increase of the average particle size, which increases from around 3.5 nm for undoped TiO_2 to 4.2 nm for $Ti_{0.8}Fe_{0.2}O_2$, and about 10 nm in the case of $Ti_{0.7}Al_{0.3}O_2$, is observed in Table 2. This effect could be due to the different temperatures used at the final thermal treatment performed on the powders necessary to obtain a well crystallized phase. A slight increment in the particle dimensions was also observed as the amount of Al or Fe dopant is increased. However no remarkable variations in the lattice parameters due to the doping process were observed in the analyzed samples, since Al^{3+}, Fe^{3+} and Ti^{4+} present similar ionic radii (0.53, 0.69 and 0.61 Å respectively), which makes the cationic substitution

Table 2 Cell parameters, average size (D) and wellness factors of the Rietveld analysis performed on anatase undoped TiO_2 and TiO_2 doped with Al (10, 20, 30% cat.) and Fe (10, 20% cat.)

	a (Å)	c (Å)	D (Å)	R_p	R_{wp}	R_{exp}	χ^2
TiO_2	3.79(1)	9.46(2)	35.38 ± 0.02	3.47	4.36	3.90	1.25
$Ti_{0.9}Al_{0.1}O_2$	3.79(1)	9.46(4)	57.49 ± 0.04	3.37	4.21	2.53	2.76
$Ti_{0.8}Al_{0.2}O_2$	3.79(8)	9.48(8)	54.50 ± 0.02	3.15	3.96	2.51	2.49
$Ti_{0.7}Al_{0.3}O_2$	3.79(3)	9.47(4)	97.35 ± 0.04	2.47	3.17	2.34	1.84
$Ti_{0.9}Fe_{0.1}O_2$	3.79(1)	9.45(3)	39.60 ± 0.04	2.34	3.04	1.79	2.89
$Ti_{0.8}Fe_{0.2}O_2$	3.81(2)	9.48(2)	42.22 ± 0.02	2.33	2.93	1.78	2.71

more feasible up to the upper cationic limit employed in this work. It is only for $Ti_{0.8}Fe_{0.2}O_2$ that a slight increase in the lattice parameters was measured, as shown in Table 2. Some other studies report minor variation in the corresponding lattice parameters due to slight differences between the ionic radii, as Al^{3+} and Fe^{3+} radii are slightly lower and higher than Ti^{4+}. However in our case that effect should be compensated probably by the higher presence of Ti^{3+} and oxygen deficiency for Al and Fe doped samples respectively.

TEM measurements confirm the average size dimensions deduced by the Scherrer formula. Fig. 2a shows a low magnification TEM micrograph corresponding to undoped anatase TiO_2 nanoparticles, where homogeneity in size and shape can be observed. A HRTEM micrograph of an isolated undoped TiO_2 nanoparticle, with dimensions higher than 5 nm, is shown in Fig. 2b, where interplanar distances about 0.351 nm corresponding to (101) TiO_2 anatase planes can be measured.

In Fig. 3a a low magnification image of $Ti_{0.7}Al_{0.3}O_2$ nanoparticles, which is representative of the Al doped nanoparticles, is depicted, showing the homogeneity both in size and shape achieved by the synthesis method. Fig. 3b shows the HRTEM micrograph corresponding to an isolated and well crystallized $Ti_{0.7}Al_{0.3}O_2$ nanoparticle at higher magnification along the [100] axis, as confirmed by the corresponding FFT pattern (Fig. 3c). No extra spots or streaking can be observed, indicating that compositional variations are randomly distributed along the anatase structural type. Interplanar distances of 3.7 Å and 9.5 Å can be measured, corresponding to the "*a*" and "*c*" reticular parameters of the anatase structure. These values agree with those estimated by the Rietveld refinement. The unit cell of the material (marked on the image) can be clearly observed in the I-FFT (Fig. 3d).

Fig. 4a shows a TEM image corresponding to the $Ti_{0.8}Fe_{0.2}O_2$ nanoparticles, which is representative of the Fe doped nanoparticles, where a high homogeneity of size and shape can be observed. Fig. 4b shows a HRTEM image of a $Ti_{0.8}Fe_{0.2}O_2$ nanoparticle along the [001] axis, which is the basal plane of the anatase crystal structure, as confirmed by the corresponding FFT pattern (Fig. 4c). Interplanar distances of 3.6 Å can be measured along both perpendicular directions, corresponding to the "*a*" reticular lattice parameter of the basal plane of the anatase structure. Both distances are indicated in the I-FFT image (Fig. 4d), together with the unit cell marked as a square.

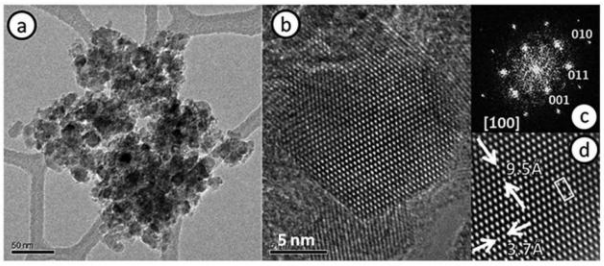

Fig. 3 (a) Low magnification TEM image of $Ti_{0.7}Al_{0.3}O_2$ nanoparticles. (b) HRTEM image of a single nanoparticle. (c) FFT of the [100] zone axis and (d) I-FFT image showing reticular parameters and a unit cell.

Raman spectroscopy is a suitable technique to analyze the modifications promoted by the nanoscale structure and the presence of dopants in the lattice vibrational properties of TiO_2, therefore it has been employed in the characterization of the undoped and doped (Al, Fe) TiO_2 nanoparticles analyzed in this work. In this study, the lowest laser intensity (0.1 I_0) has been used during measurements, in order to avoid a possible phase transition from anatase to rutile. An initial analysis of the Raman spectra corresponding to undoped TiO_2 anatase nanoparticles in comparison with commercial anatase TiO_2 formed by micrometric grains, used as a reference, has been carried out in order to describe the influence of the particle size on the TiO_2 Raman signal and distinguish these effects from those related to doping.

Fig. 5a shows the Raman spectra of undoped TiO_2 nanoparticles, synthesized in this work, and commercial TiO_2 anatase micropowders used as a reference. In both spectra only peaks corresponding to anatase active vibration modes[15] are identified at 150 cm^{-1} (E_g), 198 cm^{-1} (E_g) 401 cm^{-1} (E_g), 523 cm^{-1} (B_{1g} + A_{1g}), 635 cm^{-1} (E_g) as well as a weak wide contribution at around 800–840 cm^{-1}, the origin of which is not fully clear but it is commonly assigned to a B_{1g} overtone scattering[16] and frequently observed in nanosized titania. These peaks are broadened and blue shifted for the nanoparticles, as compared with the micropowders. This effect can be explained by the weakening of the selection rule $q_o \approx 0$ as the lattice periodicity is interrupted at the surface of the nanoparticles. Besides,

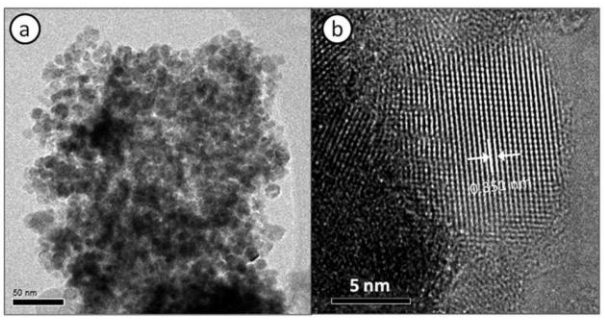

Fig. 2 (a) Low magnification TEM image of anatase undoped TiO_2. (b) HRTEM image of an isolated nanoparticle, where interplanar distances of 0.351 nm are measured.

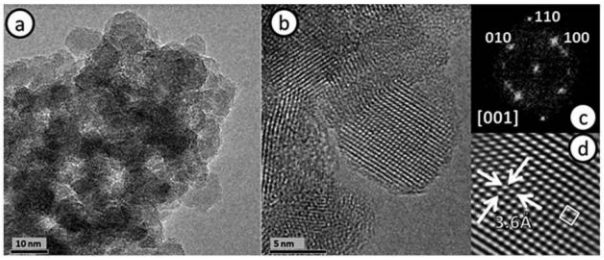

Fig. 4 (a) Low magnification TEM image of $Ti_{0.8}Fe_{0.2}O_2$ nanoparticles. (b) HRTEM image of a single nanoparticle. (c) FFT of the [001] zone axis and (d) I-FFT image showing the "*a*" parameter and a unit cell.

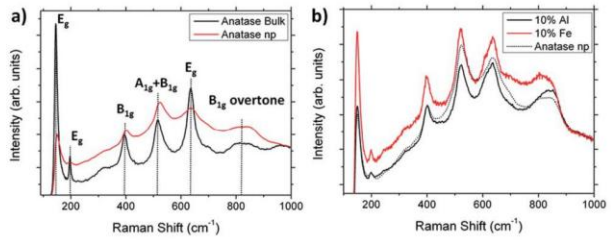

Fig. 5 (a) Raman spectra showing the vibration modes of commercial anatase TiO_2 micrograins and anatase TiO_2 nanoparticles synthesized in this work. (b) Raman spectra from anatase undoped TiO_2 and Al, Fe doped (10% cat.) TiO_2 nanoparticles.

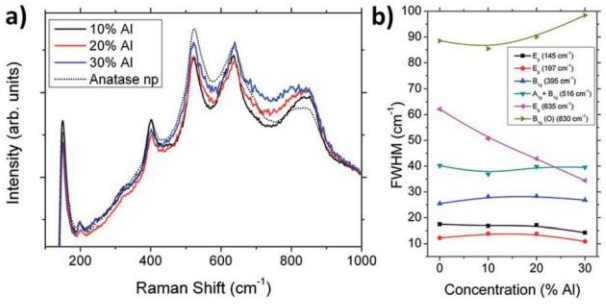

Fig. 6 Raman spectra of Al doped TiO_2 nanoparticles with Al cationic concentration of 10, 20, and 30%. The Raman spectrum from undoped TiO_2 is also shown as a reference. (b) Variation of the FWHM corresponding to the vibration modes as a function of the concentration of Al.

significant differences in the relative intensity of the Raman peaks are also observed in Fig. 5a, mainly in the E_g vibration modes at around 150 cm^{-1} and 635 cm^{-1}, which are dominant in the case of bulk TiO_2, while for the nanoparticles the dominant Raman peak is centered at around 516 cm^{-1} (B_{1g} + A_{1g}), which seem to be more surface sensitive.

In order to analyze the influence of the dopants, Raman spectra from Al and Fe doped TiO_2 nanoparticles (both with the same 10% cat. fraction), as well as undoped TiO_2 nanoparticles used as a reference, have been acquired, as shown in Fig. 5b. Variations in the relative intensities of the Raman peaks as a function of the dopant can be observed. Vibrational modes A_{1g} + B_{1g} (523 cm^{-1}) and E_g (635 cm^{-1}) are dominant for both undoped and Al doped TiO_2, while in the case of Fe doped TiO_2 vibrational modes E_g (150 cm^{-1}) and A_{1g} + B_{1g} (523 cm^{-1}) are the most intense ones. This effect could be associated with differences in the incorporation of each dopant in the TiO_2 lattice, as among the Raman active modes characteristic of anatase, A_{1g} + B_{1g} (523 cm^{-1}) are related to antisymmetric and symmetric bending vibrations of O–Ti–O, whereas E_g (150 cm^{-1}), the relative intensity of which is increased for Fe doped TiO_2, is associated with O–Ti–O symmetric stretching vibrations.[17] Moreover slight differences in the position of some of these modes, mainly in that centered at around 830 cm^{-1}, can also be observed in Fig. 5b. This latter mode, which is scarcely studied so far, can be deconvoluted in this case by two Gauss–Lorentzian contributions at 800 cm^{-1} and 851 cm^{-1}. The former can be attributed to the first B_{1g} overtone, while the latter is occasionally associated with stretching modes of short apical Ti–O bonds at the surface[18] involving bond strength and short range order.

Raman spectra have also been analyzed as a function of the dopant cationic concentration. Fig. 6a shows Raman spectra from TiO_2 nanoparticles doped with Al (10, 20 and 30% cat. concentration), as well as undoped anatase TiO_2 nanoparticles for comparison. According to the Raman measurements, mode E_g (~635 cm^{-1}) and the mode at around 830 cm^{-1} are the most sensitive to the presence of Al in the anatase TiO_2 host lattice. In particular, the former is blue-shifted from 634 to 640 cm^{-1}, and the latter is red-shifted from 836 to 831 cm^{-1} as the amount of Al increases from 10 to 30% cat.

In addition, a significant correlation between the FWHM of some of these peaks and the concentration of Al has been observed for both modes. As the amount of Al increases up to 30% cat. the FWHM of the E_g mode (~635 cm^{-1}) clearly decreases, whereas the FWHM of the mode at ~830 cm^{-1} increases, as observed in Fig. 6b where FWHM values from the Raman active modes are plotted as a function of the Al concentration. This latter mode could be a composition of two contributions located at 809 cm^{-1} and 856 cm^{-1}, as estimated by means of a Gauss–Lorentzian deconvolution. The positions of these components are blue-shifted with respect to those estimated for undoped TiO_2. As XRD and TEM analyses indicate slight variations in size, below 10 nm, for the Al (10, 20, 30% cat.) doped TiO_2 nanoparticles, size effects can be neglected during the analysis of the peak broadening observed in the Raman spectra. In this case, relevant variations due to thermal effects can also be discarded as all the spectra were collected at room temperature and using the same laser power density. Hence, main variations in the position and FWHM of the Raman peaks can be analyzed on the basis of the changes in the stoichiometry and defects caused by doping, as also reported by other authors.[19] Aluminium is usually incorporated into the TiO_2 lattice as Al^{3+} by substituting Ti^{4+} in octahedral sites, which involves the formation of oxygen vacancies due to charge imbalance.[20,21] In particular, E_g modes are more sensitive to the concentration of oxygen vacancies in TiO_2, as they are related to planar O–O interactions.[22] This can explain the variations observed in the Raman spectra as the blue-shifted E_g mode, owing to the creation of oxygen vacancies associated with substitutional Al^{3+}. In addition, the formation of Ti^{3+} related defects can also be generated due to oxygen deficiency, as Ti atoms surrounding removed neutral oxygens can capture electrons migrated from O 2p states. In the analysis of the Raman spectra corresponding to the samples with the higher concentration of Al, the occupancy of interstitial sites by Al^{3+}, in addition to the substitutional ones, cannot be ruled out, as referred by Gesenhues *et al.*[23]

Fe doped TiO_2 nanoparticles (10 and 20% cat.) have also been investigated by means of Raman spectroscopy, as shown in Fig. 7a. All the peaks in the spectra correspond to the TiO_2 anatase phase, however in this case major differences are found for the mode at around 830 cm^{-1} which is broadened as the

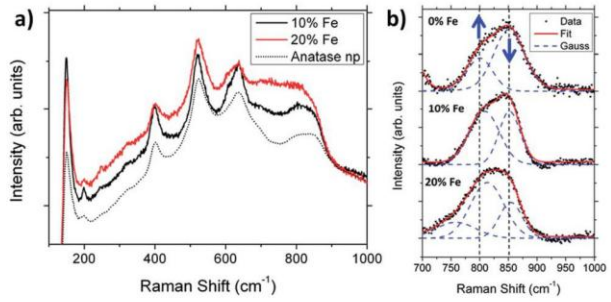

Fig. 7 Raman spectra of Fe-doped TiO_2 nanoparticles with Fe cationic concentrations of 10, and 20%. The Raman spectrum from undoped TiO_2 is also shown as a reference. (b) Deconvolution of the Raman signal around 830 cm^{-1} corresponding to the Raman spectra shown in (a).

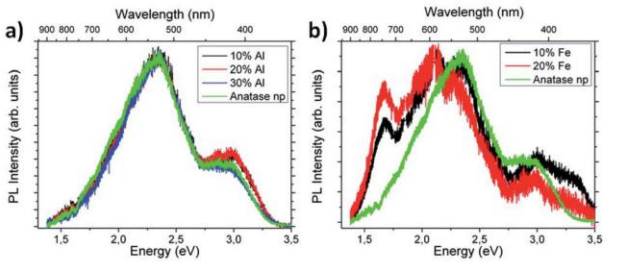

Fig. 8 PL spectra from (a) Al and (b) Fe doped TiO_2 nanoparticles with variable cationic concentration of dopant. The PL of the undoped TiO_2 sample, as a reference, is included both in (a) and (b).

amount of Fe increases. The rest of the Raman peaks, with the exception of the E_g (150 cm^{-1}), are weakly broadened and slight variations in their relative intensities can be observed as well, probably associated with defects related to doping. Among the vibrational modes, that centered at ~830 cm^{-1} appears to be more sensitive to the Fe doping, the E_g mode (150 cm^{-1}) being the least modified by the presence of Fe. The mode at ~830 cm^{-1} has been analyzed in detail by means of Gauss–Lorentzian deconvolutions, as those shown in Fig. 7b corresponding to undoped and Fe doped TiO_2 (10%, 20% cationic fraction) nanoparticles. The calculated bands for the 10% and 20% Fe doped TiO_2 nanoparticles are centered at 808 cm^{-1} and 852 cm^{-1}, and 758 cm^{-1}, 813 cm^{-1} and 854 cm^{-1}, respectively. For the undoped TiO_2 nanoparticles these bands are located at 800 and 851 cm^{-1}, therefore not only the peaks are blue-shifted as the content of Fe increases, but also an inversion in their relative intensity has been induced by the presence of Fe in the TiO_2 lattice. As afore-mentioned these modes can be associated with B_{1g} overtone and stretching modes of short apical Ti–O bonds at the surface. Hence, the observed decrease of the latter mode through Fe doping could involve a relaxation in the Ti–O bond at the surface of the Fe doped nanoparticles, as compared with undoped and Al doped TiO_2 for which the opposite behavior was observed. In order to explain the blue shift and broadening of the Raman peaks, non-stoichiometry effects associated with the variable incorporation of Fe into the TiO_2 lattice, due to its multivalency, and the resulting structure of defects should be mainly considered. As for the case of Al doped TiO_2 nanoparticles, both size and thermal effects can be excluded in the study of the Raman peaks corresponding to Fe doped TiO_2. Despite the fact that Fe is commonly incorporated as substitutional Fe^{3+} involving creation of oxygen vacancies and related Ti^{3+} interstitials, the presence of Fe^{2+} and Fe^{4+} can also be considered, which may result in different structure of defects.

Photoluminescence (PL) measurements have been carried out in order to improve the understanding of the influence of dopants (Al, Fe) on the optical properties of anatase TiO_2 nanopowders. Both undoped and Al doped TiO_2 show similar PL signals (normalized in Fig. 8a) consisting of a broad band in the visible region, with the maximum around 2.35 eV, and a less intense contribution around 2 eV, together with a high energy emission centered at around 3 eV. The broad green emission, peaked at 2.35 eV, has been usually assigned to surface defects mainly associated with oxygen deficiency and related intragap states,[24–27] as well as to Ti^{3+} associated with neighbouring oxygen vacancies.[28,29] The less intense emission at higher energy (~3 eV) is related to self-trapped excitons localized at TiO_6 octahedra.[30,31] Only slight differences in the high energy region are observed between the undoped and Al doped TiO_2 nanoparticles. The relative intensity of this emission is higher for Al doped TiO_2 (10% cat.), and decreases as the amount of Al increases, which could be related to the presence of Al^{3+} and the resulting lattice disorder in highly Al doped samples. Shirley *et al.*[32] reported that substitutional aluminium does not lead to band-gap states, which can explain the similarity between PL signals from undoped and Al doped samples.

Fig. 8b shows the normalized photoluminescence spectra corresponding to the Fe doped TiO_2 nanoparticles (10, 20% cat.), as well as the undoped anatase TiO_2 for comparison. The total emission from Fe doped TiO_2 is less intense than the PL signal corresponding to undoped and Al doped TiO_2. A decrease of the PL emission related to the increase of Fe has also been reported by different authors,[24,33] due to the inhibition of the recombination of photogenerated electrons and holes resulting from the presence of Fe^{3+}, which enhances the photocatalytic activity. Gaussian deconvolution indicates the presence of bands at 1.66, 2.10, 2.35, 3.0 and 3.30 eV for these samples. Apart from the band at 2.35 eV associated with oxygen deficiency, also observed for undoped and Al doped TiO_2, intense emissions at 1.66 eV and 2.1 eV can be observed for the Fe doped TiO_2 nanoparticles. The emission at 2.1 eV, which in this case dominates the spectra, can be associated with oxygen vacancy related defects and undercoordinated Ti acting as electron traps.[5,29] Raman measurements also suggested high oxygen deficiency resulting from Fe doping. Different authors associate the near-IR emission at 1.66 eV with the presence of Fe^{3+} in tetrahedral coordination.[34] In our case the relative intensity of this near-IR emission increases as the amount of Fe increases in the nanoparticles, as observed in Fig. 8b, which indicates a higher presence of Fe^{3+} as the cationic fraction of Fe is increased up to 20% cat. The emission in the near UV region (~3 eV), the relative intensity of which decreases by increasing

the amount of Fe, presents significant differences as compared with undoped TiO_2 anatase. In this case, the high energy emission is composed of two bands at 3 eV and 3.3 eV. The former (3 eV) has been previously related to self-trapped excitons in anatase TiO_2, while the latter (3.3 eV) can be associated with near band edge emission (as the bandgap for anatase TiO_2 is 3.2 eV at 300 K). A slight red-shift can be observed in this emission as the amount of Fe is increased (Fig. 8b). According to different authors[35,36] the presence of Fe^{3+} substituting Ti^{4+} generates bandgap-narrowing and red-shift in the absorption edge towards the visible range, which results in enhanced optical absorption.

XPS measurements have been performed on the undoped and doped (Al, Fe) TiO_2 nanoparticles, as shown in Fig. 9, in order to achieve surface sensitive chemical analysis. The XPS spectra have been calibrated with respect to the C (1s) core level at 284.6 eV. Fig. 9a shows the Ti ($2p_{3/2}$) core level from undoped TiO_2, while Fig. 9b and c show Ti ($2p_{3/2}$) core levels corresponding to Al (20% cat.) and Fe (20% cat.) doped TiO_2. Deconvolution of the XPS spectra shows three main bands centered at 455.3, 456.8 and 458.6 eV corresponding to Ti^{2+}, Ti^{3+} and Ti^{4+} in TiO_2, respectively, in agreement with the NIST database. As observed in Fig. 9, all the photoelectron spectra are dominated by the contribution centered at 458.6 eV, which corresponds to Ti^{4+} in TiO_2. The relative intensity of the band at 456.8 eV, attributed to Ti^{3+} in the near surface region, varies as a function of the probed sample. In particular this band, filled in the spectra shown in Fig. 9, increases for the Al doped samples, while is hardly noticeable for the Fe doped ones, as compared with undoped TiO_2 samples. The contribution at 455.3 eV, associated with Ti^{2+}, can be only observed for undoped and Al doped TiO_2 samples, showing higher intensity for the latter. The Ti^{3+} to Ti^{4+} atomic ratio can be estimated from the analysis of the integrated areas of the corresponding bands in the XPS spectra. This Ti^{3+}/Ti^{4+}value varies from 0.2, when probing undoped TiO_2, to 0.025 and 0.4 when analyzing Fe doped and Al doped TiO_2 nanoparticles respectively, which suggests that Al doping can be associated with a higher concentration of Ti^{3+} at the surface, while the opposite behavior can be observed when doping with Fe. Variations in the oxidation state of Ti are not so noticeable in Fe doped TiO_2, possibly due to the multivalency of Fe which can compensate charge imbalance usually associated with oxygen related defects, contrary to the case of Al doped TiO_2. Variations observed in these samples by Raman spectroscopy can be related to differences in the presence of Ti^{3+} at the surface. The presence of surface Ti^{3+} sites plays a key role in the photocatalyst activity of TiO_2, and could be involved in the ART process, hence huge interest is invested in their study.

In order to analyze the thermal evolution of the anatase phase, thermo-diffraction measurements have been performed at temperatures ranging from 25 to 1000 °C. As an example, Fig. 10 shows the evolution of the region between 20 and 30° in the XRD patterns corresponding to undoped and Al (10% cat.) doped TiO_2, where diffraction peaks related to (101) and (110) from anatase (A) and rutile (R), respectively, are marked.

The rutile phase, as determined by the corresponding (110) peak, appears at temperatures about 800 °C for undoped TiO_2 and at 920 °C for Al (10% cat.) doped TiO_2, as marked with asterisks in Fig. 10a and b, respectively. As the annealing temperature increases, peaks at the XRD patterns are narrower due to grain growth. In Fig. 11, the annealing temperatures at

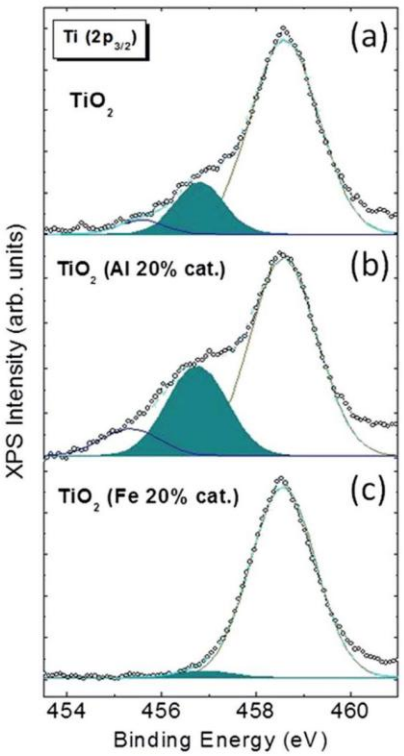

Fig. 9 XPS spectra of Ti $2p_{3/2}$ acquired on (a) undoped, (b) Al (20% cat.) doped, and (c) Fe (20% cat.) TiO_2. The band corresponding to Ti^{3+} is filled in the spectra.

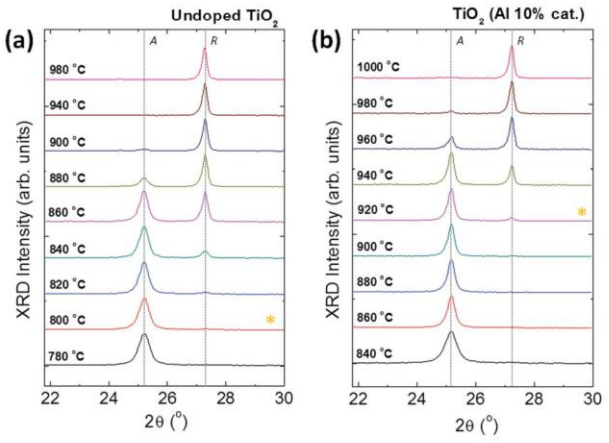

Fig. 10 Thermo-diffraction XRD patterns acquired at increasing annealing temperatures on (a) undoped and (b) Al (10% cat.) doped TiO_2 nanoparticles. XRD patterns at which the rutile phase starts to be noticeable are marked with the asterisk in the corresponding XRD pattern.

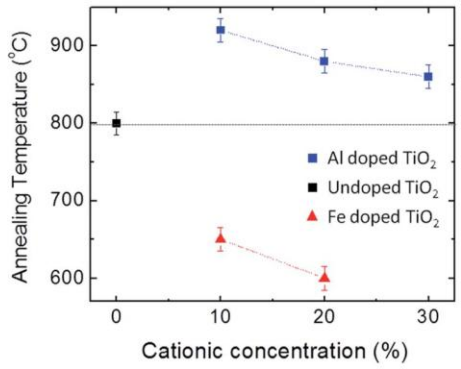

Fig. 11 Variation of the temperature at which the rutile phase appears in the XRD patterns as a function of the cationic concentration of the dopants (Al, Fe).

which the rutile phase appears, according to the XRD patterns, are plotted as a function of the dopant (Al, Fe) cationic concentration. Thermo-diffraction measurements confirm that Fe doping promotes the ART which occurs at around 600 °C, while Al doping retards it up to temperatures near 900 °C. It should be mentioned that even when the ART starts around the above mentioned temperatures, higher temperatures are required in order to complete the phase transition. Therefore the rutile phase is dominant only at temperatures over 710 °C for TiO_2 (Fe 20% cat.) and above 950 °C for TiO_2 (Al 10% cat.), being possible to find the anatase phase even at higher temperatures in both cases. In the case of Al doped TiO_2, mixed anatase/rutile phases can be obtained up to 1000 °C, which should be considered as different studies reported higher photocatalytic activity for the mixed phases. The cationic concentration of the dopant also modifies the ART process, which occurs at lower temperature as the amount of dopant increases, as observed in Fig. 11. As an example, the temperatures at which the rutile phase starts to appear in TiO_2 doped with Al 30, 20 and 10% cat. correspond to 860, 880 and 920 °C respectively. As dopant-based secondary phases were not detected in the analysis of the XRD patterns, this effect could be related to a possible precipitation of the excess of dopants (Al or Fe), more feasible in the highly doped samples, which can facilitate the phase transition.[11]

Despite the fact that some other studies reported stabilization of TiO_2 at high temperatures, only a few of them are focused on nanosized TiO_2. It is commonly accepted that ART occurs at lower temperatures around 550 °C for nanoparticles, as reported in different studies.[37,38] In our case, the anatase phase has been stabilized at higher temperatures for samples which consist of nanoparticles with increasing size as a function of annealing temperature. Apart from doping, some other approaches have been followed to achieve anatase stabilization, in most of which surface modification plays an important role. As an example, Etacheri *et al.*[39] reported stabilized anatase up to 1000 °C in H_2O_2 surface modified TiO_2, due to strong Ti–O–Ti bonds. In our case, Raman measurements suggested variations in the surface order of the doped anatase nanocrystals, as Al and Fe doping generates contraction or relaxation of apical Ti–O bonds, respectively, which could inhibit or facilitate the phase transition. Besides, the higher presence of Ti^{3+} at the surface of the nanoparticles, as confirmed by XPS, can be associated with the inhibition of the ART. Various authors have reported that the presence of Ti^{3+} interstitials inhibits the anatase to rutile transition through lattice constrain[3] as they hinder the atom rearrangement involved in the ART, which agrees with the results shown in this work.

In addition to the thermally induced ART, this phase transition can also be promoted during laser irradiation using the highest laser intensity (I_0) achieved without neutral filters. Therefore, special attention should be paid during measurements in order to avoid or induce the phase transition. That is the reason for the use of neutral filters during the Raman measurements shown in this work, as it results in 0.1 I_0, thus avoiding ART. However, if the ART was induced by laser irradiation using the highest intensity, it has been observed that Fe doping promotes the ART, while Al doping inhibits it, which confirms the effects of these dopants on the phase transition observed by thermo-diffraction. As an advantage, laser irradiation allows higher local control of the ART, which could be useful in the design of optimized devices based on rutile, anatase or mixed phases. Hence, further research based on laser irradiation is in progress in order to achieve a deeper understanding of the anatase-to-rutile transition.

Stabilization of the anatase phase, as that induced by Al doping in this work, could be essential in extending the range of applicability of the anatase TiO_2 in devices involving high temperature processes, such as gas sensors and catalysts, where phase transformation may alter the performance of the device.

Conclusions

To summarize, the synthesis method used in this work allows the growth of anatase TiO_2 nanoparticles doped with Al or Fe with sizes around 5 nm and high cationic concentration of dopants. As the diffusion process is enormously favored by means of the liquid solution involved in the synthesis process, cationic concentrations up to 30% were achieved when doping with Al, while when using Fe as a dopant values over 20% cat. result in the formation of ternary compounds. Raman spectroscopy measurements suggested variations in the surface order of the doped anatase nanocrystals, as Al and Fe doping generates contraction or relaxation of apical Ti–O bonds, respectively, which could inhibit or facilitate the phase transition. Variations in the luminescence, mainly associated with oxygen deficiency and Ti^{3+} related defects, have also been investigated in the doped nanoparticles. In particular, the emission at 1.66 eV observed in the Fe doped nanoparticles could indicate the presence of Fe^{3+} in tetrahedral coordination. XPS measurements confirmed the high presence of Ti^{3+} in the near surface region of the Al doped nanoparticles, the concentration of which decreases when doping with Fe. According to these results a higher concentration of Ti^{3+} at the surface of the nanoparticles has been associated with the inhibition of the ART. Thermo-diffraction measurements confirm that the phase

transition can be promoted by Fe doping and inhibited by Al doping. In particular, samples doped with 10% cat. Al are those for which ART is further inhibited, thus spreading the range of temperatures at which the anatase phase can operate up to values above 920 °C. Further investigation on the phenomena involved in the ART can broaden the applicability of the anatase phase in devices requiring high-temperature performance.

Acknowledgements

This work was supported by MINECO (Projects MAT2011-23068, MAT 2012-31959 and Consolider Ingenio CSD 2009-00013). The authors are grateful to National Centre for Electron Microscopy (CNME) at Universidad Complutense de Madrid.

Notes and references

1 S. C. Roy, O. K. Varghese, M. Paulose and C. A. Grimes, *ACS Nano*, 2010, **4**, 1259–1278.
2 M. Gratzel, *Nature*, 2001, **414**, 338–344.
3 D. A. H. Hanaor and C. C. Sorrell, *J. Mater. Sci.*, 2011, **46**, 855–874.
4 R. Asahi, T. Morikawa, T. Ohwaki, K. Aoki and Y. Taga, *Science*, 2001, **293**, 269–271.
5 G. C. Vásquez, M. A. Peche-Herrero, D. Maestre, A. Cremades, J. Ramírez-Castellanos, J. M. González-Calbet and J. Piqueras, *J. Phys. Chem. C*, 2013, **117**, 1941.
6 E. Setiawati and K. Kawano, *J. Alloys Compd.*, 2008, **451**, 293.
7 H. Cheng and A. Selloni, *Phys. Rev. B: Condens. Matter Mater. Phys.*, 2009, **79**, 092101.
8 D. P. Singh, A. George, R. V. Kumar, J. E. ten Elshof and H. Wagemaker, *J Phys Chem C*, 2013, **117**, 19809–19825.
9 B. Sun and P. G. Smirniotis, *Catal. Today*, 2003, **88**, 49.
10 T. Ohno, K. Tokieda, S. Higashida and M. Matsumura, *Appl. Catal., A*, 2003, **244**, 383–391.
11 S. Riyas, G. Krishnan and P. N. Mohandas, *Adv. Appl. Ceram.*, 2007, **106**, 225.
12 M. P. Pechini, U.S. Patent No. 3330697, 1967.
13 M. A. Peche-Herrero, G. C. Vásquez, D. Maestre, J. Ramírez-Castellanos, A. Cremades, J. Piqueras and J. M. González-Calbet (Universidad Complutense de Madrid), OEPM Patent P201400722, 2014.
14 M. Vila, C. Díaz-Guerra and J. Piqueras, *Appl. Phys. Lett.*, 2012, **101**, 071905.
15 T. Ohsaka, F. Izumi and Y. Fujiki, *J. Raman Spectrosc.*, 1978, **7**, 321–324.
16 L. Miao, S. Tanemura, S. Toh, K. Kaneko and M. Tanemura, *J. Cryst. Growth*, 2004, **264**, 246–252.
17 F. Tian, Y. Zhang, J. Zhang and C. Pan, *J. Phys. Chem. C*, 2012, **116**, 7515–7519.
18 S. V. Chong, N. Suresh, J. Xia, N. Al-Salim and H. Idriss, *J. Phys. Chem. C*, 2007, **111**, 10389–10393.
19 A. Li Bassi, D. Cattaneo, V. Russo, C. E. Bottani, E. Barborini, T. Mazza, P. Piseri, P. Milani, F. O. Ernst, K. Wegner and S. E. Pratsinis, *J. Appl. Phys.*, 2005, **98**, 074305.
20 A. Iwaszuk and M. Nolan, *J. Phys.: Condens. Matter*, 2011, **23**, 334207.
21 Y. J. Choi, Z. Seeley, A. Bandyopadhyay, S. Bose and S. A. Akbar, *Sens. Actuators, B*, 2007, **124**, 111–117.
22 J. C. Parker and R. W. Siegel, *J. Mater. Res.*, 1990, **5**, 1246–1252.
23 U. Gesenhues and T. Rentschler, *J. Solid State Chem.*, 1999, **143**, 210–218.
24 J. Zhang, X. Chen, Y. Shen, Y. Li, Z. Hu and J. Chu, *Phys. Chem. Chem. Phys.*, 2011, **13**, 13096–13105.
25 Y. Lei, L. D. Zhang, G. W. Meng, G. H. Li, X. Y. Zhang, C. H. Liang, W. Chen and S. X. Wang, *Appl. Phys. Lett.*, 2001, **78**, 1125.
26 R. Sanjinés, H. Tang, H. Berger, F. Gozzo, G. Margaritondo and F. Levy, *J. Appl. Phys.*, 1994, **75**, 2945.
27 S. Ghosh, G. G. Khan, K. Mandal, A. Samanta and P. M. G. Nambissan, *J. Phys. Chem. C*, 2013, **117**, 8458.
28 D. P. Colombo, K. A. Roussel, J. Saeh, D. E. Skinner, J. J. Cavaleri and R. M. Bowman, *Chem. Phys. Lett.*, 1995, **232**, 207.
29 C. C. Mercado, F. J. Knorr, J. L. McHale, S. M. Usmani, A. S. Ichimura and L. V. Saraf, *J. Phys. Chem. C*, 2012, **116**, 10796.
30 Y. Zhang, L. Wu, E. Xie, H. Duan, W. Han and J. Zhao, *J. Power Sources*, 2009, **189**, 1256.
31 S. Sahoo, A. K. Arora and V. Sridharan, *J. Phys. Chem. C*, 2009, **113**, 16927.
32 R. Shirley, M. Kraft and O. R. Inderwildi, *Phys. Rev. B: Condens. Matter Mater. Phys.*, 2010, **81**, 075111.
33 Q. Wu, J. Ouyang, K. Xie, L. Sun, M. Wang and C. Lin, *J. Hazard. Mater.*, 2012, **199–200**, 410.
34 M. Kayama, H. Nishido, S. Toyoda, K. Komuro, A. A. Finch, M. R. Lee and K. Ninagawa, *Am. Mineral.*, 2014, **99**, 65.
35 S. George, S. Pokhrel, Z. Ji, B. L. Henderson, T. Xia, L. Li, J. I. Zink, A. E. Nel and L. Mädler, *J. Am. Chem. Soc.*, 2013, **133**, 11270.
36 Q. Yu, L. Jin and C. Zhou, *Sol. Energy Mater. Sol. Cells*, 2011, **95**, 2322.
37 H. Zhang and J. F. Banfield, *J. Phys. Chem. B*, 2000, **104**, 34813487.
38 H. Zhang and J. F. Banfield, *Chem. Mater.*, 2005, **17**, 3421.
39 V. Etacheri, S. Pillai, M. K. Seery and S. J. Hinder, *Adv. Funct. Mater.*, 2011, **21**, 3744–3752.

2. EFECTOS DEL DOPADO CON METALES DE TRANSICIÓN EN EL CRECIMIENTO Y PROPIEDADES DE NANOPARTÍCULAS DE TiO_2 RUTILO

En un escenario contrario al expuesto anteriormente, la estabilización a elevadas temperaturas del óxido de titanio con estructura tipo rutilo favorece la segregación del dopante y el crecimiento del tamaño de partícula. A continuación, se presentan los resultados obtenidos al realizar la síntesis de nanopartículas de TiO_2 con estructura rutilo, dopadas con V, Cr y Mn, empleando precursores poliméricos. Este estudio permite establecer la influencia de los distintos cationes metálicos en la estabilización de la fase rutilo y, consecuentemente, en sus propiedades. El tamaño de partícula obtenido, comprendido entre 20 y 500 nm, depende del tipo y porcentaje de dopante empleado, consiguiéndose la estabilización de la estructura tipo rutilo a 650 °C, por debajo de los datos bibliográficos. El análisis microestructural de las nanopartículas muestra buena homogeneidad catiónica en las nanopartículas dopadas. El estudio de la cátodoluminiscencia pone de manifiesto que las nanopartículas dopadas muestran una señal luminiscente relacionada con la presencia de dopantes y defectos estructurales. En particular, se observa una intensa emisión a 1.52 eV, asociada con la presencia de Ti^{3+} intersticial que domina la luminiscencia de las nanopartículas sin dopar. Además, se observan emisiones menos intensas de 3.4 eV. Se puede concluir, por tanto, que la presencia de V, Cr y Mn en las nanopartículas de TiO_2 rutilo, induce variaciones en la señal catodoluminiscente, lo que es de gran utilidad para lograr una comprensión más profunda de los procesos de dopado, así como ampliar futuras aplicaciones ópticas. La espectroscopia fotoelectrónica de rayos X (XPS) confirma la presencia de Ti^{3+} intersticial en la región cercana a la superficie de las nanopartículas, cuya concentración disminuye al dopar.

THE JOURNAL OF PHYSICAL CHEMISTRY C

Article

pubs.acs.org/JPCC

Effects of Transition Metal Doping on the Growth and Properties of Rutile TiO_2 Nanoparticles

G. Cristian Vásquez,[†] M. Andrea Peche-Herrero,[‡] David Maestre,*[,†] Ana Cremades,[†] Julio Ramírez-Castellanos,[‡] José María González-Calbet,[‡] and Javier Piqueras[†]

[†]Departamento de Física de Materiales, Facultad de CC. Físicas, Universidad Complutense de Madrid, 28040 Madrid, Spain

[‡]Departamento de Química Inorgánica I, Facultad de CC. Químicas, Universidad Complutense de Madrid, 28040 Madrid, Spain

ABSTRACT: Rutile TiO_2 nanoparticles doped with V, Cr, or Mn ions have been synthesized via a modified Pechini method using polymeric precursors. The final particle sizes range between 20 and 500 nm depending on the selected dopant. The TiO_2 rutile phase has been stabilized in the doped nanoparticles at 650 °C. Microstructural analysis shows a good crystallinity and cationic homogeneity of the doped nanoparticles. The cathodoluminescence study of the doped and undoped nanoparticles shows a luminescence signal related to the structural defects of the samples and the presence of dopants. In particular, an intense 1.52 eV emission associated with Ti^{3+} interstitials dominates the luminescence of undoped nanoparticles, which also exhibit less intense emissions extending from 2 to 3.4 eV. The presence of V, Cr, or Mn in the rutile TiO_2 nanoparticles induces variations in the associated cathodoluminescence signal which would be useful in order to achieve a deeper understanding of the doping process and spread future optical applications. X-ray photoelectron spectroscopy (XPS) confirmed the presence of Ti^{3+} in the near-surface region of the nanoparticles, the concentration of which decreases when doping. The presence of Ti^{3+} interstitials related states in the band gap is discussed.

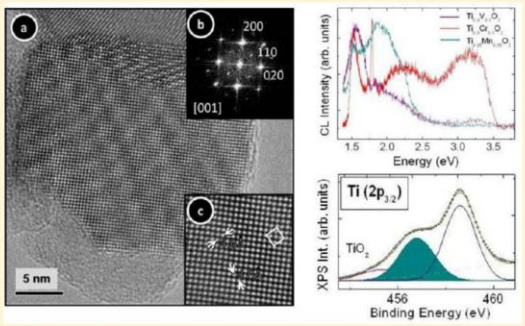

INTRODUCTION

During the past few years, TiO_2 nanoparticles have been extensively investigated due to their unique properties and demonstrated applications in different fields. In addition to its well-known photocatalytic activity, TiO_2 presents some other noteworthy applications, such as light guides, solar cells, hydrogen storage, and bioapplications, which can be optimized at the nanoscale.[1−4] In particular, nanostructured TiO_2, with its high specific surface area to volume ratio, enables improvements in catalysis or gas-sensing processes. Besides, these applications can also be improved and modulated by doping with different elements. Special attention has been recently focused on the investigation of the effects induced by transition metal dopants (e.g., V, Cr, and Mn) on the physical properties of nanocrystalline TiO_2.[5] For example, the impurity energy levels created by these dopants within the bandgap have been shown to enhance the photocatalytic activity of TiO_2 in the visible range.[6] Moreover, these doped nanocrystals emerge as an alternative to other quantum dots, due to the associated tunable emission, the spectral width, and thermal stability. Hence, an improvement in the controlled synthesis and doping of TiO_2 nanoparticles is required in order to exploit their properties in applications, as not only the chemical composition and the physical arrangement of the atoms but also the particle size influence the behavior of this material. The surface-sensitive chemical analysis provided by XPS, as well as the study of the levels induced in the bandgap by doping, represents a valuable contribution toward the understanding of the surface chemistry of TiO_2 and the doping process, as well as the luminescence properties of this material.

As it is well-known, TiO_2 crystallizes in three different polymorphs: anatase (tetragonal), brookite (orthorhombic), and rutile (tetragonal). The anatase to rutile phase transition (ART) is a nonreversible process because of the greater thermodynamic stability of rutile; therefore, control of the titania microstructure (in particular of the ART) is crucial to the performance of this material in many applications. The mechanism involved in the ART is one of nucleation and growth which involves a critical size effect[7] in order to become anatase nanoparticles more stable than the rutile ones, but only if the particle size is small enough. Doping TiO_2 with different cations can be a useful way to control the ART, and thus stabilize rutile nanoparticles at low temperatures. Since the solubility of dopants is usually higher in the anatase phase than in the rutile phase, segregation of dopant oxides might occur during the ART when preparing doped rutile nanoparticles. A control of all the synthesis parameters during the fabrication of the materials is necessary in order to avoid segregation.

Among the most extended methods to fabricate doped nanoparticles,[8−11] the use of polymeric precursors in the

Received: October 15, 2012
Revised: December 21, 2012
Published: January 18, 2013

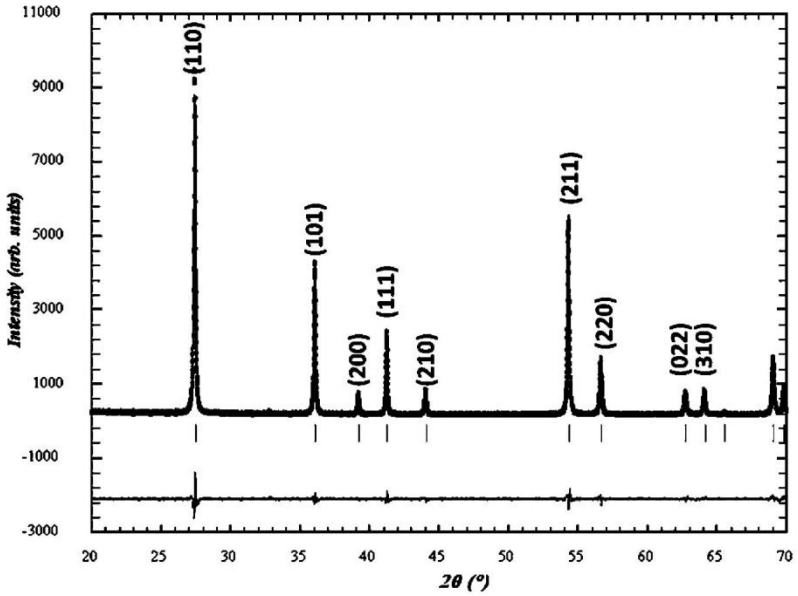

Figure 1. Refined XRD data of $Ti_{0.95}Mn_{0.05}O_2$ [a = 4.590, c = 2.958; D = 494.26 ± 0.22 Å; R_p, 6.12; R_{wp}, 8.32; R_{exp}, 6.47; χ^2: 1.66]. All maxima correspond with the rutile structure.

synthesis of ceramic materials, such as that employed in this investigation, is believed to have significant advantages, since it ensures the homogeneity in the distribution of the additives in the final material and allows for a high control of the particle size. This research reports on the synthesis, and the microstructural, chemical, and luminescent characteristics of $Ti_{1-x}M_xO_2$ (M = V, Cr, and Mn, and $0 \leq x \leq 0.1$) rutile solid solutions prepared by a modified Pechini method.[12]

■ EXPERIMENTAL SECTION

$Ti_{1-x}M_xO_2$ (x = 0, 0.05, 0.1; M = V, Cr, Mn) nanopowders were prepared using a "liquid-mix method". $Ti(OBu)_4$ (Aldrich 97%), NH_4VO_5 (Aldrich 99%), $Cr(NO_3)_3{\cdot}9H_2O$ (Aldrich 99%), $MnCO_3$ (Aldrich 99%), citric acid, and ethylene glycol (Aldrich) were used for the material synthesis. First of all, a 0.65 M solution of citric acid was prepared with deionized water. Second, stoichiometric amounts of $Ti(OBu)_4$ and the selected dopant precursor were added to the aqueous solution while it was continuously stirred. In order to obtain the preferred rutile phase, a small amount of hydrochloric acid was added as a catalyst. Afterward, 5% (v/v) of ethylene glycol was added to start the gelation, and as the water evaporated, resin was formed. Finally, the resin was calcined and a fine powder consisting of a mixture of doped titanium oxide nanoparticles was obtained for each dopant.

The powders were treated at 350 °C for 30 h in order to completely remove organic residues. To obtain a complete transition from anatase to rutile, the samples were treated at 650 °C for 15 h.

The samples were studied by X-ray diffraction (XRD) using a Siemens D5000 difractometer. Data were collected at 2θ between 10° and 70°, with a step size of 0.04° and a collection time of 1 s/step. Working radiation was Cu Kα (λ = 1.5418 Å). In order to obtain the cell parameters and Rietveld refinement analysis, XRD patterns were taken by using a Panalytical X'Pert Pro Alpha1 instrument, which is equipped with a primary fast X'Celerator detector operating at 45 kV and 40 mA, and fitted with a primary curved Ge 111 monochromator in order to obtain Cu Kα1 radiation (λ = 1.5406 Å).

Selected area electron diffraction (SAED) and high resolution transmission electron microscopy (HRTEM) were performed in a JEOL 3000 FEG electron microscope, and fitted with a double-tilting goniometer stage (±22°, ±22°). Local composition was analyzed by energy-dispersive X-ray spectroscopy (EDS) with an Oxford INCA analyzer system attached to the aforementioned microscope. Further HRTEM characterization was carried out with Digital Micrograph 3.9.3 software (Gatan Inc.) by using fast Fourier transform (FFT) and inverse fast Fourier transform (I-FFT) calculations. Image simulation was performed by using a MacTempas 2.3.24 program (Total Resolution Inc.).

The cathodoluminescence (CL) measurements were carried out in a Hitachi S2500 SEM at different temperatures ranging from 80 to 300 K, and using a beam energy of 18 keV. A Hamamatsu R928 photomultiplier and a Hamamatsu PMA-11 charge-coupled device camera were utilized for the analysis of the CL signal. Initial powders consisting of transition metal doped TiO_2 nanoparticles were compacted into pellets in order to facilitate the analysis of their luminescence.

Spatially resolved X-ray photoemission spectroscopy was performed at the ESCA microscopy beamline of the Elettra-Synchrotron facility in Trieste, Italy. Photoemission spectra were measured with a 640 eV photon energy while keeping a 0.2 eV energy resolution.

■ RESULTS AND DISCUSSION

Structural Characterization. Powder XRD characterization shows that all samples can be indexed on the basis of the TiO_2 rutile structure (sp. gr. $P4_2/mnm$, z = 2 with lattice parameters $a = b$ = 4.59 Å, c = 2.96 Å) with no appreciable variation in their lattice parameters due to size effects or doping. The range of stability of the obtained $Ti_{1-x}M_xO_2$ solid solutions depends on the dopant cation. Actually, Mn-doped rutile samples are only obtained up to a doping level of 5%, due

to the different solubility of the Mn in the anatase and rutile phases. Doped samples with higher Mn concentrations present segregation of Mn oxides occurring during the ART. Small quantities of transition metal ions improve the ART, as confirmed by XRD, so that all dopants studied in this research stabilize the rutile phase at 650 °C.

The effect of dopants on the morphology of the samples can be observed by comparing the V-doped samples with Cr- or Mn-doped samples. The former present an average particle size of 500 nm (microparticles), whereas the other materials show an average particle size from 20 to 70 nm, as deduced by the Scherrer formula: ($D = k\lambda/B \cos\theta$) where $B \equiv$ fwhm, after a Rietveld analyses of the monochromatic X-ray data (Figure 1). When synthesizing the V-doped samples, NH_4VO_3 is used as vanadium precursor. V^{5+} is a dopant that increases the oxygen vacancies concentration due to its small size and high charge, acting as promoter of the ART. Because the ART follows a nucleation−growth mechanism from anatase to rutile, when the formation of anatase is inhibited with the presence of V^{5+}, the sample directly nucleates as rutile and grows during the thermal treatment, which results in bigger particles than in the case of the Cr- and Mn-doped samples. These results were also confirmed by microscopy techniques. Figure 2 shows a low

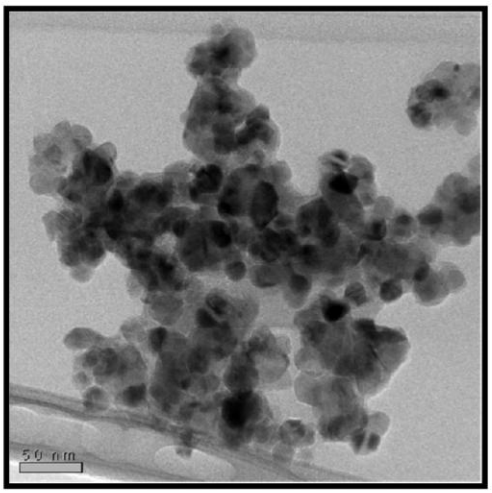

Figure 2. Low-magnification TEM image of $Ti_{0.9}Cr_{0.1}O_2$ nanoparticles.

magnification TEM micrograph corresponding to the $Ti_{0.9}Cr_{0.1}O_2$ sample, where an average size of 25−30 nm can be observed. Figure 3a shows the HRTEM micrograph corresponding to an isolated and well-crystallized $Ti_{0.9}Cr_{0.1}O_2$ nanoparticle at higher magnification along the [001] axis, which is the basal plane of the rutile crystal structure, as confirmed by the corresponding FFT pattern (Figure 3b). No extra spots or streaking can be observed, indicating that compositional variations are randomly distributed along the rutile structural type. Interplanar distances of 4.6 Å can be measured along both perpendicular directions, corresponding to the *a* reticular lattice parameter of the basal plane of the rutile structure. The unit cell of the material (marked on the image as a square) can be clearly observed in Figure 3c. Figure 4a shows a HRTEM image of the $Ti_{0.9}V_{0.1}O_2$ sample along the [100] rutile zone axis. The SAED pattern is shown in Figure 4b with the maxima of the [100] zone axes. Lattice parameters of $b = 4.64$ Å and $c = 2.87$ Å are

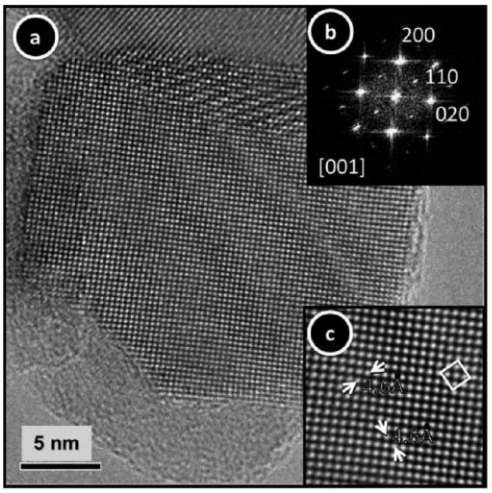

Figure 3. (a) HRTEM image of a $Ti_{0.9}Cr_{0.1}O_2$ nanoparticle; (b) FFT pattern along the [001] axis of the rutile structure; and (c) I-FFT image showing reticular parameters and unit cell of the rutile basal plane.

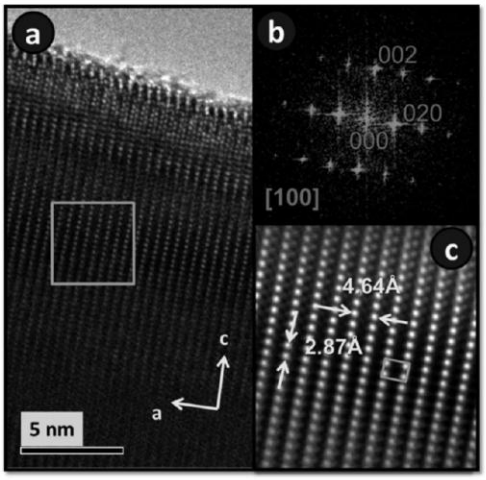

Figure 4. (a) HRTEM image of the $Ti_{0.9}V_{0.1}O_2$ sample. (b) Selected area electron diffraction (SAED) pattern along the [100] axis of the rutile structure. (c) I-FFT image showing reticular parameters and unit cell of the rutile [100] zone axis.

indicated in the I-FFT image (Figure 4c), together with the unit cell marked as a square.

Table 1 shows the EDS data of the samples, which confirms the incorporation of dopants close to 5% and 10%, respectively, and their compositional homogeneity.

Cathodoluminescence. The luminescent properties of undoped and doped TiO_2 nanoparticles have been investigated in the visible and near-infrared ranges by CL in SEM. First, the

Table 1. EDX Data of the $Ti_{1-x}M_xO_2$ (M = V, Cr, and Mn) Samples' Cationic Concentration

X (%)	V (%)	Cr (%)	Mn (%)
5	4.1 ± 2.4	5.1 ± 0.2	5.3 ± 0.4
10	6.4 ± 3.7	10.8 ± 0.5	

dx.doi.org/10.1021/jp3101656 | J. Phys. Chem. C 2013, 117, 1941−1947

CL signal from the undoped TiO_2 nanoparticles has been analyzed as a function of the temperature, as shown in Figure 5.

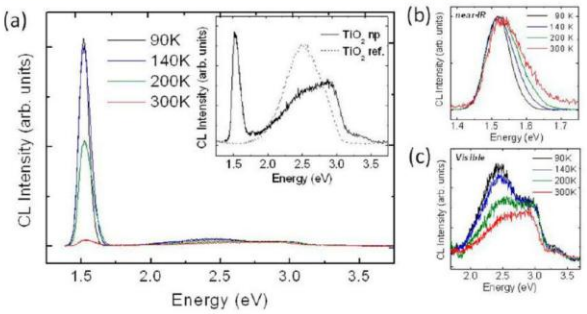

Figure 5. (a) CL spectra from undoped TiO_2 nanoparticles obtained at temperatures ranging from 90 to 300 K. CL spectrum from polycrystalline TiO_2 acquired at 300 K is also shown as an inset. Detailed near-infrared (normalized) and visible regions from (a) are shown in (b) and (c), respectively.

The CL spectra consist of a complex broad band in the visible region, extending from 2 to 3.4 eV, and a narrower band in the near-infrared range peaked at 1.52 eV, which clearly dominates the spectra, mainly at low temperatures. The inset of Figure 5a shows the spectra at 300 K of the nanoparticles and of commercial polycrystalline rutile TiO_2 powders, as a reference. Details of the spectra shown in Figure 5a corresponding to the near-infrared (normalized) and the visible ranges are shown in Figure 5, b and c, respectively. The defect structure of TiO_2 usually includes titanium interstitials, as well as oxygen vacancies and some other oxygen-related defects. The narrow and intense near-infrared emission at 1.52 eV observed in the CL spectra has been previously attributed to the presence of Ti^{3+} interstitials in the lattice;[13] hence our CL results confirm the high concentration of these defects in the TiO_2 nanoparticles under study. Ti^{3+} defect states are formed within the bandgap at 0.7−0.8 eV below the Fermi level[13,14] leading to this near-infrared emission, and are related with oxygen deficiency, as they can be formed by removal of neutral oxygen in the TiO_2 rutile cell. By the creation of an oxygen vacancy, the two electrons previously occupying O 2p states in the valence band can migrate into the conduction band, the bottom of which is formed by Ti 3d states. Therefore, each Ti atom surrounding the removed oxygen can capture one of these electrons, which causes the formation of Ti^{3+}-related defect states within the bandgap. Ti^{3+} sites have been demonstrated to be photocatalytically active sites,[15] as they behave as coordinatively unsaturated ions, and hence special attention should be paid to their study especially in photooxidation and photocatalysis. In our case, the near-infrared emission at 1.52 eV is favored in the TiO_2 nanoparticles, as compared to the polycrystalline commercial rutile TiO_2, the CL spectrum of which is also shown in Figure 5a (inset) as a reference. It has been demonstrated[15] that the presence of Ti^{3+} is enhanced as the particle size is reduced, which agrees with our CL results. Previous studies on sintered TiO_2 revealed that this near-infrared emission also appears when the commercial powder is sintered at low temperatures and is quenched at high sintering temperatures due to the defect recovery process involved during the treatment.[9]

The CL signal from undoped TiO_2 nanoparticles has been also investigated in the visible range (Figure 5c). Two main emissions, centered on 2.40 and 3 eV, have been observed. The broad luminescence band at 2.40 eV can be attributed to surface states which create shallow traps at energies between 0.27 and 0.87 eV below the conduction band.[14] Some of these surface states are associated with oxygen vacancies and deep levels related to Ti^{4+} ions adjacent to oxygen vacancies.[16] Previous studies[9] deconvoluted this emission into three bands centered at 2.19, 2.30, and 2.55 eV, respectively. These emissions could be explained not only attending to the presence of oxygen vacancies related defects (2.19 eV) but also due to titanate groups near defects (2.55 eV), and oxygen adsorbed on the surface.[17,18]

The high energy emission centered on 3 eV, also observed in Figure 5c, can be associated with radiative transitions due to free excitons localized at TiO_6 octahedral units, resulting from the interaction between electrons located in Ti 3d states in the conduction band and holes formed essentially by the O 2p states at the valence band. These excitonic transitions involve shallow levels within the gap.[19] Some authors considered a possible blue shift caused by quantum confinement effects due to the reduced size of similar sized nanoparticles[20−22] (as the bandgap of rutile TiO_2 is 3.05 eV). However, the Bohr radius for rutile TiO_2 is substantially smaller (0.8 nm)[23] than the average nanocrystallite size in our case, and therefore we disregard any quantum confinement effect on the luminescence.[24]

The dependence of the CL signal with the temperature has been investigated in the range from 90 to 300 K, as shown in Figure 5a. Decreasing the temperature induces an enhancement of the CL intensity, in particular in the near-infrared range. The intensity of this emission (1.52 eV) increases by a factor 30 when the temperature decreases from 300 to 90 K. In addition, the band broadens toward higher energies as the temperature rises, as observed in Figure 5b which shows normalized spectra. Variations in the CL signal as a function of the temperature are not so noticeable in the visible range. An increase in the intensity of the band at 2.40 eV as compared to the 3 eV is observed as the temperature rises (Figure 5c). Therefore, different activation energies should be associated with the near-infrared and the visible emissions.

Variations in the CL signal have been also found as a function of the doping element and its concentration. Figure 6a shows CL spectra corresponding to TiO_2 nanoparticles doped with different amounts of V, Cr, or Mn. Comparison with undoped TiO_2 reveals that the dopant incorporation into the host lattice causes a marked effect on the luminescence. As the dopant concentration increases, the total CL intensity decreases. As a general trend for all doped samples, the ratio between the intensity of the near-infrared emission (1.52 eV) and the intensity of the emissions at higher energies is significantly reduced compared with the undoped samples, as observed in Figure 6a. This effect could indicate that the presence of the dopant ions decreases the concentration of Ti^{3+} defects, either by substitution or charge balance due to the multivalence of some of these transition metal cations. Moreover, variations on the complex CL emission in the visible range take place due to the presence of dopant-induced deep levels in the bandgap. Two different behaviors are observed in the spectra as a function of the energy range covered by the CL signal. TiO_2 nanoparticles doped with Cr exhibit broad CL spectra which extend from 1.4 to 3.5 eV, while V- and Mn-doped TiO_2 nanoparticles show a narrower CL emission from 1.4 to 2.6 eV. The presence of V and Mn inhibits

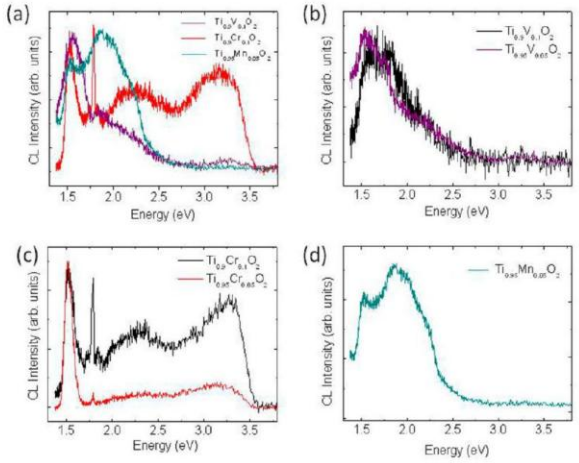

Figure 6. (a) Normalized CL spectra from V-, Cr-, and Mn-doped TiO_2 nanoparticles. (b,c,d) CL spectra from TiO_2 nanoparticles doped with different amounts of V, Cr, and Mn, respectively.

the emissions at energies over 2.6 eV observed in undoped TiO_2 nanoparticles. In order to investigate the influence of the transition metal ions in the luminescence of the nanoparticles, different set of CL spectra have been acquired as a function of the concentration of each dopant, as shown in Figure 6.

V-doped samples present a dominant emission around 1.5−1.6 eV, as well as a shoulder at 2.2 eV and a weak emission at 3.2 eV, as observed in the normalized CL spectra of Figure 6b. As the cationic concentration of vanadium in the lattice increases, the total CL intensity decreases, in particular the emission at the near-infrared region. This emission could be attributed to Ti^{3+} defects, as for undoped TiO_2; however, vanadium can generate deep levels situated 1.6 eV above the valence band as a consequence of the low 3d energy of the V atom[25] which can also contribute to this near-infrared emission. Previous studies[26] stated that vanadium is present as V^{4+} substitutional in rutile TiO_2, generated by reduction of V^{5+} due to the presence of Ti^{3+} defects in the lattice, as could occur in our case. V^{4+} creates levels 2.1 eV below the conduction band, which can be associated with the shoulder at 2.2 eV observed in Figure 6b.

Cr-doped samples present a complex CL spectrum which covers the whole visible range, from the near-infrared to the ultraviolet. The total CL intensity decreases as the amount of chromium rises. In addition to the 1.52 eV emission, a narrow and intense emission peaked at 1.79 eV can be also observed (Figure 6c). This emission corresponds to the $^2E-^4A_2$ intraionic transition associated with Cr^{3+} ions in octahedral coordination, as referred by different authors.[27] The presence of this emission indicates that chromium has been incorporated as Cr^{3+} into the rutile TiO_2 lattice, and behaves as optically active center without the requirement of further treatments. In some cases, a less intense broad band is superimposed to this emission at 1.79 eV, as in Figure 6c, which is associated with $^4T_2-^4A_2$ transitions of Cr^{3+}. As the amount of Cr^{3+} increases, causing the enhancement of the 1.79 eV emission, the intensity of the 1.52 eV band (associated with Ti^{3+}) is reduced. This competitive process suggests that Cr^{3+} ions substitute Ti^{3+} interstitials in the TiO_2 rutile, although charge transfer from matrix to the Cr^{3+} ion should be also considered. Other emissions are observed around 2.2 and 3.3 eV, as shown in Figure 6c. The former could be associated with deep levels in the bandgap due to oxygen vacancy related defects, as the presence of these defects is promoted by Cr^{3+} in order to maintain the charge balance. The high energy emission above 3.0 eV is increased in these samples as compared to the undoped TiO_2 nanoparticles.

Mn-doped samples present luminescence bands in the near-infrared (1.52 eV) and the red-orange (1.9−2.3 eV) regions, while no emission in the high-energy range is observed (Figure 6d). Some authors[28] attributed the band at 1.9−2.0 eV to $^4T_1-^6A_1$ transitions related to Mn^{2+} octahedrally coordinated in TiO_2. Other emissions such as $^5E-^5T_2$ transitions related to Mn^{3+} at 2.75 eV, or tetrahedrally coordinated Mn^{2+}, are not observed in the CL spectra (Figure 6d), which indicates that manganese is predominantly present as octahedral Mn^{2+} in the lattice. This could cause a charge imbalance in the rutile TiO_2 decreasing oxygen-related defects as well as the related luminescence around 2.4 eV. In this case, only $Ti_{0.95}Mn_{0.05}O_2$ samples are studied, as higher doping levels induce segregation of Mn oxides and anatase formation.

X-ray Photoelectron Spectroscopy. The chemical analysis of the TiO_2 nanoparticles was performed by core-level surface-sensitive XPS. The photoelectron spectra have been calibrated with respect to the C(1s) core level centered at 284.6 eV. Characteristic $Ti(2p_{1/2})$ and $Ti(2p_{3/2})$ splitting due to spin−orbit coupling have been observed in the photoelectron spectra, although this study is focused on the more intense $Ti(2p_{3/2})$ contribution. XPS $Ti(2p_{3/2})$ spectrum corresponding to undoped TiO_2 nanoparticles is depicted in Figure 7a (upper spectrum). Moreover, XPS Ti(2p) spectrum

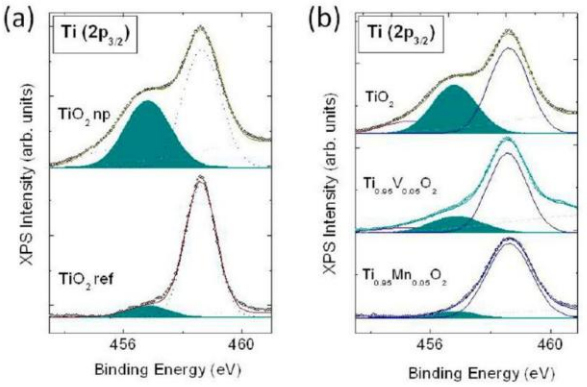

Figure 7. (a) XPS spectra from undoped TiO_2 nanoparticles and polycrystalline TiO_2 used as a reference. (b) XPS spectra from undoped TiO_2 nanoparticles and V- and Mn-doped TiO_2 nanoparticles.

from commercial polycrystalline rutile TiO_2 powders is also included in Figure 7a as a reference (lower spectrum). This latter is dominated by a peak centered at 458.6 eV which corresponds to Ti^{4+} in rutile TiO_2.[29] A weak shoulder can be also appreciated at lower binding energies around 456.8 eV. This contribution, filled in the spectrum, is attributed to lower oxidation states species, in particular to Ti^{3+}. On the other hand, XPS spectrum from the undoped TiO_2 nanoparticles under study is composed of three peaks centered at 455.3 eV, 456.8 and 458.6 eV, which can be attributed to Ti^{2+}, Ti^{3+}, and Ti^{4+}, respectively, in agreement with the NIST database. The higher binding energy contribution (458.6 eV) associated with

dx.doi.org/10.1021/jp3101656 | J. Phys. Chem. C 2013, 117, 1941−1947

Ti^{4+} in rutile TiO_2 dominates the photoelectron spectrum, although a significant increase in the contribution associated with Ti^{3+} can be clearly appreciated (filled in the spectrum). The Ti^{3+} to Ti^{4+} atomic ratio, deduced from the relative integrated areas of the corresponding peaks in the XPS spectra, increases from 0.12 to 0.59 when probing the reference polycrystalline TiO_2 powders or the nanoparticles, respectively. These results agree with those obtained by cathodoluminescence, where a higher concentration of Ti^{3+} interstitials was detected in the undoped TiO_2 nanoparticles. Some other authors also confirmed the increase in the Ti^{3+} sites in TiO_2 as the particle size is reduced.[15] These Ti^{3+} sites play an important role in the photocatalyst properties of TiO_2, and therefore huge interest is invested in their study in nanoparticles.

XPS spectra have been also recorded in the doped TiO_2 nanoparticles. In this case, only V- and Mn-doped TiO_2 samples were able to be investigated, as the Cr-doped TiO_2 samples showed high charge effects due to the reduced conductivity, which hinders their study. Figure 7b shows XPS spectra obtained in V- and Mn-doped TiO_2 nanoparticles, as well as in undoped TiO_2 nanoparticles as a reference. It can be appreciated how the contribution peaked at 456.8 eV associated with Ti^{3+}, filled in the spectra, decreases in the doped nanoparticles. This effect is more evident in the Mn than in V-doped TiO_2. The Ti^{3+} to Ti^{4+} atomic ratio varies from 0.59 in the undoped nanoparticles to 0.32 and 0.14 in the V- and Mn-doped TiO_2, respectively, which indicates a decrease of the concentration of Ti^{3+} sites when doping. Our CL results also support this behavior, as the emission related to Ti^{3+} interstitials also decreases in the doped samples. Figure 8, a and b, shows V(3p) and Mn(3p) core levels at 40.4 and 49.5 eV, respectively, which confirms the presence of these dopants in the probed nanoparticles.

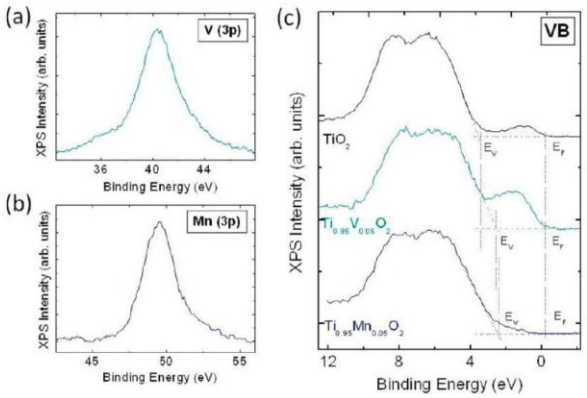

Figure 8. (a) V (3p) and (b) Mn (3p) XPS core levels. (c) Valence band XPS spectra acquired on undoped as well as V- and Mn-doped TiO_2 nanoparticles.

More insight can be obtained from the study of the valence band (VB) photoelectron spectra. At the top of the VB contributions from O(2p) nonbonding states around 4 eV, as well as O(2p) π and O(2p) σ states around 5 and 8 eV, respectively, resulting from the crystal field splitting, can be appreciated,[30] as shown in Figure 8c. Moreover, a peak centered around 1 eV below the Fermi level (E_F), associated with Ti(3d)-derived states, is observed in the XPS spectra from undoped, and V-doped TiO_2 nanoparticles (Figure 8c). This defect state has been usually attributed to oxygen vacancies, in particular to bridging oxygen vacancies;[29,31] however, recent research revised this model and associated this contribution with Ti interstitials in the near-surface region.[32] Our results support this possibility, as the CL and XPS measurements also indicate the presence of Ti^{3+} in those samples where the Ti(3d)-derived state appears in the valence band region. Nevertheless, the presence of oxygen vacancies cannot be ruled out. In the case of the V-doped nanoparticles, this contribution in the spectra is slightly modified as not only Ti(3d) states but also V(3d)-derived states are present in the valence band region below the Fermi level.

V and Mn doping reduces the relative position of the Fermi level with respect to the valence band maximum (VBM) around 0.6 eV, as observed in Figure 8c, which is consistent with a p-type character of the surface induced by doping. Similar behavior has been referred in Mn-doped In_2O_3.[33]

■ CONCLUSIONS

The "liquid-mix" method enables the synthesis of doped TiO_2 rutile nanoparticles with a high degree of crystallinity and homogeneous cation distribution, as confirmed by EDS microanalysis. Nanoparticles sizes are between 20 and 70 nm for Mn- and Cr-doped samples, and 500 nm on average for V-doped samples. All dopants used in this research improve the ART and stabilize the TiO_2 rutile phase at 650 °C. Cationic concentration of up to about 10% is obtained for Cr and V doping. Undoped TiO_2 nanoparticles show a luminescence dominated by an emission at 1.52 eV associated with Ti^{3+} interstitials. Emissions of lower intensity, extending from 2 to 3.4 eV, are related to oxygen vacancies, titanate groups near defects, and the near band emission of free excitons. The CL emission of doped nanoparticles varies as a function of the selected dopant and its concentration. As a general result, the intensity of the near-infrared emission at 1.52 eV is highly reduced by doping. Either Ti^{3+} interstitials could be partially substituted by the dopant cations, as in the case of Cr^{3+}, or a change in the charge state of Ti^{3+} could be induced with the charge imbalance introduced by the preferential incorporation of vanadium as V^{4+} and manganese as Mn^{2+}, respectively. This would lead to the decrease of the 1.52 eV emission in all cases. V-doped samples are characterized by luminescence emissions at 1.6 and 2.1 eV from deep levels related with V^{4+} incorporation, as well as a reduction of emissions related to oxygen vacancies. The incorporation of Cr^{3+} is characterized by the sharp intraionic emission at 1.79 eV, the increase of oxygen vacancies related emissions, and the near-band emission at around 3.3 eV. Furthermore, the study of Mn-doped nanoparticles demonstrated that the emission at 1.9 eV is related with intraionic emission from octahedral coordinated Mn^{2+} in the TiO_2 lattice. A substantial contribution from Ti^{3+}, in addition to Ti^{4+}, in the nanoparticles has been confirmed by XPS. The presence of these Ti^{3+} sites decreases when doping, which agrees with the CL results. Although further research is necessary in order to exploit potential applications, these results are believed to be a valuable contribution toward the understanding of the doping process and the dopant-induced levels in the bandgap, which controls the luminescence properties.

■ AUTHOR INFORMATION

Corresponding Author

*E-mail: davidmaestre@fis.ucm.es.

Notes

The authors declare no competing financial interest.

■ ACKNOWLEDGMENTS

This work was supported by MICINN (MAT-2009-07882, CSD 2009-00013, MAT2011-23068). The authors are grateful to National Center for Electron Microscopy (CNME) at Universidad Complutense de Madrid. The authors are grateful to the ESCA microscopy beamline staff for useful advice on XPS measurements at the Elettra Sincrotron in Trieste.

■ REFERENCES

(1) Hoffmann, M. R.; Martin, S. T.; Choi, W.; Bahnemann, D. W. *Chem. Rev.* **1995**, *95*, 69−69.
(2) Grätzel, M. Photoelectrochemical Cells. *Nature* **2001**, *414*, 338−344.
(3) Linsebigler, A. L.; Lu, G.; Yates, J. T. *Chem. Rev.* **1995**, *95*, 735−758.
(4) Millis, A.; Le Hunte, S. J. *Photochem. Photobiol. A* **1997**, *108*, 1−35.
(5) Kronawitter, C. X.; Bakke, J. R.; Wheeler, D. A.; Wang, W. C.; Chang, C.; Antoun, B. R.; Zhang, J. Z.; Guo, J.; Bent, S. F.; Mao, S. S.; Vayssieres, L. *Nano Lett.* **2011**, *11*, 3855−3861.
(6) Zhu, Y.; Zhang, L.; Yao, W.; Cao, L. *Appl. Surf. Sci.* **2000**, *158*, 32−37.
(7) Reidy, D. J.; Holmes, J. D.; Morris, M. A. *J. Eur. Ceram. Soc.* **2006**, *26*, 1527−1534.
(8) Trentler, T. J.; Denler, T. E.; Bertone, J. F.; Agrawal, A.; Colvin, V. L. *J. Am. Chem. Soc.* **1999**, *121*, 1613−1614.
(9) Maestre, D.; Cremades, A.; Piqueras, J. *Nanotechnology* **2006**, *17*, 1584−1588.
(10) Wu, J. J.; Yu, C. C. *J. Phys. Chem. B* **2004**, *108*, 3377−3379.
(11) Lei, Y.; Zhang, L. D.; Fan, J. C. *Chem. Phys. Lett.* **2001**, *338*, 231−236.
(12) Pechini, M. P. US Patent No. 3330697, 1967.
(13) Fernández, I.; Cremades, A.; Piqueras, J. *Semicond. Sci. Technol.* **2005**, *20*, 239−243.
(14) Sanjinés, R.; Tang, H.; Berger, H.; Gozzo, F.; Margaritondo, G.; Levy, F. *J. Appl. Phys.* **1994**, *75*, 2945−1−2945−7.
(15) Kumar, P. M.; Badrinarayanan, S.; Sastry, M. *Thin Solid Films* **2000**, 358 122.130.
(16) Colombo, D. P.; Roussel, K. A.; Saeh, J.; Skinner, D. E.; Cavaleri, J. J.; Bowman, R. M. *Chem. Phys. Lett.* **1995**, *232*, 207−214.
(17) Lei, Y.; Zhang, D.; Meng, G. W.; Li, G. H.; Zhang, X. Y.; Liang, C. H.; Chen, W.; Wang, S. X. *Appl. Phys. Lett.* **2001**, *78*, 1125−1127.
(18) Wu, J. M.; Shih, H. C.; Wu, W. T.; Tseng, Y. K.; Chen, I. C. *J. Cryst. Growth* **2005**, *281*, 384−390.
(19) Suisalu, A.; Aarik, J.; Mändar, H.; Sildos, I. *Thin Solid Films* **1998**, *336*, 295−298.
(20) Liu, S. W.; Song, C. F.; Lü, M. K.; Gu, F.; Wang, S. F.; Xu, D.; Yuan, D. R.; Wang, C. *Mater. Sci. Eng., B* **2003**, *104*, 49−53.
(21) Satoh, N.; Nakashima, T.; Kamikura, K.; Yamamoto, K. *Nat. Nanotechnol.* **2008**, *3*, 106−111.
(22) Peng, H.; Li, J.; Li, S. S.; Xia, J. B. *J. Phys. Chem. C* **2008**, *112*, 13964−13969.
(23) Enright, B.; Fitzmaurice, D. *J. Phys. Chem.* **1996**, *100*, 1027−1035.
(24) Monticone, S.; Tufeu, R.; Kanaev, A. V.; Scolan, E.; Sánchez, C. *Appl. Surf. Sci.* **2000**, *162*−*163*, 565−570.
(25) Osorio-Guillén, J.; Lany, S.; Zunger, A. *Phys. Rev. Lett.* **2008**, *100*, 036601−1−036601−4.
(26) Klosek, S.; Raftery, D. *J. Phys. Chem. B* **2001**, *105*, 2815−2819.
(27) Nogales, E.; García, J. A.; Méndez, B.; Piqueras, J. *J. Appl. Phys.* **2007**, *101*, 033517−1−033517−4.
(28) Song, C. F.; Lü, M. K.; Yang, P.; Gu, F.; Xu, D.; Yuan, D. R. *J. Sol-Gel Sci. Technol.* **2003**, *28*, 196−197.
(29) Diebold, U. *Surf. Sci. Rep.* **2003**, *48*, 53−229.
(30) Luciu, I.; Bartali, R.; Laidani, N. *J. Phys. D: Appl. Phys.* **2012**, *45*, 345302−1−345302−9.
(31) Thomas, A. G.; Flavell, W. R.; Mallick, A. K.; Kumarasinghe, A. R.; Tsoutsou, D.; Khan, N.; Chatwin, C.; Rayner, S.; Smith, G. C.; Stockbauer, R. L.; Warren, S.; Johal, T. K.; Patel, S.; Holland, D.; Taleb, A.; Wiame, F. *Phys. Rev. B* **2007**, *75*, 035105−1−035105−12.
(32) Wendt, S.; Sprunger, P. T.; Lira, E.; Madsen, G. K. H.; Li, Z.; Hansen, J. O.; Matthiesen, J.; Blekige-Rasmussen, A.; Laegsgaard, E.; Hammer, B.; Besenbacher, F. *Science* **2008**, *320*, 1755−1759.
(33) Maestre, D.; Martinez de Velasco, I.; Cremades, A.; Amati, M.; Piqueras, J. *J. Phys. Chem. C* **2010**, *114*, 11748−11752.

3. MICROTUBOS Y MICROVARAS DE TITANIA DOPADAS CON Cr SINTETIZADAS POR UN MÉTODO DE VAPOR-SÓLIDO

Con objeto de estudiar la influencia del dopante en los procesos de crecimiento, se ha realizado la síntesis de microtubos y microvaras mediante el método de vapor-sólido, a partir de las nanopartículas de TiO_2 obtenidas en el estudio anterior, debido a la elevada reactividad que presentan por su tamaño nanométrico. Las microestructuras crecidas presentan una sección cuasi cuadrada de unas pocas micras de ancho y hasta 100 micras de longitud. El empleo de tratamientos térmicos más largos o de temperaturas más elevadas favorece la relación de microvaras respecto a la de microtubos. La presencia de oquedades parcialmente llenas, con escalones de crecimiento en las caras internas de los tubos, indica que estos se transforman en varas cuando aumenta el tiempo o temperatura de tratamiento, lo que permite el control de la microestructura, tubos o varas, al variar los parámetros del tratamiento térmico. Se ha observado que la incorporación del Cr es homogénea a lo largo del eje de crecimiento, con cantidades que varían entre 1.2 y 2.8% de la fracción catiónica, que depende del contenido de Cr del precursor y los parámetros de crecimiento. El estudio de las propiedades optoelectrónicas pone de manifiesto que la activación óptica de los iones Cr con cátodoluminescencia en el microscopio electrónico de barrido.

CrystEngComm

RSCPublishing

PAPER

Cr doped titania microtubes and microrods synthesized by a vapor–solid method

Cite this: *CrystEngComm*, 2013, **15**, 5490

G. Cristian Vásquez,[a] M. Andrea Peche-Herrero,[b] David Maestre,*[a] Ana Cremades,[a] Julio Ramírez-Castellanos,[b] José M. González-Calbet[b] and Javier Piqueras[a]

Received 22nd March 2013,
Accepted 8th May 2013

DOI: 10.1039/c3ce40513c

www.rsc.org/crystengcomm

Cr doped TiO_2 rutile nanoparticles have been used as precursor of microrods and microtubes grown by a vapor–solid method. The grown microstructures have nearly square cross-sections of a few microns wide and lengths of up to about 100 microns. By longer thermal treatments or higher growth temperatures, the ratio of microrods to microtubes increases. The presence of partially filled openings with growth steps in the internal faces of the tubes indicates that the tubes transform into rods by extended or intense thermal treatments, which enables to control the nature of the microstructures, tubes or rods, by varying the parameters of the thermal treatment. Cr incorporation has been found to be homogeneous along the growth axis, with amounts in the range from 1.2 to 2.8% of cationic fraction, which depend on the Cr content in the precursor and on the growth parameters. Optical activation of the Cr ions has been demonstrated by cathodoluminescence in the scanning electron microscopy, and crystallographic assessment of the structures has been carried out using Raman spectroscopy and electron backscattered diffraction.

Introduction

Titanium dioxide (TiO_2 or titania) nanoparticles, and other low dimensional structures have been extensively investigated in relation to different applications in the fields of photocatalysis, gas sensing, and solar cells.[1–3] In particular, nanostructured TiO_2 with high specific surface area enables the improvement of catalysis or gas sensing processes. Synthesis of titania nanoparticles[4–7] as well as of nanotubes and nanowires[8–13] have been often reported in the past years. The physical and chemical properties of the nanoparticles and other structures can be improved, or controlled by doping with different elements. For instance, titania nanoparticles doped with Pd and Pt,[14] N,[15] Au,[16] Er,[17] and different transition metals,[18] and nanowires doped with Fe,[19] N,[20] Sn,[21] and Cr[22] have been reported. Recently nanocomposites based on TiO_2 combined with carbon nanomaterials, such as carbon nanotubes and graphene, have demonstrated a remarkable improvement in their photocatalytic activity.[23,24] In the particular case of Cr, also doped TiO_2,[25] and titanate nanotubes[26] have been synthesized. Doping with Cr and other transition metal ions has been found to influence the photocatalytic activity of titania.[18,27,28] In addition, doped titania nano- and microstructures have potential applications related to tunable optical emission and thermal stability. In a recent work[29] we have reported on the use of a modified Pechini method to synthesize Cr doped (5 or 10% cationic fraction) TiO_2 rutile nanoparticles with a high degree of cationic homogeneity. Cr incorporation was assessed by energy dispersive spectroscopy (EDS) and by the 1.79 eV emission corresponding to the ^2E–$^4A_2$ intraionic transition of Cr^{3+}. In the present work a powder consisting of these Cr doped nanoparticles has been used as precursor for the thermal growth, by an evaporation–deposition process, of Cr doped microtubes and microrods. The method used enables the control of the Cr content in the microstructures which depends on the thermal treatment and on the amount of dopant in the precursor. Tubular TiO_2 structures have been scarcely reported as the rutile TiO_2 microtubes of ref. 30, but to our knowledge Cr doped TiO_2 microtubes, such as those described in this work, have not been reported so far. The microtubes and microrods were characterized by X-ray diffraction (XRD), scanning electron microscopy (SEM), energy dispersive X-ray spectroscopy (EDS), cathodoluminescence (CL) and electron backscattered diffraction (EBSD) in SEM, and microRaman spectroscopy in a confocal microscope.

Experimental method

A powder of Cr doped TiO_2 nanoparticles was used as a precursor to grow doped TiO_2 microtubes and microrods. The powder, with 5 or 10% cationic fraction of Cr, synthesised as reported in ref. 29, was compacted to form disks of about 7

[a]*Departamento de Física de Materiales, Facultad de Ciencias Físicas, Universidad Complutense de Madrid, 28040 Madrid, Spain. E-mail: davidmaestre@fis.ucm.es*
[b]*Departamento de Química Inorgánica I, Facultad de Ciencias Químicas, Universidad Complutense de Madrid, 28040 Madrid, Spain*

mm diameter and thickness of about 1 mm. The samples were then annealed under argon flow at temperatures between 1200 °C and 1400 °C for 10 or 15 hours. For XRD studies a Philips X'Pert Pro diffractometer using Cu Kα radiation was employed. The morphology of the microtubes and microrods grown on the surface of the compacted pellets during the thermal treatment was studied with a Leica 440 and a Fei Inspect SEM. EDS was performed with a Bruker AXS Quantax system in a Leica 440 SEM. For CL measurements in SEM a Hamamatsu R928 photomultiplier or a PMA-11 charge-coupled device camera were used. CL measurements were performed at temperatures between 100 and 300 K. Raman characterization at room temperature was carried out with a Horiba Jobin–Yvon LabRam Hr800 confocal microscope with a 325 nm He–Cd laser. A Bruker e-Flash electron backscattered diffractometer (EBSD) was used for the structural analysis of single microstructures in a FEI Inspect SEM.

Results and discussion

XRD measurements show that the as-grown microstructures consist of rutile TiO_2, as observed in the XRD pattern of the sample treated at 1300 °C shown in Fig. 1. The peaks at 2θ values of around 27.4°, 36.1° and 54.3° indicate that the preferential crystal orientations correspond to (110), (101) and (211) respectively. No peaks from chromium oxides or ternary compounds have been observed.

Sintering effects are appreciated in samples annealed at 1200 °C and only isolated elongated structures are observed. After annealing treatments at 1250 °C for 10 hours, microrods and microtubes were found to grow on the surface of the disks prepared from powder either with 5% or 10% Cr cationic fraction, as shown in Fig. 2.

Temperatures of 1300 °C also generate microrods and microtubes with sizes slightly larger than those grown at 1250 °C. The presence of these microstructures is drastically reduced after treatments at higher temperatures (1400 °C), at which supersaturation and other thermodynamic conditions

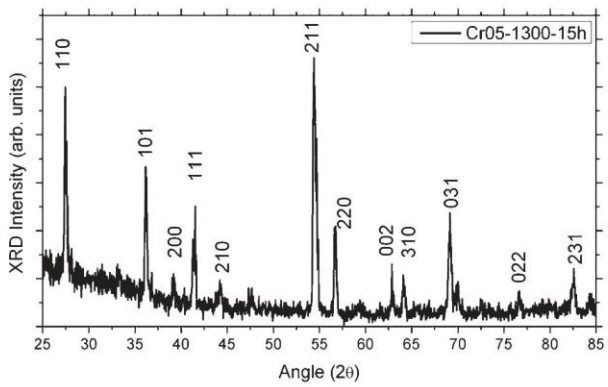

Fig. 1 XRD pattern from Cr doped TiO_2 microstructures grown at 1300 °C.

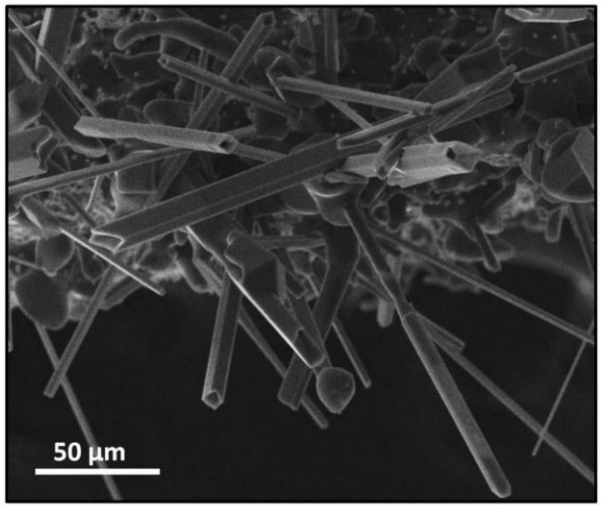

Fig. 2 SEM image from Cr doped TiO_2 tubes and rods grown at 1250 °C.

vary, and grain growth and sintering effects are promoted instead of the growth of elongated microstructures.

The microtubes grown at temperatures between 1250–1300 °C exhibit flat surfaces and nearly square cross-section of few microns width and lengths of up to about 100 microns (Fig. 3a). Most of these tubes present a characteristic four-peaked tip appearance, as observed in Fig. 3b. The proportion of rods to tubes appears to be higher in samples annealed at 1300 °C. In fact, in these samples a number of the tubes have a partially filled opening (Fig. 3c and 3d) which suggests that the rods form from the tubular structures during intense thermal treatments. The inset in Fig. 3d shows steps around the central hole which could indicate a growth of wall thickness toward the center of the tube, also observed in other tetragonal

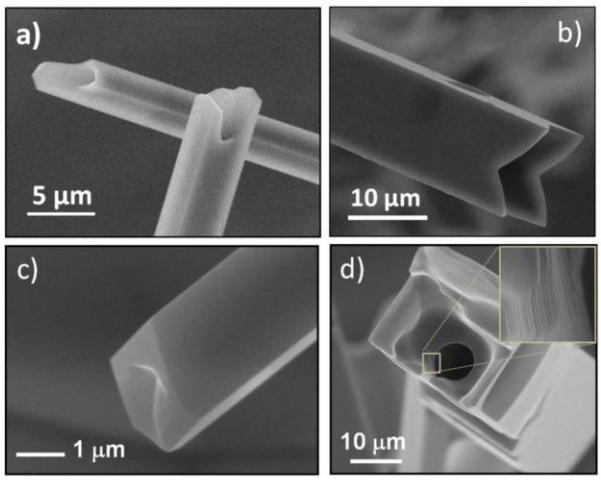

Fig. 3 (a) SEM images from Cr doped TiO_2 microtubes, (b) some of which show a four-peaked tip. (c) SEM images of tubes with partially filled openings and (d) growth steps in the internal faces indicating that the tubes transform into rods.

systems.[31,32] By increasing the annealing time to 15 hours at 1300 °C, most of the resulting structures were microrods and only small number of tubes was observed. The size and shape of the rods and tubes do not depend on the Cr content (5 or 10% of cationic fraction) in the precursor.

In order to study the growth of these elongated microstructures, some of their crystallographic aspects have been further investigated by EBSD and Raman spectroscopy. EBSD measurements in a SEM allow us to identify the crystallographic orientation of the surfaces forming the microrods and microtubes. Firstly the microstructures were carefully detached from the sintered pellet and then placed onto a Si (100) substrate in order to assure the correct orientation assessment. Fig. 4 shows the indexed EBSD pattern (Fig. 4b) and the EBSD pole figure (Fig. 4c) of the surface marked in the microtube of Fig. 4a. The EBSD pattern and pole figure show that the probed face of the microtube corresponds to the (110) plane of rutile TiO_2. Similar results were obtained by measuring in different microtubes. According to these results the {110} planes form the single crystalline lateral faces of the microtubes, the growth direction of which would be [001]. The lowest surface energy of {110} faces, in comparison with other faces, explains the observed preferential growth. A schematic model of one of these microtubes is shown in Fig. 4d. A similar crystallographic configuration has been recently proposed by Niwa *et al.*[30] on undoped TiO_2 microtubes grown from metallic titanium.

The growth direction of the microtubes under study with lateral faces corresponding to the {110} family planes can be confirmed by means of polarized Raman spectroscopy, as some of the Raman modes are very sensitive to the laser polarization.[33,34] Fig. 5 shows characteristic Raman spectra of a microtube where active modes at 236 cm^{-1} (multi-photon), 447 cm^{-1} (E_g), 612 cm^{-1} (A_{1g}) and 812 cm^{-1} (B_{2g}), corresponding to rutile TiO_2, are observed. Measurements have been carried out under two different configurations, by rotating the microtubes around their surface normal at a fixed set up for the polarizer and analizer. The coordinate system, fixed at the sample holder, has been chosen in such a way that the *x*, *y*, and *z* axes correspond to the crystal directions [−110], [011] and [001] respectively, as indicated in Fig. 5. Experimental geometries named as –Y(XX)Y and –Y(ZZ)Y, according to the Porto notation,[33,34] are shown in Fig. 5a and 5b. In this manner –Y(XX)Y configuration implies a laser incidence under the *y*-axis and a laser polarized under the *x*-axis, orthogonal to the microtube long axis, with the backscattered signal collected under the *y*-axis. By rotating the sample 90° with the polarizer fixed, a second measurement geometry is selected, –Y(ZZ)Y, with the laser polarization along the microtube long axis. The Raman spectra corresponding to both configurations are shown in Fig. 5c.

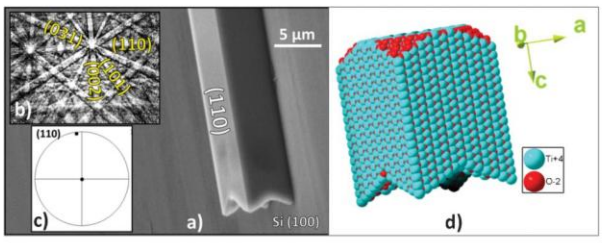

Fig. 4 (a) SEM image of a typical Cr doped TiO_2 microtube with (b) indexed EBSD pattern and (c) the corresponding EBSD pole figure indicating that the probed surface corresponds to the (110). (d) Schematic image of the microtube.

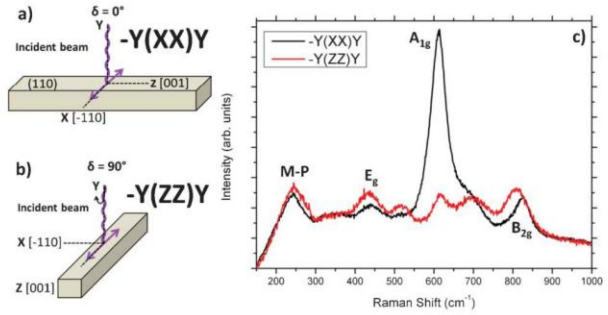

Fig. 5 (a), (b) Schematic models showing the laser incidence and the microtube relative position in both –Y(XX)Y and –Y(ZZ)Y configurations. (c) Raman spectra acquired on a microtube under –Y(XX)Y and –Y(ZZ)Y configurations.

Under these conditions, advantage can be taken from the large polarization angle dependence of the A_{1g} mode at 612 cm^{-1} in rutile TiO_2 (100). This A_{1g} phonon mode is supposed to appear as an intense peak in the –Y(XX)Y configuration (δ = 0°) and is expected to present a rather low intensity under –Y(ZZ)Y geometry (δ = 90°). This effect can be explained on the basis of the variation of the Raman scattering tensor components as a function of the polarization geometry and crystal orientation.[33] The drastic decrease of the A_{1g} mode (612 cm^{-1}) with respect to the E_g mode (447 cm^{-1}) when changing from –Y(XX)Y to –Y(ZZ)Y geometry indicates that the crystal grows along the [001] direction.

We verified this orientation dependence in a (110) rutile TiO_2 single crystal. Fig. 6 shows the gradual decrease of the A_{1g}

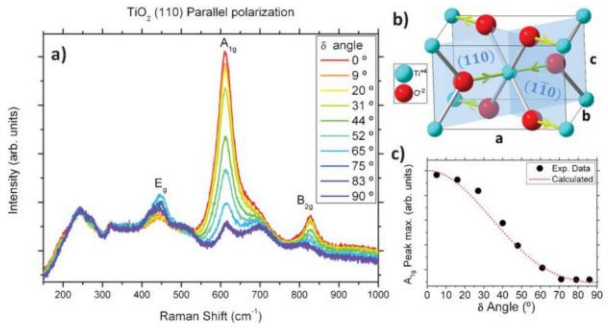

Fig. 6 (a) Raman spectra from rutile TiO_2 single crystal as a function of δ showing a decrease in the A_{1g} mode relative intensity. (b) Schematic model of rutile TiO_2 unit cell indicating (110) and (1$\bar{1}$0) planes. (c) Experimental and calculated data showing the angular dependence of the A_{1g} mode relative intensity.

mode intensity as the crystal is rotated from $\delta = 0^\circ$ to $\delta = 90^\circ$, starting from –Y(XX)Y geometry. The A_{1g} mode is related to motion of oxygen orthogonally to the *c*-axis of the rutile unit cell (Fig. 6b), while the E_g mode is associated with translational vibration of alternated oxygens along the *c*-axis, which explains their relative intensity dependence on the experimental geometry. This angular dependence of the Raman modes intensity follows the theoretical relationship $I \sim |a\cos^2\delta + b\sin^2\delta|^2$, where a and b denote Raman tensor components of the A_{1g} mode,[31] as shown in Fig. 6c. Similar results, although with less intense Raman spectra, have been obtained by rotating the polarization direction while keeping the sample fixed, which confirms the suitability of this technique. Therefore, polarized Raman spectroscopy, combined with EBSD study enables the unambiguous determination of the growth direction of the microrods and microtubes under study, which in this case corresponds to the [001] direction.

Cr content in the microstructures after thermal treatments has been found, as measured by EDS, to depend on the cationic concentration of Cr in the initial powder and on the annealing treatment parameters. Fig. 7a shows EDS spectra recorded on microstructures grown from the 5% Cr precursor under different conditions, and for comparison the spectrum of the precursor (labelled as Cr05) has been also represented. All spectra were normalized to the Ti $K\alpha_1$ intensity. Table 1 shows the measured Cr cation % corresponding to rods and tubes after the different treatments applied to grow these structures.

Higher Cr contents were measured in the elongated microstructures grown from initial powder with 10% Cr, with respect to those grown from 5% Cr. As an example, microstructures grown at 1300 °C during 10 hours have Cr contents of about 1.2% or 2.6% when starting from 5% or 10% Cr respectively. Also the Cr content depends on the annealing parameters and, in particular, decreases for higher temperatures and annealing times, as indicated in Table 1. This effect could be related to the thermally-promoted change from Cr^{3+} to Cr^{4+} assisted by oxygen vacancies at the crystal surface, as reported by Feldman *et al.*[35]

The amount of Cr in the grains of the pellet background on which rods and tubes grow was also measured and the obtained values are always higher than those in the elongated

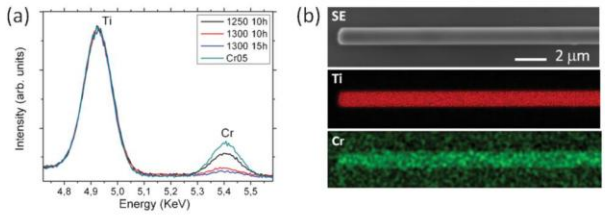

Fig. 7 (a) EDS spectra acquired on Cr doped TiO_2 microstructures grown by different thermal treatments. The EDS spectrum from Cr doped TiO_2 nanoparticles used as precursor (Cr05) is also shown as a reference. (b) EDS compositional mappings of Ti and Cr on a typical Cr doped TiO_2 microrod.

Table 1 Averaged Cr cationic concentrations measured by EBSD on microstructures grown by different thermal treatments

	5% Cr			10% Cr	
	Rod	Tube	Grain	Rod	Tube
1250 (10 h)	2.8	1.3	4.1	—	—
1300 (10 h)	2.1	1.2	2.7	2.8	2.6
1300 (15 h)	1.8	—	1.4	2.4	2.1

structures. EDS measurements also indicate that most of the probed rods show Cr contents slightly higher than in tubes. EDS mappings of microrods and microtubes grown under different annealing conditions exhibit high homogeneity of Cr and Ti distribution along axial and radial directions of the microstructures, as shown in Fig. 7b.

The CL signal allows us to investigate the incorporation of Cr into the structures. Fig. 8a shows CL spectra of the TiO_2 precursor powders containing 5% and 10% cationic fraction of Cr. These spectra are similar to that of pure TiO_2 powder recorded under the same conditions, showing a dominant band at 1.52 eV which has been associated with Ti^{3+} interstitial ions (*e.g.* ref. 12 and 36) and, as enlarged in the inset, a broad band extending from 2 to 3.4 eV. This wide emission is formed by a band at about 2.2 eV possibly related to surface states,[12] in particular to deep levels in the bandgap due to oxygen vacancy related defects, and a band at energies over 3 eV related to excitonic transitions, the relative intensity of which increases with the amount of Cr. A sharp emission at 1.79 eV, corresponding to intraionic transitions related to Cr^{3+}, can be observed in the spectra, mainly in powders with 10% Cr. In

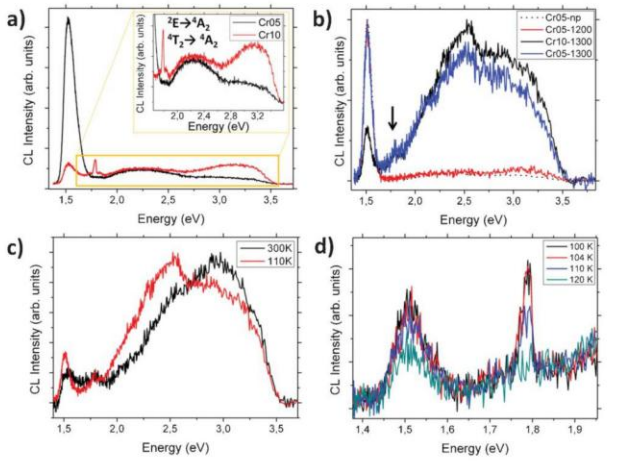

Fig. 8 (a) CL spectra of Cr doped TiO_2 nanoparticles with 5% and 10% Cr used as precursor. (b) Normalized CL spectra acquired on microstructures grown at 1300 °C starting with 5% and 10% Cr powders and CL spectra from initial 5% Cr powder and grains sintered at 1200 °C. (c) Normalized CL spectra from Cr doped TiO_2 microstructures grown at 1300 °C from 10% Cr powders acquired at 110 K and 300 K. (d) Variation of the CL signal between 100 and 120 K from a region enlarged from (c).

a previous work[29] it has been discussed that the intensity of the 1.52 eV band (associated with Ti^{3+} interstitials) is reduced as the 1.79 eV emission is enhanced due to the increase of Cr^{3+}, which suggests that Cr^{3+} ions would substitute Ti^{3+} interstitials in TiO_2 nanoparticles. A similar behaviour has been reported in some other semiconductor oxides.[37,38] Nevertheless the incorporation of Cr^{3+} substituting Ti^{4+}, which would result in the formation of oxygen vacancies in order to reach charge neutrality, cannot be ruled out.

The spectra of the thermal treated samples present differences as a function of the Cr incorporation. An example corresponding to the sample annealed at 1300 °C for 10 hours is shown in Fig. 8b, in which the normalized spectra of the microstructures grown from powders with 5% and 10% Cr are depicted (labelled as Cr05-1300 and Cr10-1300). The amounts of Cr in these microstructures correspond to 1.2 and 2.6% respectively, as measured by EDS (Table 1). The CL spectrum from initial 5% Cr precursor (Cr05-np) and from grains sintered at 1200 °C (Cr05-1200) are also shown for comparison. It can be observed that Cr incorporation in the microstructures depletes the relative intensity of the emission at 1.52 eV, associated with Ti^{3+} interstitials, and enhances the relative intensity of the emissions from 2 to 3.4 eV. This qualitative behaviour applies to samples prepared with other thermal treatments. The observed relative decrease of the emission at 1.52 eV associated with Ti^{3+} interstitials could be related to a substitution of Ti^{3+} by Cr^{3+}, although charge transfer from the matrix to the Cr^{3+} ions should be also considered. CL spectra from rods and tubes also exhibit some differences, being the relative intensity of the 1.52 eV emission lower in the rods. CL spectra show a weak emission at about 1.8 eV (indicated with an arrow in Fig. 8b). In this case the emission line at 1.79 eV associated to ^2E–$^4A_2$ intraionic transitions of Cr^{3+} is not resolved as a sharp line but it would be included in this weak band.

Variation in the CL signal is found as a function of the measurement temperature, as shown in Fig. 8c, where normalized spectra acquired at 110 K and 300 K on microstructures grown at 1300 °C are shown. The emission at 2.4 eV, and those centered at 1.79 eV and 1.52 eV, are better defined at low temperature. In particular the intensity of the emission at 1.79 eV related to Cr^{3+} is increased as the temperature decreases, as observed in Fig. 8d where emissions at 1.52 eV and 1.79 eV are depicted as the temperature varies from 100 K to 120 K. The presence of this emission at 1.79 eV demonstrates that Cr^{3+} ions have been incorporated in the microrods and microtubes and behave as optically active.

Conclusions

Cr doped TiO_2 rutile microrods and microtubes with Cr contents in the range 1.2–2.8% cationic fraction and homogeneous dopant distribution have been grown by a vapor–solid method with Cr doped TiO_2 nanoparticles as a precursor. Microtubes are a previous growth stage of the microrods and the transformation takes place by filling the tubes during extended, or higher temperature, thermal treatments. EBSD and Raman spectroscopy show that the growth axis of the structures is [001] and the lateral faces are {110} planes. CL in SEM shows a decrease of the 1.52 eV emission band, associated with Ti^{3+} interstitials, by increasing Cr content, which indicates a substitution of Ti^{3+} by Cr^{3+}. The optical activation of the Cr ions is revealed by the emission at 1.79 eV in the CL spectra. Further measurements by means of transmission electron microscopy (TEM) and X-ray photoelectron spectroscopy (XPS) are underway in order to achieve a better understanding of the growth and doping processes of TiO_2 microstructures grown by a vapor–solid method.

Acknowledgements

This work has been supported by MEC (Projects MAT2009-07882, MAT2012-39159 and Consolider CSD 2009-00013).

Notes and references

1 M. Grätzel, *Nature*, 2001, **414**, 338.
2 A. Mills and S. Le Hunte, *J. Photochem. Photobiol., A*, 1997, **108**, 1.
3 R. Asahi, T. Morikawa, T. Ohwaki, K. Aoki and Y. Taga, *Science*, 2001, **293**, 269.
4 K. Madhusudan Reddy, S. V. Manorama and A. Ramachandra Reddy, *Mater. Chem. Phys.*, 2003, **78**, 239.
5 Z. Y. Wu, J. Zhang, K. Ibrahim, D. C. Xian, G. Li, Y. Tao, T. D. Hu, S. Bellucci, A. Marcelli, Q. H. Zhang, L. Gao and Z. Z. Chen, *Appl. Phys. Lett.*, 2002, **80**, 2973.
6 J. Tang, F. Redl, Y. Zhu, T. Siegrist, L. E. Brus and M. L. Steigerwald, *Nano Lett.*, 2005, **5**, 543.
7 L. Song, Y. M. Lam, C. Boothroyd and P. W. Teo, *Nanotechnology*, 2007, **18**, 135605.
8 Y. Lei, L. D. Zhang, G. W. Meng, G. H. Li, X. Y. Zhang, C. H. Liang, W. Chen and S. X. Wang, *Appl. Phys. Lett.*, 2001, **78**, 1125.
9 G. H. Du, Q. Chen, R. C. Che, Z. Y. Yuan and L. M. Peng, *Appl. Phys. Lett.*, 2001, **79**, 3702.
10 B. D. Yao, Y. F. Chan, X. Y. Zhang, W. F. Zhang, Z. Y. Yang and N. Wang, *Appl. Phys. Lett.*, 2003, **82**, 281.
11 S. K. Pradhan, P. J. Reucroft, F. Yang and A. Dozier, *J. Cryst. Growth*, 2003, **256**, 83.
12 D. Maestre, A. Cremades and J. Piqueras, *Nanotechnology*, 2006, **17**, 1584.
13 D. Maestre, A. Cremades, L. Gregoratti and J. Piqueras, *J. Nanosci. Nanotechnol.*, 2008, **8**, 6533.
14 Y. Zhu, L. Zhang, W. Yao and L. Cao, *Appl. Surf. Sci.*, 2000, **158**, 32.
15 C. Burda, Y. Lou, X. Chen, A. C. S. Samia, J. Stout and J. L. Gole, *Nano Lett.*, 2003, **3**, 1049.
16 K. M. Rahulan, S. Ganesan and P. Aruna, *Adv. Nat. Sci.: Nanosci. Nanotechnol.*, 2011, **2**, 025012.
17 S. Jeon and P. V. Braun, *Chem. Mater.*, 2003, **15**, 1256.
18 J. Chen, M. Yao and X. Wang, *J. Nanopart. Res.*, 2008, **10**, 163.

19 N. Farhangi, R. R. Chowdhury, Y. Medina-González, M. B. Ray and P. A. Charpentier, *Appl. Catal., B*, 2011, **110**, 25.
20 A. Yu, G. Wu, F. Zhang, Y. Yang and N. Guan, *Catal. Lett.*, 2009, **129**, 507.
21 M. Xu, P. Da, H. Wu, D. Zhao and G. Zheng, *Nano Lett.*, 2012, **12**, 1503.
22 B. Tian, C. Li, F. Gu, H. Jiang and Y. Hu, *J. Inorg. Mater.*, 2009, **24**, 661.
23 W.-J. Ong, M. M. Gui, S.-P. Chai and A. R. Mohamed, *RSC Adv.*, 2013, **3**, 4505.
24 Y. Zhang, N. Zhang, Z.-R. Tang and Y.-J. Xu, *Phys. Chem. Chem. Phys.*, 2012, **14**, 9167.
25 A. Ghicov, B. Schmidt, J. Kunze and P. Schmuki, *Chem. Phys. Lett.*, 2007, **433**, 323.
26 C. Díaz-Guerra, P. Umek, A. Gloter and J. Piqueras, *J. Phys. Chem. C*, 2010, **114**, 8192.
27 M. K. Nowotny, L. R. Sheppard, T. Bak and J. Nowotny, *J. Phys. Chem. C*, 2008, **112**, 5275.
28 K. Wilke and H. D. Breuer, *J. Photochem. Photobiol., A*, 1999, **121**, 49.
29 C. Vásquez, M. A. Peche-Herrero, D. Maestre, A. Cremades, J. Ramírez-Castellanos, J. M. González-Calbet and J. Piqueras, *J. Phys. Chem. C*, 2013, **117**, 1941.
30 K. Niwa, T. Taguchi, T. Tokunaga and M. Hasegawa, *Cryst. Growth Des.*, 2011, **11**, 4427.
31 R. S. Chen, H. M. Chang, Y. S. Huang, D. S. Tsai and K. C. Chiu, *Nanotechnology*, 2005, **16**, 93.
32 D. Maestre, A. Cremades and J. Piqueras, *J. Appl. Phys.*, 2005, **97**, 044316.
33 S. P. S. Porto, P. A. Fleury and T. C. Damen, *Phys. Rev.*, 1967, **154**, 522.
34 V. Presser, B. E. Schuster, M. B. Casu, U. Heinemeyer, F. Schreiber, K. G. Nickel and T. Chassé, *J. Raman Spectrosc.*, 2009, **40**, 2015.
35 R. Feldman, Y. Shimony and Z. Burshtein, *Opt. Mater.*, 2003, **24**, 333.
36 I. Fernández, A. Cremades and J. Piqueras, *Semicond. Sci. Technol.*, 2005, **20**, 239.
37 W. Zheng, K. Singh, Z. Wang, J. T. Wright, J. Van Tol, N. S. Dalal, R. W. Meulenberg and G. G. Strouse, *J. Am. Chem. Soc.*, 2012, **134**, 5577.
38 E. Nogales, J. A. García, B. Méndez and J. Piqueras, *J. Appl. Phys.*, 2007, **101**, 033517.

4. DOPADO CONTROLADO CON METALES DE TRANSICIÓN DE NANOPARTICULAS DE SnO_2 CON LUMINISCENCIA REGULABLE

Debido a la similitud estructural existente entre la fase rutilo del óxido de titanio y la fase casiterita del óxido de estaño se ha llevado a cabo un estudio de los parámetros de síntesis que afectan a la morfología de estos óxidos, así como de la influencia del dopante. Teniendo en cuenta estas ideas, las nanopartículas de SnO_2 dopadas con metales de transición (V, Cr y Mn) se han preparado mediante dos métodos por vía húmeda. En primer lugar, se ha usado el método HDT, obteniéndose aglomerados de partículas que presentan alta dispersión de tamaños. Por otra parte, nanopartículas obtenidas mediante la técnica LQM presentan una morfología bastante regular, tamaño medio de 6 nm y composición homogénea de acuerdo, en todos los casos, con la nominal. Los estudios de luminiscencia ponen de manifiesto la existencia de una gran dependencia entre las señales de CL con el dopado con metales de transición, induciendo emisiones roja, verde o naranja al dopar con Cr, V o Mn, respectivamente.

CrystEngComm

PAPER

View Article Online
View Journal | View Issue

Cite this: *CrystEngComm*, 2014, **16**, 2969

The controlled transition-metal doping of SnO_2 nanoparticles with tunable luminescence

M. A. Peche-Herrero,[a] D. Maestre,*[b] J. Ramírez-Castellanos,[a] A. Cremades,[b] J. Piqueras[b] and J. M. González-Calbet[a]

Received 28th October 2013,
Accepted 8th January 2014

DOI: 10.1039/c3ce42188k

www.rsc.org/crystengcomm

SnO_2 nanoparticles doped with transition metals (V, Cr, Mn) have been synthesized by both the hydrothermal method (HDT) in a basic media and the liquid mixed method (LQM) based on the Pechini method. Nanocrystalline particles obtained *via* a liquid mixed technique show a well-defined chemical composition and an average size of 6 nm, with a high degree of both crystallinity and chemical homogeneity. Nanoparticles prepared *via* a hydrothermal method exhibit a high dispersion in size as well as agglomeration effects. As the LQM demonstrates advantages with respect to the HDT, a more detailed investigation has been carried out on the SnO_2 nanoparticles doped with V, Cr and Mn grown by this method. The microstructure of the materials was elucidated by means of X-ray Diffraction (XRD), Selected-Area Electron Diffraction (SAED), and High-Resolution Transmission Electron Microscopy (HRTEM). Luminescence from undoped and doped SnO_2 nanoparticles was characterized by cathodoluminescence (CL). The luminescence studies demonstrate a strong dependence of CL signals with transition metal doping, thus inducing red, green or orange emissions when doping with Cr, V or Mn respectively.

Introduction

SnO_2 cassiterite is a wide-band gap n-type semiconductor (E_g = 3.6 eV at 300 K) with excellent electrical, optical and electrochemical properties[1,2] which make it suitable for numerous technological applications. During previous years the capabilities of this material have been exploited in diverse fields such as gas sensing,[3–5] solar cells,[6] catalysis,[7] optoelectronics,[8,9] or as a diluted magnetic semiconductor (DMSO),[10,11] in all of which low dimensional structures play a key role. Facing these applications, new challenging performances of SnO_2 have been recently developed, such as SnO_2/graphene nanocomposites and SnO_2 nanoparticles as promising materials for high capacity Li-ion battery anodes,[12,13] or SnO_2-based spintronic devices,[14] among others. Hence, in order to optimize these potential applications and to extend the applicability of this material, it is important to improve the synthesis methods that are able to control with high accuracy the size, morphology and composition of the SnO_2 nanostructures. In particular the achievement of a controlled doping of nanostructures, with a high concentration of doping atoms and cationic ordering, is a difficult issue in which great efforts are invested, as it is of the utmost importance for the control of the performance of SnO_2 based electronic and optoelectronic devices.

Several chemical methods have been developed so far in order to obtain SnO_2 nanoparticles such as hydrothermal methods,[15,16] sol–gel,[17–21] co-precipitation,[5,10,22] chemical vapor deposition (CVD),[4] mechanical synthesis,[11,23] laser pyrolysis,[24] and thermal evaporation.[25] In this paper we applied and evaluated the advantages and drawbacks of two soft chemistry methods in order to obtain optimized nanosized materials. In this sense, both the hydrothermal method (HDT) and the less extended liquid mix method (LQM)[26] have been used and evaluated in this work for the synthesis of doped nanoparticles. The HDT was chosen as a comparative soft chemical route because it is a proven method to obtain nanoparticles due to the special conditions that can be reached at low temperatures, which permits the obtention of smaller particles.[15] It has been only recently that the LQM has been employed for the synthesis of doped nanoparticles, as this synthetic pathway developed for the preparation of mixed oxides allows the production of reproducible quantities with a precise homogeneity in both composition and particle size, as demonstrated in this work. In this case the basic concept is to stabilize an aqueous solution of the desired cations with citric acid, or other hydroxy–carboxylic acids. The high-complexing potential of these acids avoids the precipitation of

[a] *Departamento de Química Inorgánica I, Facultad de Ciencias Químicas, Universidad Complutense de Madrid, 28040 Madrid, Spain*
[b] *Departamento de Física de Materiales, Facultad de Ciencias Físicas, Universidad Complutense de Madrid, 28040 Madrid, Spain. E-mail: davidmaestre@fis.ucm.es*

View Article Online

Paper CrystEngComm

the dissolved metals when the solvent is evaporated, which maintains this homogeneity in the solid state. In this way, not only a precise control of the cationic concentration is possible, but also the diffusion process is enormously favored by means of the liquid solution, as compared to other classical methods. In particular, to the best of our knowledge, the LQM has not been previously used for the synthesis of V, Cr and Mn doped SnO_2 nanoparticles, therefore these results will provide valuable knowledge both for applications and fundamental research. In addition, despite of the fact that in this work only transition metals (V, Cr, Mn) have been used as dopants, the here-described synthesis methods can be also extended to the growth of some other doped materials. In particular, transition metal (V, Cr, Mn) doped semiconductor nanoparticles, such as those investigated in this work, are emerging as promising candidates for spintronic and optoelectronic applications, hence further research should be invested on the understanding of the effects promoted by a controlled size and cationic composition on their physical–chemical properties. The structure of the defects, the effectiveness of the dopant incorporation, the achievement of a high-controlled cationic composition, the structural stability, the interplay of the native defects with the dopants, the influence of the dopants in both the growth process and the modulation of the electrical and optical properties, or the relationship between the electronic structure of the doped SnO_2 nanoparticles and their functional properties, are crucial aspects which need to be deeply investigated in order to integrate doped nanoparticles into advanced devices. In this sense, the cathodoluminescence (CL) technique is an useful tool to further analyze the structure of the defects and the effects of the doping on SnO_2, as metal ions usually introduce localized states in the band gap as well as defect related levels, mainly associated with oxygen vacancies or Sn interstitials, which influence the luminescence properties of the nanostructures.

Following these ideas, we discuss the synthesis of the undoped SnO_2 and $Sn_{1-x}M_xO_2$ (M = V, Cr and Mn, $0 \le x \le 0.15$) nanoparticles through two different preparation methods, HDT and LQM. The materials were characterized by X-Ray Diffraction (XRD), X-ray Energy Dispersive Spectroscopy (EDS), High-Resolution Transmission Electron Microscopy (HRTEM) and Cathodoluminescence (CL) in a Scanning Electron Microscope (SEM).

Materials and methods

Sample preparation

The undoped SnO_2 and $Sn_{1-x}M_xO_2$ (x = 0, 0.05, 0.1, 0.15; M = V, Cr, Mn) samples were prepared *via* two different wet chemical routes in order to obtain nanopowders with a controlled particle size, morphology and composition. In both cases, stoichiometric amounts of $Sn(CH_3COO)_2$ (Aldrich 99.99%), $SnCl_4{\cdot}5H_2O$ (Aldrich 99.99%), NH_4VO_5 (Aldrich 99%), $Cr(NO_3)_3{\cdot}9H_2O$ (Aldrich 99.99%), $MnCO_3$ (Aldrich 99.9%), NaOH, ethanol, citric acid ($C_6O_7H_8$) and ethylene glycol ($C_2O_2H_6$) (Aldrich) were used as starting materials.

In the hydrothermal method (HDT) an ethanol solution of sodium hydroxide was added dropwise to a 0.15 M aqueous solution of tin chloride and the corresponding dopant precursor, until pH = 12. The obtained solution was introduced into a Teflon lined non-stirred pressure vessel, and it was then heated in an oven for 12 hours at 180 °C. Afterwards, the oven was cooled down to room temperature and the products were rinsed with water and ethanol, and then finally dried at 60 °C.

In the polymeric precursor method, also known as the "liquid mix method" (LQM), a 0.35 M solution of citric acid in deionized water, containing stoichiometric amounts of the Sn precursor and the selected dopant precursor, was heated with continuous stirring. Hydrochloric acid was added as a catalyst to obtain a clear solution. Subsequently, ethylene glycol was added (3% v/v) to a mixture of the above-mentioned solutions in order to start the gelation as it reacted with the citric solution. This avoids the formation of partial segregations, which could modify the homogeneity of the solution. The evaporation of the solution gives a vitreous intermediate polymer, which contains all of the cations in the desired stoichiometric amounts. Finally, the resin was calcined, which resulted in a fine powder containing doped tin oxide nanoparticles. The powders were treated at 350 °C for 30 hours in order to completely remove all organic residues, and then at 450 °C overnight in order to improve the crystallinity. A schematic representation of both synthesis methods is shown in Scheme 1.

A carbon-content analysis was performed on a Perkin Elmer 2400 CHN analyzer, with ± 0.01% error. This elemental carbon analysis showed a carbon content lower than that of the quantification limit of the equipment, so that carbon impurities could be discarded.

X ray diffraction characterization

Samples were studied by X-Ray diffraction (XRD) using a Siemens D5000 diffractometer. The data were collected at 2θ

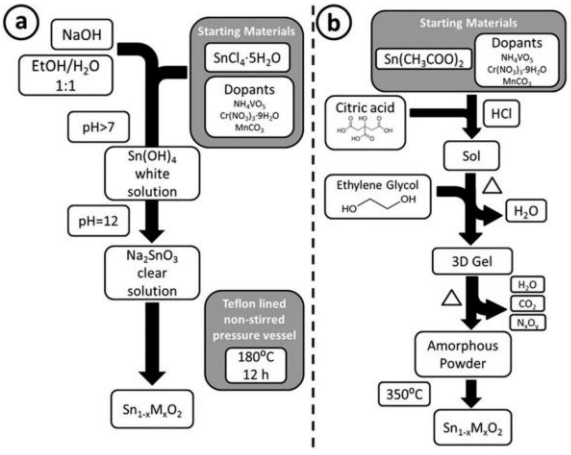

Scheme 1 The synthesis diagram of (a) the HDT and (b) LQM.

between 10° and 70°, with a step size of 0.04° and a collection time of 1 s per step. The working radiation was Cu(K_α) (λ = 1.5418 Å).

For the cell parameter measurements and Rietveld refinement analysis, the XRD patterns were taken in a Panalytical X'Pert Pro Alpha1 instrument, equipped with a primary fast X'Celerator detector operating at 45 kV and 40 mA, and fitted with a primary curved Ge 111 monochromator in order to get Cu $K_{\alpha1}$ radiation (λ = 1.5406 Å).

Selected area electron diffraction, high resolution electron microscopy and energy-dispersive X-ray spectroscopy

Selected Area Electron Diffraction (SAED) and High Resolution Electron Microscopy (HRTEM) were performed in a JEOL 300 FEG electron microscope, fitted with a GATAN double tilt goniometer stage (±22°, ±22°). The local composition was analyzed by energy-dispersive X-ray spectroscopy (EDS) using an Oxford INCA analyzer system attached to the above-mentioned microscope. Further HRTEM image analysis was performed with Digital Micrograph software, and image calculations were performed by means of a MacTempas software program.

Cathodoluminescence analysis

Cathodoluminescence measurements were carried out in a Hitachi S2500 SEM at different temperatures ranging from 80 to 300 K, with a beam energy of 18 keV. A Hamamatsu R928 photomultiplier and a Hamamatsu PMA-11 charge-coupled device camera were utilized for the analysis of the CL signal.

Results and discussion

Structural characterization

The XRD results have been systematically analyzed as a function of the type of dopant (V, Cr, Mn), as well as the cationic concentrations in which the dopants have been incorporated (5%, 10%, 15%). The XRD patterns show that all of the samples, either synthesized by the HDT or the LQM, exhibit a cassiterite structure (rutile-type, tetragonal unit cell, S.G. $P4_2/mnm$, and lattice parameters of $a = b$ = 4.74 Å and c = 3.19 Å), as observed in the refined XRD data of the undoped and V, Cr and Mn doped SnO_2 samples obtained by the LQM, which are shown in Fig. 1.

Regarding the doped samples, the substitution of Sn for V, Cr and Mn, induced a slight decrease in the lattice parameters of the LQM doped phases as compared to that of the pure SnO_2. This parameter decrease is due to the fact that the ionic radii of the incorporated dopants were smaller than the Sn radius.[27] This effect becomes more noticeable as the dopant cationic concentration is increased up to 15%, which shows that the rutile structure has adjusted to a variation in the substituted atom radius. Unlike the LQM samples, in all of the HDT doped samples the segregation of a second phase of the dopant oxide occasionally occurs, as detected by XRD.

The average grain sizes of the nanoparticles prepared by both techniques were calculated using the Scherrer formula,

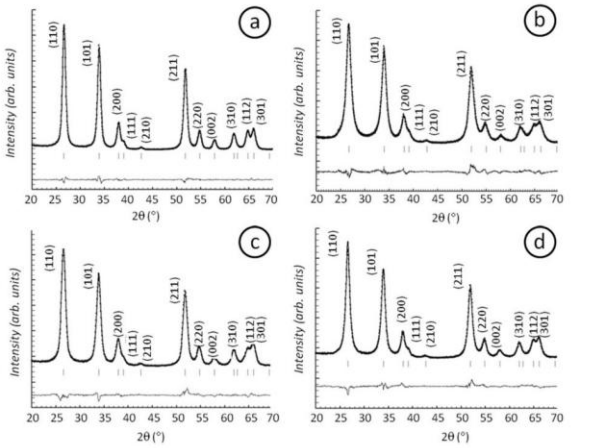

Fig. 1 The XRD patterns of the (a) undoped SnO_2 and (b) V, (c) Cr and (d) Mn doped SnO_2 synthesized by the LQM.

$D = k\lambda/B \cos\theta$, where θ is the peak position, λ is the x-ray wavelength and B is the Full Weight Half Maximum (FWHM) of the diffraction maxima.

After the Rietveld analysis of the monochromatic X-ray data, values around 8.7 nm have been obtained for the undoped SnO_2 nanoparticles synthesized by the LQM. The doped nanoparticles show reduced dimensions compared to the undoped ones, as summarized in Table 1, where the averaged sizes corresponding to samples doped with a 15% cationic fraction of V, Cr and Mn are shown. The estimated size for the Cr and Mn doped SnO_2 nanoparticles is around 6.5 nm. In the case of the vanadium-doped nanoparticles the estimated sizes were slightly smaller. X-ray data obtained from this chemical substitution study showed that the metal doping favors the growth of smaller nanoparticles. This shows that the role played by the doping element in the LQM can be discussed as an inhibitor of the crystal growth.[28]

The undoped hydrothermal samples show a higher average size of around 16 nm. The TEM techniques prove that this XRD-estimated value is an average, and that the synthesized nanoparticles obtained by this method exhibit a high degree of agglomeration, a distribution of sizes wider than the LQM case and the presence of elongated irregular nanocrystals, which can be explained in pH terms, which markedly alter the particle growth rate. During the hydrolysis process of the Sn precursor in the HDT, Sn–OH links were formed, thus producing $Sn(OH)_4$ which transforms into an amorphous phase and after hydrothermal treatment at 180 °C for 15 hours, finally

Table 1 The cell parameters, average size (D) and wellness factors of the Rietveld analysis corresponding to the undoped and doped SnO_2 nanoparticles fabricated by the LQM

	a (Å)	c (Å)	D (Å)	R_p	R_{wp}	R_{exp}	x^2
SnO_2	4.73(5)	3.18(5)	86.92 ± 0.05	3.04	4.03	4.00	1.51
$Sn_{0.85}V_{0.15}O_2$	4.72(2)	3.18(2)	51.13 ± 0.04	4.83	6.12	3.54	2.99
$Sn_{0.85}Cr_{0.15}O_2$	4.73(4)	3.18(4)	65.41 ± 0.02	4.48	5.78	3.44	2.83
$Sn_{0.85}Mn_{0.15}O_2$	4.72(5)	3.17(5)	65.26 ± 0.02	3.75	4.71	3.41	1.91

forms SnO_2. The presence of the elongated nanocrystals is an indication of the fact that particle growth occurs due to grain rotation induced by a grain coalescence mechanism.[29,30] Some reports[31] indicate that the presence of a high OH^- concentration was found to enhance the agglomeration of the nanocrystals, which favors the growth of elongated nanocrystals since the formation of the SnO_2 nanoparticles occurs *via* a meta-stable phase $Sn(OH)_4$, which does not directly transform into SnO_2, but into an amorphous phase, and then grows. Moreover, it is well known that nucleation at the interfaces (*i.e.* heterogeneous nucleation) dominates other nucleation processes. The boundaries of the amorphous solid particles offer such interfaces and therefore it is reasonable to assume that the nucleation of SnO_2 is a heterogeneous nucleation process.

A low magnification TEM micrograph of the HDT samples confirms the high degree of agglomeration and heterogeneous sizes, as nanoparticles from 5 to some tens of nanometers can be observed in Fig. 2a. A small amount of crystals with a regular shape was also found in the reaction products. The interatomic distances of 3.08 and 7.43 Å are measured in the HRTEM image of this material in Fig. 2b. The upper inset (Fig. 2c) shows the corresponding FFT pattern of the highlighted nanoparticle, indexed along the $[1\bar{1}1]$ zone axis of the rutile structure.

On the contrary, the nanoparticles obtained by the LQM show high homogeneity in size (below 10 nm) and shape, as shown in Fig. 3a, which is in good agreement with the results of the Rietveld analysis (Table 1). The high control of the dimensions of the nanoparticles fabricated *via* the LQM, as well as the associated size homogeneity, together with the fact that the dopant oxide segregation observed for the HDT samples is avoided in this case, make the LQM more appropriate for the obtention of doped nanoparticles. Therefore, a detailed TEM study of the transition metal (V, Cr, Mn) doped SnO_2 nanoparticles synthesized by the LQM has been performed. In these samples, a controlled composition of 5, 10 or 15% cationic composition has been successfully achieved, and phases with a tailored composition were stabilized. Fig. 3b shows the HRTEM image of an isolated

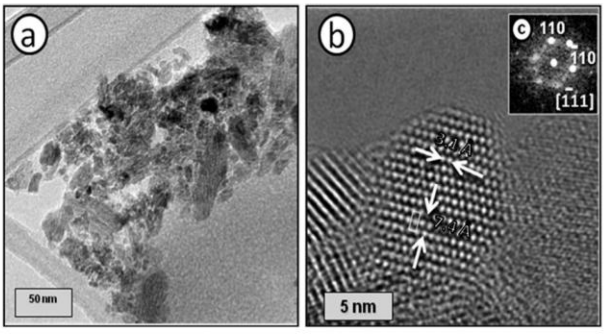

Fig. 2 (a) A low magnification TEM image of the SnO_2 hydrothermal sample, showing the high dispersion in sizes. (b) A HRTEM image with a nanoparticle highlighted. The reticular parameters and unit cell of the rutile structure are indicated. (c) The FFT pattern along the $[1\bar{1}1]$ axis.

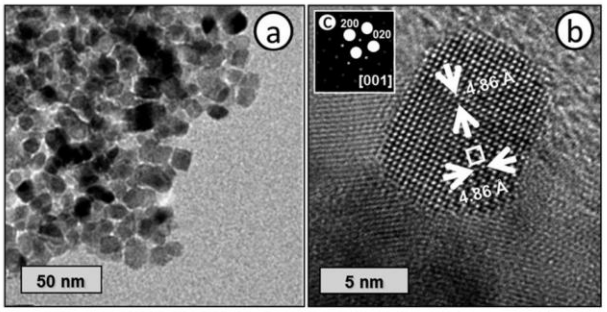

Fig. 3 (a) Low magnification HRTEM image of undoped SnO_2, (b) HRTEM image of a $Sn_{0.85}Mn_{0.15}O_2$ isolated nanoparticle prepared by the liquid mix method (LQM), the reticular parameters and unit cell of the rutile basal plane can be seen. (c) FFT pattern along the [001] axis of the rutile structure.

$Sn_{0.85}Mn_{0.15}O_2$ nanoparticle, which is representative from the Mn doped nanoparticles. The interplanar distances of 0.48 nm can be measured along both perpendicular directions, corresponding to the unit cell of the material, which is marked by a square. The FFT pattern (Fig. 3c) can be indexed on the basis of the rutile crystal structure along the [001] zone axis.

Fig. 4a shows the HRTEM image of the $Sn_{0.85}Cr_{0.15}O_2$ nanoparticles, as an example of the Cr doped nanoparticles. The corresponding FFT pattern along the [011] zone axis can be observed in Fig. 4b. The detailed I-FFT image corresponding to the marked nanoparticle, and noted with a dashed circle, clearly shows the interatomic distances of 2.65 and 4.70 Å (Fig. 4c).

As a representative example from the V doped SnO_2 nanoparticles, a HRTEM image from $Sn_{0.85}V_{0.15}O_2$ is shown in Fig. 4d. The corresponding FFT pattern along the [001] zone axis is included in Fig. 4e, while the detailed I-FFT image from the nanoparticle marked in Fig. 4d shows interatomic distances of 0.48 nm along both perpendicular directions. The unit cell is marked in Fig. 4f.

The compositional studies of these samples, performed by EDS microanalysis in the electron microscope, confirm that

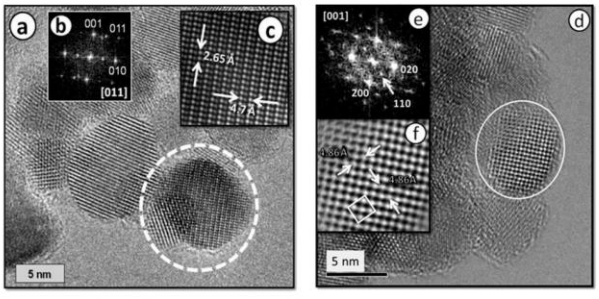

Fig. 4 (a) An HRTEM image of the $Sn_{0.85}Cr_{0.15}O_2$ nanoparticles obtained by the LQM. (b) The FFT pattern along the [011] axis of the rutile structure. (c) The I-FFT image showing the reticular parameters and the unit cell of the rutile [011] plane. (d) The HRTEM image of the $Sn_{0.85}V_{0.15}O_2$ nanoparticles synthesized by the LQM. (e) The FFT pattern along the [001] zone axis. (f) The I-FFT image showing the reticular parameters and the unit cell of the rutile structure.

View Article Online

CrystEngComm Paper

all of the crystals have a homogeneous cationic composition, which is in good agreement with the nominal composition. Fig. 5 shows the EDS spectra obtained from V, Cr and Mn doped SnO_2 nanoparticles, as an example.

Table 2 summarizes the average cationic compositions for the doped SnO_2 samples with a higher content (15%) of V, Cr and Mn, which demonstrates the high accuracy achieved in the LQM doping process even for cationic compositions as high as 15%, while keeping a high degree of crystallinity.

Cathodoluminescence

The incorporation of transition metal dopants creates intermediate energy states in the band gap of the SnO_2, thus changing the associated radiative-recombination processes in the nanoparticles. Moreover variations in the optical properties due to the reduced size of the nanoparticles and the associated structure of the defects caused by the doping could be promoted. For this reason, the study of the luminescent properties of the doped SnO_2 nanoparticles investigated in this work could lead to gain insights in the comprehension of the phenomena involved in the doping process and the dopant-dependent optical properties of the nanoparticles. The wide band gap of SnO_2 (3.6 eV at 300 K) could provide luminescence within a wide spectral range. In our case near bandgap CL emissions around 3.6 eV were not detected even at a low temperature (80 K), as band-to-band transitions or exciton recombinations are hardly observed in SnO_2 due to the dipole-forbidden nature of the energy band structure of this material. However variations on some other emission characteristics from SnO_2 as a function of the dopant have been analyzed and discussed.

In previous work[32] we have described the CL emission from undoped SnO_2, which mainly consists of three emissions in the visible range, which can be identified as the orange band (1.94 eV), the green band (2.25 eV) and the blue band (2.58 eV). It has been demonstrated that the orange band is associated with oxygen vacancy related defects, which control the conductivity in this material, acting as shallow donor levels. The blue band has been attributed to transitions involving surface states,[21] whereas the origin of the green band is still under discussion, although some works associate this emission to oxygen vacancies with two adjacent oxygen atoms missing. No emissions in the infrared range have been observed for SnO_2.

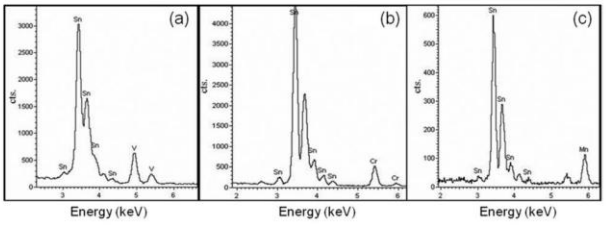

Fig. 5 The EDS spectra of the $Sn_{0.85}V_{0.15}O_2$, $Sn_{0.85}Cr_{0.15}O_2$ and $Sn_{0.85}Mn_{0.15}O_2$ samples obtained by the LQM.

Table 2 The EDS data of the $Sn_{0.85}M_{0.15}O_2$ (M = V, Cr and Mn) samples synthesized by the LQM

	$Sn_{0.85}V_{0.15}O_2$	$Sn_{0.85}Cr_{0.15}O_2$	$Sn_{0.85}Mn_{0.15}O_2$
Sn (% cat.)	86.0 ± 0.4	84.6 ± 0.4	85.3 ± 0.6
M (% cat.)	14.0 ± 0.4	15.4 ± 0.4	14.7 ± 0.6

Initially, undoped SnO_2 nanoparticles synthesized by both the HDT and the LQM have been studied. The representative CL spectra are shown in Fig. 6, where a CL spectrum from commercial bulk SnO_2 is also included for comparison. These spectra have been acquired at 80 K. The intensity of the spectra acquired at 300 K is lower, although they exhibit a similar behavior. The deconvolution of the spectra is also shown in Fig. 6. All of the normalized spectra exhibit an intense orange band (1.94 eV), which dominates in all of the spectra except for the one corresponding to the HDT nanoparticles which is dominated by the green emission (2.25 eV). As both the orange and green bands are associated to oxygen vacancies, their high relative intensity in the CL spectra indicates that these are the predominant defects in the analyzed samples. However, the emission from the LQM and HDT nanoparticles is considerably less intense than that from the bulk SnO_2 due to the decrease in the radiative defects at the nanoscale, or the increase of non-radiative recombination paths. In particular the LQM nanoparticles, the dimensions of which are smaller than those synthesized by the HDT, show the lowest CL intensity. These LQM samples also show a weak emission at 3.2 eV, which is slightly observed in the HDT samples and not observed in the bulk SnO_2. This could be related to transitions involving shallow defect levels, possibly associated with surface-related defects, as the surface-to-volume ratio increases in the nanostructured materials. The HDT nanoparticles present a shoulder at 1.8 eV, which could

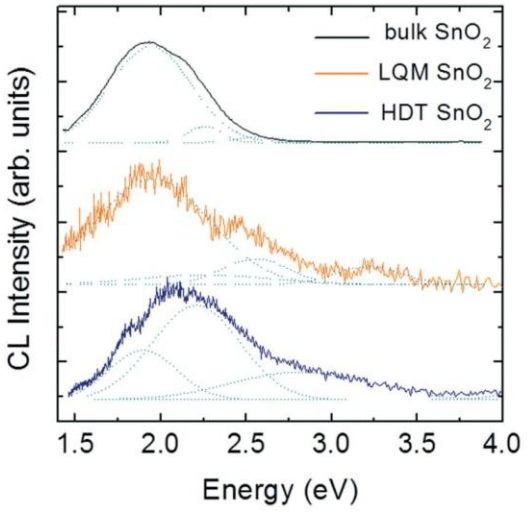

Fig. 6 The CL spectra corresponding to the undoped SnO_2 nanoparticles grown *via* the LQM and the HDT. The CL spectrum from the commercial bulk SnO_2 is shown as a reference.

be due to a variable distribution of defects possibly associated to traps related to singly and doubly ionized oxygen vacancies.[33] The luminescence from the samples grown by the LQM, consisting of SnO_2 nanoparticles doped with Cr, Mn or V in a variable content (5, 10 and 15% cationic fraction), has been investigated.

The CL spectra corresponding to the Cr doped SnO_2 nanoparticles are shown in Fig. 7a. An intense narrow emission centered at 1.79 eV clearly dominates the spectra. Other Cr doped oxides[34–37] also show a strong luminescence at this energy even for low concentrations of Cr^{3+}. The 1.79 eV red luminescence is attributed to Cr^{3+} ions in the SnO_2 lattice, in particular to the radiative transitions involving the ^2E–$^4A_2$ electronic levels, with decay times in the range of milliseconds.[38,39] The high radiative efficiency of this emission makes the nanoparticles optically active at room temperature, as observed in this work. A more detailed analysis of the CL signal confirms the presence of less intense narrow peaks at lower energies, which are attributed to variations in the environment around Cr^{3+}.[40] Increasing the Cr doping enhances the intensity of the main peak at 1.79 eV, as observed in Fig. 7a. In addition to this Cr^{3+} related peak, a less intense emission centered at 2.58 eV, as well as a weak shoulder at 2.25 eV, are observed in the CL spectra. Both emissions can be associated with the blue (2.58 eV) and green (2.25 eV) bands from SnO_2. Usually the orange band (1.94 eV) attributed to oxygen vacancies in the SnO_2 dominates the CL spectra of the undoped SnO_2, nevertheless this emission is quenched in Cr doped SnO_2 nanoparticles. The presence of Cr^{3+} ions in the lattice induces a reduction of the oxygen vacancies related defects responsible from the orange band.

Vanadium doped SnO_2 nanoparticles present a CL emission in the range between 2.1 and 2.5 eV, as observed in Fig. 7b. This green emission presents a complex behavior as it is formed by different narrow components. In particular a narrow emission centered at 2.15 eV, as well as emissions between 2.25 and 2.5 eV, can be distinguished. This green luminescence can be attributed to donor–acceptor transitions involving vanadium-related deep acceptor levels, as reported in similar vanadium doped oxides.[41] The intensity of the emission centered at 2.5 eV decreases as the content of vanadium increases, as observed in Fig. 7b. In addition, the decrease in the intensity of the orange band (1.94 eV) confirms the reduction in the concentration of oxygen vacancies induced by the presence of the vanadium ions. A less intense emission can be also observed centered at 1.68 eV. Furthermore, a weak shoulder can be distinguished for a low V concentration in the high-energy region of the spectra, around 3.6 eV, which should be related to the near band edge transitions. Emissions at 1.68 eV and 3.6 eV, as well as the total CL signals, are drastically reduced as the vanadium content increases, as observed in Fig. 7b.

The CL spectra acquired on the Mn doped SnO_2 nanoparticles are dominated by an emission around 2.0 eV (Fig. 7c) and a weak shoulder appears at 2.25 eV. As referred by different authors,[42] the dopant emission for the Mn-doped nanocrystals has been restricted to the yellow–orange spectral window. The 2.1 eV emission can be attributed to internal Mn^{2+} transitions involving the $^4T_1$–$^6A_1$ electronic states, as observed in other semiconductor hosts.[43,44] Pradhan *et al.*[42] stated that Mn^{2+} can act as an efficient luminescence center, by means of effective energy paths involving s–p electronic states from the host, which lead to luminescence at room temperature, as observed in this work. Nonetheless, the association of these emissions with the orange band (1.94 eV) and the green band (2.25 eV) in undoped SnO_2 cannot be ruled out. Samples with a low Mn content also show a low intense emission in the high-energy region of the spectra, around 3.4 eV, which could be related to near band edge transitions. In this case, an increase in the Mn dopant concentration also induces a decrease in the total CL intensity, by reducing the native radiative defects from SnO_2, or increasing the number of non-radiative pathways.

As observed in Fig. 7d, the luminescence from doped SnO_2 nanocrystals can span over a wide spectral range from near-IR to UV, as a function of the dopant. Red, green or orange emission can be promoted by doping with Cr, V or Mn respectively, which can be useful in the functionalization of these nanoparticles. Further studies are required to fully understand the mechanism involved in the doping process and the luminescence of these nanoparticles, although these results could serve as a model for other doped semiconductor oxides.

It is worth pointing out that quantum confinement effects were not observed in this luminescence study, which is different from the results reported for other semiconductor nanoparticles.[45,46] Despite the reduced size of the here investigated nanoparticles, the small bulk exciton Bohr radius for SnO_2 (2.75 nm), as well as the low efficient luminescence associated with the band gap transitions in SnO_2, could hinder these effects.

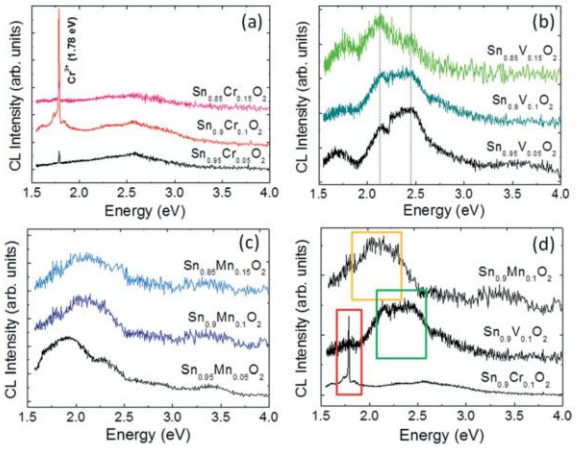

Fig. 7 The CL spectra from the (a) Cr (b) V and (c) Mn doped SnO_2 nanoparticles with a variable dopant concentration grown *via* the LQM and (d) a comparison between the CL spectra corresponding to the Cr, V and Mn doped SnO_2 nanoparticles with the same dopant concentration: $Sn_{1-x}M_xO_2$ (x = 0.1; M = V, Cr, Mn).

Conclusions

The HDT and LQM have been used to synthesize doped SnO_2 nanoparticles. It has been found that the synthesis of $Sn_{1-x}M_xO_2$ (x = 0, 0.05, 0.1, 0.15; M = V, Cr, Mn) nanoparticles using the liquid mix method (LQM) permits the achievement of a high control of both the final particle size and chemical composition. On the other hand, the hydrothermal method (HDT) induces both an agglomeration of the nanoparticles with a high dispersion of sizes and occasionally the segregation of a secondary phase. The doped nanoparticles synthesized *via* the LQM show an average particle size of around 6 nm, with a rutile-type structure and a high degree of crystallinity. The differences in the chemical kinetics can be due to the variation in the reactivity of the starting compounds in the basic solution under hydrothermal conditions, since this factor has a marked influence on the product dissolution rate, and also, a low chemical reactivity of the hydrothermal solution at temperatures below 180 °C in low concentrated NaOH solutions (0.15 M).

The cathodoluminescence results show that doping the SnO_2 nanoparticles with Cr, V or Mn, induces red, green or orange emissions, respectively. As the presence of these transition metal ions increases in the SnO_2 matrix, the total CL signal is reduced. In particular, the orange band (1.94 eV), associated with the oxygen vacancies in SnO_2 and the conductivity of the samples, decreases upon doping. The 1.79 eV emission observed in the Cr doped samples can be associated with the Cr^{3+} intraionic transitions. The green emission in the V-doped SnO_2 nanoparticles can be associated to the vanadium related deep levels, while the yellow–orange emission characteristic of the Mn doped SnO_2 involves Mn^{2+} transitions.

Acknowledgements

This work was supported by MEC (MAT2012-39159 and Consolider CSD 2009-00013). The authors are grateful to the National Centre for Electron Microscopy (CNME) at Universidad Complutense de Madrid.

Notes and references

1 C. Kiliç and A. Zunger, *Phys. Rev. Lett.*, 2002, **88**, 095501.
2 D. Maestre, J. Ramírez-Castellanos, P. Hidalgo, A. Cremades, J. M. González-Calbet and J. Piqueras, *Eur. J. Inorg. Chem.*, 2007, **11**, 1544.
3 Y. Zhang, A. Kolmakov, S. Chretien, H. Metiu and M. Moskovits, *Nano Lett.*, 2004, **4**, 403.
4 Q. Zhao, H. Lorenz, S. Turner, O. I. Lebedev, G. Van Tendeloo, C. Rameshan, B. Klötzer, J. Konzett and S. Penner, *Appl. Catal., A*, 2010, **375**, 188.
5 C. Wang and M. Chen, *Mater. Lett.*, 2009, **63**, 389.
6 Z. D. Li, Y. Zhou, T. Yu, J. G. Liu and Z. G. Zou, *CrystEngComm*, 2012, **14**, 6462.
7 W. W. Wang, Y. J. Zhu and L. X. Yang, *Adv. Funct. Mater.*, 2007, **17**, 59.
8 B. Drevillon, S. Kumar, P. Roca i Cabarrocas and J. M. Siefert, *Appl. Phys. Lett.*, 1989, **54**, 2088.
9 C. Lee, B. Nam, W. Choi, J. Lee, D. Choi and Y. Oh, *Mater. Lett.*, 2011, **65**, 722.
10 P. I. Archer, P. V. Radovanovic, S. M. Heald and D. R. Gamelin, *J. Am. Chem. Soc.*, 2005, **127**, 14479.
11 H. Kimura, T. Fukumura, M. Kawasaki, K. Inaba, T. Hasegawa and H. Koinuma, *Appl. Phys. Lett.*, 2002, **80**, 94.
12 M. J. Osiak, E. Armstrong, T. Kennedy, C. M. Sotomayor Torres, K. M. Ryan and C. O'Dwyer, *ACS Appl. Mater. Interfaces*, 2013, **5**, 8195.
13 D. H. Wang, R. Kou, D. Choi, Z. G. Yang, Z. M. Nie, J. Li, L. V. Saraf, D. H. Hu, J. G. Zhang, G. L. Graff, J. Liu, M. A. Pope and I. A. Aksay, *ACS Nano*, 2010, **4**, 1587.
14 P. D. Borges, L. M. R. Scolfaro, H. W. L. Alves, E. F. Da Silva and L. V. C. Assali, *Nanoscale Res. Lett.*, 2011, **6**, 146.
15 T. Yanagimoto, Y.-T. Yu and K. Kaneko, *Sens. Actuators, B*, 2012, **166–167**, 31.
16 M. Shoyama and N. Hashimoto, *Sens. Actuators, B*, 2003, **93**, 585.
17 R. S. Ningthoujam, V. Lahiri Debdutta Sudarsan, H. K. Poswal, S. K. Kulshreshtha, S. M. Sharma, B. Bhushan and M. D. Sastry, *Mater. Res. Bull.*, 2007, **42**, 1293.
18 Y. Zuo, S. Ge, L. Zhang, S. Yan, X. Zhou and Y. Xiao, *J. Alloys Compd.*, 2009, **475**, 60.
19 S. Sambasivam, B. C. Choi and J. G. Lin, *J. Solid State Chem.*, 2011, **184**, 199.
20 C. Van Komen, A. Thurber, K. M. Reddy, J. Hays and A. Punnoose, *J. Appl. Phys.*, 2008, **103**, 07D141.
21 A. Kar, S. Kundu and A. Patra, *J. Phys. Chem. C*, 2011, **115**, 118.
22 N. Dave, B. G. Pautler, S. S. Farvid and P. V. Radovanovic, *Nanotechnology*, 2010, **21**, 134023.
23 S. Ghosh, D. De Munshi and K. Mandal, *J. Appl. Phys.*, 2010, **107**, 123919.
24 R. Alexandrescu, I. Morjan, F. Dumitrache, R. Birjega, C. Fleaca, I. Soare, L. Gavrila, C. Luculescu, G. Prodan, V. Kuncser and G. Filoti, *Appl. Surf. Sci.*, 2011, **257**, 5460.
25 M. Hirano, H. Dozono and T. Kono, *Mater. Res. Bull.*, 2011, **46**, 1384.
26 M. P. Pechini, 1967, *U.S. Patent* no. 3330697.
27 S. D. Shannon, *Acta Crystallogr., Sect. A: Cryst. Phys., Diffr., Theor. Gen. Crystallogr.*, 1976, **32**, 751.
28 J. Hays, A. Punnoose, R. Baldner, M. H. Engelhard, J. Peloquin and K. M. Reddy, *Phys. Rev. B: Condens. Matter Mater. Phys.*, 2005, **72**, 075203.
29 K. Sato, Y. Yokoyama, J.-C. Valmalette, K. Kuruma, H. Abe and T. Takarada, *Cryst. Growth Des.*, 2013, **13**, 1685.
30 E. R. Leite, T. R. Giraldi, F. M. Pontes, E. Longo, A. Beltrán and J. Andrés, *Appl. Phys. Lett.*, 2003, **83**, 1566.
31 S. Das, S. Kar and S. Chaudhuri, *J. Appl. Phys.*, 2006, **99**, 114303.
32 D. Maestre, A. Cremades and J. Piqueras, *J. Appl. Phys.*, 2005, **97**, 044316.
33 A. Kar, M. A. Stroscio, M. Dutta, J. Kumari and M. Meyyappan, *Semicond. Sci. Technol.*, 2010, **25**, 024012.

34 G. C. Vásquez, M. A. Peche-Herrero, D. Maestre, A. Cremades, J. Ramírez-Castellanos, J. M. González-Calbet and J. Piqueras, *CrystEngComm*, 2013, **15**, 5490.

35 S. Fujihara and Y. Shibata, *J. Lumin.*, 2006, **121**, 470.

36 I. López, E. Nogales, B. Méndez, J. Piqueras, A. Peche, J. Ramírez-Castellanos and J. M. González-Calbet, *J. Phys. Chem. C*, 2013, **117**, 3036.

37 P. Gluchowski and W. Strek, *Mater. Chem. Phys.*, 2013, **140**, 222.

38 E. Nogales, J. A. García, B. Méndez and J. Piqueras, *J. Appl. Phys.*, 2007, **101**, 033517.

39 S. Wang, M.-W. Shao, G. Shao, H. Wang and L. Cheng, *Chem. Phys. Lett.*, 2008, **460**, 200.

40 I. S. Altman, P. V. Pikhitsa, M. Choi, J. I. Jeong, H.-J. Song, I. E. Agranovski and T. E. Bostrom, *Appl. Phys. Lett.*, 2003, **83**, 3689.

41 S. Müller, M. Lorenz, C. Czekalla, G. Benndorf, H. Hochmuth, M. Grundmann, H. Schmidt and C. Ronning, *J. Appl. Phys.*, 2008, **104**, 123504.

42 N. Pradhan, D. M. Battaglia, Y. Liu and X. Peng, *Nano Lett.*, 2007, **7**, 312.

43 I. S. Altman, P. V. Pikhitsa, M. Choi, H.-J. Song, A.G. Nasibulin and E. I. Kauppinen, *Phys. Rev. B: Condens. Matter*, 2003, **68**, 125324.

44 D. J. Norris, N. Yao, F. T. Charnock and T. A. Kennedy, *Nano Lett.*, 2001, **1**, 3.

45 S. S. Walavalkar, C. E. Hofmann, A. P. Homyk, M. D. Henry, H. A. Atwater and A. Scherer, *Nano Lett.*, 2010, **10**, 4423.

46 F. Gu, S. F. Wang, C. F. Song, M. K. Lü, Y. X. Qi, G. J. Zhou, D. Xu and D. R. Yuan, *Chem. Phys. Lett.*, 2003, **372**, 451.

CAPITULO IV. NANOMATERIALES BASADOS EN β-Ga_2O_3

1. In-DOPED GALLIUM OXIDE MICRO- AND NANOSTRUCTURES: MORPHOLOGY, STRUCTURE, AND LUMINESCENCE PROPERTIES
2. INFLUENCE OF Sn AND Cr DOPING ON MORPHOLOGY AND LUMINESCENCE OF THERMALLY GROWN Ga_2O_3 NANOWIRES

1. MICRO Y NANOESTRUCTURAS DE ÓXIDO DE GALIO DOPADAS CON INDIO: MORFOLOGIA, ESTRUCTURA Y PROPIEDADES LUMINISCENTES

En este capítulo se aborda el estudio de la influencia del dopado con indio en la morfología, estructura y propiedades de micro- y nanoestructuras de óxido de galio. Los materiales se han obtenido mediante oxidación térmica de galio metálico en presencia de óxido de indio. Las morfologías dominantes son tipo cintas que, en muchos casos, se doblan dando lugar a estructuras tipo muelle, poniendo de manifiesto la influencia que ejerce la difusión de indio en el Ga_2O_3.

La microscopia electrónica de alta resolución revela la presencia de maclas en las cintas. El análisis EDS en el microscopio de barrido ha detectado una segregación de impurezas de indio en los bordes de las partículas. Estos resultados sugieren que el indio juega un papel principal en las morfologías observadas y apoya la hipótesis de un mecanismo de crecimiento capa a capa. Información adicional de la influencia del indio en la estructura de defectos se ha obtenido mediante cátodoluminiscencia en el microscopio de barrido, microscopia fotoelectrónica de rayos X y espectroscopia Raman con resolución espacial.

THE JOURNAL OF PHYSICAL CHEMISTRY C

Article

pubs.acs.org/JPCC

In-Doped Gallium Oxide Micro- and Nanostructures: Morphology, Structure, and Luminescence Properties

Iñaki López, Antonio D. Utrilla, Emilio Nogales, Bianchi Méndez,* and Javier Piqueras

Departamento de Física de Materiales, Facultad de Ciencias Físicas, Universidad Complutense de Madrid, 28040 Madrid, Spain

Andrea Peche, J. Ramírez-Castellanos, and Jose M. González-Calbet

Departamento de Química Inorgánica, Facultad de Ciencias Químicas, Universidad Complutense de Madrid, 28040 Madrid, Spain

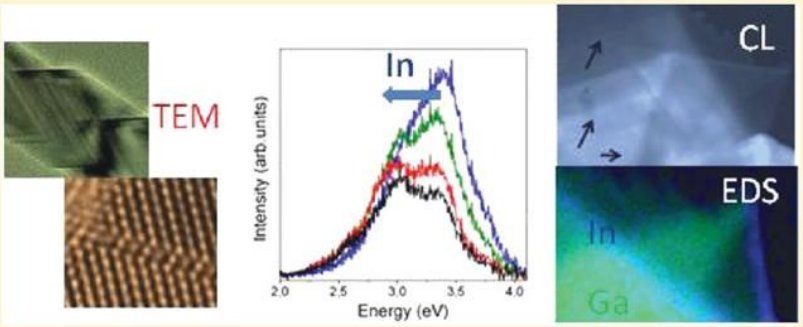

ABSTRACT: The influence of indium doping on morphology, structural, and luminescence properties of gallium oxide micro- and nanostructures is reported. Indium-doped gallium oxide micro- and nanostructures have been grown by thermal oxidation of metallic gallium in the presence of indium oxide. The dominant morphologies are beltlike structures, which in many cases are twisted leading to springlike structures, showing that In diffusion in Ga_2O_3 influences the microstructure shapes. High-resolution transmission electron microscopy has revealed the presence of twins in the belts, and energy-dispersive X-ray spectroscopy in the scanning electron microscopy (SEM) has detected a segregation of indium impurities at the edges of planar structures. These results suggest that indium plays a major role in the observed morphologies and support the assumption of a layer by layer model as growth mechanism. An additional assessment of indium influence on the defect structure has been performed by cathodoluminescence in the SEM, X-ray photoelectron microscopy, and spatially resolved Raman spectroscopy.

Trends in fabrication of nanodevices point to novel architectures, which use nanomaterials as building blocks. In this framework, transparent conductive oxide (TCO) nanostructures are considered as candidates to be incorporated into future electronic and optoelectronic nanodevices. The key factor for device applications of these oxides relies on the presence of oxygen vacancies and their interaction with dopants or alloying impurities.[1,2] Among TCOs, monoclinic β-Ga_2O_3 is one of the widest band gap semiconductor oxides (4.9 eV) with n-type conductivity related to donor centers involving oxygen vacancies and/or impurities.[3−5] Ga_2O_3 may be alloyed with other TCOs and be turned into ternary oxide material, in a similar way as indium tin oxide (ITO), which is widely used as a transparent electrode, among other applications. Recently, InGaO thin films have been proposed as channel layers in thin film transistors (TFT), and the influence of growth conditions of oxide films on their electrical properties has been studied.[6] The results in that work show that a decrease in the oxygen partial pressure during films preparation leads to an increase in the channel mobility, and variations in indium concentration influence the mobility and the turn on voltage of the TFT.[6] Therefore, the addition of doping impurities and the specific growth conditions will influence the functionality of the obtained nano- and microstructures. Thermal evaporation of powders and deposition on a substrate containing catalyst particles is one of the most reported methods to grow nanowires, nanobelts, or more complex morphologies based in ZnO, SnO_2, In_2O_3, or Ga_2O_3 oxides.[7] In our group, a thermal evaporation catalyst-free method has been developed, and several morphologies of interest for optoelectronic and sensing devices have been obtained and characterized.[8−10] In particular, our previous works have demonstrated a tunable luminescence of doped Ga_2O_3 nanowires by the addition of cations, such as Cr, Er, Eu, and Gd ions, and light emission from UV to infrared has been achieved from doped Ga_2O_3 nanowires at room temperature.[9,10] Alternatively, Si and Sn impurities in Ga_2O_3 thin films have been proposed to increase the carrier density

Received: October 25, 2011
Revised: January 12, 2012
Published: January 24, 2012

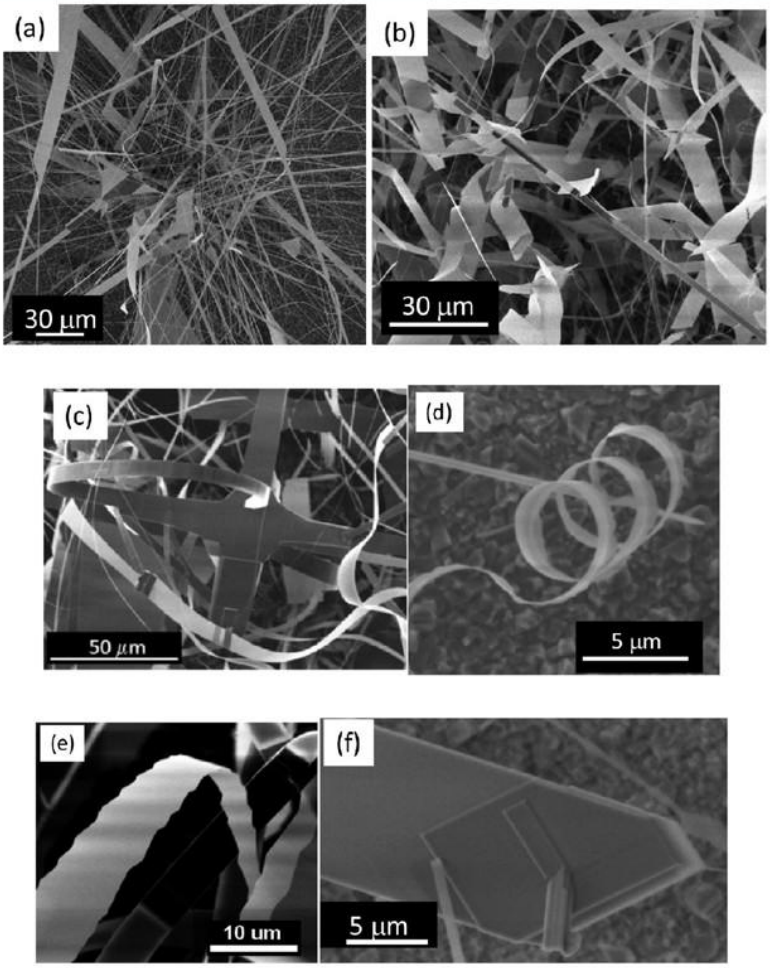

Figure 1. (a) Representative SEM image of undoped Ga_2O_3 microstructures. (b–f) SEM images of In-doped Ga_2O_3 micro- and nanostructures.

and the electrical conductivity.[5,11] In all cases, achieving an effective n-type doping of nanostructures with effective incorporation of impurities in the cationic lattice present difficulties because of out-diffusion processes, which often take place.

In this work, the incorporation of indium atoms in Ga_2O_3 micro- and nanostructures and the relationship between chemical composition, morphology, and optical properties have been investigated. Indium-doped Ga_2O_3 nanoribbons and microstructures have been obtained by controlled thermal annealing of metallic gallium in the presence of indium oxide powders under argon flow. The structure and properties of the obtained micro- and nanostructures have been investigated by means of X-ray diffraction (XRD), scanning and high-resolution transmission electron microscopy (SEM and HRTEM), cathodoluminescence (CL) in the SEM, energy dispersive X-ray spectroscopy (EDS), spatially resolved X-ray photoelectron spectroscopy (XPS), and spatially resolved Raman spectroscopy in a confocal microscope. The high spatial resolution of the employed techniques (XPS, CL, and X-ray microanalysis in the SEM and confocal Raman) enabled to investigate the defects and the indium homogeneity in the obtained structures.

In-doped Ga_2O_3 micro- and nanostructures have been obtained by a thermal evaporation method on compacted gallium oxide pellets. The growth mechanism is based on a vapor–solid (VS) process without the aid of any foreign catalyst. Metallic gallium and indium oxide powders were used as precursor materials, and after a two-step thermal treatment at 1150 °C for 3 h plus 5 h at 1250 °C, a high amount of micro- and nanostructures are formed on the pellet surface. The used temperatures are determined by the oxidation process of the gallium source and subsequent formation of nanowires, as explained elsewhere.[12,13] After the growth process, the structures were placed onto silicon wafer substrates to be characterized. The structural characterization has been carried out by X-ray diffraction (XRD) and TEM. Powder XRD patterns were collected using Cu Kα monochromatic radiation (λ = 1.54056 Å) at room temperature on a Panalytical X'PERT PRO MPD diffractometer equipped with a germanium 111 primary beam monochromator and X'Celerator fast detector. Selected area electron diffraction (SAED) and HRTEM were performed in a JEOL 3000 FEG electron microscope, fitted with a double tilting goniometry stage ($\pm$22°, $\pm$ 22°). Simulated HRTEM images were calculated by the multislice method using the MacTempas software package. Morphology,

chemical microanalysis, and luminescence have been performed in the same SEM Leica instrument, in which EDS and CL modes were implemented. The study of the structures was complemented with the aid of high resolution photoemission spectra and imaging, performed at the Sincrotrone Elettra Trieste facility (ESCA microscopy line) and Raman spectroscopy in a Horiba Jobin Ybon LabRam HR800 confocal microscope.

In previous works it was shown that the morphology of the structures strongly depends on the growth process. Thermal treatments at 1150 °C of metallic gallium on gallium oxide pellets lead to the formation of undoped nanowires and microstructures as it has been previously reported.[12,13] A representative secondary electron image is shown in Figure 1a. To dope the micro- and nanostructures, indium oxide powders were placed along with Ga onto the substrate, and a double-step thermal treatment has been used as described above. SEM images of planar microstructures, nanobelts, and springs are shown in parts b–f of Figure 1. The presence of In appears to favor the formation of belts which are only occasionally observed in the case of undoped structures. Also, a characteristic of the In-doped samples is that some of the belts are twisted leading to springs with sawlike edges (parts d and e of Figure 1). Other planar structures of variable thickness seem to be formed with some well-defined steps on the microstructure surface (figure 1f). Figure 2 shows the XRD spectrum of the

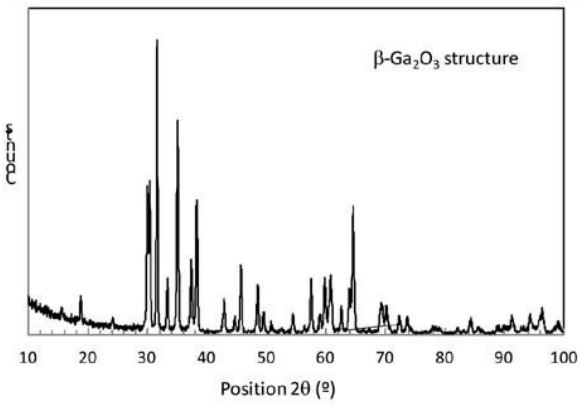

Figure 2. XRD spectrum of the obtained indium-doped Ga_2O_3 micro- and nanostructures. Peaks maxima correspond to monoclinic β-Ga_2O_3 phase.

obtained structures. All diffraction peaks can be indexed to a monoclinic gallium oxide (β-Ga_2O_3) crystal structure, $C2/m$ space group, and reticular parameters of a (Å) = 12,227, b (Å) = 3,039, c (Å) = 5,808, being $\alpha = 90°$, $\beta = 103.82°$, and $\gamma = 90°$ (JCPDS 00–041–1103). No additional peaks related to an eventual formation of an indium oxide phase during the growth process were detected.

TEM images (parts a and b of Figure 3) show the morphology of some of the structures observed by SEM with stepped borders (Figure 1e). The structure shown in figure 3 has an average width under 100 nm and a nanoherringbone appearance related to twin defects, which could be involved in the growth process and be responsible for the final morphology. Figure 3c shows the corresponding HRTEM image at higher magnification and the SAED pattern along the [100] zone axis, where streaking of the main diffraction spots

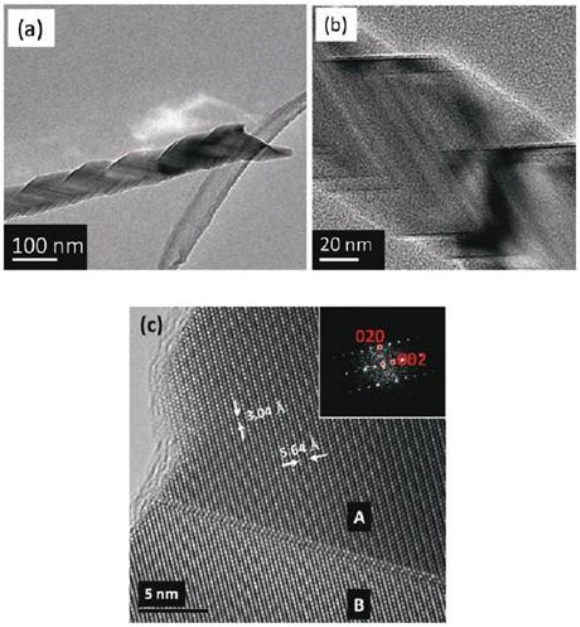

Figure 3. (a) and (b) TEM images of In-doped Ga_2O_3 nanostructures showing lateral zigzag contour. (c) HRTEM image and SAED pattern along the [100] zone axis, where streaking of the main diffraction spots along the (011) direction can be observed.

along the (011) direction can be observed. This fact is a signature of structural disorder and is due to the presence of recurrent twinning. We have calculated as well fast Fourier Transform (FFT) patterns in different domains of the nanoherringbone marked as A and B in Figure 3c. The results show identical patterns with no extra spots, hence no additional order is observed and identical crystalline structure retains in the whole nanostructure. The measured interplanar distances are 0.304 and 0.564 nm, which fit well to the b and c parameters of the β-Ga_2O_3 unit cell, respectively. In addition, EDS microanalysis shows an In content of about 5 at % and that the average Ga and In atoms distribution on both sides of the twin plane is homogeneous, which verifies that this disorder is not related to chemical composition variations at this nanoscale. Furthermore, it is worth mentioning that the electron beam focus is different in regions marked A and B, which suggests that an extra layer is introduced on an upper plane leading to a step, probably as a consequence of the crystal growth process.[14] Linear and planar defects may play a crucial role in the nucleation and growth of one-dimensional structures. For example, axial screw dislocations provide self-perpetuating steps leading to hierarchical nanostructure in ZnO nanowires on GaN substrates.[15,16] Another example is the layer-by-layer model proposed for the growth of Ga_2O_3 nanobelts formed by two single crystalline nanowires, with a twin boundary along the longitudinal axis.[17,18] Our TEM and HRTEM observations show the presence of In into the single crystalline β-Ga_2O_3 structures and that twinning is generated during the growth process of the In-doped Ga_2O_3 nanostructures.

To study the effect of the chemical composition on the luminescence properties of Ga_2O_3 we have performed correlative EDS and CL measurements of these structures in the SEM. Indium-doped structures were placed and fixed onto

a silicon wafer. The appearance of terraces and steps on the planar surfaces usually led to a zigzag edge. Parts a and b of Figure 4 show the secondary electron image and the

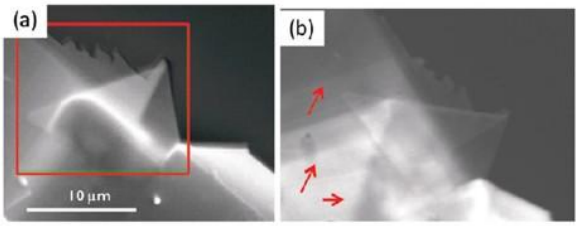

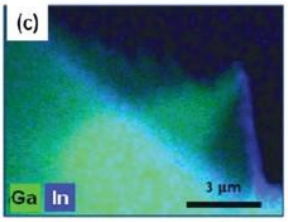

Figure 4. (a) SEM image, (b) CL image, and (c) X-ray microanalysis mapping of the same area.

corresponding CL panchromatic image of one of the structures. The CL image shows some features in the microstructure (marked with arrows in Figure 4b), not observed in the SE image. The origin of the contrast in a CL image is often related to the defect structure in the sample. Oxygen vacancies are native defects in Ga_2O_3 responsible for a broad luminescence band in the ultraviolet-blue region.[19,20] The observed contrast in the CL image suggests that defects are mainly distributed along terraces and steps of the microstructure. Ga and In X-ray microanalysis mapping of the same region is shown in figure 4c. Green color stands for Ga atoms while blue color for In ones. The image clearly shows accumulation of In atoms at certain lateral edges, which reveals impurity segregation during the growth process. Table I shows the indium concentration

Table I. EDX Data at Selected Points in Figure 5a

selected point	In at % (EDX)
A (outer)	6
B	5
C	3
D (inner)	1

obtained from the quantitative analysis of the EDX spectra from selected points in a different edge of the microstructure shown in Figure 4 (Figure 5a). These values range from 1 at % (D point) to 6 at % (A point), which correspond to inner and outer points, respectively. Local CL spectra recorded at these points are shown in Figure 5b. Blue UV emission bands have been reported in the literature for gallium oxide, and several component—2.7, 3.1, and 3.4 eV—were identified. The origin of these emissions was assigned to self-trapped excitons (UV component) and donor–acceptor pair transitions (blue band). Donors are related to oxygen vacancies or Ga interstitials, and oxygen–gallium vacancies pairs were supposed to be the acceptor centers.[20,21] The incorporation of impurities may modify the defect levels inducing luminescence changes. In our

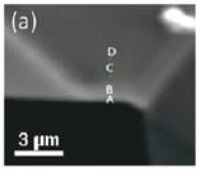

selected point	In % (EDX)
A	6
B	5
C	3
D	1

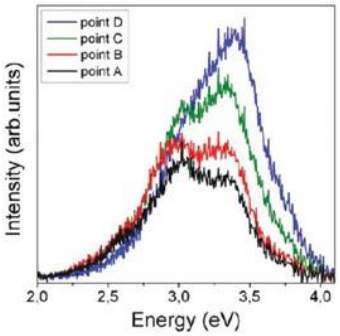

Figure 5. (a) SEM image of a microstructure. (b) CL spectra recorded from points A, B, C, and D marked in (a). Table shows data of In concentration for the marked points in (a).

case, the incorporation of In results in the relative decrease of the UV component with respect to the blue one as we go toward the structure edge (from D point to A point). This is related to the variations in In concentration detected by EDS so that the higher the indium content, the stronger is the blue (2.7 – 3.0 eV) component as shown in the CL spectrum at point A (Figure 5b), while for lower In concentration, the main CL emission corresponds to the UV band (3.4 eV), approaching the result obtained for undoped Ga_2O_3 samples.[20] This behavior shows that In atoms are strongly involved in the blue component (DAP transition), possibly by interaction with oxygen vacancies. As these native defects supply free carriers for conduction and introduce electronic energy levels in the band gap, the blue shift in CL spectra as indium concentration increases (EDS spectra) is quite relevant for potential optoelectronic devices based on In-doped Ga_2O_3 structures. Therefore, both optical and electronic properties could be tunable by modification of defect structure by In doping.

These results can be related to the growth and doping processes where In impurities and twin boundaries play a relevant role. The contrast observed in CL images show parallel fringes probably originated as a consequence of a nonuniform In concentration in the microstructures. These fringes seem to end in fronts where In atoms are accumulated as EDS data show. To explain the reason of the In segregation following parallel fronts we have to get insight into the growth and doping process. The role of twins may be relevant to explain the final morphology, as TEM results show. Planar defects are preferential places where impurities and point defects accumulate. The growth process involves indium incorporation into gallium oxide microstructures, which exhibit twin defects. Therefore, In atoms would accumulate during the growth at the twin plane, and the layer-by-layer process would result in the formation of steps and terraces, which would explain the bright stripes observed in CL images.

Additional relevant information of the local microstructure of In-doped Ga_2O_3 has been obtained by means of XPS and Raman measurements performed on In-doped and on undoped Ga_2O_3 structures. XPS spectra for Ga 3d and O 1s in undoped Ga_2O_3 nanostructures obtained with the same procedure as the In-doped ones are shown in Figure 6. Energy axis was calibrated by fixing C 1s binding energy (BE) at 284.8 eV.[22] There is a general agreement in the literature to assign 20.6 eV as binding energy of Ga^{3+} in Ga_2O_3. For example, the NIST database gives a value of 20.4 ± 0.5 eV for Ga 3d $^5/_2$ in

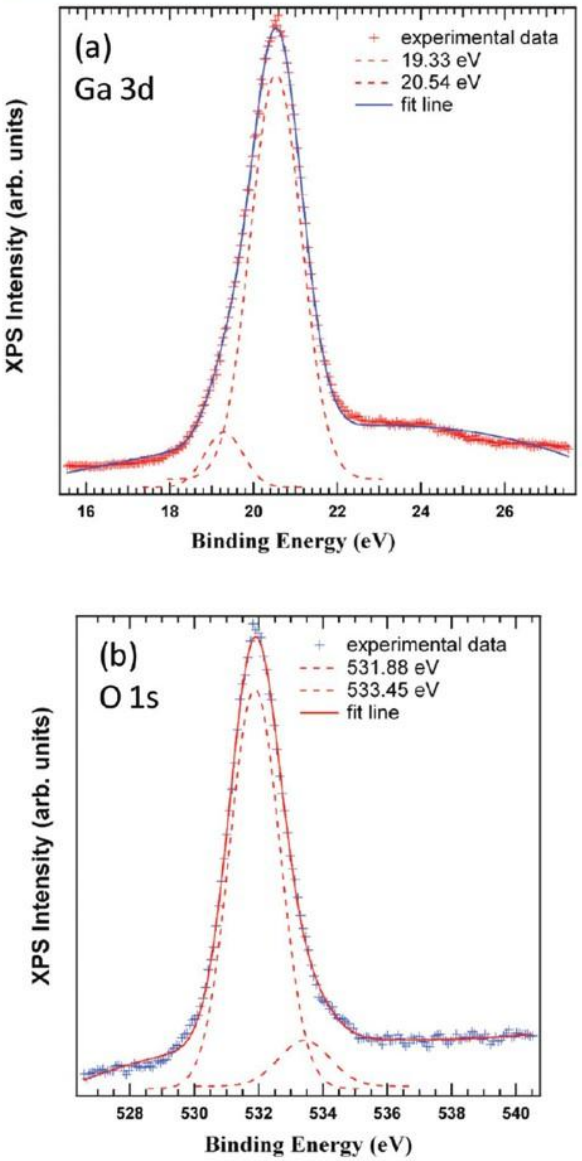

Figure 6. XPS high resolution spectra of Ga 3d (a) and O 1s (b) lines in undoped Ga_2O_3 microstructures.

Ga_2O_3.[23] Ghosh et al. have measured the XPS spectra for Ga_2O_3 standard,[24] and peaks at 20.07 and 20.52 eV were assigned to Ga 3d, while small amounts of an unidentified impurity (possibly metallic gallium) gave rise in the fitting process to peaks at 19.28 or 18.84 eV. The main peak in Figure 6a, at 20.54 eV for the Ga 3d core level, corresponds to Ga^{3+} in the Ga−O bonding, and the lower energy shoulder at 19.33 eV could be related to a small amount of metallic Ga or Ga suboxide at the surface. Figure 6b shows the XPS spectrum of the O 1s core level. Experimental data can be fitted to the sum of two Gaussians with maxima at 531.88 and 533.45 eV, respectively. These values are also consistent with those reported for Ga_2O_3 standard in the literature.[25] For metal oxides, the lower BE component is usually assigned to the oxide (i.e., Ga−O−Ga bonds). The higher BE component is usually assigned to the hydroxide (OH)/adsorbed oxygen $(O_2)^{2-}$ species and may have contributions from adsorbed water.[26] XPS images recorded with the Ga 3d, O 1s, or C 1s binding energies reveal mainly topographic contrast and no significantly local changes of XPS spectra are observed in the images.

Therefore, from the chemical point of view, the composition of the undoped Ga_2O_3 nanostructures is quite uniform, and the oxidation process of the metallic gallium was completed during the growth. The binding energies for Ga 3d and O 1s peaks in undoped Ga_2O_3 nanostructures will be used for comparison with the corresponding core levels in the In-doped ones. A survey spectrum of In-doped Ga_2O_3 nanostructures (not shown) shows peaks related to core levels of O 1s (531.8 eV), In 3d (453.07 and 445.85 eV), C 1s (284.8 eV), Ga 3p (106.7 eV), and Ga 3d (20.1 eV), along with O Auger peaks. Figure 7a displays an XPS image recorded with the In 3d binding energy of the In-doped microstructure shown in Figure 4. High-resolution XPS spectra of the O 1s and Ga 3d lines have been recorded from the two points marked in Figure 7a, at different distances from the edge. EDS measurements performed in the SEM from these points yielded a composition of 2.7 at % at A point and 1.0 at % at B point. The analysis of XPS spectra (not shown) of the Ga 3d line from both A and B points gives two components listed in Table II. The obtained values are very close to each other, and the XPS image with the Ga 3d energy is quite uniform both for undoped and for In-doped samples. The only feature observed is a slight shift of the components toward higher binding energies at point B (1 at % In) with respect to point A or undoped Ga_2O_3. Let us now consider the XPS spectra of the O 1s core level in undoped and doped Ga_2O_3 microstructures shown in parts b and c of Figure 7. Table III summarizes the data obtained after the fitting process for O 1s line. As it can be seen, the number of components needed to get a good fit varies in each sample or position.

At point A, corresponding to higher In incorporation (2.7 at % In), the main component related to Ga−O bonds at 531.87 eV and the higher binding energy component at 533.24 eV are clearly similar to those of undoped samples. In addition, a lower binding energy component (530.02 eV), which could be related to In−O bonds appears as a shoulder in the XPS spectra. The binding energy of O 1s core level for In_2O_3 is 530.2 eV, as reported in ref 25. As it has been mentioned above, indium tends to occupy gallium lattice sites in the gallium oxide lattice. As both elements participate in the bonding with the same charge state, it is expected that O 1s core levels characteristic of Ga_2O_3 and In_2O_3 may appear in the XPS spectra, as it occurs at point A (530.02 eV for In−O and 531.87 eV for Ga−O) close to the edge. On the other hand, at point B (1.0 at % In), only one component is detected in the XPS spectrum at 532.03 eV, which may be attributed to Ga−O bonds. These results indicate that the O 1s core levels are the most affected by In doping in Ga_2O_3. Also, In 3d lines have been measured, and the same values (445.59 and 453.42 eV) at both A and B points were obtained (Figure 7d). This binding energy agrees with the In^{3+} state in In_2O_3 (445.1 eV).[21] XPS measurements performed in In-doped Ga_2O_3 nanobelts and springs yielded similar results. For example, Figure 8a shows the XPS mapping recorded with the Ga 3d energy line in a springlike structure. High-resolution O 1s XPS spectra of the points marked as B and C in the inset of Figure 8a are shown in Figure 8b. Only the component at 531.7 eV is observed (Ga−O bonding in Ga_2O_3) at B point, while a shoulder at lower binding energies is clearly resolved

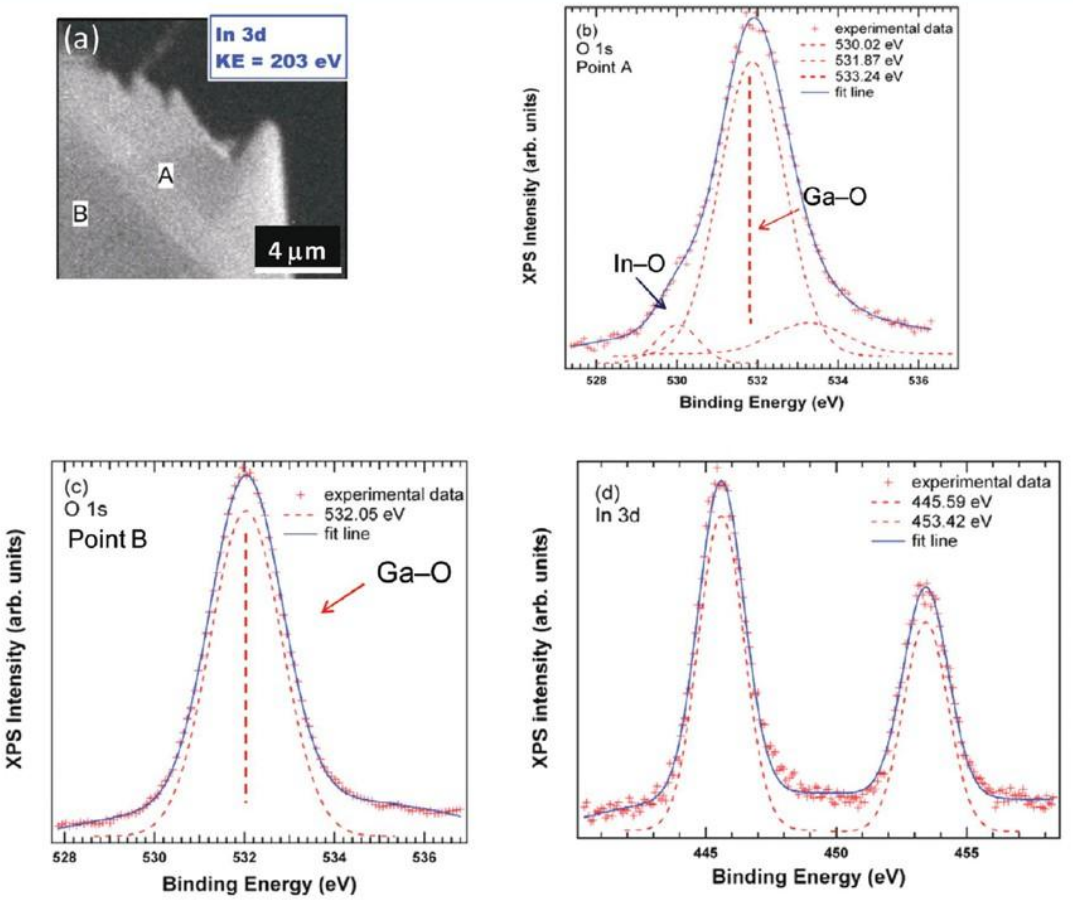

Figure 7. (a) XPS mapping recorded with the In binding energy. (b and c) High-resolution XPS spectra of O 1s lines from A and B points marked in (a), respectively. (d) XPS spectra of In 3d lines in In-doped Ga_2O_3 microstructure.

Table II. Binding Energies (in eV) of the Ga 3d Core Level in Undoped and In-Doped Samples

undoped	In-doped, point A	In-doped, point B
19.33	19.20	19.53
20.54	**20.55**	**20.61**

Table III. Binding Energies (in eV) of the O 1s Core Level in Undoped and In-Doped Samples

undoped	In-doped, point A	In-doped, point B
	530.02	
531.88	**531.87**	**532.03**
533.45	533.24	

(529.6 eV) and related to the In−O bond at C point. The analysis of high resolution XPS core level spectra of Ga 3d, O 1s, and In 3d enable to determine the oxidation degree of gallium oxide structures and the effectiveness of indium incorporation into this matrix at the chemical bonding level.

The influence of the indium concentration on the vibrational spectrum of the samples has been characterized by spatially resolved Raman spectroscopy in a confocal microscope. Figure 9a shows the Raman spectrum of an undoped β-Ga_2O_3 nanoribbon obtained by the same thermal treatment as the In-doped ones. The spectrum is similar to those reported for bulk material,[27,28] and shows the characteristic peaks at 200, 346, 416, 475, 627, 657, and 765 cm^{-1}. The peak at 520 cm^{-1} corresponds to the silicon substrate. Figure 9b shows a comparison of the different Raman peaks acquired from two points of the β-Ga_2O_3:In microstructure shown in Figures 4 and 7, where In concentration was 1 and 6 at %, respectively. The peaks from the undoped structure (Figure 9a) are also added for comparison. A different evolution of the peaks is observed when increasing the In concentration. In the case of 1 at % In concentration, virtually no changes are observed with respect to the undoped sample, except for a light increase of the 651 cm^{-1} peak intensity, as explained below. For 6 at % In concentration, the 200, 320, and 765 cm^{-1} peaks do not change while a slight broadening of the 345 and 470 cm^{-1} peaks and a stronger, asymmetric widening of the 415 and 630 cm^{-1} peaks takes place. Finally, a clear increase of the intensity ratio of the 651 cm^{-1} (A_g) and 657 cm^{-1} (B_g) with increasing In content is observed.

The β-Ga_2O_3 crystal structure consists of a double chain of GaO_6 octahedra, which is connected by GaO_4 tetrahedra.[29] Hence, there are two nonequivalent Ga^{3+} sites in the β-Ga_2O_3 lattice: Ga_I (tetrahedral coordination) and Ga_{II} (octahedral coordination and longer bond lengths). Dohy et al.[28] performed a theoretical and experimental vibrational study of the bulk β-Ga_2O_3 structure, which resulted in 15 Raman-active

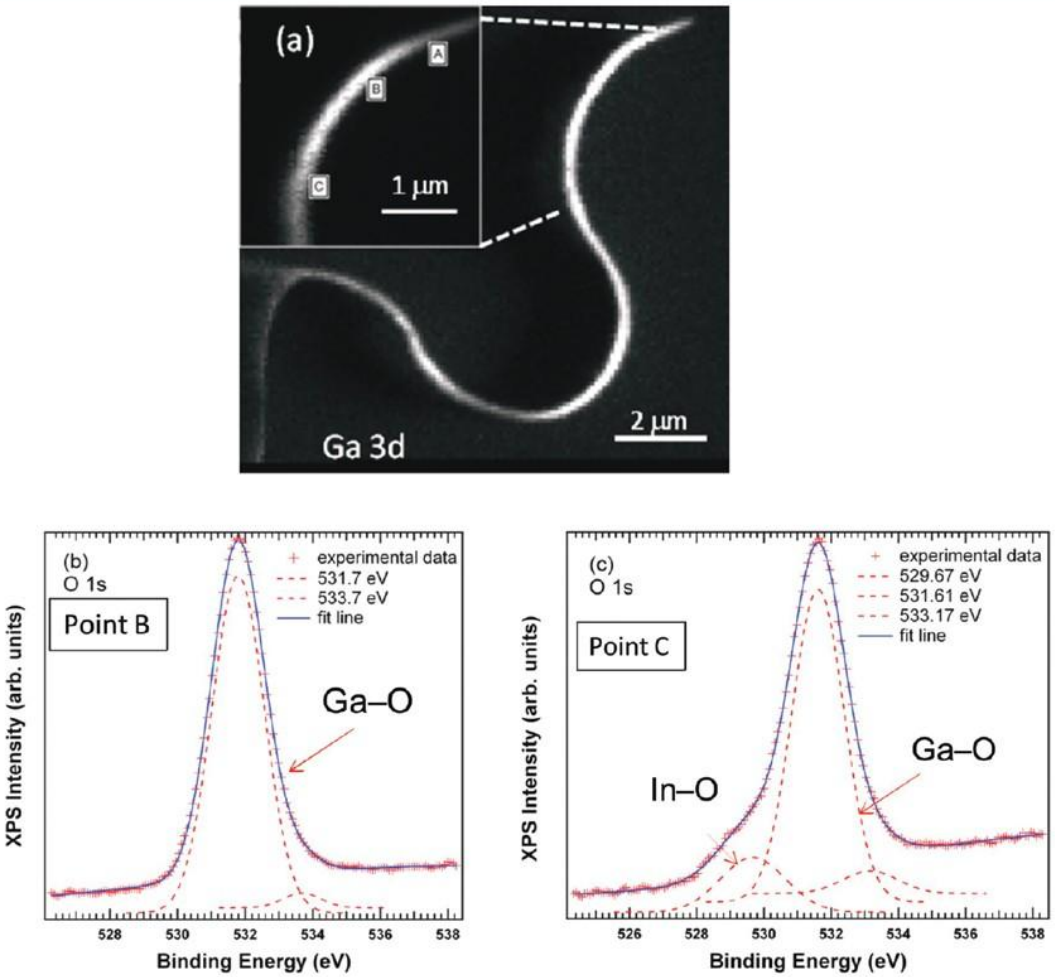

Figure 8. (a) XPS mapping with Ga 3d binding energy of an springlike structure. Inset detail at high magnification with some points marked. (b and c) High-resolution XPS spectra of O 1s lines from B and C points, respectively.

modes. The Raman spectrum was divided in three regions accordingly with the frequency peaks range: low-frequency peaks (up to 200 cm^{-1}), high-frequency peaks (above ~600 cm^{-1}), and an intermediate range between 300 and 600 cm^{-1}. These ranges were related to different vibration modes. However, they observed that vibrations seem to be heavily mixed.[28] It is well-known that impurities which are heavier than the host atoms create nonlocal modes coupled to the host continuum which results in a broadening of Raman lines.[30] It has been shown that, in β-$(Ga_{1-x}In_x)_2O_3$ solid solutions with low indium concentrations, In^{3+} ions are preferentially located in the octahedral sites,[31,32] which would imply variations in the intermediate frequency range of Raman spectra. Within this framework, the lines width increase observed in this work, stronger for 345, 417, 470, and 630 cm^{-1}, should be related to the influence of the In^{3+} located in the Ga_{II} octahedral site on these Raman modes. This effect is clearly observed in the Raman spectra recorded at points in the structure with higher In content.

On the other hand, the most noticeable effect observed in the Raman spectra of In-doped Ga_2O_3 is the enhancement of the relative intensities of the 651/657 cm^{-1} peaks, even at points with a lower In content. The 657 cm^{-1} peak was reported by some authors as a single peak[33−35] in bulk and Ga_2O_3 nanorods, although a composed peak (651−654 cm^{-1}) was also reported in bulk Ga_2O_3[28] and in Ga_2O_3−In_2O_3 solid solutions.[36] We have observed that the main component in undoped samples is the 657 cm^{-1} peak, while the 651 cm^{-1} one dominates in the In-doped region. The variation in phonon spectra due to doping or size effects could be relevant as it may affect to the heat transfer and electron−phonon interactions. Thermal management in electronic devices is of practical importance and optical phonons are usually involved in electrical and optical properties.

In summary, In-doped Ga_2O_3 micro- and nanostructures, with different morphology including nanoribbons and nanosprings, have been grown by thermal oxidation of Ga. Indium incorporation in the range 1−6 at % has been detected by several spectroscopic tools used in this work (EDS in HRTEM, EDS in SEM, and XPS). The novel morphologies, such as springs and belts with jagged edges, can be explained by taking into account the presence of twins in the crystals (HRTEM analysis). The layer-by-layer model proposed as growth mechanism is consistent with the appearance of terraces and

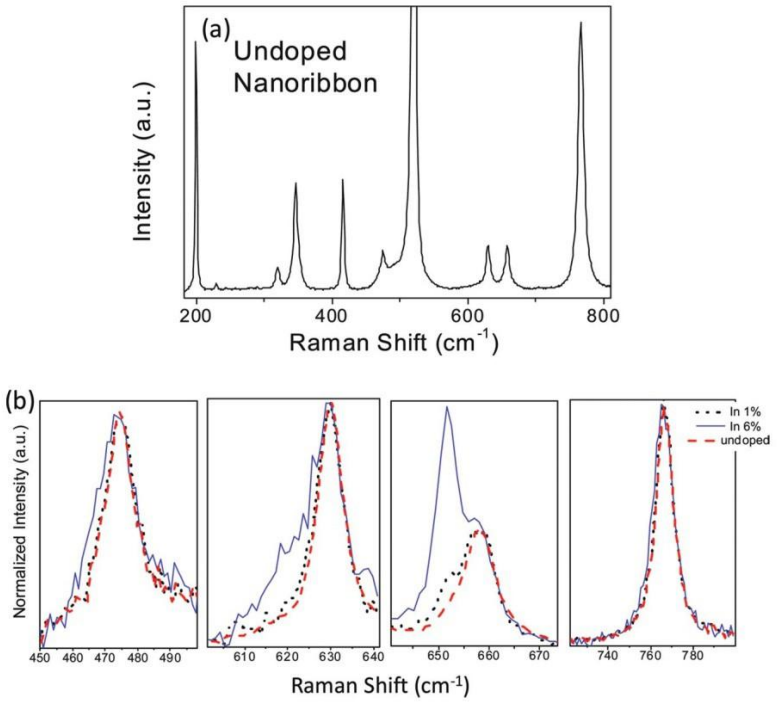

Figure 9. (a) Micro-Raman spectrum of undoped gallium oxide nanostructure where characteristic peaks of Ga_2O_3 are shown. The peak at 520 cm^{-1} corresponds to the silicon substrate. (b) Detailed Raman spectra showing the evolution of peaks at 651 and 657 cm^{-1} from undoped (dashed line), In 1 at % (dashed line) and In 6 at % (solid line).

steps in the planar surfaces. Moreover, a segregation of In impurities at the edges suggests that In may influence the growth mechanism. In incorporation modifies the native defect structure as observed by means of local CL spectra recorded at several points in the doped nanostructures. A blue, defect-related luminescence band is found to strongly increase when increasing the In content. The inclusion of In ions in the octahedral Ga sites does not result in a strong modification of the vibrational modes of the crystal up to 6 at % In, as observed by spatially resolved Raman spectroscopy, with exception of an intensity increase of the 651 cm^{-1} A_g mode and broadening of some peaks.

■ AUTHOR INFORMATION

Corresponding Author

*E-mail: bianchi@fis.ucm.es.

Notes

The authors declare no competing financial interest.

■ ACKNOWLEDGMENTS

This work has been supported by MICINN through projects MAT2009-07882 and CSD2009-0013 and by BSCH-UCM (Project GR35-10A-910146). The authors are grateful to Dr. Luca Gregoratti at the Sincrotron Trieste for useful advises on XPS measurements.

■ REFERENCES

(1) Ginley, D. S.; Bright, C. *MRS Bull.* **2000**, *25*, 15.
(2) Dai, Z. R.; Pan, Z. W.; Wang, Z. L. *Adv. Funct. Mater.* **2003**, *13*, 9.
(3) Yamaga, M.; Víllora, E. G.; Shimamura, K.; Ichinose, N.; Honda, M. *Phys. Rev. B* **2003**, *68*, 155207.
(4) Varley, J. B.; Weber, J. R.; Janotti, A.; Van de Walle, C. G. *Appl. Phys. Lett.* **2010**, *97*, 142106.
(5) Víllora, E. G.; Shimamura, K.; Yoshikawa, Y.; Ujiie, Y.; Aoki, K. *Appl. Phys. Lett.* **2008**, *92*, 202120.
(6) Chiang, H. Q.; Hong, D.; Hung, C. M.; Presley, R. E.; Wager, J. F.; Park, C. H.; Keszler, D. A.; Herman, G. S. *J. Vac. Sci. Technol. B.* **2006**, *24*, 2702.
(7) Lu, J. G.; Chang, P.; Fan, Z. *Mat. Sci. Eng. R* **2006**, *52*, 49.
(8) Hidalgo, P.; Liberti, E.; Rodríguez-Lazcano, Y.; Méndez, B.; Piqueras, J. *J. Phys. Chem. C* **2009**, *113*, 17200.
(9) Nogales, E.; García, J. A.; Méndez, B.; Piqueras, J. *Appl. Phys. Lett.* **2007**, *91*, 133108.
(10) Nogales, E; Hidalgo, P; Lorenz, K; Méndez, B; Piqueras, J; Alves, E *Nanotechnology* **2011**, *22*, 285706.
(11) Mazeina, L.; Piccard, Y. N.; Maximenko, S. I.; Perkins, F. K.; Glaser, E. R.; Twigg, M. E.; Freitas, J. A.; Prokes, S. M. *Cryst. Growth Des.* **2009**, *9*, 4471.
(12) Nogales, E.; Méndez, B.; Piqueras, J.; García, J. A. *Nanotechnology* **2009**, *20*, 115201.
(13) Nogales, E.; Méndez, B.; Piqueras, J. *Ultramicroscopy* **2011**, *111*, 1037.
(14) van de Waal, B. W. *J. Cryst. Growth* **1996**, *158*, 153.
(15) Jin, S.; Bierman, M. J.; Morin, S. A. *J. Phys. Chem. Lett.* **2010**, *1*, 1472.
(16) Morin, S. A.; Jin, S. *Nano Lett.* **2010**, *10*, 3459.
(17) Kim, H. W.; Shim, S. H. *Thin Solid Films* **2007**, *515*, 5158.
(18) Jalilian, R.; Yazpanah, M. M.; Pradhan, B. K.; Sumanasekera, G. U. *Chem. Phys. Lett.* **2006**, *426*, 393.
(19) Binet, L.; Gourier, D. *J. Phys. Chem. Solids* **1998**, *59*, 1241.
(20) Díaz, J.; López, I.; Nogales, E.; Méndez, B.; Piqueras, J. *J. Nanoparticle Res* **2011**, *13*, 1833.
(21) Shimamura, K.; Víllora, E. G.; Ujiie, T.; Aoki, K. *Appl. Phys. Lett.* **2008**, *92*, 201914.
(22) Miller, D. J.; Biesinger, M. C.; McIntyre, N. S. *Surf. Interface Anal.* **2002**, *33*, 299.

(23) http://srdata.nist.gov/xps
(24) Ghosh, S. C.; Biesinger, M. C.; LaPierre, R. R.; Kruse, P. *J. Appl. Phys.* **2007**, *101*, 114322.
(25) Hollinger, G.; Skheyta-Kabbani, R.; Gendry, M. *Phys. Rev. B* **1994**, *49*, 11159.
(26) Al-Kuhaili, M. F.; Durrani, S. M. A.; Khawaja, E. E. *App. Phys. Lett.* **2003**, *83*, 4533.
(27) Li, Y.; Liu.; Lee, C. S.; Lee, S. T. *Superlattices Microstruct.* **2009**, *46*, 585.
(28) Dohy, D.; Lucazeau, G.; Revcolevschi, A. *J. Solid State Chem.* **1982**, *45*, 180.
(29) Kudo, A.; Mikami, I. *J. Chem Soc., Faraday Trans* **1998**, *94*, 2929.
(30) *Raman scattering in materials science*; Weber, W. H., Merlin, R., Eds.; Springer, 2010.
(31) Edwards, D. D.; Folkins, P. E.; Mason, T. O. *J. Am. Ceram. Soc.* **1997**, *80*, 253.
(32) Blanco, M. A.; Sahariah, M. B.; Jiang, H.; Costales, A.; Pandey, R. *Phys. Rev. B* **2005**, *71*, 184103.
(33) Gao, Y. H.; Bando, Y.; Sato, T.; Zhang, Y. F.; Gao, X. Q. *Appl. Phys. Lett.* **2002**, *81*, 2267.
(34) Rao, R.; Rao, A. M.; Xu, B.; Dong, J.; Sharma, S.; Sunkara, M. K. *J. Appl. Phys.* **2005**, *98*, 094312.
(35) Zhao, Y.; Frost, R. L. *J. Raman Spectrosc.* **2008**, *39*, 1494.
(36) Vigreux, C.; Binet, L.; Gourier, D. *J. Solid State Chem.* **2001**, *157*, 94.

2. INFLUENCIA DEL DOPADO CON Sn Y Cr EN LA MORFOLOGIA Y EN LA LUMINISCENCIA DE NANOHILOS DE Ga_2O_3 CRECIDOS TERMICAMENTE

En este capítulo se describe la influencia de los dopantes en los mecanismos de crecimiento de estructuras alargadas de óxido de galio monoclínico, dopado con Sn, o co-dopado con Sn y Cr. La presencia de Sn durante el crecimiento ejerce una enorme influencia en la morfología de las estructuras resultantes, donde se observan hilos ramificados, fustas y agujas dopadas con Sn. El co-dopado posterior con Cr, con objeto de modificar su comportamiento fotónico, se realiza mediante difusión térmica. Se ha estudiado el mecanismo de formación de las estructuras ramificadas mediante HRTEM. En algunos casos, se ha comprobado la existencia de un crecimiento epitaxial, observado en la elevada calidad de la intercara entre la rama principal y la ramificación secundaria de las estructuras. En otros, se observa la formación de defectos extensos, como maclas, en las intercaras. La influencia de los dopantes en los niveles energéticos de Ga y O se ha estudiado mediante espectroscopia fotoelectrónica de rayos X (XPS). Se ha estudiado la influencia del dopado con Sn y co-dopado con Sn y Cr en las propiedades vibracionales de nanohilos individuales mediante espectroscopia micro-Raman. Las medidas de catodoluminiscencia (CL) muestran la existencia de una banda compleja relacionada con el Sn en las estructuras dopadas con Sn. Al estudiar la CL en función de la temperatura y la densidad de excitación se comprueba que se trata de una emisión activada térmicamente.

En las muestras co-dopadas con Sn y Cr, la emisión luminiscente roja, característica del Cr3+, bloquea las bandas observadas en las muestras dopadas con Sn. Las estructuras ramificadas co-dopadas con Sn y Cr se han estudiado mediante imagen y espectroscopia de micro-fotoluminiscencia, observándose un comportamiento de guía de luz a lo largo de los troncos y ramas de estas estructuras.

THE JOURNAL OF PHYSICAL CHEMISTRY C

Article

pubs.acs.org/JPCC

Influence of Sn and Cr Doping on Morphology and Luminescence of Thermally Grown Ga_2O_3 Nanowires

Iñaki López, Emilio Nogales,* Bianchi Méndez, and Javier Piqueras

Departamento de Física de Materiales, Facultad de Ciencias Físicas, Universidad Complutense de Madrid, 28040 Madrid, Spain

Andrea Peche, Julio Ramírez-Castellanos, and Jose M. González-Calbet

Departamento de Química Inorgánica, Facultad de Ciencias Químicas, Universidad Complutense de Madrid, 28040 Madrid, Spain

ABSTRACT: Elongated micro- and nanostructures of Sn doped or Sn and Cr codoped monoclinic gallium oxide have been grown by a thermal method. The presence of Sn during growth has been shown to strongly influence the morphology of the resulting structures, including Sn doped branched wires, whips, and needles. Subsequent codoping with Cr is achieved through thermal diffusion for photonic purposes. The formation mechanism of the branched structures has been studied by transmission electron microscopy (TEM). Epitaxial growth has been demonstrated in some cases, revealed by a very high quality interface between the central rod and the branches of the structures, while in other cases, formation of extended defects such as twins has been observed in the interface region. The influence of dopants on the energy levels of Ga and O within the structures has been studied by XPS. Micro-Raman spectroscopy was used to assess the influence of Sn doping, and Sn−Cr codoping, on the vibrational properties of single nanowires. Cathodoluminescence (CL) measurements show a Sn-related complex band in the Sn-doped structures. Temperature-dependent and excitation-density-dependent CL indicates that this is a thermally activated emission. In the Sn−Cr codoped samples, the characteristic, very intense Cr^{3+} red luminescence emission quenches the bands observed in the Sn-doped samples. Branched, Sn−Cr codoped structures were studied with microphotoluminescence imaging and spectroscopy, and waveguiding behavior was observed along the trunks and branches of these structures.

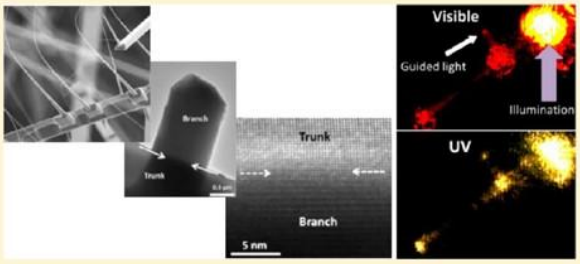

1. INTRODUCTION

Monoclinic β-Ga_2O_3 is a transparent conductive oxide (TCO) with high thermal and chemical stability and controllable n-type conductivity with suitable doping. Impurities in semiconductor matrixes are key factors for improving electrical conductivity, supplying mobile carriers or introducing electronic traps in the band gap, which influence not only their electrical but also their optical properties. Besides the tuning of its physical properties, the control of the dimensionality and morphology is also relevant for the applications of semiconductor oxides in areas of nanoscience and nanotechnology.[1,2] This point has been less explored, and the control of the nanostructures morphology by the addition of impurities during the growth process is worth investigating. Gallium oxide nanowires have been proposed for several applications, such as gas sensors,[1] solar blind sensors in the UV range,[3] white light emitting devices,[4] or waveguides for the UV−vis ranges,[5,6] among others. Regarding its electrical and optical properties, Ga_2O_3 behaves as an n-type semiconductor due to the presence of a donor band related to intrinsic defects and/or native impurities[7,8] and is transparent in the blue-UV range. An effective tuning of electrical or optical properties by the addition of impurities in oxide nanowires is still a challenge, because of the out-diffusion processes and, in many cases, of the low diffusivity of the impurities in nanowires.[9] In the past years, enhancement effects of the gas sensitivity, conductivity, or field-emission properties of Ga_2O_3 by Sn doping have been reported.[7,10−12] With regard to optical properties, light emission from tin doped gallium oxide has also been studied, and blue-green luminescence emission bands linked to the Sn dopant were reported.[10,13] In the above-mentioned works, the study of the influence of Sn doping was focused into the detection of changes in the physical properties of doped gallium oxide; however, the nanowire morphology was retained during the growth process. Undoped gallium oxide nanowires have been obtained by several thermal methods with the aid of metal nanoparticles[2] or by catalyst-free methods.[14,15] In order to dope the nanowires, a possible route is starting with an alloy or a mixture of the precursor elements required, as reported for example in refs 5 and 14. We have previously grown undoped Ga_2O_3 nanowires by using pure metal as gallium source and carrying out a controlled thermal treatment under a dynamic atmosphere in an open furnace.[6,14] To get

Received: September 21, 2012
Revised: December 17, 2012
Published: January 4, 2013

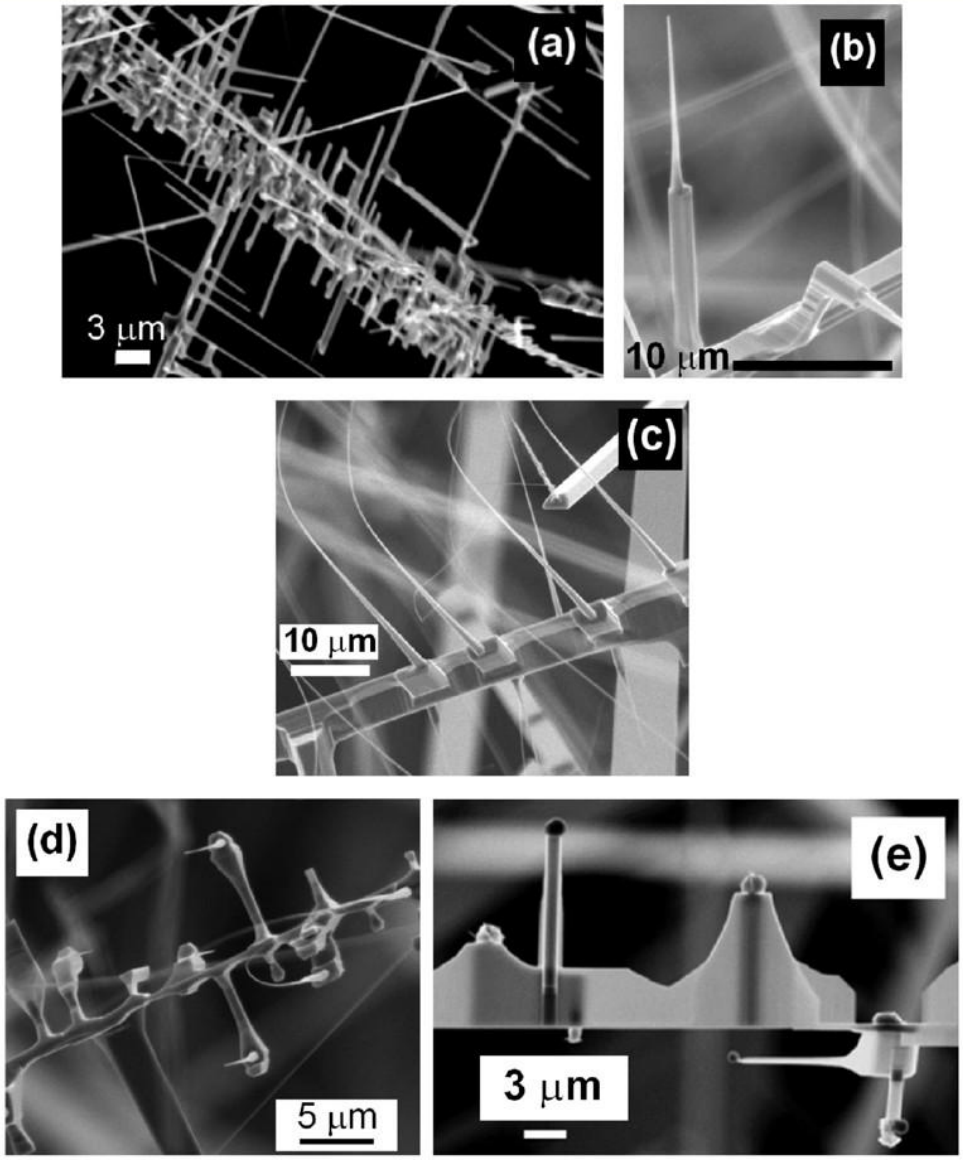

Figure 1. SEM images of Sn doped β-Ga_2O_3 micro- and nanostructures: (a) branched structures, (b) needle structure, (c) whiplike structure, (d) complex needle structures, and (e) branched structures with a round particle at the end of the tip.

doped nanowires within this approach, suitable precursors have to be incorporated into the furnace.[5,14,16]

In this work, SnO_2 or Cr_2O_3 and metallic Ga were used as starting materials, and as a result of the thermal treatment, branched and complex structures with incorporation of dopants were obtained. The results show that Sn impurities may be used to modify the morphology of the resulting nanostructures. The morphological and structural characterization of these branched structures and a tentative explanation of the growth process are provided.

2. EXPERIMENTAL SECTION

The Sn doped β-Ga_2O_3 structures were grown by thermal oxidation at 1100 °C of metallic Ga in the presence of SnO_2 under an inert gas flow on a Ga_2O_3 pellet used as substrate. The same procedure has been reported for undoped Ga_2O_3 nanowires elsewhere.[14] The morphology of the doped structures is influenced by the presence of tin during growth resulting for example in the formation of branched structures, as we will see below. Some of these structures were gently detached from the pellet and placed on a silicon wafer for further characterization. In a second stage, the rest of the structures were used as starting material to obtain codoped (Sn,Cr)-Ga_2O_3 branched structures by a further thermal treatment at 1500 °C for 15 h in the presence of chromium oxide powders. After the growth, the codoped structures were removed from the pellet and placed on a silicon wafer for further characterization.

Morphological characterization has been carried out in a FEI Inspec S50 scanning electron microscope (SEM) and a Leica

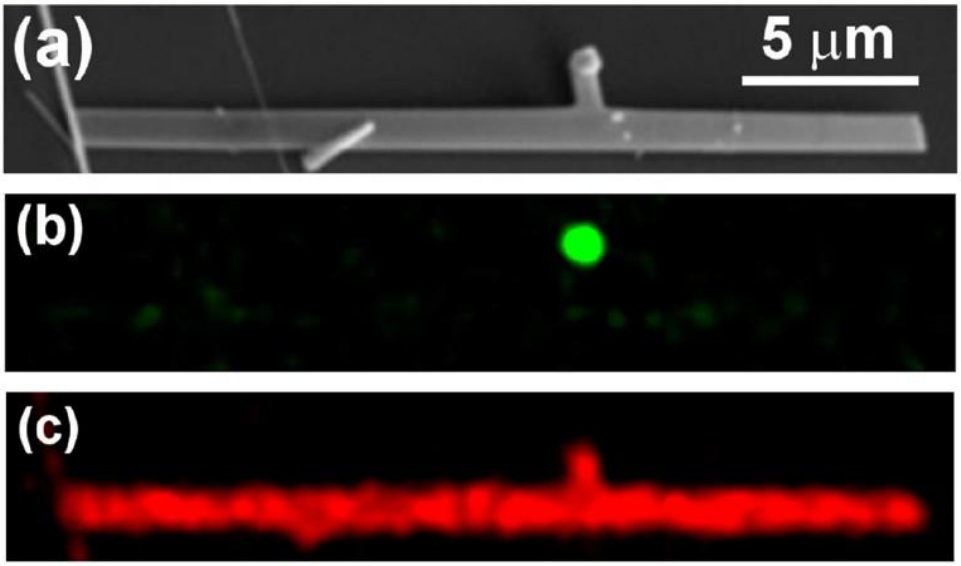

Figure 2. (a) SE image and EDX (b) Sn and (c) Ga maps of a branched structure. The droplet in the end of the branch is shown to be composed by Sn.

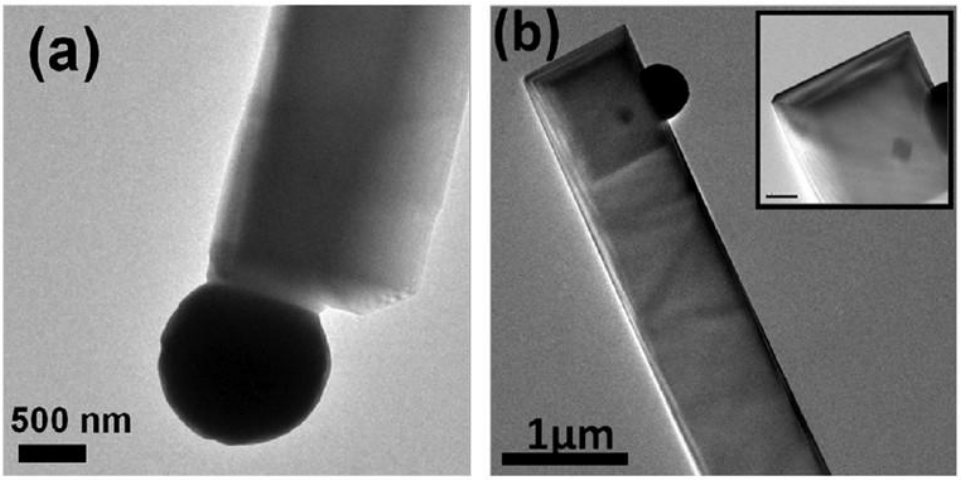

Figure 3. Low magnification bright-field TEM images of Sn doped Ga_2O_3 wires: (a) a nanowire with a Sn ball in its tip and (b) nanoribbon shaped structure. The inset shows the morphological shape of the nanostructure end.

Stereoscan 440 SEM. Selected area electron diffraction (SAED) and high resolution transmission electron microscopy (HRTEM) were performed in a JEOL 3000 FEG electron microscope, fitted with a double tilting goniometry stage (±22°, ± 22°). Simulated HRTEM images were calculated by the multislice method using the MacTempas software package. Energy dispersive X-ray microanalysis spectroscopy (EDS) and cathodoluminescence (CL) measurements were carried out in the above-mentioned Leica SEM. Photoluminescence (PL) spectroscopy and imaging have been performed in a Horiba Jobin Ybon LabRam HR800 Raman confocal microscope. The excitation light was the 325 nm line of a HeCd laser. All PL measurements were performed at room temperature. Raman measurements and XRD were also performed to assess the crystal quality of the wires. The study of the structures was complemented with the aid of high resolution photoemission spectra and imaging, performed at the Sincrotrone Elettra Trieste facility (ESCA microscopy line).

3. RESULTS AND DISCUSSION

3.1. Influence of Doping on Morphology and Crystalline Structure. Figure 1 shows representative SEM images of Sn-doped (Figure 1a–e) Ga_2O_3 structures grown on a gallium oxide compacted pellet. The Sn doped structures present a branched shape (Figure 1a), with trunks whose lengths can reach several hundred micrometers and widths in the range of a few hundred nanometers up to a few micrometers. The branches tend to reach up to several micrometers in length and have widths in the range of a few hundred nanometers. Needlelike (Figure 1b) and whiplike (Figure 1c) structures are also formed in the Sn doped structures obtained by this method. Similar kinds of whiplike

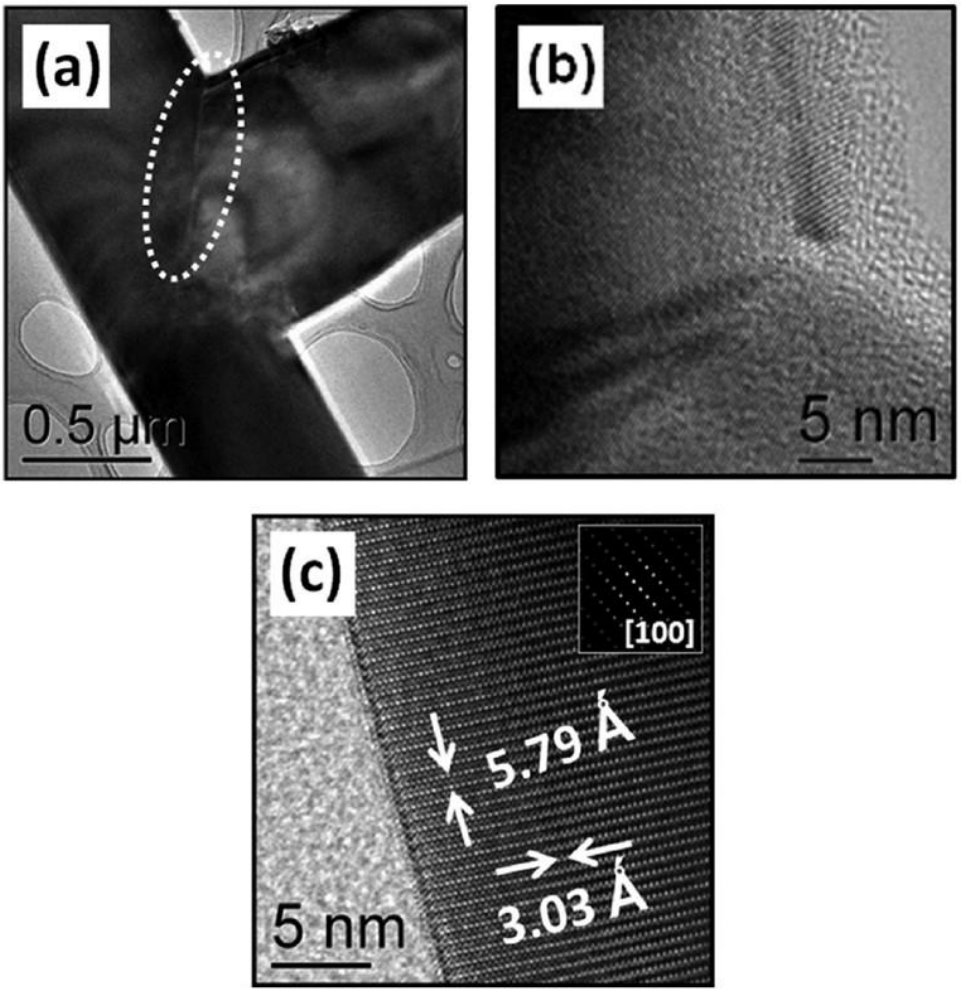

Figure 4. (a) Region where the branch starts growing from the trunk at lower magnification. The dashed ellipse highlights the presence of an extended defect that separates the trunk and the branch. (b) The HRTEM image of the interface and (c) HRTEM image of a branch corresponding to the [100] zone axis shown in the inset.

structures have been also observed in Sn doped GeO_2.[17] XRD measurements (not shown) of Sn doped complex structures show that the crystal structure of the nanowires mesh is the monoclinic β-Ga_2O_3 (JCPDS 00-041-1103). No peaks corresponding to other phases are found. In some cases (Figure 1e), the presence of droplets at the end of a secondary branch is observed. Some of the synthesized structures were placed onto silicon wafer substrates for X-ray microanalysis in the SEM. Figure 2a shows the SEM image of one branched wire with a round particle at the end of its branch. These round particles are also observed in Figure 1e. Figure 2b,c shows the corresponding EDX mapping for Sn and Ga, respectively, showing that the particle at the end of the branch is composed by tin. These observations point out to the formation of small tin aggregates at the surfaces of the primary wires, which favors the catalytic growth of secondary branches. Therefore, as a result of the growth process, the tin droplet could be formed, leaving behind Sn doped β-Ga_2O_3 nanowires. This feature was also observed for Si doped β-Ga_2O_3 nanostructures grown by a similar method.[18]

The small lateral branches of the complex structures were investigated by TEM. Low magnification bright-field TEM images of such structures are depicted in Figure 3. They have nanobelt shape with average lateral size of around 1 μm. Figure 3a shows a nanobelt with a tin ball, which was found to be amorphous, at its end. This shows the existence of a metal-catalyzed vapor−liquid−solid (VLS) growth mechanism.[2] The EDS microanalysis performed within the TEM shows that the chemical composition of this droplet is Sn, in agreement with the results shown in Figure 2 for EDX in the SEM. In the VLS mechanism the metal particle size usually determines the wire diameter, but in our case, the width of the belt does not perfectly fit to the tin ball diameter. On the other hand, tin balls have also been observed attached to the lateral surface of the belts as Figure 3b shows. The inset in Figure 3b shows the detail of the final end of the belt with a flat shape. These results support that tin could play a catalyst-like role in order to develop elongated structures. However, as tin particles are formed not only at the end of the wires, but also at lateral points along the main trunk, branched structures are formed, as observed.

Figure 4 shows the TEM and HRTEM images of a branched structure. The region where a branch starts growing from the trunk is shown in Figure 4a. Figure 4b shows a HRTEM image, with the detail of the defect marked with a dashed line in Figure 4a. Both images show the existence of defects; however, there is structural continuity from the trunk to the branch (Figure 4b). Figure 4c shows a very well-crystallized branch, where the measured interplanar distances of 5.79 Å and 3.03 Å correspond to the [100] zone axis (inset). The growth direction obtained from this image is [001].

These branched structures could be interesting for applications in light generation, detection, or waveguiding.[19] Therefore, it is important to note that the microstructure is crucial in order to understand how light generates or propagates through the nanostructures, since extended defects can be sometimes observed and may act as dispersion centers.

We have studied the possibility of tuning the optical properties of these branched structures by suitable doping with optically active ions, such as Cr, while keeping the branched morphology. Cr ions are chosen because of their high quantum efficiency and the characteristic shape of their red emission bands in gallium oxide nanostructures.[16] To this purpose a thermal treatment of the branched structures in the presence of chromium oxide powders was performed. This subsequent codoping with Cr does not modify essentially the branched morphology of the structures, as shown in Figure 5. However, the structures tend to further grow, and the lateral dimensions were slightly increased.

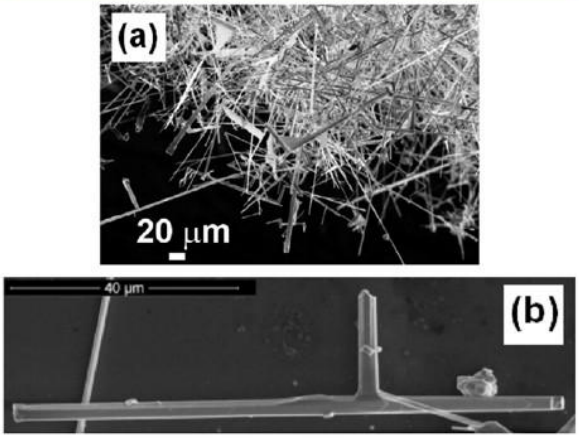

Figure 5. SEM images of codoped Sn, Cr Ga_2O_3 branched wires: (a) structures on the pellet and (b) a single structure on silicon wafer.

In order to characterize the crystal quality of Cr doped branched structures after the Cr diffusion process, some samples were studied by TEM. Figure 6a shows the low magnification TEM image of one of these branched structures, where a junction of a trunk and a branch marked by arrows in the figure, is observed.

The SAED along the [100] zone axis corresponding to the branch is depicted in Figure 6b. The HRTEM image at higher magnification of the same area (Figure 6c) shows a very well-crystallized material. No structural defects are present. The measured interplanar distances are 3.03 and 5.79 Å, which fit well to the b and c parameters of the β-Ga_2O_3 unit cell, respectively, and are the same as those shown in Figure 4c for the Sn doped sample. As in that case, the growth direction obtained from this image is [001]. EDS microanalysis performed on this branch shows a very homogeneous chemical composition and confirms the presence of Sn and Cr.

Figure 7a shows a HRTEM image of a junction area, where two different crystal orientations are observed, that corresponds to the trunk and the branch, respectively. The FFT pattern along [201] (Figure 7b) was obtained from the trunk. Its I-FFT shows a contrast due to heavy atom positions and typical interplanar distances (3.03 and 3.33 Å) of the monoclinic β-Ga_2O_3 phase (Figure 7c). On the other hand, the FFT pattern of the branch is depicted in Figure 7d, which can be indexed along the [100] zone axis. The corresponding I-FFT image (Figure 7e) shows the interplanar distances a = 3.03 and c = 5.79 Å. Finally, the FFT pattern (Figure 7f) of the junction area (marked by dashed arrows in Figure 7a) reveals the overlapping of the diffraction spots of both branch and trunk FFT patterns, which reveals a good match between both crystal orientations. The first layers of the branch seem to adjust quite well, suggesting a good epitaxial growth of these branched structures and a very high crystal quality. It should be noticed that actually, during the Cr diffusion process, no extra tin was incorporated into the furnace, and only chromium oxide powders were added for doping purposes. The Sn doped branched morphology is retained after the doping process, although an overgrowth of the structures is achieved, as we have already shown.

This TEM analysis indicates that epitaxial growth is responsible for the growth of some branches in these samples, as seen in Figures 6 and 7. In other cases, however, the growth of branches is related to the formation of extended defects, such as twins, as observed in Figure 4. In all cases, the branches present very high crystal quality.

3.2. Influence of Doping on Raman Spectra and Chemical Bonds. The local structure of chemical bonds in Sn doped and Sn and Cr codoped Ga_2O_3 branched structures has been investigated by Raman spectroscopy and XPS techniques. Figure 8 shows the peaks of the Raman spectra obtained from undoped, Sn doped, and Sn, Cr codoped nanowires. All the peaks correspond to β-Ga_2O_3.[20,21] For Sn doped structures, Raman spectra show almost no differences in the peak positions or the fwhm of the Raman peaks, in comparison with undoped Ga_2O_3, as could be expected since the tin concentration is very low. The only appreciable difference is the intensity ratio of the peaks at 651 and 657 cm^{-1} (Figure 8e). This difference was also observed in In doped β-Ga_2O_3, in which the 651 cm^{-1} peak dominated the In doped region.[21] Nevertheless, although Sn impurities influence the final morphology and shape of the microstructures, the crystalline quality of branched structures remains very high, as shown by TEM. This quality is also reflected in the vibrational spectra in these structures.

On the other hand, for Cr doped branched structures, some differences in the Raman spectra arise. In particular, a clear broadening of the peak and a higher energy shoulder are observed in the 350 cm^{-1} region (Figure 8b). The appearance of an additional component, usually at higher energy, is expected for dopant ions which have the same valence state and are lighter than the host ion,[22] which is the case of Cr^{3+} substituting Ga^{3+}. The monoclinic gallium oxide unit cell contains four Ga_2O_3 molecules. Two chemically distinguishable cationic sites are coordinated either tetrahedrally or octahedrally with oxygen ions. The crystal structure is a double chain of GaO_6 octahedra arranged parallel to the b-axis of the lattice,

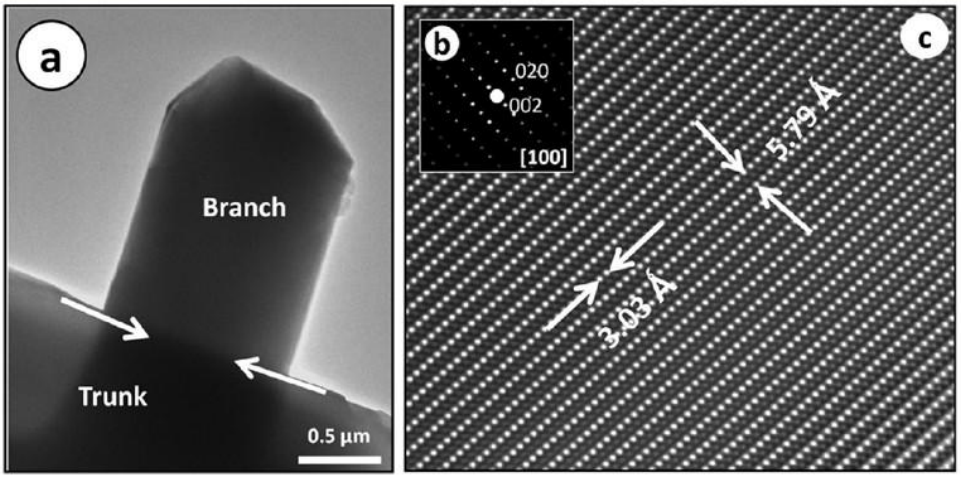

Figure 6. (a) Low magnification TEM image of a junction of a trunk and a branch in a branched structure.b SAED pattern along the [100] zone axis and (c) and the corresponding HRTEM micrograph.

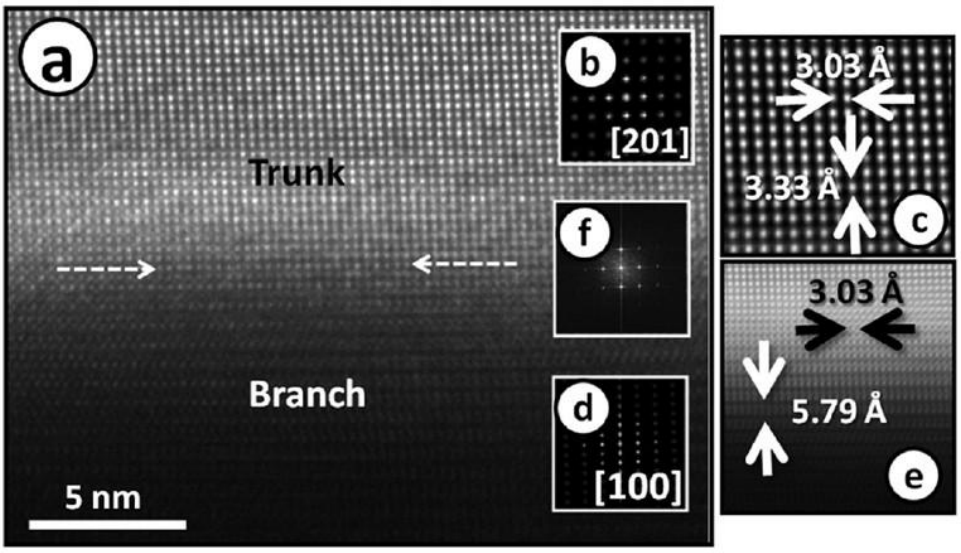

Figure 7. (a) HRTEM image of the interface region marked in Figure 6. (b) FFT pattern of the trunk along the [201] direction (c), and corresponding I-FFT. (d) FFT pattern along [100] direction of the branch and (e) corresponding I-FFT (e). At the interphase (marked by dashed arrows) the overlapping between both of the FFT patterns is seen in part f.

which is connected by GaO_4 tetrahedra. It is well-known that Cr^{3+} ions in β-Ga_2O_3:Cr^{3+} replace the Ga^{3+} ions in oxygen octahedral sites[23] and the 350 cm^{-1} Raman peak was associated to octahedron modes.[20] Therefore, the inclusion of Cr as a dopant explains the appearance of the higher energy shoulder for the 350 cm^{-1} peak. Codoping with Sn and Cr also enhances the intensity ratio variation of the 651 and 657 cm^{-1} peaks, as observed in Figure 8e. The rest of the peaks present very slight differences in positions and fwhm.

X-ray photoelectron spectroscopy (XPS) technique with spatial resolution has also been applied to investigate the local electronic features of these branched structures, and the results are summarized in Figure 9. Energy axis in high resolution XPS spectra was calibrated by fixing the C 1s binding energy (BE) at 284.8 eV.[21] Figure 9a shows an XPS map representing the intensity of the Ga 3d line of a Sn doped structure, which is representative of the samples investigated. The corresponding XPS spectra of Ga 3d and Sn 4d core levels at two different points of the wire are shown in Figure 9b. The results confirm the presence of tin in the Ga_2O_3 nanowires. High resolution XPS spectra and their deconvolution into Gaussian components of Sn 3d and O 1s core levels from this structure are shown in Figure 9c,d. The Sn $3d_{5/2}$ and Sn $3d_{3/2}$ peaks are centered at 488.2 and 497.0 eV, respectively. A value of 486.6 eV has been assigned to Sn $3d_{5/2}$ peak for Sn^{4+} in SnO_2 host.[24,25] This value is slightly lower than our measured data which is due to the fact that the actual host for Sn atoms is Ga_2O_3. On the other hand, the binding energy of O 1s core level in oxides is usually very sensitive to variations in its chemical binding. In our case, we have found that the XPS spectra of the O 1s line can be decomposed into four peaks, centered at 531.2, 531.9, 532.7, and 533.4 eV. This reveals the

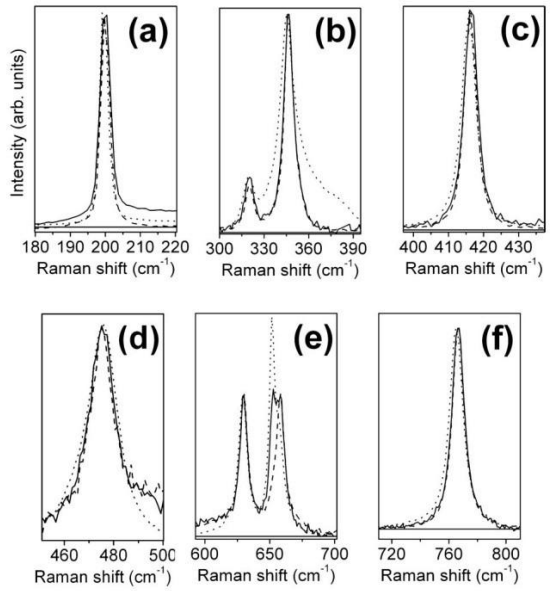

Figure 8. Comparison of the Raman peaks (normalized intensity) for undoped (---), Sn doped (—), and Cr, Sn codoped (···) nanostructures.

complexity in chemical bonds involving oxygen. In undoped Ga_2O_3, two peaks were found (531.88 and 533.45 eV) for O 1s core levels, which were assigned to Ga−O−Ga bonds and to the hydroxide (OH)/adsorbed oxygen $(O_2)^{2-}$ species, respectively.[21] They coincide with the second and the fourth components found in the Sn doped Ga_2O_3 branches. In addition, some of the oxygen atoms may be bonded to tin atoms. Values in the range 531.0−531.5 eV have been reported for the binding energy of O 1s peak in SnO_2[24,25] which enables us to assign the lower energy component at 531.2 eV peak (first component in our spectrum) to Sn−O bond. Finally, the third component at 532.7 eV could be related to some impurities in the surface. Therefore, XPS results show that Sn atoms have been effectively incorporated into the oxide matrix and participate in the chemical bonding.

After the codoping process, the XPS analysis does not reveal either Cr (e.g., Cr 3p with BE ≈ 44 eV or 3s with BE ≈ 77 eV[25]) or Sn core levels energies, indicating a very low concentration of these elements on the surface of the structures. However, differences with respect to the Sn doped sample occur. Figure 9e shows the high resolution XPS spectrum of the O 1s peak, for a Cr, Sn codoped wire, with a complex structure. Besides the binding energy components (531.3, 531.9, 532.6, and 533.5 eV) observed for Sn doped wires, two additional components seem to be necessary to fit experimental data with binding energies of 529.6 and 530.2 eV, which could be assigned to O 1s in Cr_2O_3 or in SnO.[25]

Codoping with Sn and Cr is obtained during the second thermal treatment, using the branched structures as starting material as detailed in the Experimental Section. Due to the fact that XPS is surface sensitive, these results indicate that the amount of Sn close to the surface of these samples is below the detection limit of this technique. This can be due to the fact that during the Cr diffusion process no extra tin was incorporated into the furnace. On the other hand, we have previously shown[5,16] that Cr is incorporated into the nanowires by the thermal diffusion process used in this work. This is further confirmed by the luminescence results shown below. The fact that Cr is not observed by XPS indicates that, close to the surface, the concentration is too low to be detected by this technique.

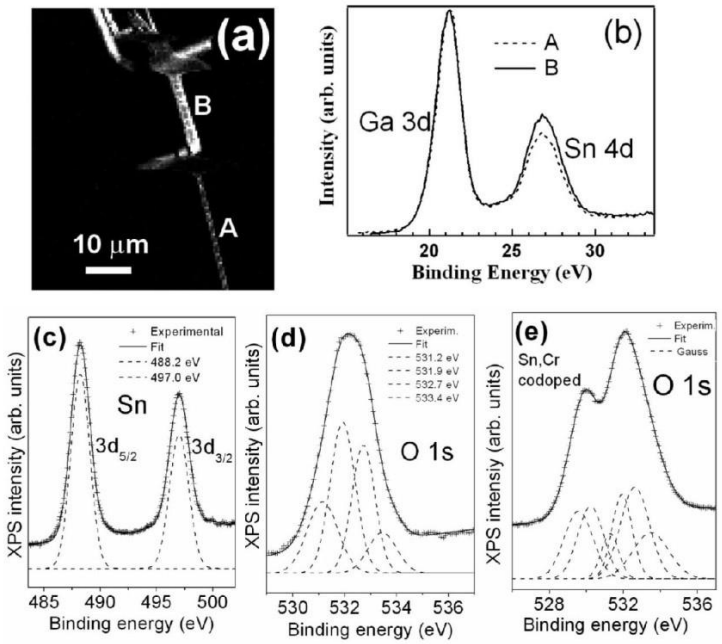

Figure 9. (a) XPS Ga 3d map. (b) Ga 3d and Sn 4d, (c) Sn 3d, and (d) O 1s spectra from a Ga_2O_3:Sn wire. (e) O 1s spectra from Ga_2O_3:Sn,Cr nanowire.

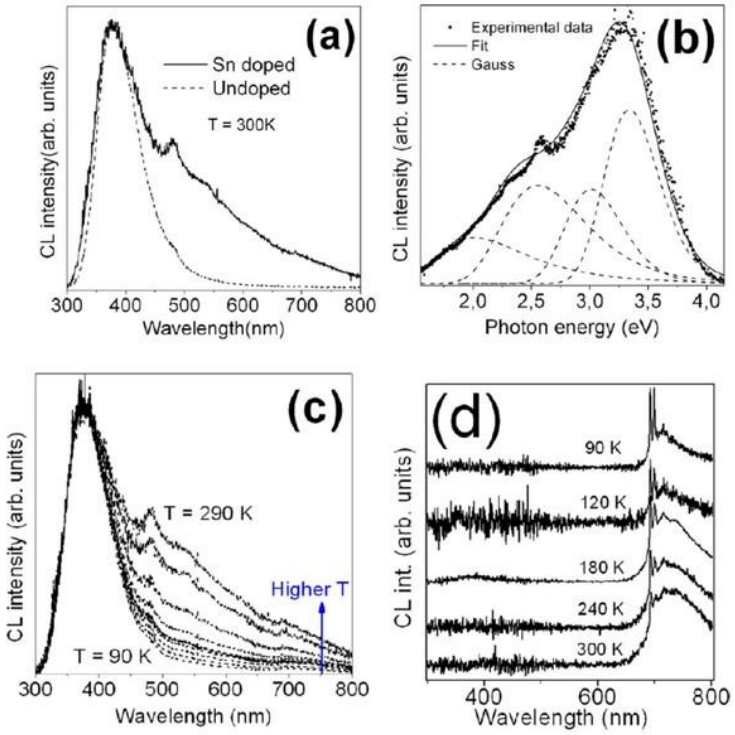

Figure 10. (a) CL spectra at RT from Sn doped sample and undoped β-Ga_2O_3 sample. (b) Detail of the composed bands in Sn doped Ga_2O_3 structures. (c) Temperature evolution of the CL emission from the Sn doped sample and (d) temperature evolution from the Sn−Cr codoped sample.

3.3. Influence of Doping on Luminescence Properties of Branched Structures. Although the main impact of Sn impurities during the growth of Ga_2O_3 nanowires seems to be connected with morphology and shape features leading to the formation of branched wires, an effective doping of these wires is also achieved during the growth process. The concentration of tin has been detected by XPS and EDS in TEM. As these structures could be used as templates for optical applications as we will show below, the characterization of their luminescence properties is worth doing. We have assessed the effect of Sn doping in the optical properties of Ga_2O_3 branched structures by cathodoluminescence (CL) in the SEM. Figure 10a plots the room temperature (RT) CL spectrum from a bunch of Sn doped nanowires. A CL spectrum from undoped nanowires is also included for comparison. In spite of the low Sn concentration in the wires, a broad band in the whole visible range is observed, in clear contrast with the undoped wires, in which a narrower characteristic β-Ga_2O_3 UV-blue emission is obtained.[26] Figure 10b shows the Gaussian deconvolution of the CL spectrum shown in Figure 10a, with three main components centered at 2.4, 3.1, and 3.4 eV. The 3.1 and 3.4 eV bands are well-known in β-Ga_2O_3 and have been assigned to intrinsic defects, such as oxygen vacancies, or some very low concentration of impurities.[7,26] The green band (2.4 eV) would be related to the presence of Sn in the wires which agrees with some previous reports. In particular, Miyata et al. obtained by electroluminescence in Sn doped Ga_2O_3 films a similar broad emission with a main peak at around 450 nm and a shoulder with its maximum in the green region,[13] which resembles the spectrum observed by CL in our experiments. Maximenko et al. have also reported a broad visible emission in Sn doped Ga_2O_3 nanowires with a main peak at around 400 nm with a shoulder in the green region,[10] which they attribute to recombination between donor levels, introduced by the incorporation of Sn atoms, and holes at the valence band in Ga_2O_3. Figure 10c shows the temperature evolution of the luminescence of Sn-doped nanowires, from 90 K to room temperature. The interesting feature observed is the quenching of the green band when the temperature decreases, so that at low temperature the CL spectrum is only composed by the characteristic bands of undoped β-Ga_2O_3 at T = 90 K. This result seems to indicate a thermally activated (phonon assisted) transition to promote carriers to the Sn-related emitting center level, or a faster increase of the intensity of the rest of the components at lower temperatures. Figure 10d shows the CL spectra of the Sn and Cr codoped sample at different temperatures. In this case, the dominant band corresponds to the red band related to Cr ions while other emissions previously observed in the Sn doped wires are completely quenched. This strong red emission is due to the characteristic Cr^{3+} R lines and phonon assisted $^4T_2 - {}^4A_2$ band.[16] The evolution with temperature is the expected one for the competition between the R lines and the broad $^4T_2-{}^4A_2$ band.[16]

These results show the high quantum efficiency of Cr ions' emission, even at room temperature, in gallium oxide hosts, which led to the quenching of the green and the violet-blue emissions which are in competition with the Cr^{3+} intraionic transition. The very high efficiency of Cr ions quenches the radiative transitions between energy levels related to native defects in Ga_2O_3.

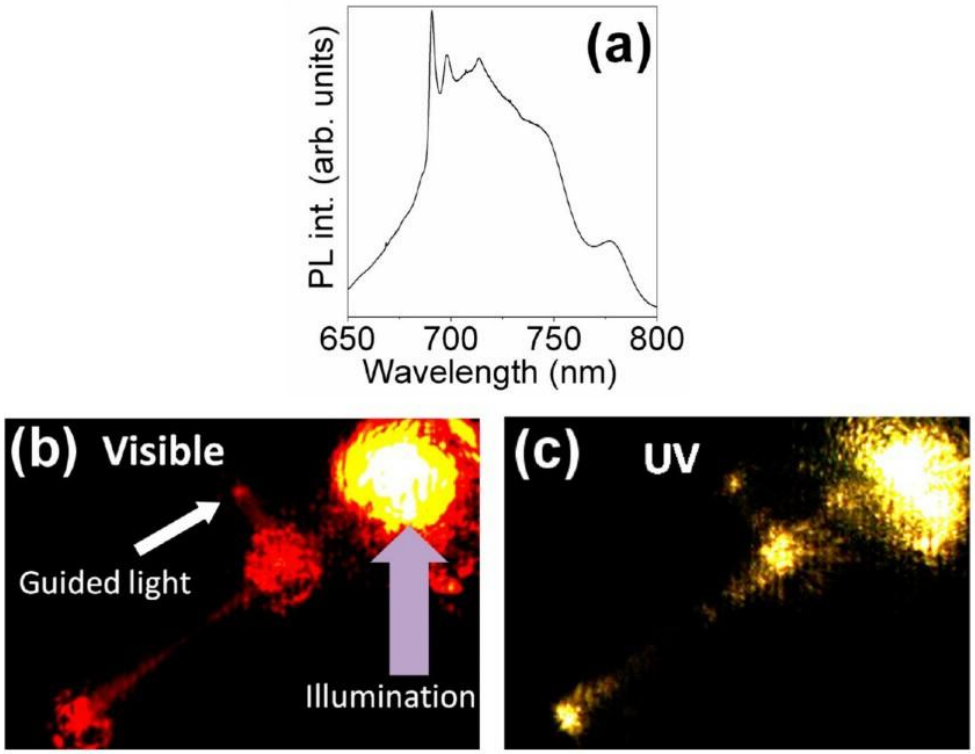

Figure 11. (a) PL spectrum from the branched wire shown in Figure 5b. (b) Room temperature μ-PL with a 325 nm HeCd laser line excitation of the same branched structure. (c) UV radiation bright field image.

We have used the codoped samples to study the propagation that the red light generated by Cr ions follows through these branched structures. Figure 11a shows the micro-PL spectrum from the Sn, Cr codoped wire shown in Figure 5b. In this case, the 325 nm (3.82 eV) HeCd laser line of the confocal microscope produces below band gap excitation, and strong red emission due to the Cr^{3+} intraionic transitions is observed. Excitation of the Cr^{3+} is indeed obtained through the excitation band centered at around 3.9 eV present for this ion in β-Ga_2O_3.[16] Figure 11b shows the corresponding visible μ-PL image of the wire. Under illumination with the laser at the upper end of the wire (violet arrow), the intense luminescence created is guided along the trunk and also transmitted through the perpendicular branch, as is clearly seen in the bright red spot highlighted with a white arrow in Figure 11b. UV laser radiation is also guided along the trunk and branch, as seen in Figure 11c for the 325 nm line of the laser.

As shown in the CL spectra, the luminescence of β-Ga_2O_3 nanowires covers the whole visible range, and the emission wavelength can be adjusted by properly selecting the kind and concentration of dopants. In fact, doping of these branched structures with other optically active ions in order to obtain luminescence from the UV to the IR is possible by other doping methods such as ion implantation.[27] Besides, the branched morphology can be very useful for some specific applications such as photonic routers and beam splitters.[19,28,29] Besides, resonant modes have been found within these structures.[30]

■ CONCLUSIONS

Elongated Sn doped gallium oxide structures have been obtained through a thermal evaporation method. The presence of Sn leads to the formation of branches. In a further thermal step, the branched structures have been codoped also with Cr. The crystal quality has been found to be very high by TEM–HRTEM analysis, and the mechanisms for the formation of the branches have been discussed, finding epitaxial growth as one of them. The presence of Sn and Cr within these structures does not strongly influence the vibrational properties, as analyzed by Raman microspectroscopy. Luminescence in the whole visible range is obtained by codoping with Sn and Cr. For the first dopant, a broad emission covering most of the visible range is observed by CL, with strong peaks in the UV-blue and green ranges. When codoping with chromium, the luminescence is virtually composed exclusively by the intense red band characteristic of Cr^{3+} in this oxide. Branched, Sn, Cr codoped structures behave as efficient waveguides along their trunks and branches, both for the UV and visible light, as observed with microphotoluminescence imaging.

■ AUTHOR INFORMATION

Corresponding Author

*E-mail: emilio.nogales@fis.ucm.es.

Notes

The authors declare no competing financial interest.

■ ACKNOWLEDGMENTS

This work has been supported by MICINN through Projects MAT 2009-07882 and Consolider Ingenio CSD 2009-00013.

The authors are grateful to Dr. Luca Gregoratti at the Sincrotrone Elettra Trieste for useful advice on XPS measurements.

REFERENCES

(1) Barth, S.; Hernandez-Ramirez, F.; Holmes, J. D.; Romano-Rodriguez, A. *Prog. Mater. Sci.* **2010**, *55*, 563−627.
(2) Lu, J. G.; Chang, P.; Fan, Z. *Mater. Sci. Eng., R* **2006**, *52*, 49−91.
(3) Feng, P.; Zhang, J. Y.; Li, Q. H.; Wang, T. H. *Appl. Phys. Lett.* **2006**, *88*, 153107-1−153107-3.
(4) Vanithakumari, S. C.; Nanda, K. K. *Adv. Mater.* **2009**, *21*, 1−4.
(5) Nogales, E.; Garcia, J. A.; Mendez, B.; Piqueras, J. *Appl. Phys. Lett.* **2007**, *91*, 133108-1−133108-3.
(6) Nogales, E.; Mendez, B.; Piqueras, J. *Ultramicroscopy* **2011**, *111*, 1037−1042.
(7) Shimamura, K.; Víllora, E. G.; Ujiie, T.; Aoki, K. *Appl. Phys. Lett.* **2008**, *92*, 201914-1−201914-3.
(8) Varley, J. B.; Weber, J. R.; Janotti, A.; Van de Walle, C. G. *Appl. Phys. Lett.* **2010**, *97*, 142106-1−142106-3.
(9) Ronning, C.; Borschel, C.; Geburt, S.; Niepelt, R. *Mater. Sci. Eng., R* **2010**, *70*, 30−43.
(10) Maximenko, S. I.; Mazeina, L.; Picard, Y. N.; Freitas, J. A.; Bermudez, V. M.; Prokes, S. M. *Nano Lett.* **2009**, *9*, 3245−3251.
(11) Higashiwaki, M.; Sasaki, K.; Kuramata, A.; Masui, T.; Yamakoshi, S. *Appl. Phys. Lett.* **2012**, *100*, 013504−1−013504−3.
(12) Lopez, I.; Nogales, E.; Hidalgo, P.; Mendez, B.; Piqueras, J. *Phys. Status Solidi A* **2012**, *209*, 113−117.
(13) Miyata, T.; Nakatani, T.; Minami, T. *J. Lumin.* **2000**, *87*−*89*, 1183−1185.
(14) Nogales, E.; Mendez, B.; Piqueras, J.; Garcıa, J. A. *Nanotechnology* **2009**, *20*, 115201-1−115201-5.
(15) Wang, J.; Zhuang, H.; Zhang, X.; Zhang, S.; Li, J. *Vacuum* **2011**, *85*, 802−805.
(16) Nogales, E.; Garcia, J. A.; Mendez, B.; Piqueras, J. *J. Appl. Phys.* **2007**, *101*, 033517-1−033517-4.
(17) Hidalgo, P.; Mendez, B.; Piqueras, J. *Nanotechnology* **2008**, *19*, 455705−1−455705−5.
(18) Diaz, J.; Lopez, I.; Nogales, E.; Mendez, B.; Piqueras, J. *J. Nanopart. Res.* **2011**, *13*, 1833−1839.
(19) Zheng, J. Y.; Yan, Y.; Wang, X.; Zhao, Y. S.; Huang, J.; Yao, J. *J. Am. Chem. Soc.* **2012**, *134*, 2880−2883.
(20) Dohy, D.; Lucazeau, G.; Revcolevschi, A. *J. Solid State Chem.* **1982**, *45*, 180−192.
(21) López, I.; Utrilla, A. D.; Nogales, E.; Mendez, B.; Piqueras, J.; Peche, A.; Ramirez-Castellanos, J.; Gonzalez-Calbet, J. M. *J. Phys. Chem. C* **2012**, *116*, 3935−3943.
(22) *Raman Scattering in Materials Science*; Weber, W. H., Merlin, R., Eds.; Springer: New York, 2010.
(23) Yeom, T. H.; Kim, I. G.; Lee, S. H.; Choh, S. H.; Yu, Y. M. *J. Appl. Phys.* **2003**, *93*, 3315−3319.
(24) Kwoka, M.; Ottaviano, L.; Passacantando, M.; Santucci, S.; Czempik, G.; Szuber, J. *Thin Solid Films* **2005**, *490*, 36−42.
(25) http://srdata.nist.gov/xps
(26) Binet, L.; Gourier, D. *J. Phys. Chem. Solids* **1998**, *59*, 1241−1249.
(27) Nogales, E.; Hidalgo, P.; Lorenz, K.; Mendez, B.; Piqueras, J.; Alves, E. *Nanotechnology* **2011**, *22*, 285706-1−285706-7.
(28) Mieszawska, A. J.; Jalilian, R.; Sumanasekera, G. U.; Zamborini, F. P. *Small* **2007**, *3*, 722−756.
(29) Kurt, H.; Giden, I. H.; Citrin, D. S. *Opt. Express* **2011**, *19*, 26827−26838.
(30) López, I.; Nogales, E.; Mendez, B.; Piqueras, J. *Appl. Phys. Lett.* **2012**, *100*, 261910−1−261910−3.

CAPÍTULO V. ÓXIDOS DE LA SERIE HOMÓLOGA $In_2Zn_kO_{3+k}$

1. INTRODUCCION

Los óxidos de estaño e indio (conocidos como *indium tin oxides, ITO*) son los materiales TCO que mejores propiedades presentan actualmente. Sin embargo, la escasez de indio y, por tanto, su elevado coste hacen necesaria la búsqueda de nuevos materiales TCO, que se consoliden como alternativas más viables económicamente. Entre ellas, cabe resaltar el empleo de óxido de zinc, ZnO, un material barato, abundante y no tóxico, con una resistividad comparable a la que presentan los ITO. En este sentido, se han estudiado los óxidos de zinc dopados con indio para mejorar las propiedades optoelectrónicas.

Cuando se preparan óxidos mixtos de zinc e indio se observa que, para bajas concentraciones de indio, los cationes In^{3+} ocupan posiciones del Zn^{2+} de la estructura tipo wurtzita, dando lugar a disoluciones sólidas [1, 2]. Sin embargo, para concentraciones superiores de In, aparecen nuevas estructuras. A finales de la década de los 60, H. Kasper [3, 4] describió la preparación y caracterización estructural de estos óxidos, de fórmula general $Zn_kIn_2O_{k+3}$, con $2<k<7$. Los distintos términos de la serie se obtuvieron por el método cerámico al reaccionar cantidades estequiométricas de ZnO con In_2O_3 a elevadas temperaturas. Estas estructuras complejas con mayor concentración de indio, pueden describirse como intercrecimientos ordenados de ambos óxidos, donde bloques de ZnO, perpendiculares al eje *c* hexagonal, alternan ordenadamente con capas de In_2O_3. Esto da lugar a una serie homóloga, que denominaremos IZO, de simetría hexagonal o romboédrica, caracterizada por presentar un eje c largo y parámetro *a* similar al de la wurtzita. El primer estudio mediante difracción de electrones y microscopia electrónica fue realizado por P.J. Cannard y R. J. D. Tilley [5], que describieron la estructura como bloques de ZnO separados por faltas de apilamiento basadas en In_2O_3. Estos autores propusieron un modelo donde definían estas faltas como dos planos {111} de In_2O_3 ordenados, que dan lugar a una serie homóloga de nuevas fases. Estas nuevas fases, con fórmula general $Zn_kIn_2O_{3+k}$, cristalizan en celdas hexagonales y se describen como un intercrecimiento periódico de una capa pura de $InO2^-$ de estructura bixbyita en una matriz $In_{1/(k+1)}Zn_{k/(k+1)}O_{1/(k+1)}^+$ de tipo wurtzita (*figura 1*).

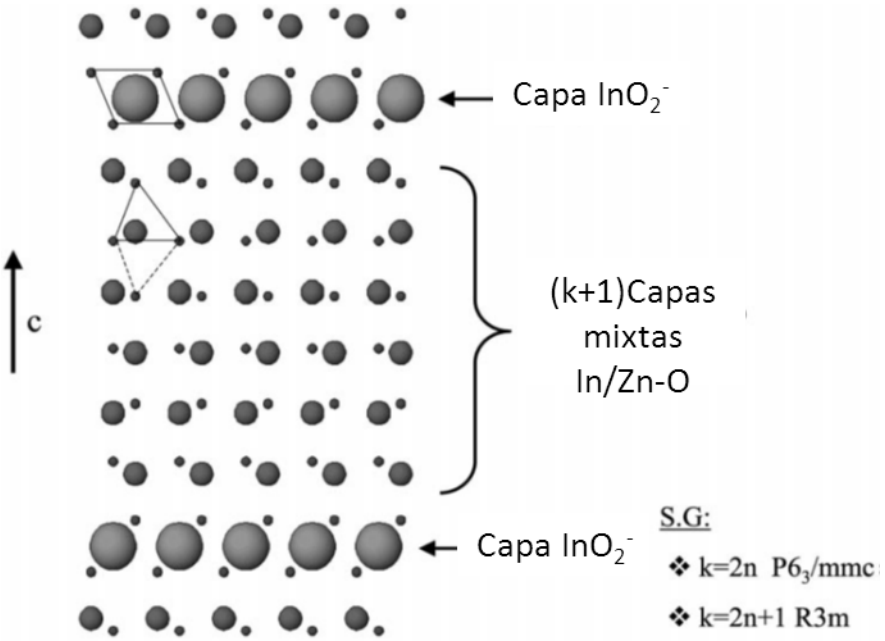

Figura 1. Estructura en capas del politipo ZnkIn2Ok+3 a lo largo del eje de zona [010].

La estructura se caracteriza por un eje *a* corto, similar al de la wurtzita y casi invariable con *k*, y un eje *c* largo cuyo valor depende tanto de las *k+1* capas de Zn/In entre dos capas puras de indio como del grupo espacial.

Estructura Electrónica y Propiedades

Los materiales TCO se caracterizan por su elevada conductividad eléctrica (>1000 S/cm) y su elevada transmisión de fotones en el visible (>80%) [6]. La conductividad eléctrica está relacionada con la estructura de bandas, mientras que la transparencia depende del intervalo de energía prohibida, las reglas de selección de transiciones ópticas y la concentración de portadores [7].

Como se observa en la *figura 2,* el In_2O_3 posee la banda de conducción más baja (mayor afinidad electrónica), por lo que puede soportar elevadas concentraciones de portadores de carga (electrones), lo que da lugar a una conducción eléctrica degenerada. En los IZO, la banda de valencia se encuentra fundamentalmente localizada en la red Zn-O (compuesta por la banda *d* del Zn hibridada con la *p* del O), y la de conducción viene determinada principalmente por la red de In-O (contribuyen orbitales *s* de Zn, In y O) [8].

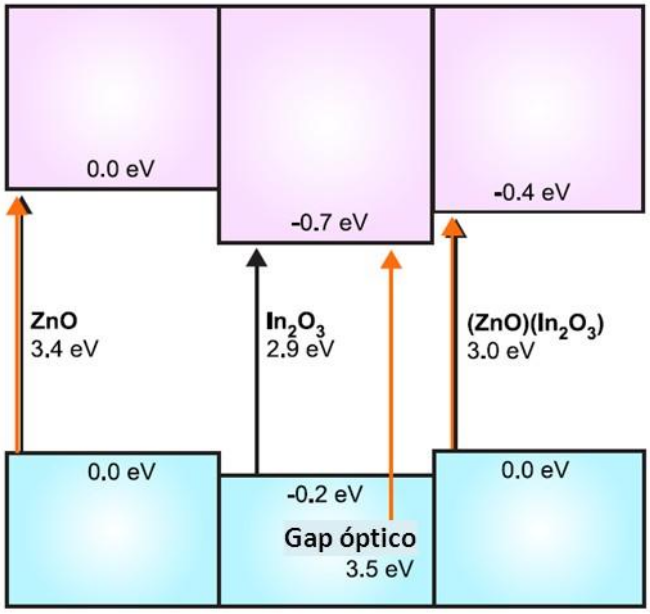

Figura 2. Estructura de bandas para ZnO, In2O3 y (ZnO)(In2O3).

Las fases de esta serie homóloga presentan un comportamiento semiconductor de tipo *n* intrínseco, igual que el ZnO y el In_2O_3. Su conductividad eléctrica disminuye al aumentar *k*, ya que disminuye el número de portadores de carga y la movilidad de los mismos [9]. Sin embargo, el rango óptico de energías prohibidas y la transparencia en el visible de estos materiales aumenta con el valor de *k*, además de tener permitidas las transiciones ópticas dipolo-dipolo por simetría para todos los términos. Esta dependencia de las propiedades con respecto al valor de *k*, resumida en la *figura 3*, se debe principalmente a la estructura electrónica de cada término que, a su vez, depende enormemente de la estructura cristalina del material [10].

Hay que resaltar que, además de sus propiedades como TCO, la serie homóloga y, en especial, los términos de mayor *k*, poseen interesantes propiedades termoeléctricas para la producción energética. Estos óxidos presentan una excelente estabilidad química y estructural a alta temperatura. Su estructura laminar, que produce una reducción de la conductividad térmica, les hace aún más adecuados para este propósito [11].

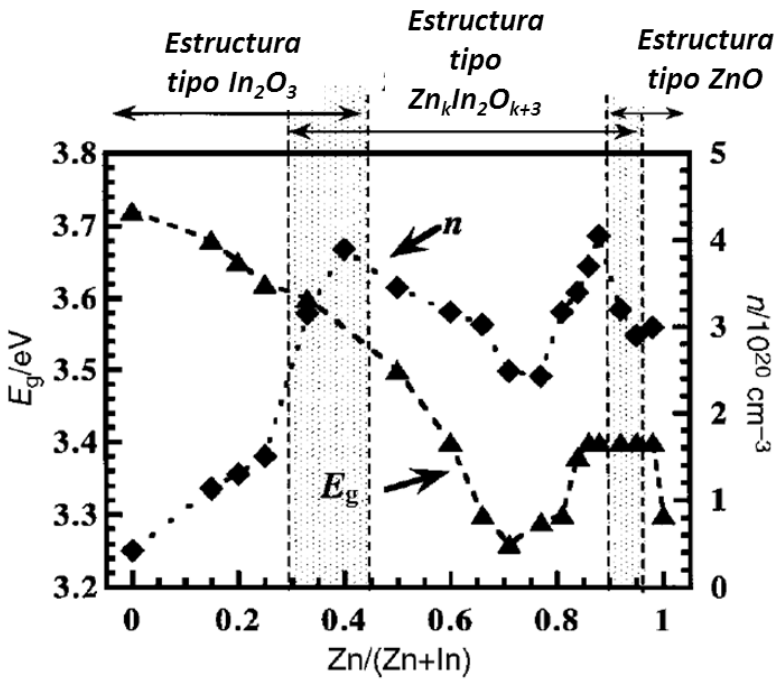

Figura 3. Variación del número de portadores (n) e intervalo de energía prohibida (Eg) en función de la composición del IZO.

El comportamiento de estos materiales obviamente depende de la concentración de portadores de carga. En este sentido, entre los estudios dirigidos a determinar los mecanismos que gobiernan la variación de la conductividad en la serie homóloga, se describen dos mecanismos de creación de defectos en función de la relación In/Zn: para valores de k bajos, predominan los defectos de átomos de Indio en posiciones antisitio (un átomo de indio ocupando una posición del Zn en la red (In_{Zn}^{+}) y para valores de *k* mayores, los defectos predominantes son vacantes oxígeno (V_o). El primero es el candidato más probable de ser el productor de portadores de carga intrínsecos tipo *n*, debido a su nivel energético poco profundo, mientras que las V_o tienden a no liberar los electrones.

Teniendo en cuenta estas consideraciones, se ha realizado la síntesis de los términos de la serie homóloga $In_2Zn_kO_{3+k}$, con *k*=3-6, 7, 9, 11 y 13, con un control exhaustivo de las condiciones de síntesis, con objeto de obtener materiales monofásicos. Se realiza la caracterización estructural y microestructural que permita establecer la relación entre la estructura y las propiedades del material. Uno de los principales retos es elucidar el origen de la modulación que se produce en el seno de los bloques estructurales de In/ZnO mediante el empleo de técnicas microscópicas con resolución atómica.

2. PREPARACIÓN DE MATERIALES

El diagrama de fases In_2O_3-ZnO, recogido en la *figura 4*, fue establecido por primera vez por Moriga y col. [9]. Se puede observar la presencia de regiones bifásicas, aunque existe una disolución sólida, en el margen de composición 0-0.45% at en In a 1200 °C [2]. Teniendo en cuenta esta información, hemos llevado a cabo la preparación de los términos $3 \leq k \leq 13$ de la serie homóloga $Zn_kIn_2O_{k+3}$. Todas las muestras se han sintetizado por reacción en estado sólido partiendo de la mezcla estequiométrica de los reactivos ZnO (*Aldrich*, 99,99%) e In_2O_3 (*Aldrich*, 99,99%), según la reacción:

$$k\ ZnO + In_2O_3 \rightarrow In_2Zn_kO_{3+k}$$

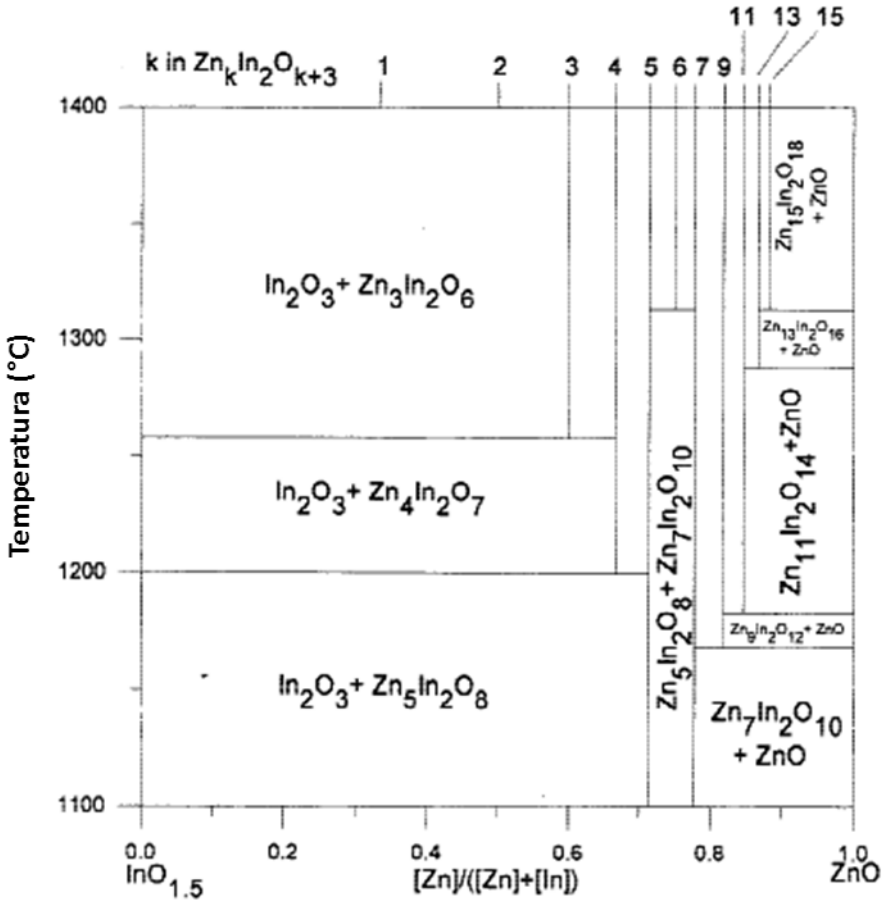

Figura 4.- Diagrama de fases para el sistema In_2O_3-ZnO en el margen de temperatura 1200-1400 °C.

Los reactivos se mezclan en mortero de ágata, para después ser empastillados. Con objeto de evitar la contaminación de las muestras y limitar la pérdida de Zn por volatilización a alta temperatura, se cubren las pastillas con un ligero exceso de mezcla de la misma composición, evitando la formación de fases con contenidos inferiores de zinc.

Se realizaron diferentes tratamientos térmicos para la síntesis de los distintos términos de la serie homóloga. En primer lugar, se realizó un tratamiento a 1400 °C de todos los términos ya que, como se observa en el diagrama de fases de la *figura 4*, todos los términos son estables a dicha temperatura. Sin embargo, en estas condiciones de síntesis, la mayoría de términos se descomponen o dan lugar a mezclas de fases. Teniendo en cuenta estos resultados, cada término se preparó a la temperatura más baja dentro de su margen de estabilidad. Todos los tratamientos térmicos realizados hasta obtener el material monofásico son acumulativos. En todos los casos, se realizaron moliendas y empastillados intermedios. El enfriamiento de los materiales se realizó mediante "*quenching*" desde alta temperatura a temperatura ambiente. Las composiciones preparadas, los tratamientos térmicos realizados, así como las fases identificadas mediante difracción de rayos X, se detallan en la tabla I.

Tabla I: Tratamientos térmicos realizados.

Tratamiento	Temperatura (°C)	Tiempo (h)	Fases	Observaciones
1	1000	24	In_2O_3+ ZnO	Descarbonatación de reactivos
2A	1200	24x5	$In_2Zn_4O_7$	Monofases
			$In_2Zn_9O_{11}$	
			$In_2Zn_{11}O_{14}$	
2B	1300	24x4	$In_2Zn_3O_6$	
			$In_2Zn_6O_9$	
			$In_2Zn_{13}O_{16}$	
2C	1400	24x3	$In_2Zn_5O_8$	
			$In_2Zn_7O_{10}$	

Los resultados obtenidos indican que la disminución de la temperatura precisa tiempos de reacción más largos, hasta la obtención de materiales monofásicos, como cabe esperar en este tipo de síntesis.

3. CARACTERIZACIÓN ESTRUCTURAL Y MICROESTRUCTURAL

Consideraciones estructurales

El In_2O_3 cristaliza en el tipo estructural bixbyita (a=10.117 Å; S.G: Ia-3) que se puede describir a partir de la estructura tipo fluorita, CaF_2, como un empaquetamiento compacto incompleto de átomos de oxígeno. Los átomos de Indio ocupan las posiciones octaédricas de calcio, mientras que los oxígenos ocupan ¾ de las posiciones aniónicas (*figura 5a*). En la bixbyita, cada plano {111} contiene ambos tipos de átomos, con una composición $InO_{1.5}$ por capa. El ZnO cristaliza en la estructura wurtzita (a=3.249, c=5.206Å; S.G: $P6_3mc$), que se describe como un empaquetamiento hexagonal compacto de oxígeno (*figura 5b*) con la mitad de posiciones tetraédricas ocupadas por átomos metálicos. Los átomos metálicos y los iones oxígeno se encuentran en planos separados, cada uno ocupando planos {001} alternos [12].

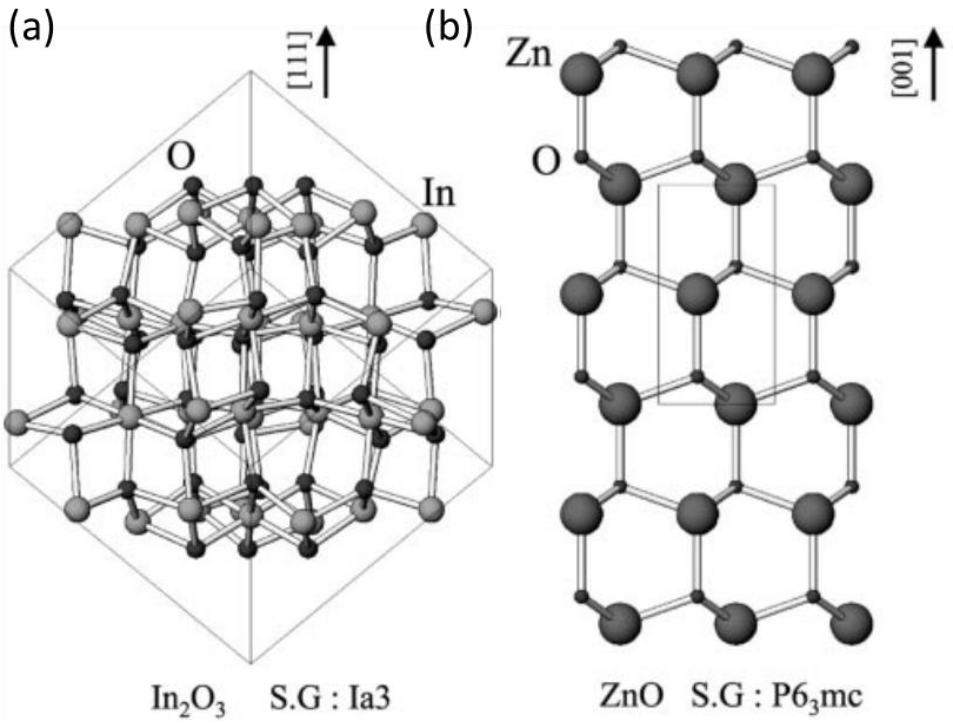

Figura 5. a) Proyección [11-2] de la estructura bixbyita del In_2O_3; b) estructura tipo wurtzita del ZnO a lo largo de [100].

Por lo tanto, de acuerdo con la descripción de Cannard y Tilley [5], cada falta de apilamiento que separa *k* bloques de ZnO aporta un bloque In_2O_3, de forma que cada miembro de la serie tiene una composición $Zn_kIn_2O_{3+k}$ y las capas mantienen la siguiente relación estructural

$$[111]\ In_2O_3\ (\text{tipo C})//[001]_{hex}\ ZnO\ (\text{wurtzita})$$

En la doble capa descrita por los autores existen dos posiciones no equivalentes para el indio: en coordinación octaédrica y en coordinación de bipirámide trigonal. Además, la presencia del indio crea un desplazamiento de 1/3{10-10} entre bloques de ZnO a ambos lados de la doble capa de óxido de indio.

Kimizuka [13,14] y Nakamura [15-17], mediante microscopía electrónica de transmisión de diversos sistemas ternarios que contenían el binario In_2O_3-ZnO, caracterizaron varios términos de la serie homóloga de acuerdo con la estructura descrita para $LuFeO_3(ZnO)_k$ (*k*= 1, 4-6) [18] e $InFeO_3(ZnO)_k$ (*k*=1-9) [19]. Estos autores propusieron un modelo estructural donde la variación en el apilamiento se originaba por un plano {111} de óxido de indio, que actúa como frontera de inversión de dominio (*inversion domain boundaries, IDB*) que, a su vez, separa dominios en los que la orientación de los tetraedros Zn-O es diferente.

Para confirmar la validez de estos modelos estructurales, M. A. McCoy y col. [20] examinaron las energías de estabilización de un intercrecimiento de defectos planos extensos ordenados de In_2O_3 en ZnO, de acuerdo con los modelos que se habían propuesto con anterioridad. Así mismo, para esclarecer la estructura de los defectos recurrieron a la simulación de imágenes HRTEM, concluyendo que la incorporación de indio se produce de acuerdo con el modelo propuesto por Cannard y Tilley [5] para la serie $Zn_kIn_2O_{k+3}$ con *k*<4.

Por lo que se refiere a la simetría de la serie homóloga $Zn_kIn_2O_{k+3}$, el grupo espacial es R-3m para valores impares de *k* y $P6_3/mmc$, para *k* pares. Esta variación en el grupo espacial se puede explicar fácilmente en términos de empaquetamiento cúbico (*c*) o hexagonal (*h*) de las capas. En el caso de *k* impar, la estructura se describe con un numero par de capas hexagonales $In_{1/(k+1)}Zn_{k/(k+1)}O^{1/(k+1)+}$ separadas por una capa InO_2^- de empaquetamiento cubico. Por tanto, la secuencia de empaquetamiento compacto será:

$$cc\ \{h\}_{k+1\ veces}\ cc$$

Y el empaquetamiento de las capas de oxígeno:

$$([AB]_{k+1\ veces}[CA]_{k+1\ veces}[BC]_{k+1\ veces})$$

Cabe destacar que para obtener la verdadera periodicidad es necesario considerar tres unidades estructurales básicas $\{InO_2^-/(k+1)(In_{1/k}Zn_{k/k+1})O^{1/(k+1)+})/InO_2^-\}$, ya que presenta

simetría trigonal. Por otro lado, cuando *k* es par la secuencia de empaquetamiento compacto es:

$$cc\ \{h\}_{k+1\ veces}\ cc$$

y el empaquetamiento de las capas de oxígeno es diferente:

$$([AB]_{k+1\ veces}\ A|C\ [BC]_{k+1\ veces})$$

En este caso la simetría es hexagonal y son necesarias solo dos unidades estructurales básicas para encontrar la verdadera periodicidad [21].

Esta relación es de gran utilidad para la identificación de los politipos mediante HRTEM. Para ello, se normaliza el eje largo, ***c***, dividiéndolo por el número de fórmulas por celda unidad, lo que proporciona la distancia entre dos capas consecutivas de indio (*figura 6*).

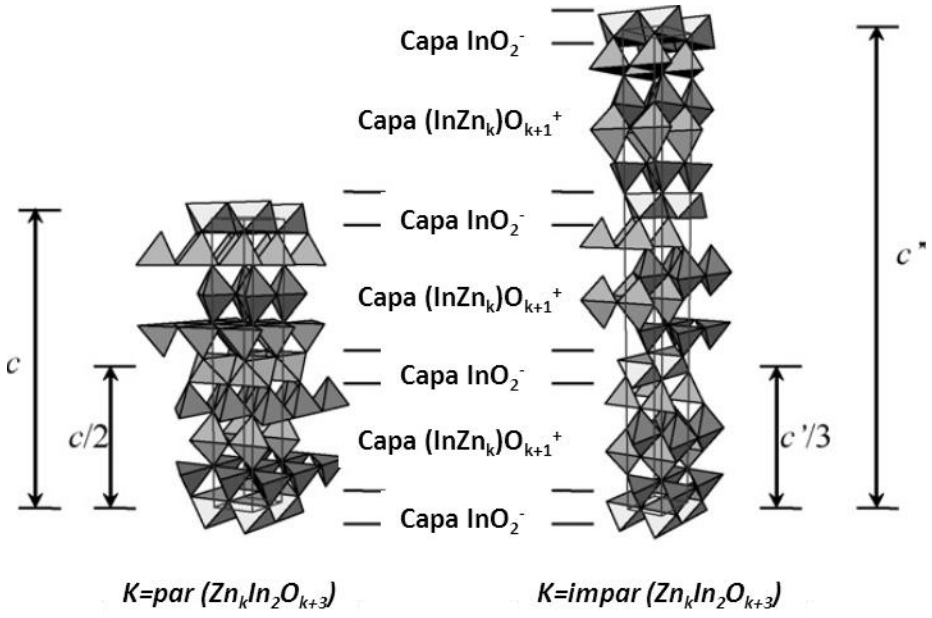

Figura 6.-Estructura cristalina para los términos con *k* par (a) e impar (b) de la serie homóloga $Zn_kIn_2O_{k+3}$.

La capa In-O, compuesta por octaedros InO_6^{3-} que comparten vértices, actúa como límite de inversión de dominio basal (*basal inversion domain boundaries, b-IDB*) [22] y su composición condiciona la periodicidad de las estructuras moduladas [23], ya que al dopar con otros cationes metálicos, el indio se mantiene preferentemente en las posiciones octaédricas, siendo los otros cationes, como por ejemplo el Fe, los que se encuentran en los bloques ZnO. La capa In/Zn-O posee un comportamiento más complejo. Como se ha mencionado previamente, existe una inversión de dominio en las capas de In-O, lo que hace que las polaridades de la capa wurtzita estén invertidas a cada lado de dicha capa.

Consecuentemente, las polaridades han de invertirse de nuevo en el seno de la capa In/Zn-O, o lo que es lo mismo, ha de existir otra inversión de dominio que cambie las polaridades. Existen varios modelos posibles que expliquen esta inversión: o bien la existencia de una capa extra de bipirámides trigonales paralela al plano basal en donde los átomos de Zn o In se encuentran penta-coordinados o bien que una modulación en zig-zag, con los átomos de In en coordinación de bipirámide trigonal que conlleve la inversión de dominios que reciben el nombre de límites piramidales de inversión de dominio (*pyramidal inversion domain boundaries, p-IDB*) [24].

Sobre la base de estas ideas y con objeto de establecer la relación entre la composición y los diferentes tipos de intercrecimientos que se obtienen y las propiedades de los términos a los que dan lugar se ha realizado un estudio por microscopia electrónica de alta resolución.

a) DIFRACCIÓN DE RAYOS X

Los diagramas de difracción de rayos X monocromáticos de los materiales (*figura 7*) se pueden asignar a una simetría hexagonal, con grupo espacial R-3m para aquellos términos con *k* impar, y $P6_3/mmc$ para *k* par [9].

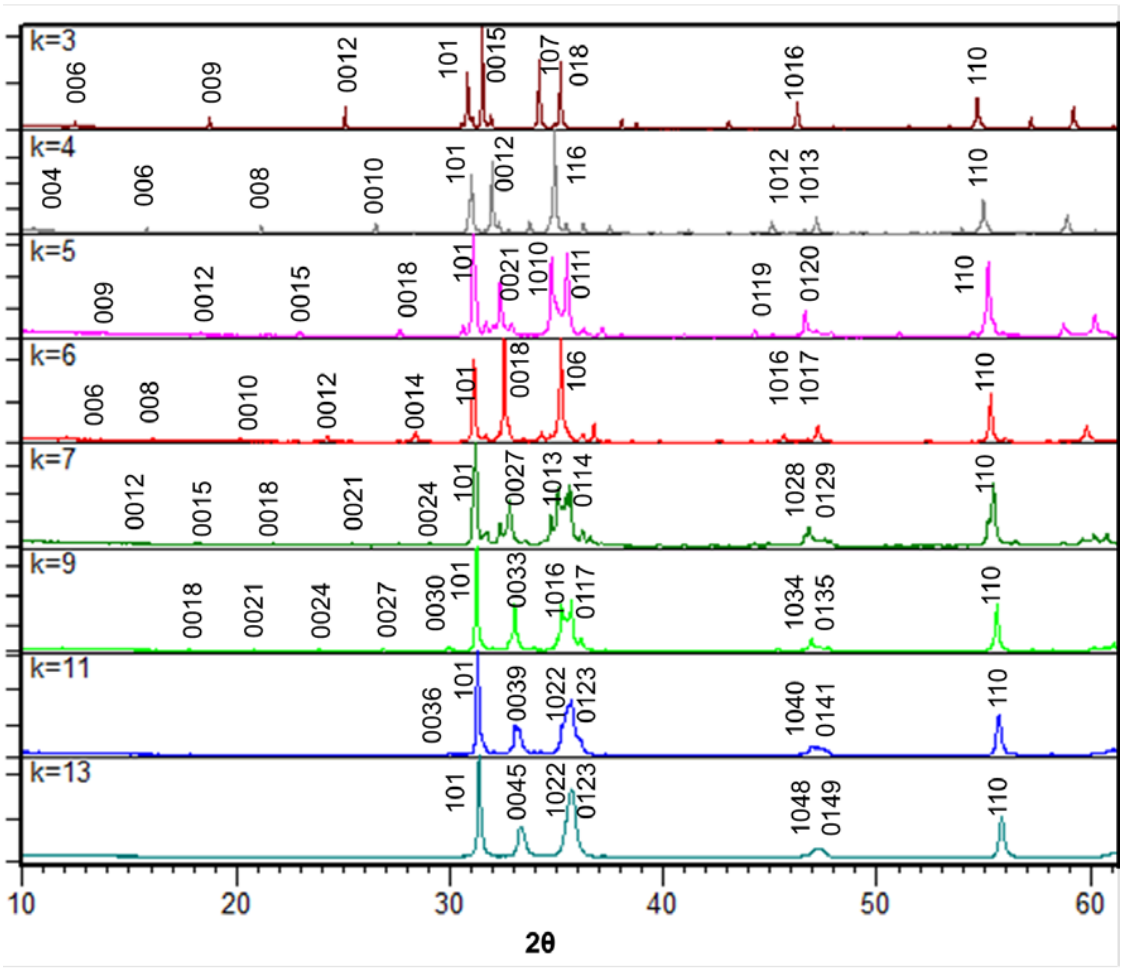

Figura 7. Diagramas de difracción de rayos X de las muestras IZO preparadas.

Puede observarse que para los términos superiores de la serie se produce un solapamiento de los máximos de difracción en el intervalo $32° \leq 2\theta \leq 40°$, dificultando la identificación inequívoca de los miembros sucesivos de la serie homóloga. Efectivamente, los datos publicados por Moriga y col. [9], recogidos en la *figura 8*, confirman la dificultad que existe para identificar con precisión si los términos de mayor *k* son monofásicos, o se trata de una mezcla de fases de diferentes *k*, que pudiera estar formada por el intercrecimiento desordenado de varios términos, defecto estructural muy habitual en las series homólogas.

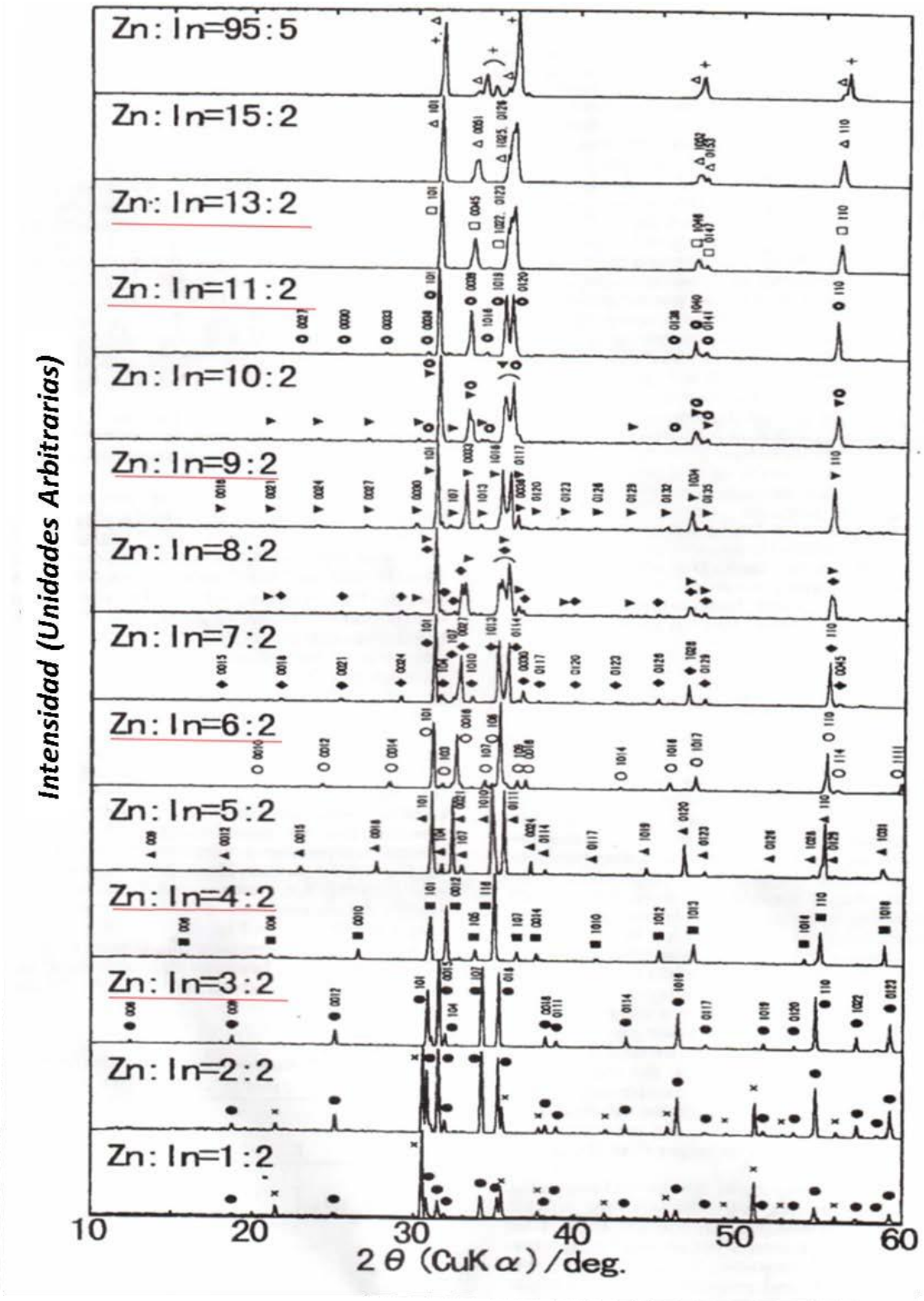

Figura 8.- Diagramas de difracción de rayos X para diferentes composiciones de ZnO-In2O3 a una temperatura de reacción de 1400 °C.

Los parámetros de red calculados a partir de los datos XRD para las muestras obtenidas se recogen en la *tabla II*.

Tabla II.-Parámetros de red obtenidos por XRD para cada fase aislada.

k	***Zn/(Zn+In) %at***	**Parámetros de red**		
		a (Å)	**c (Å)**	**c* (Å)= c/z**
3	0.60	3.44(3)	42.46(8)	14.15
4	0.66	3.33(6)	33.54(1)	16.77
5	0.71	3.32(8)	58.18(5)	19.39
6	0.75	3.31(7)	43.94(6)	21.97
7	0.77	3.31(6)	73.77(1)	24.59
9	0.81	3.29(6)	89.08(5)	29.69
11	0.84	3.28(6)	105.02(0)	35.00
13	0.86	3.14(7)	120.71(2)	40.23

Puede observarse que el valor del parámetro “a” disminuye ligeramente al aumentar el valor de *k*, de acuerdo con los datos recogidos en la literatura [9], lo que puede ser consecuencia de la influencia de los bloques de ZnO, que definen el parámetro “a” al aumentar el valor de *k*. Para poder comparar entre los distintos términos, se normaliza el parámetro “c”, dividiéndolo por el número de fórmulas unidad por celda unidad (*z*). De este modo, se obtiene el parámetro “*c**” normalizado, que equivale a la distancia entre planos consecutivos de InO1.5. Se observa que el parámetro “*c**” aumenta linealmente con el valor de *k*, un valor equivalente a un medio de la constante “*c*” de la estructura de ZnO (una capa Zn-O).

b) Espectroscopia de dispersión de energías (EDS)

Los espectros EDS proporcionan datos del contenido catiónico en % atómico, lo que permite calcular la fracción y, por tanto, establecer, en una primera aproximación, el término obtenido (*tabla III*).

Tabla III: Fracción *Zn/(Zn+In) %at* para distintos términos *k*

k	Teórico	Experimental (EDS)
3	0.60	0.61
4	0.66	0.67
5	0.71	0.70
6	0.75	0.76
7	0.77	0.77
9	0.81	0.80
11	0.84	0.83
13	0.86	0.85

Los datos obtenidos experimentalmente están de acuerdo con las composiciones nominales de los distintos términos de la serie homóloga. En la *figura 9* se muestra a modo de ejemplo los espectros correspondientes a los términos *k* = 3, 6 y 9.

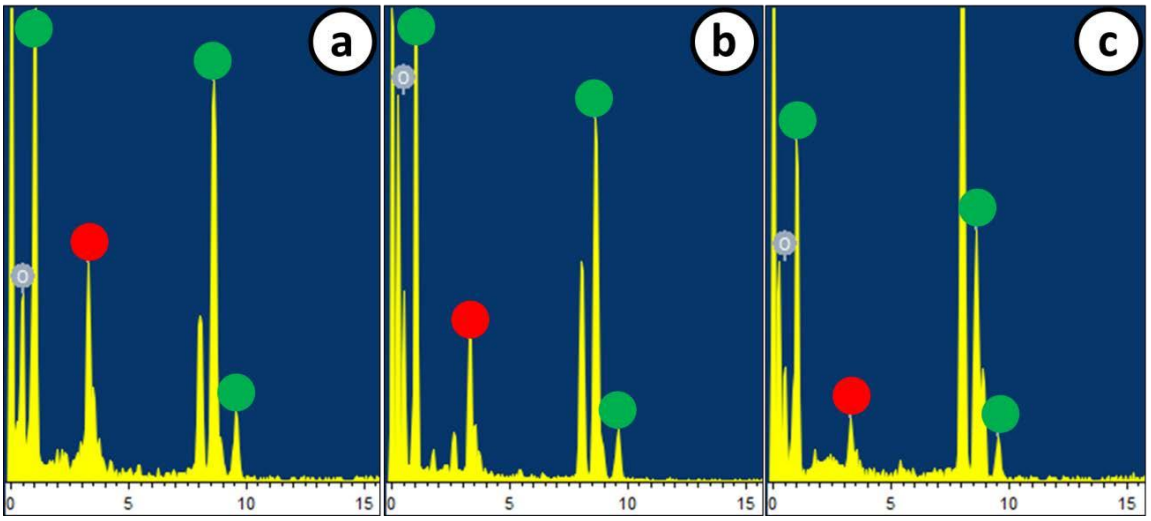

Figura 9. Espectros EDS de las muestras a) *k*=6, b) *k*=9, c) *k*=13. (●) In, (●) Zn

c) DIFRACCIÓN DE ELECRONES DE AREA SELECCIONADA (SAED) Y MICROSCOPÍA ELECTRÓNICA DE ALTA RESOLUCIÓN (HRTEM).

La difracción de rayos X proporciona información estructural "media" del conjunto del material, donde las fases se caracterizan por unos parámetros reticulares promedio y, por tanto, no proporciona toda la información necesaria para la caracterización estructural del material. Por otro lado, la microscopia electrónica de alta resolución permite observar los defectos estructurales que pueden ocurrir en un cristal del material masivo, e identificar los términos concretos obtenidos, por lo que resulta imprescindible para el estudio de estas fases.

Las imágenes obtenidas ponen de manifiesto que los materiales son aparentemente ordenados, sin que se aprecie la presencia de defectos extensos. En la *figura 10a* se muestra el diagrama SAED a lo largo del eje de zona [001] de la estructura hexagonal (plano basal,) del término *k*=3 de la serie homóloga. En la imagen HRTEM correspondiente (*figura 10b)* se indica la celda unidad hexagonal, común a todos los términos de la serie y se indica el parámetro reticular "**a**" de la estructura. Efectivamente, dada la relación cristalográfica existente entre las estructuras de ZnO y In_2O_3, el plano basal de las estructuras IZO es equivalente al plano basal de la wurtzita, siendo común para todos los términos de la serie, independientemente del número entero *k*.

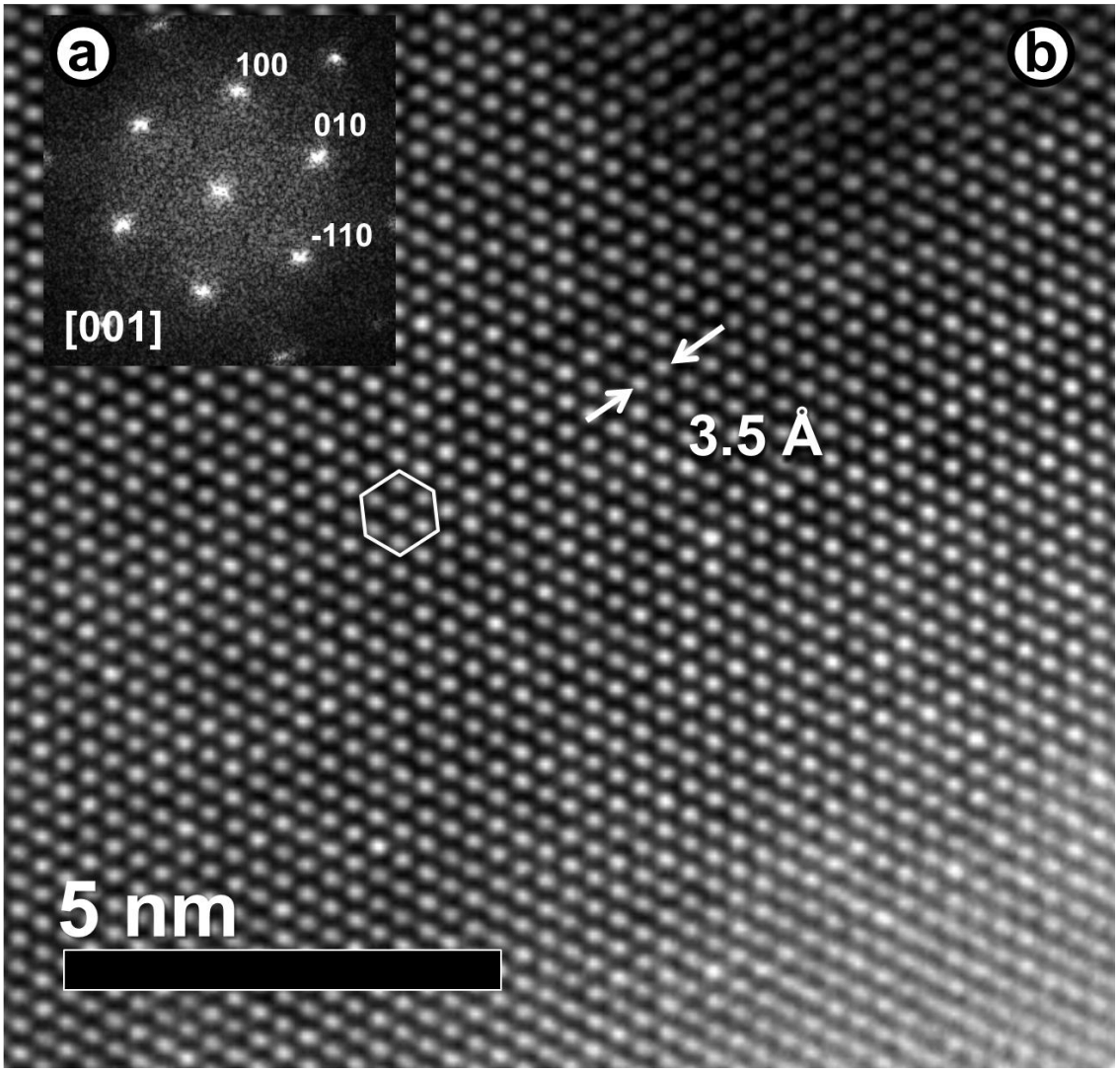

Figura 10. a) Diagrama SAED a lo largo del eje de zona [001] b) imagen HRTEM correspondiente, del término *k*=3.

A partir de esta información es necesario el estudio de las proyecciones que contengan la contribución del parámetro *c* para una correcta caracterización estructural.

En la *figura 11a* se observa el diagrama SAED del término *k*=3, y su correspondiente imagen estructural monodimensional (*figura 11b*). Estas imágenes permiten obtener información estructural exclusivamente en una dirección, en este caso a lo largo de [001]*. Los máximos del diagrama SAED se indexan a lo largo del eje c, como se indica en la figura. Como muestra la ampliación (*figura 11c*) el parámetro c=42.27 Å es equivalente a tres veces la distancia existente entre dos planos consecutivos de In_2O_3, 14.09 Å. Las líneas de contraste oscuro se identifican con las capas In-O, perpendiculares al eje c, cuya periodicidad se observa claramente, lo que permite establecer el número y distribución de estos apilamientos de

bloques ZnO con capas In-O. Estas imágenes estructurales monodimensionales permiten visualizar la secuencia de apilamiento en estructuras complejas [25].

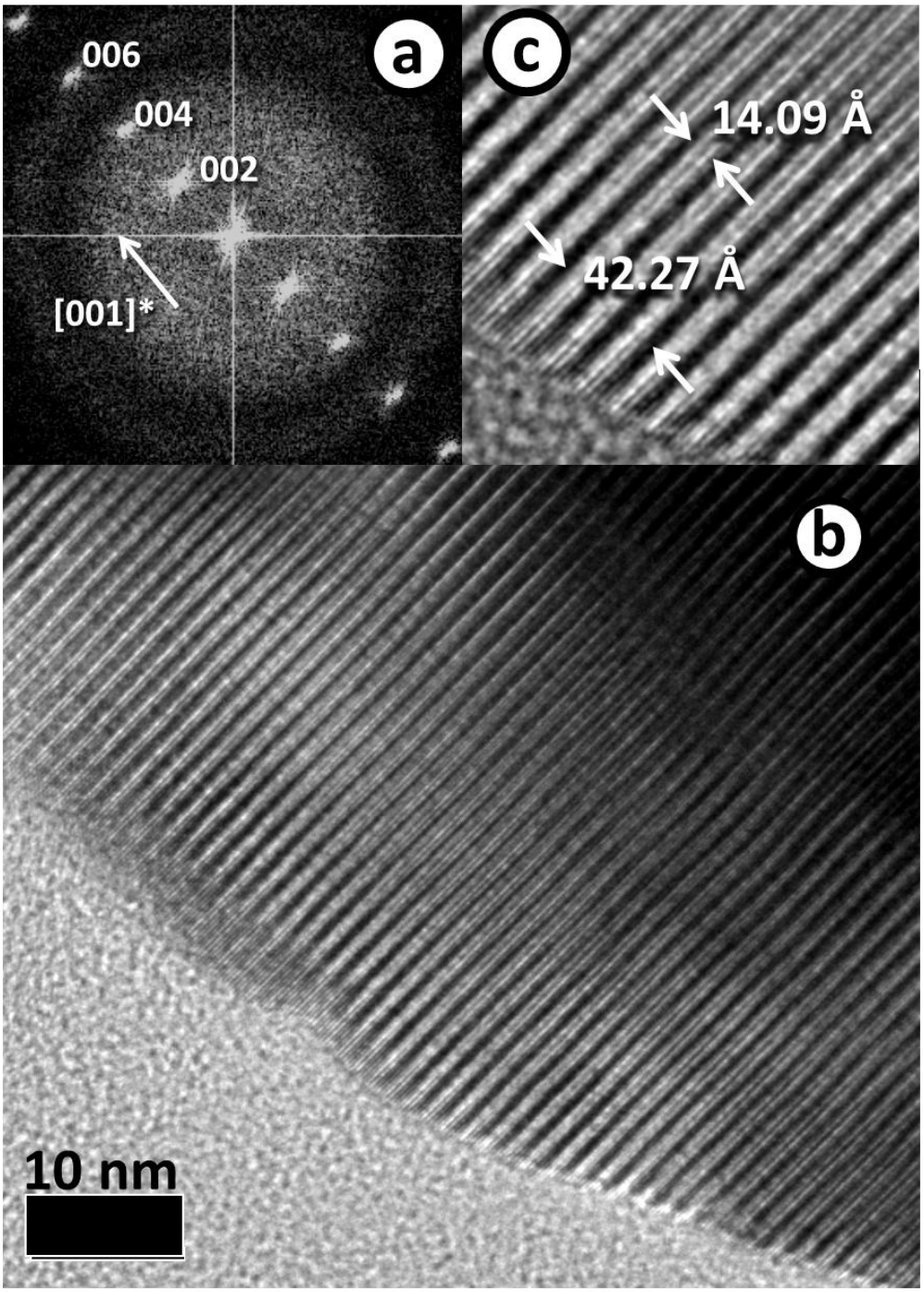

Figura 11. a) Diagrama SAED a lo largo del eje de zona [010], b) imagen HRTEM correspondiente, c) I-FFT, del término *k*=3.

En la *figura 12a* se muestra el diagrama SAED del término *k*=6 a lo largo del eje de zona [010] de la estructura. En la *figura 12b* se presenta la imagen HRTEM correspondiente.

Al tratarse de un término par de la serie homologa, el parámetro reticular "***c***" corresponde al doble del espaciado entre dos capas consecutivas de In2O3. A partir de la I-FFT (*figura 12c*) se miden las distancias correspondientes a los parámetros ***a***= 3.3 Å, y ***c***= 44 Å, de la estructura del término *k*=6.

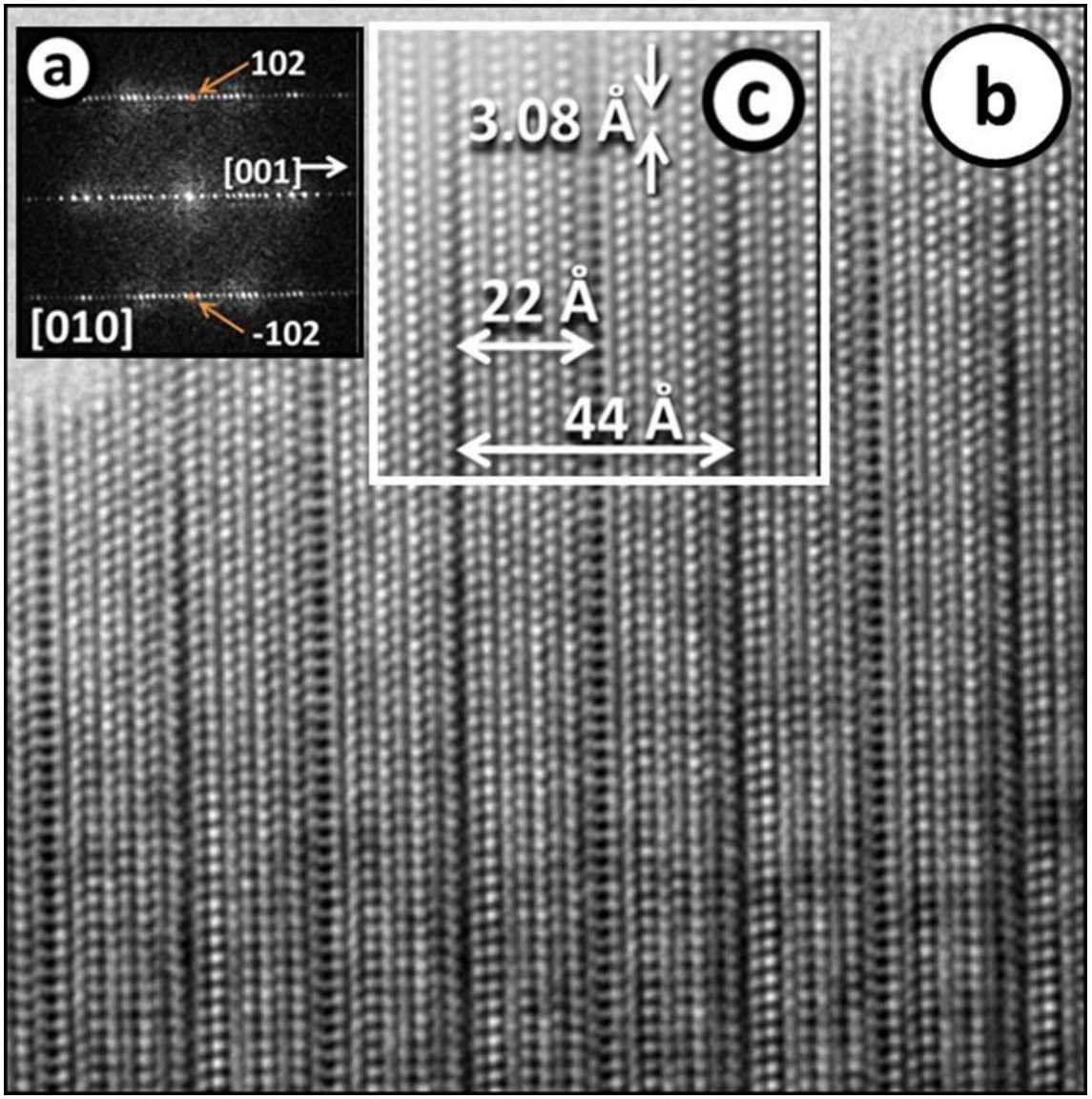

Figura 12. a) diagrama SAED correspondiente a lo largo del eje de zona [010],b) Imagen HRTEM, c) I-FFT término *k*=6.

En la *figura 13a* se muestra el diagrama FFT del término *k*=9, correspondiente a la imagen estructural monodimensional mostrada en la *figura 13b*. Como se observa en la periodicidad de los contrastes, el parámetro ***c***=90 Å equivale a tres veces la distancia existente entre planos consecutivos de In_2O_3 (30 Å).

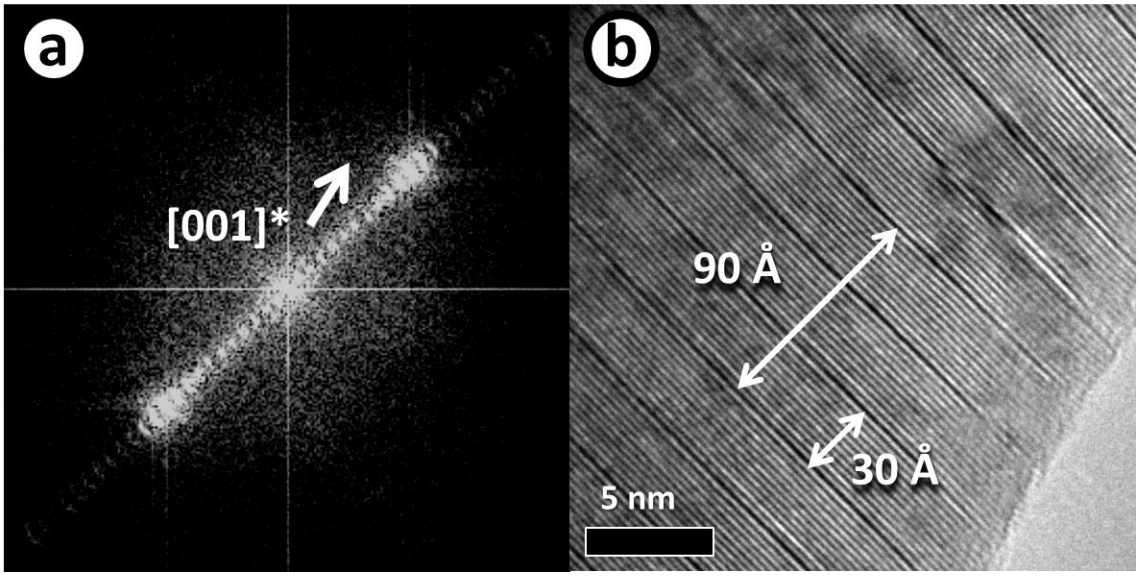

Figura 13. a) Diagrama FFT del término *k*=9, b) imagen HRTEM correspondiente.

La *figura 14a* muestra el diagrama SAED correspondiente al eje de zona [010] del término *k*=13 de la serie homóloga, en el que se observa la existencia de un alargamiento de los máximos de difracción a lo largo del eje c, lo que sugiere la existencia de defectos extensos a lo largo de dicho eje. En la *figura 14b* se muestra la imagen HRTEM, donde se indican la distancia entre capas consecutivas de In_2O_3 (40 Å) y el parámetro ***c***=120 Å (equivalente a tres veces dicha distancia). En la *figura 14c* se muestra la I-FFT correspondiente a la región indicada de la imagen. Se puede observar la distancia interatómica de 3.1 Å, correspondiente al parámetro "***a***" de la estructura, y su correspondiente diagrama FFT (*figura 14d*), a lo largo del eje de zona [010].

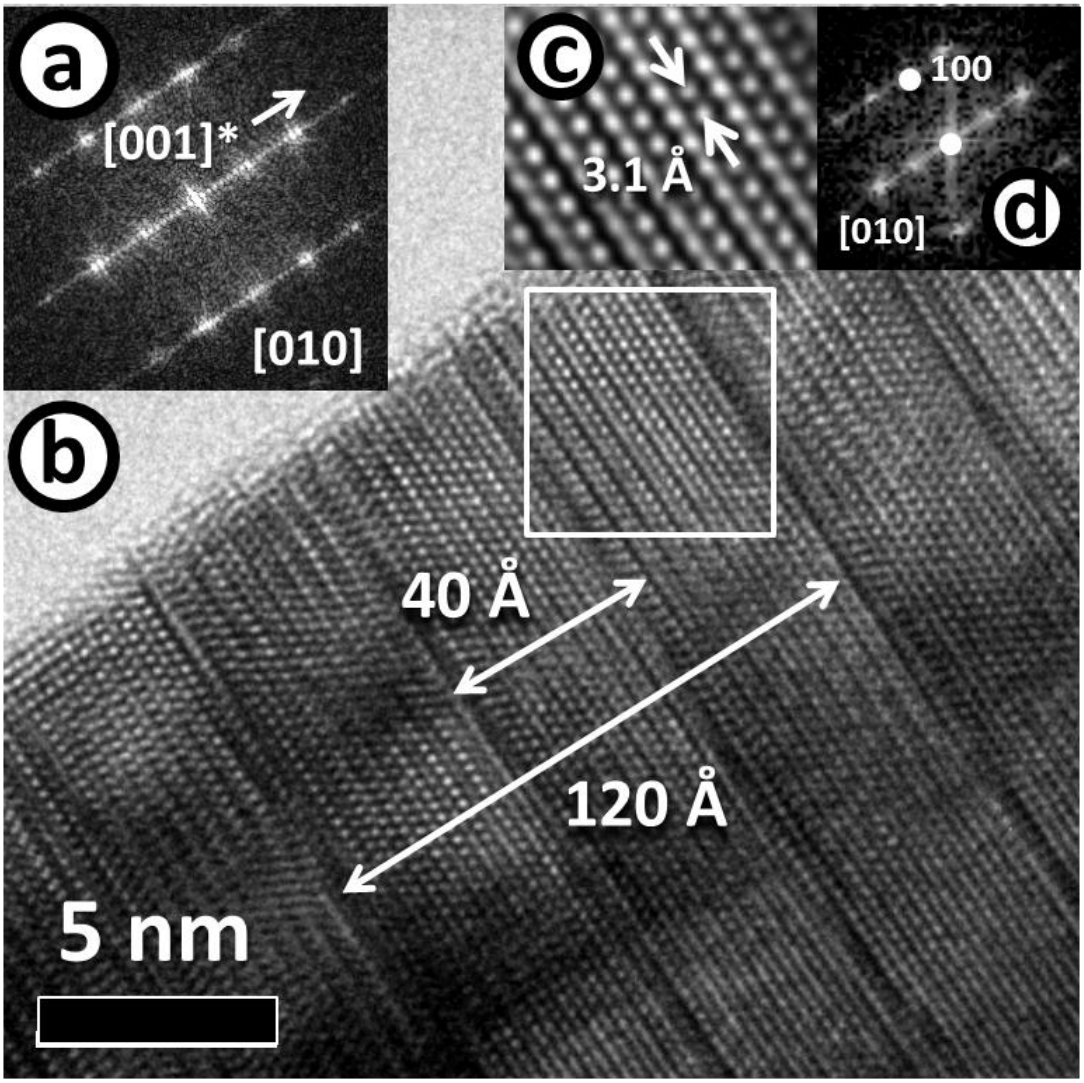

Figura 14. a) Diagrama SAED a lo largo del eje de zona [010] del término *k*=13, b) imagen HRTEM correspondiente, c) I-FFT del área resaltada, d) FFT correspondiente.

Esta imagen parece indicar que se trata de una monofase del término *k*=13. Sin embargo, el estudio de otros cristales de la muestra, *figura 15*, pone de manifiesto la existencia de faltas de apilamiento a lo largo del eje c como consecuencia de intercrecimientos desordenados de distintos términos de la serie homóloga, de acuerdo con la información obtenida a partir de su diagrama SAED.

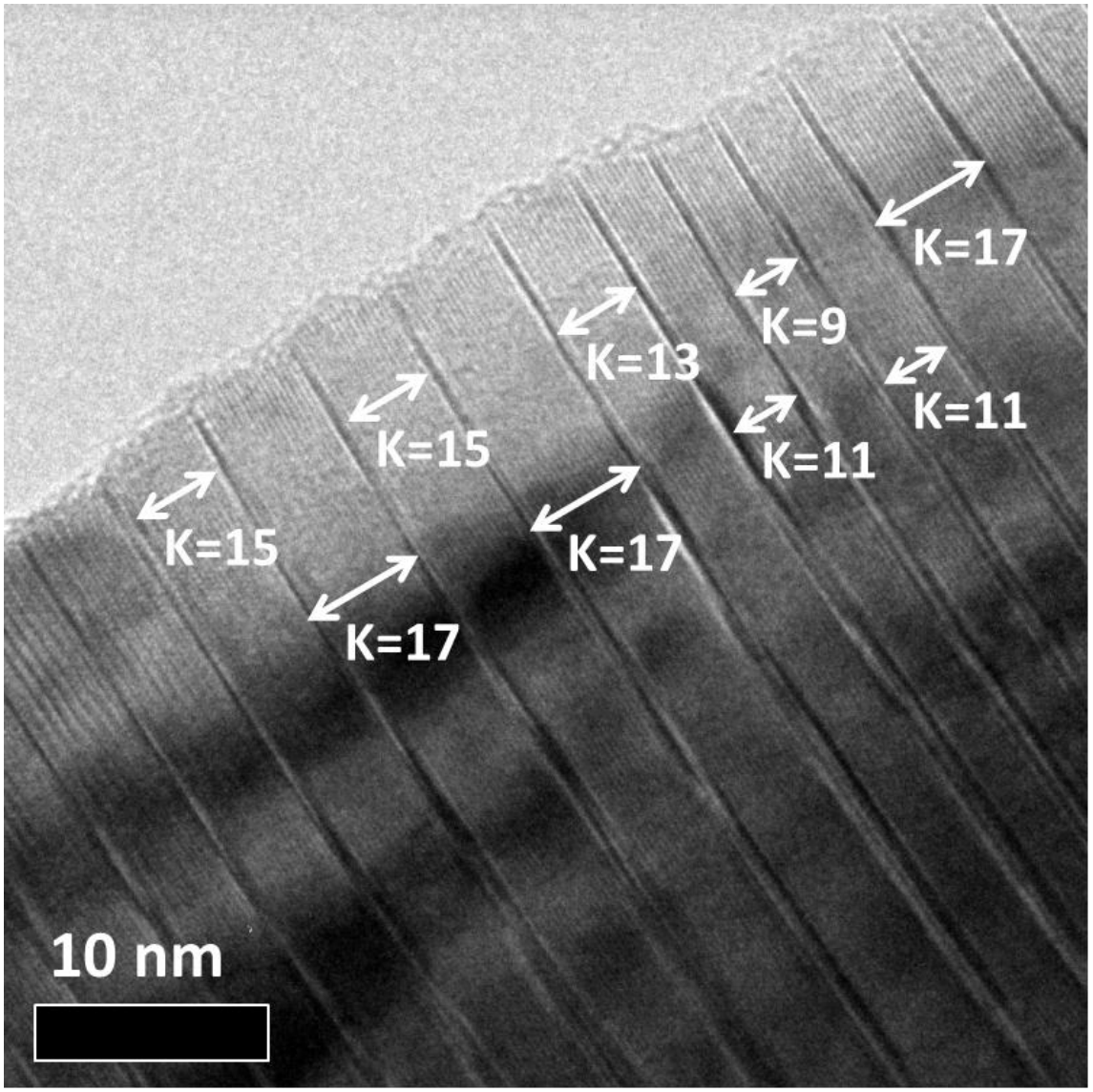

Figura 15. Imagen HRTEM del término *k*=13.

La existencia de un intercrecimiento desordenado de distintos términos está de acuerdo con las observaciones realizadas por Moriga *y col.*, que sugerían esta posibilidad ante la dificultad de asignar inequívocamente los máximos de difracción a términos consecutivos de la serie homóloga [9]. Este desorden estructural se observa con claridad en los términos superiores de la serie. Efectivamente, las imágenes de microscopia electrónica de transmisión confirman que en la muestra *k*=13 intercrecen varios términos con valores de *k* próximos, de forma que su diagrama de difracción de rayos X muestra máximo de difracción de rayos X relativamente anchos como resultante de la contribución de los términos presentes, próximos al término *k*=13.

Cuando se estudian regiones delgadas del cristal mediante HRTEM, las estructuras moduladas del interior del cristal no presentan contrastes bien definidos mientras que el contraste de las capas In-O se observa claramente. Por otro lado, en los bloques In/Zn-O coexisten ambos átomos metálicos, con un entorno de coordinación muy similar al que se da en el ZnO tipo wurtzita, por lo que no se observa un contraste claro.

Un estudio minucioso de los diagramas SAED del término *k*=9 muestra la existencia de máximos extra de difracción, o reflexiones satélite, que parecen reflejar la existencia de una modulación estructural. Efectivamente, en la *figura 16* se presenta el diagrama SAED a lo largo del eje de zona [010] de la muestra *k*=9, donde los máximos principales se pueden asignar a una celda de simetría hexagonal. Estas reflexiones satélite de intensidad débil (señaladas con un círculo rojo) indican la existencia de una leve modulación en la estructura. Como se observa en la *figura 16* (marcada en verde), la intensidad de la difracción satélite parece mantenerse constante al alejarse del centro del difractograma, lo que parece indicar que esta modulación es de carácter desplazativo, y no composicional.

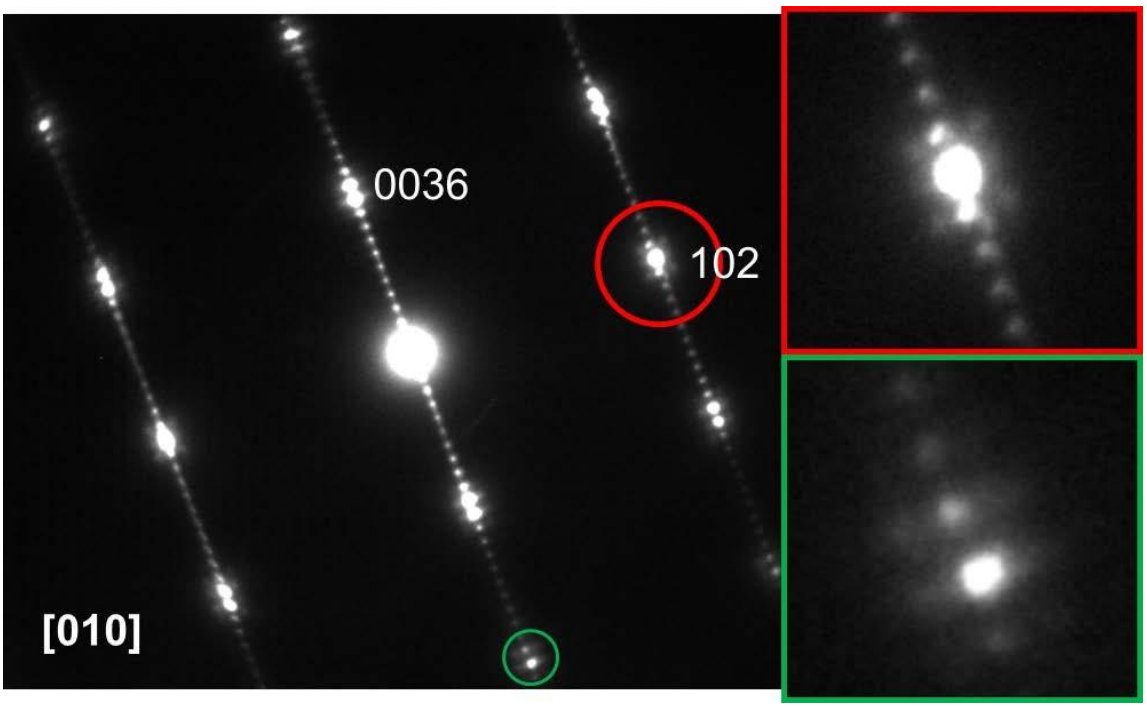

Figura 16. Diagrama SAED del término *k*=9 a lo largo del eje de zona [010]

El estudio de estos diagramas SAED confirma que existe una modulación desplazativa que se encuentra dentro del plano basal, en forma de función sinusoidal a lo largo de la dirección ***a*** y paralela a ***c***, indicando la participación de la capa de In-O en la formación de la modulación.

La flexibilidad composicional y/o desplazativa de una estructura, modulación, suele dar lugar a la presencia de reflexiones satélite. Una modulación estructural puede describirse como formada por dos partes, una estructura promedio y una perturbación de la misma caracterizada por uno o más vectores linealmente independientes [26]. En la *figura 17* se representan los modelos idealizados que describen la modulación composicional y desplazativa, en una estructura ideal de dos átomos. La modulación composicional se representa con el cambio en el sombreado de los átomos en negro y la modulación desplazativa por las flechas que indican vectores de desplazamiento.

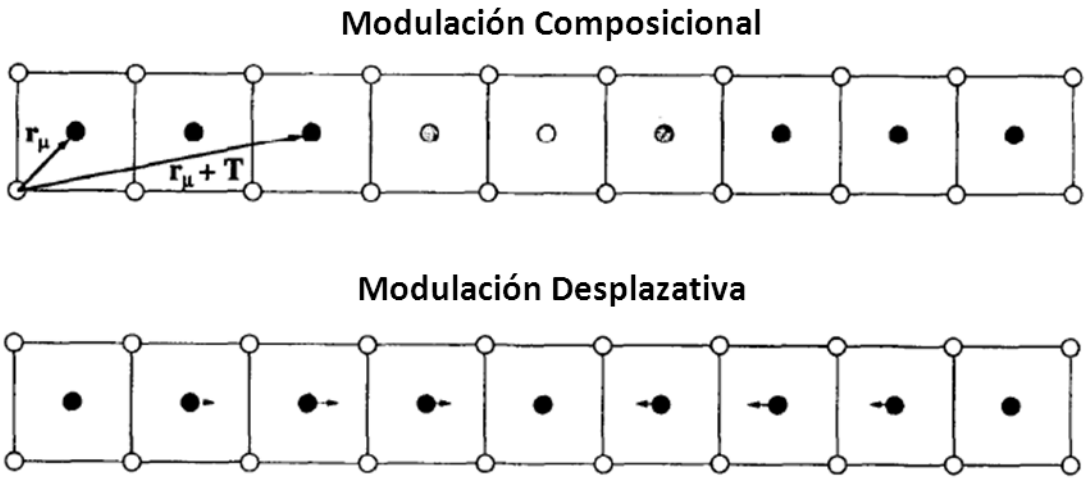

Figura 17. Representación esquemática de la modulación composicional y la modulación desplazativa.

Los modelos aquí presentados son inconmensurables con la celda unidad, por lo que, estas modulaciones composicionales y/o desplazativas dan lugar a la aparición de reflexiones satélite en los diagramas de difracción en posiciones inconmensurables con la celda unidad, que acompañan a los máximos de difracción de la estructura.

Los resultados obtenidos en el estudio de la estructura cristalina del $InFeO_3(ZnO)_k$, isoestructural con la serie homóloga, pusieron de manifiesto la existencia de una estructura modulada, que puede observarse en la zona gruesa de los cristales correspondientes a los términos k= 6, 13 [27], que sugieren que prevalece para la serie $In_2O_3(ZnO)_k$, con k>7 [28]. La "posible" presencia de esta modulación motivó la revisión de los modelos estructurales

propuestos previamente [14, 18, 29, 30], donde se describe la estructura laminar como una sucesión de una capa In-O de composición InO_2^-, y capas M/Zn-O de composición $(MZn)_kO_{k+1}^+$ (donde M es un catión trivalente), a lo largo del eje c. Dado que no se observaban máximos de difracción extra, se asumió que los átomos trivalentes de la capa Zn/M-O se encontraban distribuidos al azar. Uchida y col. [29] observaron reflexiones extra para varios términos [30], que se localizaban en posiciones no equivalentes de la red, lo que podría indicar la presencia de una modulación estructural. En las imágenes de HRTEM observaron una variación en el contraste, que formaba un zig-zag en el bloque M/Zn-O, que los autores relacionaron con la presencia de M^{3+} en dicha modulación. Esta modulación había sido pasada por alto en los estudios anteriores, debido probablemente a que el contraste era apreciable solo a partir de cierto grosor del cristal, mientras que en los estudios de microscopía electrónica de alta resolución se buscan las zonas más delgadas de los cristales para su caracterización.

Siguiendo estas observaciones, Schinzer et al. [31] revisaron la estructura cristalina del término $Zn_3In_2O_6$ mediante análisis Rietveld, indicando que los átomos de indio se localizan preferentemente en coordinación 5, considerando la presencia de una capa paralela compuesta por bipirámides trigonales. Otros estudios basados en cálculos de densidad funcional han determinado que la ocupación de las distintas posiciones por el indio es energéticamente equivalente para este término de la serie [32]. Para el término *k*=5, los estudios realizados también ponen de manifiesto la existencia preferente de una monocapa de In^{3+}, en coordinación bipirámide trigonal, en medio del bloque Zn/In-O [33]. En cambio, para el término *k*=7 se han realizado cálculos que ponen de manifiesto su estabilidad con *p*-IDB (*pyramidal inversion domain boundaries)* y su buena concordancia con los resultados obtenidos mediante holografía electrónica, aunque los autores no consideran la posibilidad de que exista modulación [34].

Varios autores coinciden en que la causa de esta modulación está relacionada con el desajuste estructural producido en la red por el mayor tamaño de los iones In^{3+}, su par de electrones solitario, y las vacantes en las capas ricas en Zn que se ocasionan al incorporarse el indio en posiciones de geometría de bipirámide trigonal [35]. La inversión de polaridad por la presencia de la modulación en zig-zag está respaldada por cálculos de teoría de densidad funcional realizados por diversos autores para términos con *k*>6 [36, 37]. En la

figura 18 se muestra la disposición estructural de los modelos. La diferencia energética entre ambos modelos aumenta al aumentar *k*, lo que sugiere que la modulación es más probable en los términos superiores.

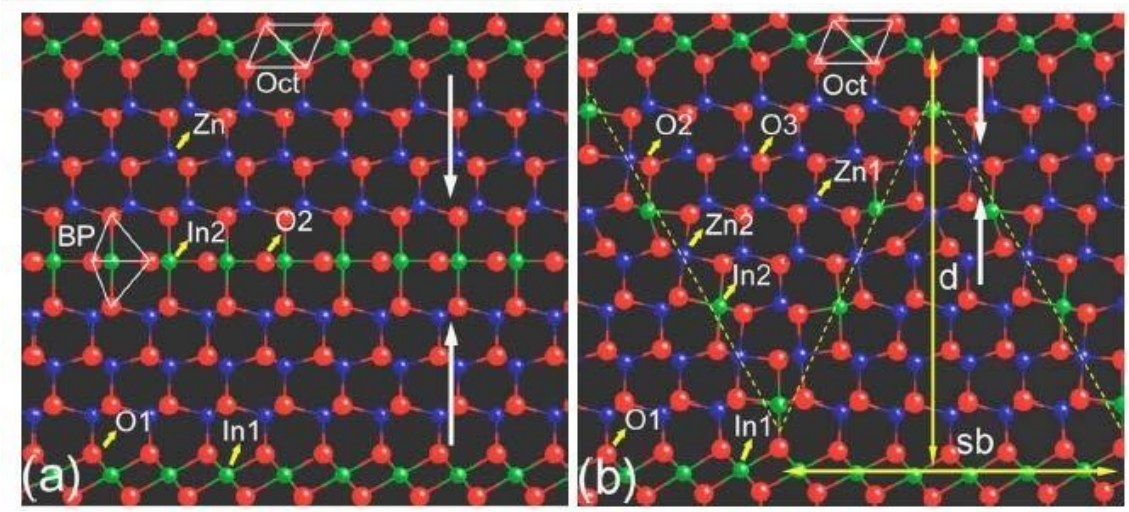

Figura 18. Modelos estructurales para sistemas In2O3-ZnO con (a) límite paralelo, (b) límite en zig-zag en el bloque In/Zn-O.

Partiendo de la información anterior, el empleo de técnicas como la obtención de imágenes de alto ángulo anular en campo oscuro (*high angle annular dark field, HAADF*) en microscopios electrónicos con correctores de aberración permite obtener información precisa del entorno químico de los IDB, llegando a visualizar columnas de átomos de oxigeno empleando detectores anulares de campo claro (*annular bright field, ABF*) [38-41], que permiten una interpretación directa de la estructura. Estos avances han permitido profundizar en la inversión de dominios que se produce en los bloques de In/Zn-O.

En la *figura 19* se presenta una imagen de contraste Z obtenida en modo HAADF. El análisis detallado de los contrastes observados revela las posiciones de los átomos de In (Z=49) que aparecen con una intensidad mayor que las posiciones catiónicas ocupadas por Zn (Z=30), es decir, los bloques con estructura ZnO. Sin embargo, como se ha discutido previamente, en todos los casos los átomos de In parecen difundir hacia el interior del bloque ZnO.

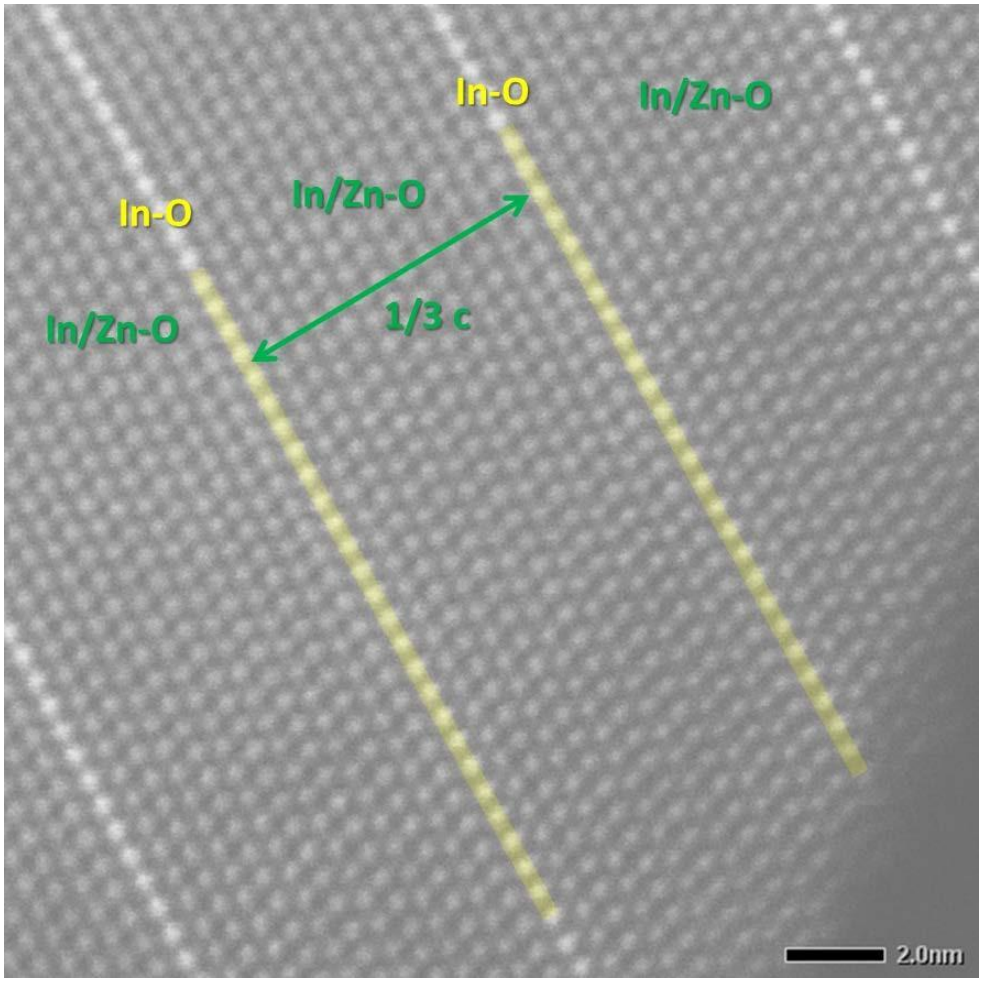

Figura 19. Imagen HAADF del término *k*=9.

En la siguiente imagen de ADF, *figura 20a*, se puede observar la presencia de intercrecimientos desordenados de términos con distinta *k*, como se ha observado y discutido previamente. Cuando se compara esta imagen ADF con su correspondiente imagen en modo BF (*figura 20b*), se observa la existencia de un contraste en zig-zag en los bloque tipo In/Zn-O. Por otro lado, cuando se estudia la misma región del cristal en campo oscuro no muestra ninguna variación de contraste en los bloques, lo que indica que el origen de este contraste no se debe a variaciones de la composición. Por lo tanto, este contraste puede ser debido a la presencia de tensiones reticulares. Este mismo hecho ha sido observado por W. Yu et al [42] en el término $In_2O_3(ZnO)_7$, y ha sido interpretado como una distorsión de la subred aniónica.

El origen de la modulación a escala atómica parece difícil de precisar, pero estos resultados parecen estar justificados teniendo en cuenta el diferente proceso de formación de las imágenes en modo STEM. Mientras en modo HAADF el contraste viene determinado por la

diferente composición del cristal, en modo BF el contraste observado está fuertemente influenciado por contraste de fase (en conexión con la formación de imágenes en modo TEM). Este contraste de fase justifica la aparición de la modulación desplazativa, en forma de zig-zag, observado en modo BF y no en modo HAADF.

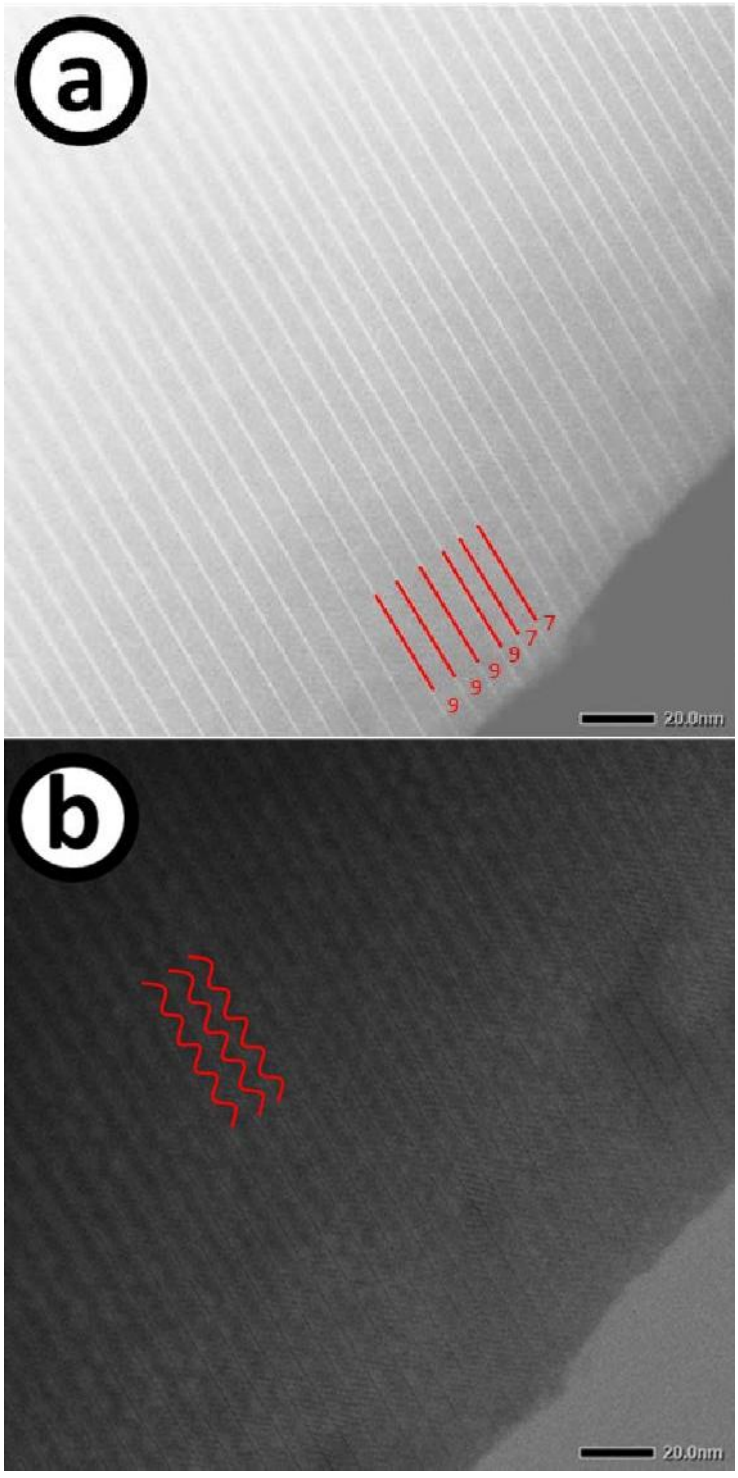

Figura 20. a) Imagen ADF, y b) Imagen BF del término *k*=9.

Parece, por tanto, que el único factor que puede dar lugar a una modulación en la estructura, originando estos contrastes, es la presencia de tensiones reticulares, que se deben a la deformación de un cuerpo elástico por fuerzas externas o internas y, por las cuales, las distancias de enlace se alteran respecto a su valor en equilibrio, dando lugar a la aparición de una modulación desplazativa en el cristal.

Los cálculos teóricos mediante DFT establecen que existen unas configuraciones más favorables energéticamente en las que se cumplen dos condiciones límite: se han de ocupar tantos planos diferentes como se pueda entre los dominios IDB, y minimizar la fracción de indio en el entorno [34]. Como resultado, la estructura es más estable cuando se consigue la máxima distancia posible entre átomos de In, manteniendo una distribución homogénea de indio en el dominio. La distribución de carga según este modelo hace que cuanto más próximo esté un átomo de In al centro del dominio mayor será su carga neta. Esto se debe a un ligero cambio en la esfera de coordinación del oxígeno, caracterizado por una disminución en la distancia promedio In-O. Esto puede entenderse también como una estructura modulada desplazativa inducida por la distribución de carga [43, 44].

Estos resultados parecen indicar que en las estructuras de este tipo de la serie homóloga $(In/M)_2Zn_kO_{3+k}$ la modulación está siempre presente, y cuando se sustituye parte de los átomos de In por cationes metálicos (M), la modulación pasa de ser desplazativa a composicional, como es el caso de los IFZO donde M=Fe [27, 28].

4. PROPIEDADES CÁTODOLUMINISCENTES

La *figura 21* muestra la variación de los espectros en función del parámetro *k* del sistema $ZnkIn_2O_{k+3}$. Los espectros de CL de las diferentes estructuras muestran una banda principal, ancha y compleja comprendida entre 1,5 y 2 eV, aproximadamente.

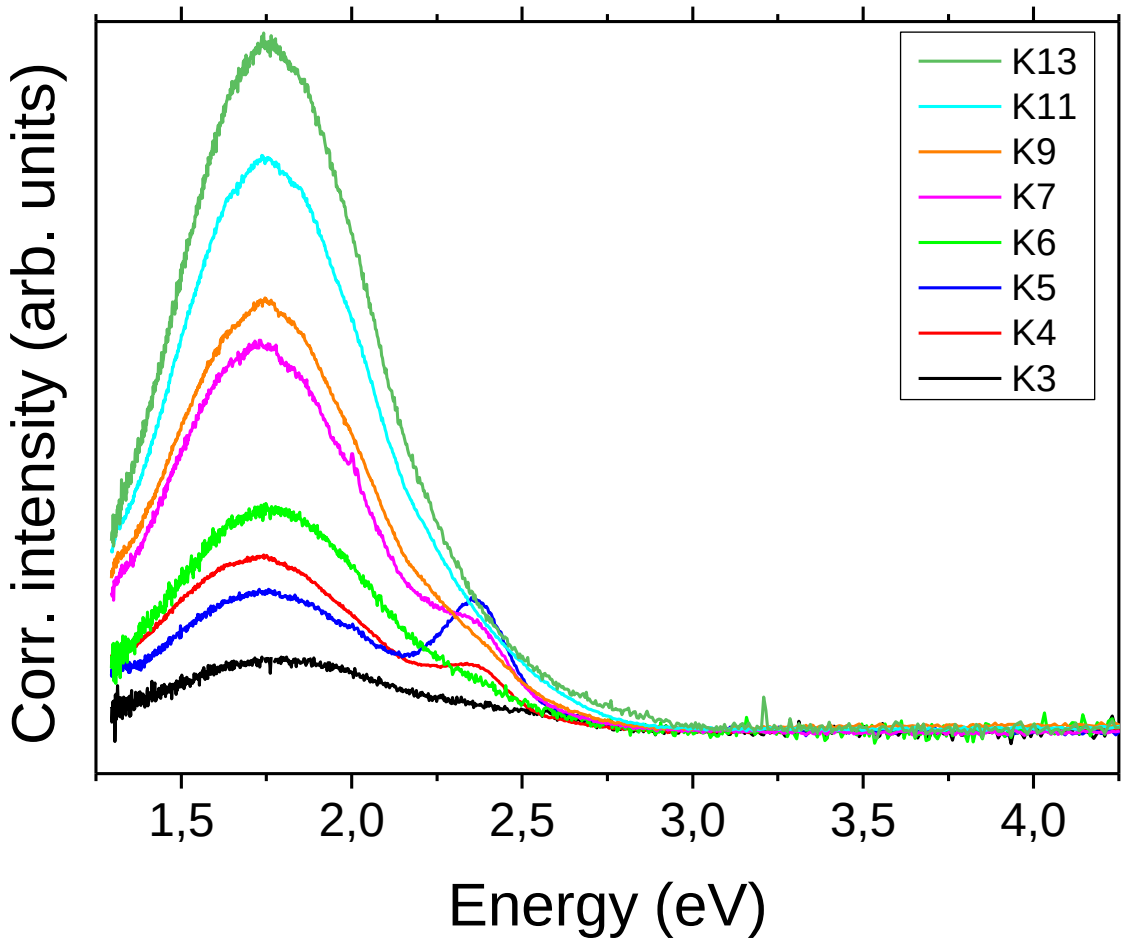

Figura 21. Espectro CL correspondiente a las muestras estudiadas.

La posición del pico principal se desplaza hacia energías más elevadas a medida que aumenta la concentración de Zn, mientras que el ancho de la banda varía muy poco en función de la cantidad de Zn salvo para las muestras de menor *k*, donde es más ancha. En la *figura 22* se presentan los espectros normalizados para favorecer su comparación. También se observa un hombro alrededor de 2,3 eV, bien definido para términos inferiores de *k* y, especialmente, en la muestra *k*=5 donde domina el espectro.

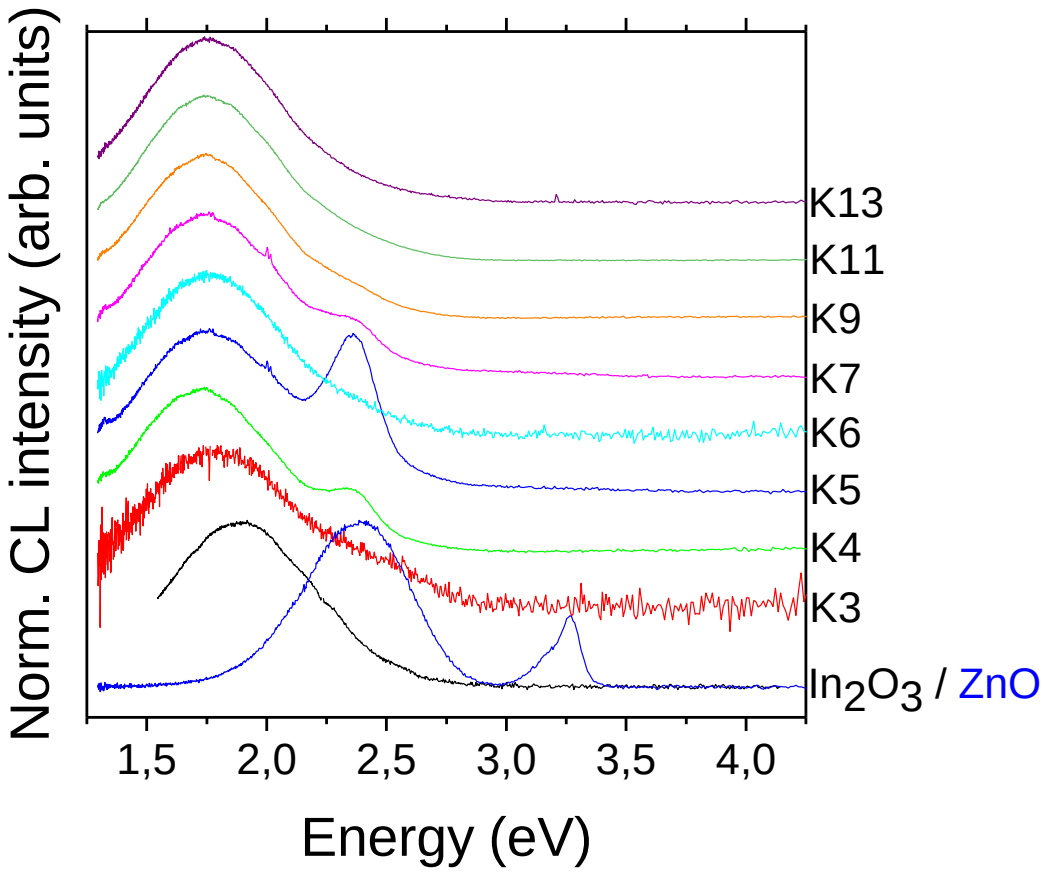

Figura 22. Espectros normalizados de los IZO; en la parte inferior los de los precursores In2O3 y ZnO.

En la *figura 22* se muestran también los espectros de CL correspondientes a los reactivos de partida, que se utilizan como referencia para la discusión posterior de resultados. El espectro de ZnO presenta una emisión, a 3,1 eV, correspondiente al borde de banda [45, 46]. En la región de baja energía de este espectro se observa una emisión asociada a la presencia de defectos centrada sobre 2,5 eV.

En este sentido, en la bibliografía se describe otra banda en torno a 2,9 eV que aumenta al disminuir el tamaño de grano. Según los estudios de Jin *y col.* [47], esta banda de emisión se debe a una transición entre la banda de valencia y un nivel localizado a 0,33 eV por debajo de la banda de conducción, asociado a la presencia de trampas interfaciales localizadas en las fronteras de grano en ZnO [48]. Debido a la ruta sintética empleada para la obtención de estos materiales, el tamaño de grano es muy elevado por lo que en el espectro obtenido se encuentra una contribución moderada asociada a la banda de 2,9 eV (es necesario aumentar la señal para apreciarla correctamente debido a su baja intensidad).

La banda de emisión centrada en torno a 2,5 eV del ZnO provendría de una transición entre un aceptor profundo (probablemente una vacante de zinc, VZn), y un donor poco profundo [49, 50]. De acuerdo con estos trabajos, en las láminas de ZnO con tamaño de grano menor, el número de defectos nativos parece ser mayor. Esta banda presenta varias contribuciones por lo que Reynolds *y col*. [51] sugieren que son varios los centros responsables de la emisión, ya que la posición del máximo de esta banda no siempre es la misma, variando ligeramente según el tipo de muestra (*bulk*, láminas delgadas o nanoestructuras) y los tratamientos térmicos y dopado que se hayan efectuado sobre ella.

Al observar el espectro de In_2O_3 se aprecia una banda centrada en 1,9 eV asociada a defectos, mientras que no hay emisión asociada al borde de banda. Este pico de luminiscencia ha sido observado en trabajos anteriores, tanto en medidas de fotoluminiscencia (PL) en láminas delgadas [52], como de CL en nanoestructuras [53], aunque su origen está lejos de ser consensuado. El comportamiento de esta banda bajo tratamientos oxidantes, en presencia de una elevada concentración de oxígeno [54], excluye a las vacantes de oxígeno como los defectos relacionados con esta emisión. Por el contrario, debe originarse debido a defectos cuya concentración aumente al incrementarse el contenido en oxígeno, como los intersticiales de oxígeno O_i, los oxígenos en antisitios de indio, O_{In} o las vacantes de indio, V_{In}. También se han descrito en la literatura emisiones en el rango verde-azul para nanoestructuras de óxido de indio sin dopar, que se han relacionado con la presencia de vacantes oxígeno.

En el caso de la banda principal de los IZO, esta se encuentra desplazada en energías hacia el rojo, respecto de la banda de 1,9 eV del óxido de indio sin dopar. Sin embargo, sus características, próximas a esta banda del óxido de indio, parecen sugerir que sus orígenes pueden ser muy similares y producirse en las zonas de la superestructura del IZO predominantemente formadas por óxido de indio, aunque es necesario continuar el estudio de dicha banda.

La emisión alrededor de 2,34 eV que observamos en el caso de las muestras de IZO, especialmente de k=3-7, se ha relacionado anteriormente con una emisión propia del ternario con k=4, medida sobre pirámides de In_2O_3 dopadas con Zn, cuya superficie estaba formada por pequeños cristales de IZO [55]. También, se ha identificado una emisión con un máximo a 2.37 eV en nanocintas de IZO con k= 4 [56]. Debido a las distintas características

de la emisión, como su anchura a media altura respecto de la banda de defectos propia del ZnO es mayor, los autores excluyen como origen la banda del óxido de zinc, y su origen debe de ser intrínseco y asociado a la formación de los ternarios de IZO. Por ello, en las muestras estudiadas en este trabajo, esta banda se atribuye a la formación del ternario. No existe, sin embargo, en la bibliografía información que permita asociar esta emisión luminiscente con la estructura electrónica concreta de los niveles electrónicos profundos que puedan aparecer en estos ternarios.

Bartolomé *y col.* [57] pusieron de manifiesto que la posición del nivel de Fermi está fuertemente correlacionada con la concentración de Zn. La intensidad de la emisión catodoluminiscente se favorece con la presencia de Zn, dando lugar a cambios espectrales y un ensanchamiento de la banda de emisión. Todo esto lleva a pensar que las propiedades de estos materiales pueden ser fácilmente controlables, lo que sin lugar a dudas favorece sus aplicaciones tecnológicas y les aporta versatilidad para proceder a codopados con otros elementos.

Cuando aparecen las modulaciones en términos con valores elevados de *k*, los portadores de carga se ven confinados en las capas de InO_2^-. Esta modulación también contribuye en la banda de conducción, produciendo una distribución electrónica modulada en la estructura de bandas [10], lo que justifica la existencia de una conductividad eléctrica anisotrópica. Se dan dos caminos de conducción: la capa In-O, principal camino de conducción y el límite en zig-zag, que es el principal camino de conducción fuera de plano. Estas vacantes poseen una preferencia de sitio y, por tanto, una distribución espacial anisotrópica: la mayoría ocupan sitios en el límite modulado del bloque Zn/In-O [58]. En condiciones de equilibrio, las vacantes de oxígeno (V_o) e In intersticiales (In_{Zn}) tienden a ocurrir en este zig-zag y al formarse las asociaciones de defectos, bloquean los caminos de conducción al actuar como centros dispersantes y contribuyendo al comportamiento anisotrópico [59].

Así, por ejemplo, se ha propuesto la sustitución de Zn o In por cationes con estados de oxidación mayores para mejorar las propiedades eléctricas de los politipos $Zn_kIn_2O_{k+3}$, en las que el dopante puede dar lugar a la formación de niveles dadores o bandas dadoras localizadas a un nivel de energía *KbT* eV por debajo de la banda de conducción. Masuda *y col.* [60] llevaron a cabo con éxito la sustitución química de Zn^{2+} por Mg^{2+} o de In^{3+} por Co^{3+}, Y^{3+} o Fe^{3+} (y, por tanto, sin dopado electrónico) en el politipo $Zn_5In_2O_8$, sin cambios

estructurales. Sin embargo, Maugy *y col*. [6] han publicado sustituciones parciales de In^{3+} por Sn^{4+} o Zr^{4+} y Zn^{2+} por Al^{3+}, lo que involucra un cambio en el número de electrones y, por tanto, en las propiedades. Los resultados obtenidos, por estos autores, mediante difracción de rayos X (XRD) y microscopia electrónica de alta resolución (HRTEM) ponen de manifiesto que todas las fases obtenidas por ellos están formadas por intercrecimientos desordenados, de diferentes términos de la serie homóloga $Zn_kIn_2O_{k+3}$, así como de una fase secundaria de composición In_2O_3.

CONCLUSIONES

Se ha realizado la síntesis por el método cerámico de los términos *k*= 3-7, 9, 11 y 13, de la serie homóloga $Zn_kIn_2O_{k+3}$, realizando un control exhaustivo de los parámetros de síntesis. Los datos obtenidos mediante difracción de rayos X confirman que se han obtenido monofases para todos los términos. Debido a las características estructurales de la serie homóloga, todas las fases presentan un plano basal común, equivalente al [001] de la wurtzita, por lo que es necesario estudiar los ejes de zona perpendiculares, que contengan el eje "c" para caracterizar correctamente cada uno de los términos. Por medio de difracción de electrones y microscopia electrónica de alta resolución se ha observado que solo en los términos superiores existen intercrecimientos desordenados entre diferentes miembros de la serie homóloga.

A partir de los datos obtenidos mediante microscopia con aberración corregida en sonda, se observa que existe una modulación desplazativa en las estructuras de la serie homóloga para k>6, según una función sinusoidal en el plano basal y paralela a la dirección ***c***; esta modulación pasa a ser composicional al dopar los materiales con otros cationes metálicos trivalentes.

En los espectros de cátodoluminescencia obtenidos, se observa una banda principal, ancha y compleja entre 1.5 y 2 eV, cuya intensidad aumenta notablemente con *k*, posiblemente relacionada con la presencia de In3+ en posiciones intersticiales de bipirámide trigonal. Existe una segunda banda de interés, para los términos *k*=3-7, centrada a ~2.4 eV cuyo origen estaría relacionado con la formación del ternario. Estos resultados parecen indicar que se puede regular la respuesta luminiscente en función de la composición de los materiales.

BIBLIOGRAFÍA

[1] D.J. Goyal, C. Agashe, M. G. Takwale, V. G. Bhide, S. Mahamuni, S. K. Kulkarni, *J. Mater. Res.* 8 **(1993)** 1052-1026.

[2] R. Wang, A. W. Sleight, R. Platzer, J. A. Gardner, *J. Solid State Chem.* 122 **(1996)** 166-175.

[3] H. Kasper, *Z. Anorg. Allg. Chem.* 349 **(1967)** 113-123.

[4] H. Kasper, *Z. Anorg. Allg. Chem.* 364 **(1969)** 215-224.

[5] P. J. Cannard, R. J. D. Tilley, *J. Solid State Chem.* 73 **(1988)** 418-426. [6] G. Thomas, *Nature,* 389 **(1997)** 907-908.

[7] A. Walsh, J. L. F. Da Silva, S.-H. Wei, *J. Phys. Condens. Matter.* 23 **(2011)** 334210.

[8] C. Li, Y. Bando, M. Nakamura, N. Kimizuka, *Micron,* 31 **(2000)** 543-550.

[9] T. Moriga, D. D. Edwards, T. O. Mason, G. B. Palmer, K. R. Poepperlmeier, J. L. Schindler, C. R. Kannewurf, I. Nakabayashi, *J. Am. Ceram. Soc.* 81 **(1998)** *5,* 1310-1316.

[10] A. Walsh, J. L. F. Da Silva, Y. Yan, M. M. Al-Jassim, S.-H. Wei, *Phys. Rew. B,* 79 **(2009)** 073105.

[11] N. Naghavi, C. Marcel, L. Dupont, A. Rougier, J.-B. Leriche, C. Guéry, *J. Mat. Chem.* 10 **(2000)** 2315-2319.

[12] C. Maugy, L. Dupont, N. Naghavi, C. Guéry, J.-M. Tarascon, *J. Phys. Chem. Solids,* 62 **(2001)** 1375-1386.

[13] N. Kimizuka, T. Mohri, M. Nakamura, *J. Solid State Chem*. 81 **(1989)** 70-77.

[14] N. Kimizuka, M. Isobe, and M. Nakamura, *J. Solid State Chem.* 116 **(1995)** 170- 178.

[15] M. Nakamura, N. Kimizuka, T. Mohri, *J. Solid State Chem.* 86 **(1990)** 16-40.

[16] M. Nakamura, N. Kimizuka, T. Mohri, *J. Solid State Chem.* 93 **(1991)** 298-315.

[17] M. Nakamura, N. Kimizuka, T. Mohri, *J. Solid State Chem.* 105 **(1993)** 535-549.

[18] M. Isobe, N. Kimizuka, M. Nakamura, T. Mohri, *Acta Cryst. C,* 50 **(1994)** 332- 336.

[19] N. Kimizuka, T. Mohri, Y. Matsui, K. Siratori, *J. Solid State Chem.* 74 **(1988)** *1,* 98-

109.

[20] M. McCoy, R. W. Grimes, W. E. Lee, *Philos. Mag. A.* 76 **(1997)** *6,* 1187-1201.

[21] L. Dupont, C. Maugy, N. Naghavi, C. Guery, J.-M. Tarascon, *J. Solid State Chem.* 158 **(2001)** 119-133.

[22] Y. Yan, S. J. Pennycook, J. Dai, R. P. H. Chang, A. Wang, T. J. Marks, *Appl. Phys. Lett.* 73 **(1998)** *18,* 2585-2587.

[23] C. Li, Y. Bando, M. Nakamura, N. Kimizuka, *J. Solid State Chem.* 142 **(1999)** 174- 179.

[24] A. Yoshinari, K. Ishida, K. Murai, T. Moriga, *Mat. Res. Bull.* 44 **(2009)** 432-436.

[25] D. Shindo, K. Hiraga, "High-Resolution Electron Microscopy for Materials Science", **(1998)** Springer.

[26] R. L. Withers, S. Schmid, J. G. Thompson, *Prog. Solid St. Chem.* 26 **(1998)** 1-96.

[27] N. Uchida, Y. Bando, M. Nakamura, N. Kimizuka, *J. Electron. Microsc.* 43 **(1994)** *3,* 146-150.

[28] C. Li, Y. Bando, M. Nakamura, N. Kimizuka, *J. Electron. Microsc.* 46 **(1997)** *2,* 119-127.

[29] M. Nakamura, N. Kimizuka, T. Mohri, M. Isobe, *J. Alloys Compds.* 192 **(1993)** 105.

[30] M. Nespolo, M. Nakamura, H. Ohashi, *J. Solid State Chem.* 150 **(2000)** 96-103.

[31] C. Schinzer, F. Heyd, S. F. Matar, *J. Mater. Chem.* 9 **(1999)** 1569-1573.

[32] S. Yoshioka, K. Toyoura, F. Oba, A. Kuwabara, K. Matsunaga, I. Tanaka, *J. Solid State Chem.* 181 **(2008)** 137-142.

[33] W. Pitschke, K. Koumoto, *Powder Diffraction,* 14 **(1999)** *3,* 213-218.

[34] F. Röder, A. Lubk, H. Lichte, T. Bredow, W. Yu, W. Mader, *Ultramicroscopy,* 110 **(2010)** 400-410.

[35] C. Li, Y. Bando, M. Nakamura, M. Onoda, N. Kimizuka, *J. Solid State Chem.* 139 **(1998)** 347-355.

[36] Y. Yan, J. L. F. Da Silva, s.-H. Wei, M. Al-Jassim, *Appl. Phys. Lett.* 90 **(2007)** 261904.

[37] J. L. F. Da Silva, Y. Yan, S.-H. Wei, *Phys. Rev. Lett.* 100 **(2008)** 255501.

[38] S. D. Findlay, N. Shibata, H. Sawada, E. Okunishi, Y. Kondo, T. Yamamoto, Y Ikuhara, *App. Phys. Lett.* 95 **(2009)** 200895.

[39] S. D. Findlay, N. Shibata, H. Sawada, E. Okunishi, Y. Kondo, T. Yamamoto, Y Ikuhara, *Ultramicroscopy* 110 **(2010)** 903.

[40] I.N. González-Jiménez, A. Torres-Pardo, A.E. Sánchez-Peláez, Á. Gutiérrez, M. García-Hernández, J.M. González-Calbet, M. Parras, A. Varela, *Chem. Mater.* 26 **(2014)** 2256

[41] L. Ruiz-González, D. González-Merchante, R. Cortés-Gil, J. M. Alonso, J. L. Martínez, A. Hernando, J. M. González-Calbet, *Chem. Mater*. 27 **(2015)** 1397

[42] W. Yu, W. Mader, *Ultramicroscopy*, 110 **(2010)** 411-417.

[43] H. Schmid, E. Okunishi, T. Oikawa, W. Mader, *Micron,* 43 **(2012)** 49-56.

[44] H. Schmid, E. Okunishi, W. Mader, *Ultramicroscopy,* 127 **(2013)** 76-84.

[45] E. Tomzig, R. Helbig, *J. Lumin.* 14 **(1976)** 403.

[46] K. Wolf, A. Naumov, T. Reisinger, M. Kastner, H. Stanzl, W. Kuhn, W. Gebhardt, *J. Crys. Growth,*135 **(1994)** 113**.**

[47] B. J. Jin, S. Im, S. Y. Lee, *Thin Solid Films,* 366 **(2000)** 107.

[48] J. F. Cordaro, Y. Shim, J. E. May, *J. Appl. Phys.* 60 **(1986)** 4186. [45] B. J. Jin, S. H. Bae, S. Y. Lee, S. Im, *Mat. Sci. Eng. B*71 **(2000)** 301.

[49] J. M. Myoung, W. H. Yoon, D. H. Lee, I. Yun, S. H. Bae, S. Y. Lee, *Jpn. J. Appl. Phys*. 41 **(2002)** 28.

[50] D. C. Reynolds, D. C. Look, B. Jogai, *J. Appl. Phys.* 89 **(2001)** 6189.

[51] M-S. Lee W. Ch. Choi, E. K. Kim, Ch. K. Kim, S-K. Min. *Thin Solid Films,* 279 **(1996)** 1.

[52] D. A. Magdas, A. Cremades, J. Piqueras. *Appl. Phys. Lett.* 88 **(2006)** 113107.

[53] M. Mazzera, M. Zha, D. Calestani, A. Zappettini, L. Lazzarini, G. Salviati, L. Zanotti, *Nanotechnology,* 18 **(2007)** 355707.

[54] J. Bartolomé, D. Maestre, M. Amati, A. Cremades, J. Piqueras, *J. Phys. Chem. C,* 115 **(2011)** 8354–8360.

[55] B. Alemán, P. Fernández, J. Piqueras, *Appl. Phys. Lett.* 95 **(2009)** 013111.

[56] J. Bartolomé, D. Maestre, A. Cremades, M. Amatti, J. Piqueras, *Acta Mater.* 61 **(2013)** 1932–1943.

[57] E. M. Hopper, H. Peng, S. A. Hawks, A. J. Freeman, *J. Appl. Phys.* 112 **(2012)** 093712.

[58] E. M. Hopper, Q. Zhu, J.-H. Song, H. Peng, A. J. Freeman, T. O. Mason, *J. Appl. Phys.* 109 **(2011)** 013713.

[59] H. Peng, J.-H. Song, E. M. Hopper, Q. Zhu, T. O. Mason, A. J. Freeman, *Chem. Mater.* 24 **(2012)** 106-114.

[60] Y. Masuda, M. Otha, W-S. Seo, W. Pitschke, K. Koumoto, *J. Solid State Chem.* 150 **(2000)** 221.

CONCLUSIONES GENERALES

Del conjunto de resultados presentados en este trabajo pueden extraerse las siguientes conclusiones:

1. Mediante el denominado método "*Liquid-Mix*" (LQM) se han obtenido nanopartículas dopadas de TiO_2 y SnO_2, de composición general $M_{1-x}M'_xO_2$ (con M= Ti o Sn, y M'= V, Cr, Mn, Fe, Al), aparentemente ordenadas y distribución catiónica homogénea, como se confirma mediante espectroscopia por dispersión de energías (EDS).

2. El margen de estabilidad de las distintas fases se puede controlar mediante dopado con metales de transición: el dopado con Al o Fe estabiliza la fase anatasa del TiO_2, mientras que V, Cr o Mn estabilizan la fase rutilo. Además, se observa un aumento del margen de estabilidad estructural de cada fase, obteniéndose materiales rutilo a temperaturas inferiores a 650 °C y anatasa estables hasta 900 °C.

3. La transición anatasa-rutilo puede ser inducida en las nanopartículas dopadas con Fe, mediante irradiación laser, pero no en el resto de muestras. Se describe el comportamiento PL de las muestras dopadas con Fe, antes y después de la transformación.

4. Las nanopartículas de fase tipo anatasa dopadas con Al presenta un sobretono B_{1g} en el espectro Raman equivalente al que posee el material sin dopar, compuesto por dos bandas principales. Sin embargo, en el caso de las dopadas con Fe se genera una banda compleja en dicho sobretono, compuesto por tres bandas.

5. La señal luminiscente de las nanopartículas de SnO_2 puede ser controlada mediante el uso de dopantes. Los resultados de cátodoluminiscencia muestran que al dopar nanopartículas de SnO_2 con Cr, V o Mn, se inducen emisiones roja, verde o naranja, respectivamente. Al aumentar la presencia de iones de metales de transición en la matriz de SnO_2, se reduce la señal total de CL.

6. En la obtención de nanoestructuras en fase vapor basadas en β-Ga_2O_3, el uso de distintos dopantes ejerce una gran influencia en la morfología de los materiales obtenidos. El dopado con Indio favorece la aparición de estructuras macladas, al alterar la estructura de defectos nativos, además de propiciar una banda de emisión en el azul cuya intensidad es proporcional al contenido del dopante.

Por otro lado, el dopado con Sn de nanoestruturas de β-Ga_2O_3 da lugar a la aparición de ramificaciones, mediante un mecanismo de crecimiento epitaxial. El co-dopado con Sn y Cr permite obtener emisión luminiscente en todo el rango del visible, por lo que estas estructuras se comportan como eficientes guías de luz, a lo largo de sus troncos y ramas, tanto para la luz visible como la UV

7. Por último, se han aislado varios términos de la serie homóloga $In_2Zn_kO_{3+k}$ ($3<k<13$). El estudio sistemático mediante SAED y HRTEM permite esclarecer la estructura cristalina de los materiales de esta serie de la cual depende su comportamiento luminiscente. En este sentido, el uso de microscopia electrónica con correctores de aberración esférica permite describir la modulación que presentan los miembros de la serie con $k>6$. Las medidas CL ponen de manifiesto que el comportamiento luminiscente de estos materiales viene determinado por su estructura cristalina y varía de manera directamente proporcional al valor de *k*.

ANEXO I TÉCNICAS DE CARACTERIZACIÓN DE PROPIEDADES FÍSICAS

1. CATODOLUMINESCENCIA (CL)

La cátodoluminiscencia (CL) es la emisión de luz como resultado de la incidencia de un haz de electrones sobre un material semiconductor. Permite estudiar la estructura de bandas tanto de materiales aislantes como semiconductores y, en particular, el efecto que producen en esta estructura la presencia de dopantes en el material, así como la morfología y el tamaño de partícula.

La fuente de electrones puede ser tanto de un microscopio electrónico de barrido (SEM) o de transmisión (TEM). En el presente trabajo se han estudiado los materiales en un microscopio electrónico de barrido (SEM), operando a potenciales de aceleración entre 5 y 30 kV.

Cuando un haz de electrones de alta energía incide sobre la muestra, se producen distintos tipos de interacción del haz con el sólido, *figura 1*. En la cátodoluminiscencia, debido a la elevada energía que poseen los electrones del haz acelerado, se crea una gran concentración de pares electrón-hueco, lo que permite excitar de forma eficiente muchos de los centros luminiscentes presentes en el sólido. La emisión que se origina es resultante de todos los mecanismos luminiscentes del material. Estos mecanismos pueden interpretarse como las distintas señales que se recogen, características del material, y que proporcionan información sobre las propiedades físico-químicas del mismo [1].

La recombinación radiativa de los pares electrón-hueco generados presenta dos tipos de mecanismos: intrínsecos y extrínsecos. Los mecanismos intrínsecos son debidos a transiciones banda-banda, donde la energía del fotón emitido coincide con la energía de la banda prohibida; se denomina emisión del borde de banda. Los mecanismos extrínsecos ocurren a través de niveles energéticos asociados a defectos y/o impurezas, que dan lugar a la emisión de fotones de menor energía.

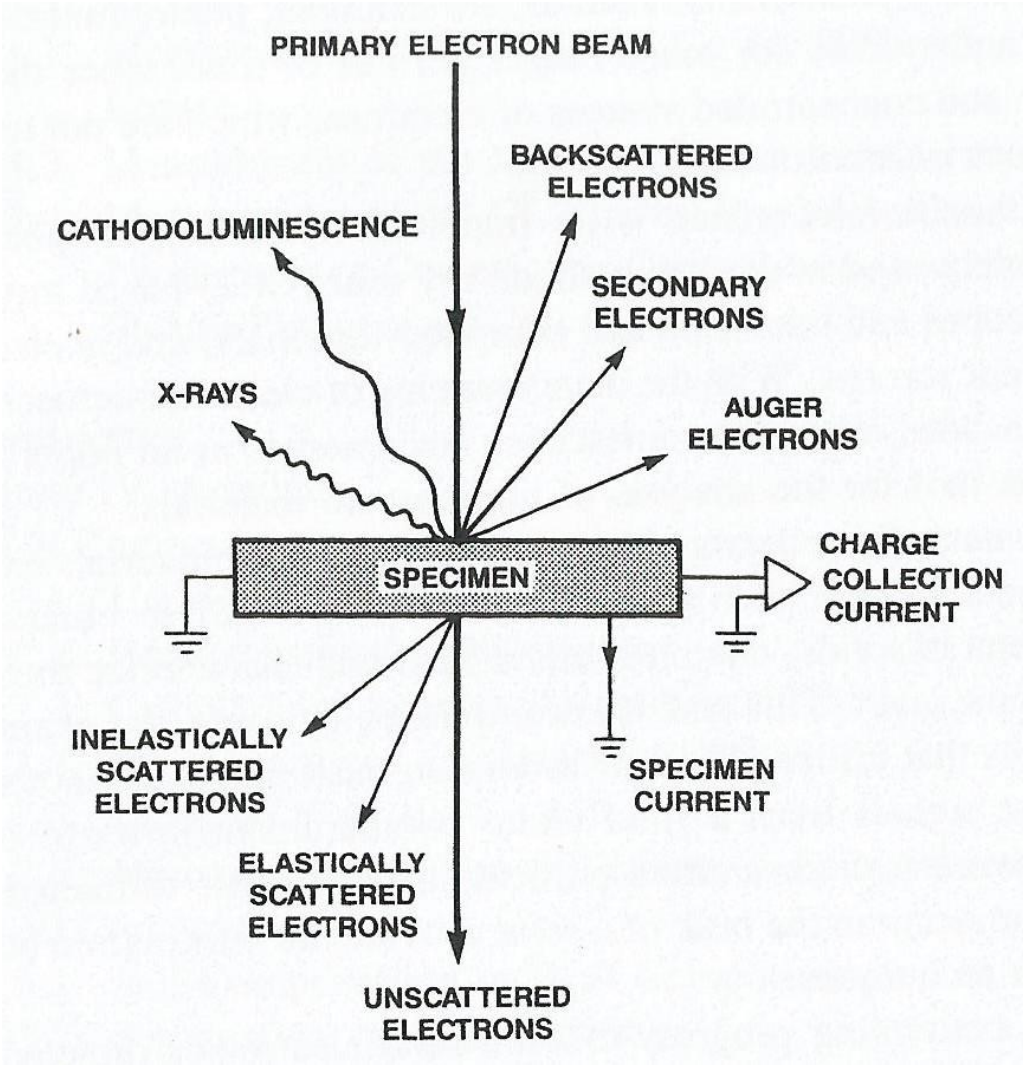

Figura 1. Posibles tipos de interacción de un haz de electrones con un sólido [21].

Dependiendo de la estructura de bandas del material se distinguen dos tipos de transiciones de borde de banda: directa e indirecta (*figura 2*). Durante las transiciones electrónicas ha de conservarse tanto energía como momento. En la transición directa se produce una recombinación, sin variación del momento, entre el electrón y el hueco con la consiguiente emisión del fotón de energía equivalente al intervalo de energías prohibidas. En los procesos denominados indirectos, se necesita la participación de un fonón para que se conserve el momento. De modo que la recombinación de pares electrón-hueco ha de ir acompañada por la emisión de un fotón.

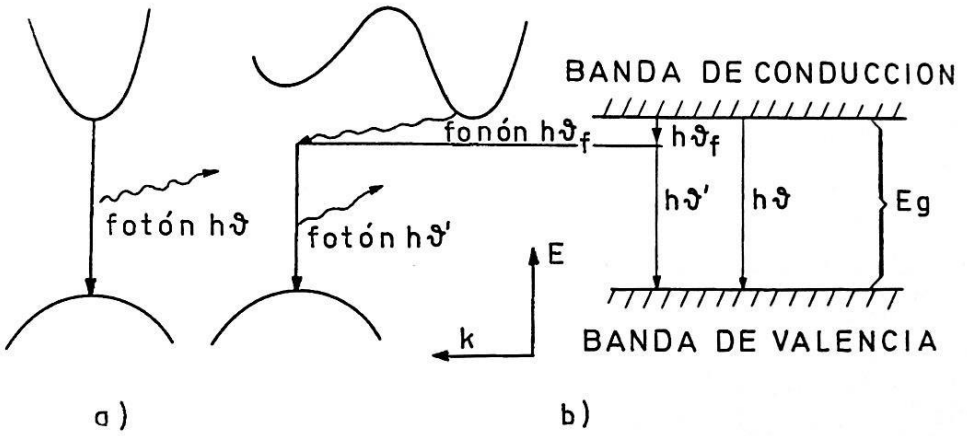

Figura.2. Posibles transiciones radiativas entre la banda de conducción y la banda de valencia, a) directa, b) indirecta con la consecuente participación de un fonón.

En la *figura 3* se recogen esquemáticamente los procesos radiativos que provocan la emisión extrínseca.

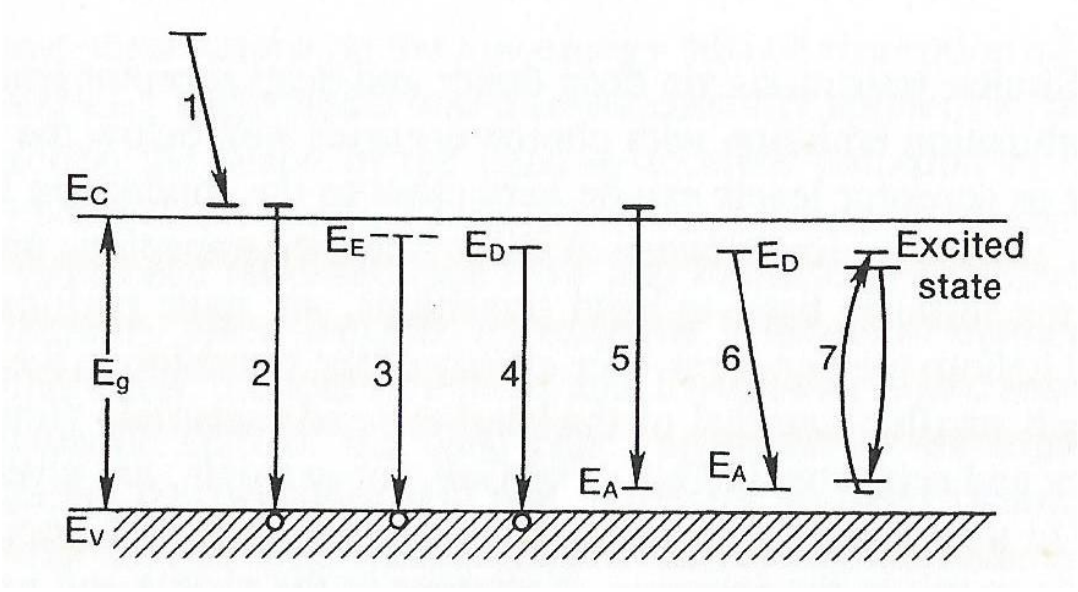

Figura 3. Diagrama esquemático de las transiciones radiativas entre la banda de conducción (E_C), banda de valencia (E_V) y niveles de aceptores (E_A), donores (E_D) y excitones (E_E) en un material semiconductor.

El proceso 1 es una transición intrabanda, que conlleva una emisión de un fonón. El proceso 2, corresponde a una transición interbanda, que produce la luminiscencia intrínseca. El proceso 3 ocurre a bajas temperaturas, cuando los pares electrón-hueco forman un estado confinado, denominado excitón, cercano a la banda de conducción, cuya recombinación produce una emisión cercana a la de borde de banda. Los procesos 4, 5 y 6 comienzan y/o terminan en estados localizados debidos a la presencia de impurezas en el intervalo de energías prohibidas, son responsables de la luminiscencia extrínseca de los materiales. Por

último, el proceso 7 corresponde con la excitación y la desexcitación radiativa de una impureza con capas externas incompletas, como es el caso de los metales de transición y de tierras raras.

Cuando la recombinación radiativa es el proceso dominante, la intensidad de la CL debe ser exclusivamente proporcional al voltaje del haz de electrones. En cambio, si dominan los procesos no radiativos han de considerarse por separado los casos donde se emplea distinto voltaje.

La señal CL está influenciada por la temperatura a la que se encuentre la muestra. A temperatura ambiente, las transiciones radiativas compiten con las transiciones no radiativas en las que intervienen fonones lo que da lugar a anchas bandas de emisión. Al disminuir la temperatura, disminuye la contribución de los fonones y la señal se intensifica, por la disminución de la vibración térmica y la localización electrónica. Por lo que los espectros CL a baja temperatura presentan bandas de emisión más intensas y estrechas o localizadas.

El volumen del que procede la señal de catodoluminiscencia, denominado volumen de excitación, depende de la composición del material y de la energía del haz incidente, según la ecuación de Kanaya y Okayama [2]:

$$R_e = (0.0276A \ \ \rho Z^{0.889}) E_b^{1.67} \ (\mu m)$$

Donde R_e es el rango de penetración ρ es la densidad en gr/cm^3 y E_b la energía del haz de electrones en keV, A es el peso atómico en gr/mol y Z es el número atómico. La forma del volumen de excitación depende de Z, así, para Z pequeños el volumen de generación presenta forma de pera, siendo aproximadamente esférico para 15<Z<40 y semiesférico para Z mayores.

El análisis espectral de la señal de catodoluminiscencia permite identificar y estimar la distribución y concentración relativa de los diversos centros luminiscentes presentes en un material, así como estudiar su comportamiento al variar las condiciones de observación (densidad de excitación, temperatura, etc.). Las condiciones de elevada densidad de excitación corresponden a aquéllas en las que se enfoca el haz electrónico sobre la superficie de la muestra, de modo que éste reparta su energía sobre un área menor. Por el

contrario al desenfocar el haz, disminuye el número de electrones inyectados en la muestra por unidad de área, lo que genera una densidad de excitación menor. La señal total de CL aumenta desenfocando el haz, ya que al irradiar un área mayor se eleva el número de procesos excitados que contribuyan a la luminiscencia. Sin embargo, las distintas emisiones que componen la señal CL evolucionan de modo desigual.

En la *figura 4* se muestra un esquema del sistema experimental utilizado para obtener los espectros de catodoluminiscencia.

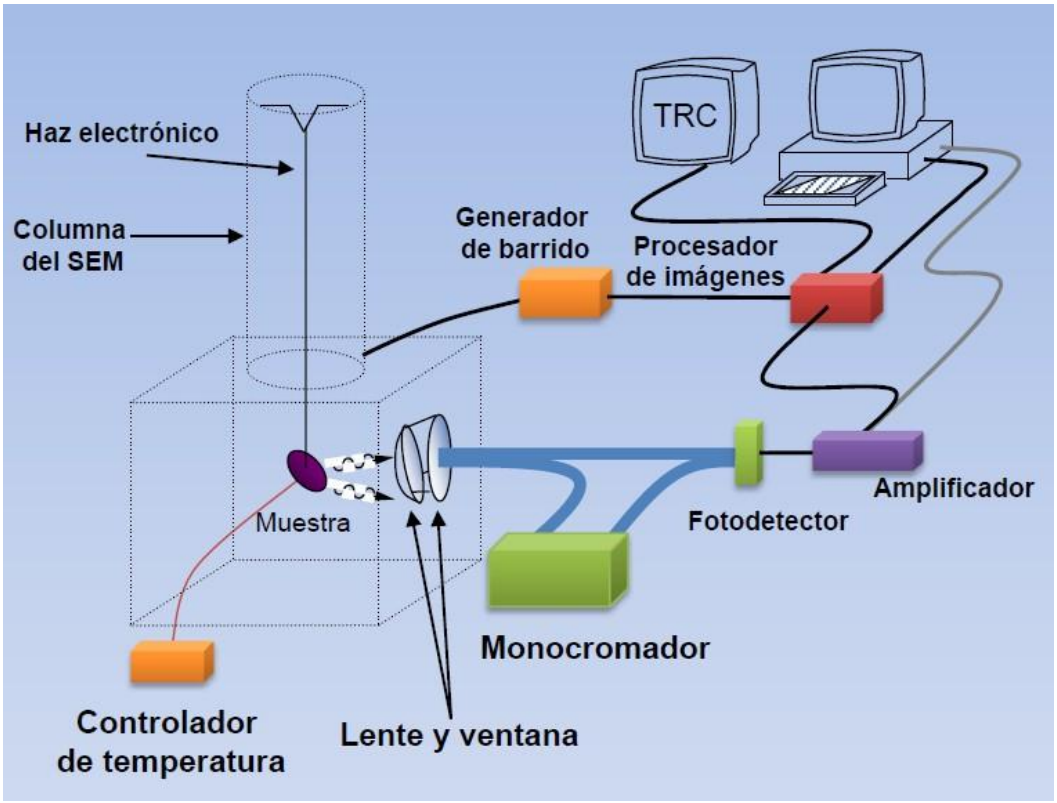

Figura 4.- Sistema experimental de obtención de espectros de catodoluminiscencia en un microscopio.

2. ESPECTROSCOPIA RAMAN

La espectroscopía Raman es una técnica no destructiva que proporciona información química y estructural del material a analizar. Se basa en el análisis de la luz dispersada inelásticamente por un material, al incidir sobre el mismo un haz de luz monocromático. Cuando un fotón incide sobre la red cristalina del material, puede interaccionar inelásticamente con los modos de vibración o fonones de la red. Parte de su energía será absorbida por el fonón de la red, dando lugar a un fotón resultante con una energía E_f desplazada de la energía inicial o incidente, E_i, en una cantidad proporcional a fonón Ω, denominado desplazamiento de Stokes. También es posible el proceso contrario donde el fotón absorbe un fonón dando lugar a un fotón final de energía final equivalente a la E_i más Ω (desplazamiento anti-Stokes). Estos procesos ocurren de acuerdo con las leyes de conservación de momento y energía:

$$Ef=Ei\pm\Omega$$

En un espectro Raman se miden las variaciones en la frecuencia de la luz láser que interacciona con la muestra, a partir de las cuales, se obtiene información sobre la estructura cristalina, pudiendo determinar los estados vibracionales y enlaces químicos de las especies que componen la muestra, además de los efectos que introduzcan desorden, como puede ser, daño por implantación, irradiación, tensiones, etc.

En los espectros Raman se representa la intensidad de la luz en función del desplazamiento en frecuencias que sufre el haz incidente al ser dispersado inelásticamente por el material.

3. ESPECTROSCOPIA DE FOTOEMISION DE RAYOS X

La espectroscopía de fotoemisión de rayos X *(X-Ray Photoemission Spectroscopy*, XPS) se basa en la fotoemisión de electrones debido a la irradiación con un haz de rayos X. El proceso de fotoemisión, figura 5, se produce cuando un fotón de elevada energía interacciona con un electrón de un orbital atómico, cediéndole su energía y provocando que éste abandone su posición y escape con cierta energía [3]. Mediante un espectrómetro que recogen y analizan los electrones fotoemitidos (fotoelectrones) clasificándolos en función de su energía cinética.

La energía del fotoelectrón obedece el principio de conservación de energía por lo que, la energía de enlace se calcula mediante la siguiente ecuación:

$$E_{kin} = h\nu - E_{bind} - \Phi$$

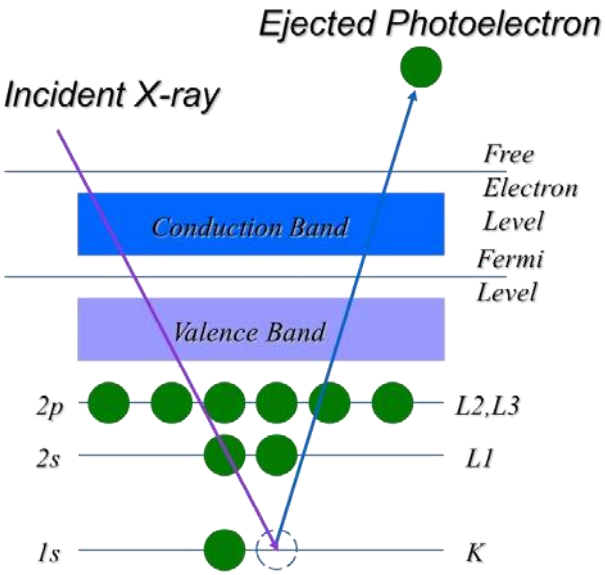

Figura 5. Efecto fotoeléctrico.

Donde E_{kin} es la energía cinética del fotoelectrón emitido, *hv* es la energía de los fotones incidentes (normalmente se emplean rayos X "suaves", con energías comprendidas entre 300-1000 eV), E_{bind} es la energía de enlace del electrón y Φ es la función de trabajo del espectrómetro. Esta técnica requiere el uso de condiciones de alto o ultra-alto vacío. Los puntos fuertes de la espectroscopia de fotoemisión son su elevada sensibilidad química e idoneidad para el estudio de la superficie de una gran variedad de materiales. La energía de enlace del fotoelectrón contiene de por sí información sobre la composición química de la muestra, ya que para cada uno de los elementos hay una energía de enlace, E_{bind}, asociada a

cada uno de sus posibles estados electrónicos/ orbitales atómicos. Además, se obtiene información sobre el entorno químico en el que se encontraba el electrón antes de producirse la fotoemisión (tipo de enlace, estado de oxidación, presencia de sustancias adsorbidas,…) ya que todo esto produce un desplazamiento característico en la energía de enlace.

La elevada sensibilidad a la superficie de la técnica XPS se comprende mejor al tener en cuenta el reducido recorrido libre medio de los electrones en un sólido (de tan solo unos pocos Å). Por lo tanto los fotoelectrones analizados mediante XPS provienen de las primeras capas del sólido, haciendo de esta técnica una poderosa herramienta para el análisis químico y estudio de la superficie de los sólidos.

BIBLIOGRAFÍA

[1] B. G. Yacobi y D. B. Holt *"Cathodoluminescence Microscopy of Inorganic Solids"* **(1990)** Plenum Press.

[2] K. Kanaya, S. Okayama, *J. Phys. D: Appl. Phys.* 5 **(1979)** 43.

[3] A. Einstein*, Ann. Physik,* 17 **(1905)** 132; **1921** *Nobel Prize in Physics*.